

# Understanding deep eutectic systems from solid–liquid equilibria perspective: Experimental study and thermodynamic modeling

Ahmad Alhadid

Vollständiger Abdruck der von der TUM School of Life Sciences der Technischen Universität München zur Erlangung eines

Doktors der Ingenieurwissenschaften (Dr.-Ing)

genehmigten Dissertation.

Vorsitz:

Prof. Dr. Heiko Briesen

Prüfende:

1. Prof. Dr. Mirjana Minceva
2. Prof. Dr. Jakob Burger
3. Prof. Dr. Piotr Cysewski

Die Dissertation wurde am 02.06.2022 bei der Technischen Universität München eingereicht und durch die TUM School of Life Sciences am 26.09.2022 angenommen.

# Table of Contents

Acknowledgments .....	2
Abstract .....	3
Kurzzusammenfassung.....	4
1. Introduction .....	6
2. Theory.....	10
2.1 Eutectic mixtures.....	10
2.2 Types of phase diagram .....	11
2.3 Experimental determination of SLE .....	13
2.3.1 Visual and centrifugation methods.....	13
2.3.2 DSC .....	14
2.4 Thermodynamics of SLE .....	21
2.4.1 Melting properties of pure components .....	23
2.4.2 Activity coefficients .....	25
2.4.3 Modeling SLE phase diagram .....	30
3. Results.....	33
3.1 Paper I.....	34
3.2 Paper II.....	64
3.3 Paper III.....	80
3.4 Paper IV.....	99
3.5 Paper V.....	118
3.6 Paper VI.....	143
4. Discussion .....	164
4.1 Measuring and modeling SLE.....	164
4.2 DES formation .....	167
5. Conclusion.....	171
6. Outlook .....	172
Abbreviations.....	174
Symbols.....	175
List of figures .....	177
References.....	178

## Acknowledgments

I am sincerely appreciative to Prof. Minceva for her supervision, guidance, time, and consideration during the work on this thesis. I thank Prof. Burger and Prof. Cysewski for their time and consideration in evaluating the thesis and Prof. Briesen for accepting the role of the chair of the examination committee.

Words cannot express my gratitude to Dr. Mokrushina, the mastermind behind the proposed question of the thesis. A sincere thank goes to Dr. Jandl for the great and fruitful collaboration over the last two years of the thesis.

I came to know great people during my stay at the Biothermodynamics group, Anja, Heinrich, Yasemin, Caren, Franzi, Simon, Martin, Raena, Andy, Rana, Lukas, Ana Maria, Kamila, Marko, Vlad, Melanie, Vanessa, Jan, Benedikt, Daili, Pei, and Sahar. I thank you all for the great time we had, and I'm looking forward to continuing my next years in the group. I'm grateful for the opportunity to work with and supervise many awesome and hardworking students, Lea, Irsa, Deniz, Joel, Maeliss, and Christoforos. Many thanks to Thomas, Sharad, and Ali for sharing their wisdom and expertise in academic life.

I dedicate this thesis to my parents, my dearests and support, to my only love and best friend, Manal, and to my joy givers, Nawal and Yusuf. I would like to thank my brother, sisters, and family for their love and support. Lastly, I would be remiss in not mentioning our dear friends Mohammad and Meli for the great moments even during the difficult CORONA times.

الْحَمْدُ لِلَّهِ رَبِّ الْعَالَمِينَ

## Abstract

Deep eutectic solvents (DES) are a class of designer solvents that can be prepared by mixing two or more compounds to form a solution with a freezing temperature significantly lower than that of pure constituents. Because the DES physicochemical properties correlate with those of pure constituents, the solvent properties can be tuned by selecting the constituents and their molar ratio. Having a liquid solution at the desired operating temperature is of utmost importance to employing DESs as solvents in various applications. The melting temperature of the mixture at any molar ratio can be obtained from the solid–liquid equilibria (SLE) phase diagram. However, as DESs can be prepared from a large pool of substances, obtaining the SLE phase diagram experimentally becomes a demanding task that often accompanies many difficulties. Therefore, understanding DES formation is a vital goal to preselect the constituents and define the suitable molar ratio range to tune the solvent properties accordingly.

This thesis aims to understand the reason for the formation of eutectic mixtures with a significant depression of the melting temperature at the eutectic point from a SLE perspective. To achieve this, SLE in binary eutectic mixtures was studied based on experimental and theoretical investigations. The SLE phase diagram of 11 eutectic systems of various complexity was measured and modeled. Moreover, seven cocrystals not reported before were identified in four different eutectic systems. The SLE phase diagrams reported in this thesis were obtained by combining rigorous thermal analysis using differential scanning calorimetry and solid phase characterization using X-ray diffraction, where the latter is often lacking in literature studies leading to incorrect interpretation of SLE phase diagrams. Furthermore, the capability of correlative and predictive activity coefficient models, namely, the non-random two-liquid (NRTL) model and conductor-like screening model for realistic solvation (COSMO-RS), in describing the nonideality in strongly nonideal eutectic systems with complex phase diagrams was evaluated.

Based on the thesis results, DESs were found to form as a result of significant negative deviation from ideal behavior and very low melting enthalpy and entropy of constituents. The very low melting entropy is a unique character of substances with highly disordered and symmetrical crystal structures, i.e., plastic crystalline materials. Therefore, the selection of DES constituents is narrowed down from arbitrary salts and organic substances to plastic crystalline materials. The thesis findings will aid in selecting DES constituents to improve the design approaches and the utilization of DES in various applications.

## Kurzzusammenfassung

Tief eutektische Lösungsmittel (DES) stellen eine Klasse von Designerlösungsmitteln dar, die durch Mischen von zwei oder mehr Verbindungen hergestellt werden können. Dadurch entsteht eine Lösung, die eine Gefriertemperatur aufweist, welche deutlich unter der der reinen Bestandteile liegt. Da die physikochemischen Eigenschaften von DES mit denen der reinen Bestandteile zusammenhängen, können die Lösungsmittleigenschaften durch Auswahl der entsprechenden Bestandteile und Molverhältnisse eingestellt werden. Um bei gewünschter Betriebstemperatur eine flüssige Lösung vorliegen zu haben, ist der Einsatz von DES als Lösungsmittel in verschiedenen Anwendungen von größter Bedeutung. Die Schmelztemperatur des Gemischs bei einem beliebigen Molverhältnis lässt sich anhand des Phasendiagramms des Fest-Flüssig-Gleichgewichts (SLE) ablesen. Da DESs jedoch aus einer Vielzahl an Substanzen hergestellt werden können, ist die experimentelle Vorgehensweise zur Ermittlung des SLE-Phasendiagramms eine anspruchsvolle Aufgabe, die oft mit vielen Schwierigkeiten verbunden ist. Daher ist ein Verständnis der Bildung von DES für die Vorauswahl der Bestandteile und die Festlegung des geeigneten Molverhältnisses von entscheidender Bedeutung, um die Lösungsmittleigenschaften entsprechend einstellen zu können.

Ziel dieser Arbeit ist es, die Ursache für die Bildung eutektischer Gemische mit signifikant niedriger eutektischer Temperatur aus der Perspektive der SLE zu verstehen. Zu diesem Zweck wurden die SLE in binären eutektischen Mischungen auf der Grundlage von experimentellen und theoretischen Untersuchungen betrachtet. Das SLE-Phasendiagramm von 11 eutektischen Systemen mit unterschiedlicher Komplexität wurde erfasst und modelliert. Darüber hinaus wurden in vier verschiedenen eutektischen Systemen sieben bisher nicht angegebene Kokristalle identifiziert. Die in dieser Arbeit dargestellten SLE-Phasendiagramme konnten anhand einer Kombination einer strengen thermischer Analyse und einer Festphasencharakterisierung erhalten werden, wobei letztere in Literaturstudien oft fehlt, was zu einer falschen Interpretation der SLE-Phasendiagramme führt. Darüber hinaus wurde die Fähigkeit von korrelativen und prädiktiven thermodynamischen Modellen zur Beschreibung der Nichtidealität in stark nicht-idealen eutektischen Systemen mit komplexen Phasendiagrammen bewertet.

Ausgehend von den Ergebnissen der Dissertation konnte festgestellt werden, dass die Bildung von DES das Ergebnis einer signifikanten negativen Abweichung vom idealen Verhalten und einer sehr niedrigen Schmelzenthalpie und -entropie der Bestandteile ist. Die sehr niedrige

Schmelzentropie ist ein Alleiniges Merkmal von Stoffen mit einer hochgradig ungeordneten und symmetrischen Kristallstruktur, d. h. von plastischen kristallinen Materialien. Daher wird die Auswahl der DES-Bestandteile von beliebigen Salzen und organischen Substanzen auf plastisch-kristalline Materialien beegrenzt. Die Ergebnisse dieser Arbeit werden bei der Auswahl von DES-Bestandteilen helfen, um die Designansätze und die Nutzung von DES in verschiedenen Anwendungen zu verbessern.

## 1. Introduction

The establishment of green and sustainable chemistry concepts in process applications calls for the utilization of green solvents.<sup>1</sup> Green solvents should not only comply with the principles of green chemistry but also be potential alternatives to conventional solvents while being economically feasible.<sup>2</sup>

One of the first classes of solvents that has been proposed to be green is Ionic liquids (ILs).<sup>3-6</sup> ILs are salts with relatively low melting temperature—compared to conventional salts—that contain organic cations and organic or inorganic anions.<sup>7</sup> Being salts, ILs possess negligible vapor pressure and are nonflammable.<sup>8</sup> The variety of combinations of cations and anions that can form ILs suggests that the properties of ILs can be tailored for a specific task.<sup>9</sup> Although ILs fulfill some of the requirements for green solvents, they bring some concerns. First, each IL should be chemically synthesized, necessitating the use of conventional organic solvents and producing wastes that may be potentially hazardous.<sup>10</sup> Second, from an economic point of view, ILs are still significantly more expensive than conventional solvents, which is undoubtedly the main drawback of using ILs in industrial-scale applications.<sup>11</sup>

In 2001, Abbott et al.<sup>12</sup> performed the first trials to liquefy quaternary ammonium halide salts with the formula  $[\text{Me}_3\text{NC}_2\text{H}_4\text{Y}]\text{Cl}$  ( $\text{Y} = \text{OH}, \text{Cl}, \text{OC}(\text{O})\text{Me}, \text{OC}(\text{O})\text{Ph}$ ) by mixing them with zinc or tin chlorides. Out of several quaternary ammonium halide salts investigated in the study, mixtures containing choline chloride (ChCl) had the lowest melting temperature. These mixtures were called deep eutectics due to the large depression in the melting temperature of the mixture at the eutectic point relative to pure constituents' melting temperature. The significant depression in the melting temperature was attributed to the formation of complex zinc or tin chloride ions, e.g.,  $[\text{ZnCl}_3]^-$ ,  $[\text{Zn}_2\text{Cl}_5]^-$ , and  $[\text{Zn}_3\text{Cl}_7]^-$ . The deep eutectic mixtures resemble ILs in terms of properties however overcome some of their drawbacks, e.g., preparation by chemical synthesis and feasibility.

The search for other so-called “complexing agents” continued by the same group. Abbott et al.<sup>13</sup> showed in 2003 that urea could replace zinc and tin chlorides to form deep eutectics. Further studies showed that various carboxylic acids could also be used, suggesting that any hydrogen bond donor (HBD) can form deep eutectics when mixed with ChCl.<sup>14</sup> Later, the term deep eutectic solvents (DES) was introduced and defined as a mixture of a hydrogen bond acceptor

(HBA) and HBD with a eutectic temperature significantly lower than the melting temperature of pure constituents.<sup>15</sup>

Soon after, the number of studies related to understanding the formation of DES and the search for new and improved DESs increased sharply.<sup>16-28</sup> The main hypothesis of these studies was that hydrogen bonding and complex formation are the reason for DES formation. Moreover, DESs have been postulated as a special type of liquids that are microscopically heterogeneous and complex.<sup>29</sup> Therefore, investigations relied on quantum mechanical, molecular simulation, and experimental methods to unravel the microscopic nature of DES and understand their formation.<sup>16, 17, 20, 23-25, 30-46</sup> However, it was impossible to quantify the eutectic ratio and temperature from theoretical and experimental microscopic studies.<sup>18</sup>

Later, after a series of papers investigating the solid–liquid equilibria (SLE) in DES, Coutinho and coworkers proposed another definition for DES.<sup>47</sup> First, they defined DES as physical mixtures from a thermodynamic point of view. Second, they noticed that the formation of DES could be due to strong hydrogen bonding and negative deviation of the system from ideal solution behavior. Third, DES is a term that describes the mixture at any composition and is not specific to the mixture at the eutectic composition, which probably might not be of a specific ratio, such as 1:1 or 1:2 molar ratios. Accordingly, Martins et al.<sup>47</sup> suggested that only eutectic mixtures with negative deviation from ideal behavior should be called DES.

The main feature of the proposed definition of Coutinho and coworkers, which was also adopted by other groups,<sup>48, 49</sup> is the rationalization of the understanding and designing of DES, i.e., the selection of the constituents and their ratio. SLE phase diagram provides information on the melting temperature of the mixture at any ratio between constituents—including the eutectic point—as well as on the intermolecular interactions between unlike molecules. However, due to the large number of substances that can form eutectic mixtures, it is impossible to measure the phase diagram of all possible DES. Therefore, the number of DES with available SLE data is significantly lower than the number of DES studied in the literature.

Although the study of DES from the SLE perspective can provide direct interpretation for the melting temperature of the mixture, SLE studies are difficult to be comprehended and executed by nonexperts in thermodynamics. Consequently, the term DES is usually used arbitrarily for any eutectic mixtures forming a liquid at room temperature, though in some, one or both constituents are liquid at or near room temperature. Out of many DES constituents proposed in the literature,



## Introduction

ChCl and a few other quaternary ammonium halide salts are the only constituents that can form eutectic mixtures with a eutectic temperature significantly below the melting temperature of pure constituents. This might hint that the observed significant depression in the mixture melting temperature at the eutectic point in ChCl-based DES is due to the unique character of ChCl. Hence, it might be possible to obtain a DES by an appropriate selection of constituents without the need for SLE or microscopic structure studies.

Regardless of their definition or nature, DES has been proved to outperform conventional solvents in various applications. DESs have been shown to efficiently extract bioactive compounds from various natural sources.<sup>50-56</sup> From a process application perspective, DESs have shown great potential as solvents for gas capture,<sup>57-61</sup> liquid chromatography,<sup>62-67</sup> and extractive distillation.<sup>68-71</sup> Besides using DES in their liquid states, the depression in the melting temperature of the DES has been employed to improve the solubility of active pharmaceutical compounds and modify their crystal structure.<sup>72-79</sup> Because a large pool of substances can form DESs, they can be utilized in a vast number of applications, of which only a part has been investigated so far.

Although the physicochemical properties of eutectic mixtures may correlate with intermolecular interactions between molecules in the liquid solution, the reason why the eutectic mixtures could replace conventional solvents in various applications does not necessarily originate from a specific microscopic structure or strong intermolecular interactions in the liquid solution. Instead, understanding the physicochemical properties of eutectic mixtures and correlating them with the pure constituents' physicochemical properties is required to form eutectic mixtures with tunable properties as alternative solvents for a specific application. However, the superiority of DESs over common eutectic mixtures is the large depression in the mixture melting temperature, which provides a wider selection of systems that can be liquid at or near room temperature to be used as solvents.

This thesis aims to investigate the reason for the formation of eutectic mixtures with significantly low eutectic temperatures from a SLE perspective. A comprehensive and systematic experimental and theoretical study of SLE in various eutectic mixtures was performed to investigate why a DES can be formed. First, the proper experimental determination and modeling of SLE were carried out to obtain SLE data of eutectic mixtures of various complexity. Second, the parameters influencing the phase diagram and the position of the eutectic point of eutectic

## Introduction

mixtures, namely, melting properties, nonideality of the liquid phase, and solid complex formation, were examined.

The thesis is organized into six sections. In Section 2, the pertinent theory is introduced, covering the basic definitions for eutectic mixtures, thermal characterization, and thermodynamic modeling. The results are presented in the form of six published papers in Section 3 along with a summary of each paper. A thorough discussion of the papers findings and comprehensive analysis of the thesis topic is given in Section 4. Section 5 contains the general conclusions. In Section 6, the outlook for the future work is presented.

## 2. Theory

The current section covers the theory and the methods used to obtain the findings of the thesis. First, an overview of eutectic mixtures is presented in Section 2.1. Second, a brief description of the SLE phase diagram of different complexity is covered in Section 2.2. Third, the thermal characterization techniques used to measure SLE are presented in Section 2.3, including a throughout discussion about differential scanning calorimetry (DSC) analysis. Fourth, models and approaches used to model SLE in eutectic mixtures of different complexity are presented in Section 2.4.

### 2.1 Eutectic mixtures

Eutectic mixtures are mixtures of two or more components that crystallize as immiscible or partially immiscible solids.<sup>80</sup> Figure 1 shows a schematic representation of the SLE phase diagram of a binary mixture in which the components crystallize as a miscible solid phase (Figure 1A) or immiscible solid phases (Figure 1B). The liquidus lines (blue lines) represent the temperature at which the last solid disappears upon heating, i.e., the melting temperature of the mixture. The solidus lines (orange lines) depict the temperature at which the first drop of the liquid appears upon heating. The liquidus and solidus lines define the two-phase region in which a liquid phase and a solid phase are in equilibrium. As seen in Figure 1A, the liquidus temperature of the mixture at any composition lies between the melting temperature of the pure components. In contrast, as seen in Figure 1B, the melting temperature of the eutectic mixture can be lower than the melting temperature of the pure components. The lowest possible melting temperature of the eutectic mixture is observed at the eutectic point (marked with a red circle in Figure 1B). At the eutectic point, three phases are in equilibrium, solid A, solid B, and a liquid solution, according to the following reaction



The reaction in Equation (1) is called the eutectic reaction, from which the name eutectic system was derived (means easily melted in ancient Greek).<sup>80</sup>

## Theory

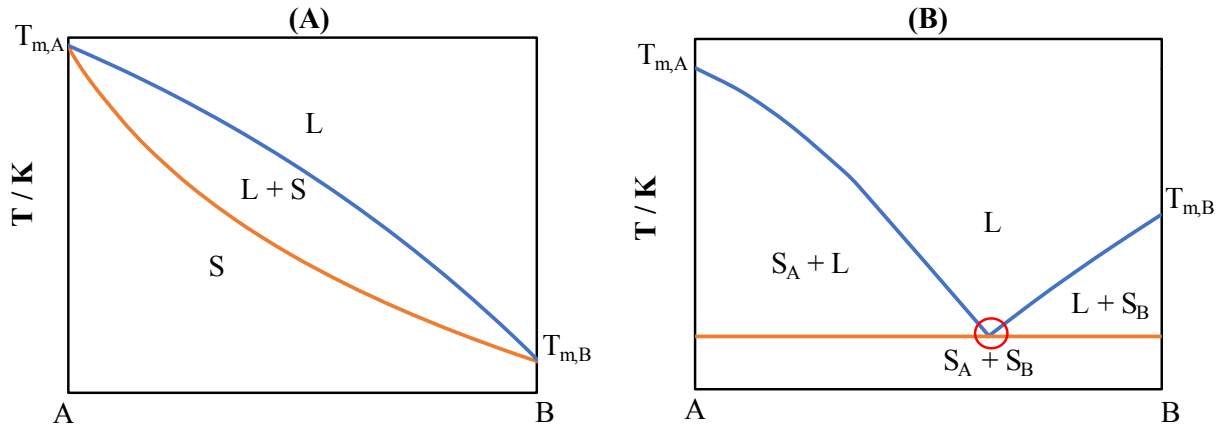


Figure 1. Schematic representation of solid–liquid phase diagram of (A) binary mixture with miscibility in the solid state and (B) binary eutectic mixture.

### 2.2 Types of phase diagram

As described in Section 2.1, the melting temperature of the eutectic mixture at any composition, i.e., liquidus temperature, can be obtained from its SLE phase diagram. In the following, the possible shapes of the binary eutectic mixture phase diagram are presented. The complexity of measuring and modeling SLE is commonly attributed to the complexity of the solid rather than the liquid phase.<sup>81</sup> Figure 2 shows the probable types of the SLE phase diagram of eutectic mixtures. Figure 2A shows the simplest case possible for any binary eutectic mixture. Systems having this type of SLE phase diagram are called simple eutectic systems. In the simple eutectic type, the constituents crystallize as pure solids. Moreover, the system has only one eutectic point. The eutectic point position depends on the course of the two liquidus lines of pure constituents.

The phase diagram shown in Figure 2B is also of the simple eutectic type. However, pure component A undergoes a solid–solid transition at  $T_{S_A \rightarrow S'_A}^{tran}$ . The melting properties of solid  $S_A$  and solid  $S'_A$  may be different, which leads to a different course of the liquidus line of component A at temperatures higher and lower than the solid–solid transition temperature.

Theory

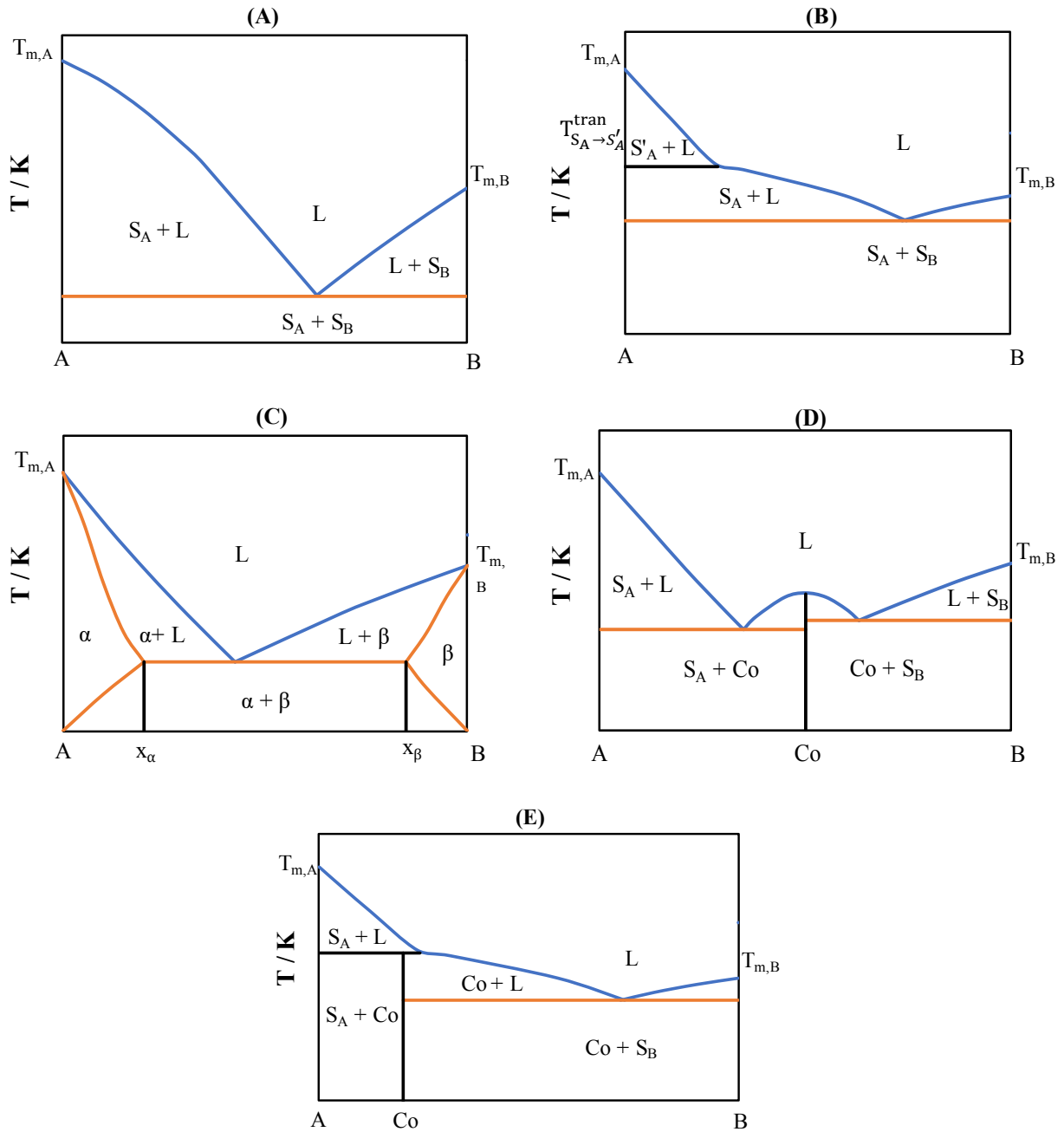


Figure 2. Schematic representations of solid–liquid phase diagrams of different types, defining the crystallized solid phases in each binary eutectic system.

Figure 2C shows the schematic representation for a binary eutectic mixture with partial miscibility in the solid phase. In the example shown in Figure 2C, the eutectic system has two solid solution regions. The  $\alpha$  solid phase has the same crystal structure as pure component A. However, some of the molecules of component A are replaced by component B molecules in the  $\alpha$  solid phase while preserving the same crystal structure of component A. The solubility of component B in

solid component A is temperature-dependent and has a maximum limit of  $x_{\alpha}$ . On the other hand, component A is also soluble in the solid component B forming the  $\beta$  solid phase. Similarly, the solubility limit of component A in solid component B is  $x_{\beta}$ . The formation of solid solution regions is expected when the constituents have very similar molecular and crystal structures. Thus, solid solution regions in organic binary eutectic mixtures are quite uncommon.<sup>82</sup>

The phase diagrams presented in Figures 2D and 2E depict the formation of solid compounds, i.e., a cocrystal between components A and B. The cocrystal formed between components A and B in the phase diagram shown in Figure 2D is a congruently melting cocrystal, i.e., a cocrystal that melts to a binary liquid solution with the exact stoichiometry as that of the cocrystal. In contrast, the cocrystal formed between components A and B in the phase diagram shown in Figure 2E is an incongruently melting cocrystal, i.e., a cocrystal that melts to a solid A and a liquid solution with a different stoichiometry than that of the cocrystal. As seen in Figure 2D, the eutectic system with a congruently melting cocrystal has two eutectic points. Principally, the number of eutectic points for a system with congruently melting cocrystals equals the number of cocrystals plus one. On the other hand, the number of incongruently melting cocrystal does not increase the number of eutectic points for the system.

It is worth mentioning that combining any of the previously discussed cases is possible. For example, a eutectic system containing a component that undergoes a solid-solid transition might show the formation of several congruently and incongruently melting cocrystals in addition to solid solution regions. The complexity of measuring and modeling SLE in such eutectic systems is discussed in the following sections.

## *2.3 Experimental determination of SLE*

### *2.3.1 Visual and centrifugation methods*

Thermal analysis methods can be used to obtain the SLE data of binary eutectic mixtures by determining the melting temperature of the mixture at various compositions. Several thermal analysis methods have been proposed in the literature to determine the SLE data of binary eutectic mixtures.<sup>83, 84</sup> The melting temperature of the mixture can be determined by visual methods, such as a melting point apparatus<sup>85-90</sup> or microscopy.<sup>91</sup> The advantage of using visual methods is that the interpretation of the melting temperature of the mixture is straightforward. However, several important phase transitions, such as solid–solid transition or solidus

temperature, cannot be observed visually. Hence, visual methods might be only suitable for eutectic mixtures of the simple eutectic type.

Van der Bruinhorst et al.<sup>84</sup> proposed a more sophisticated method to obtain the solid–liquid phase diagram of eutectic mixtures. The proposed method depends on equilibrating the eutectic mixture of a certain composition at a temperature in the two-phase region. The liquid and solid phases in equilibrium at a specific composition are separated by centrifugation, and the liquid phase composition is analyzed to determine the liquidus line. The method is advantageous for eutectic mixtures prone to supercooling and glass formation. However, homogenization of the liquid phase is critical before its analysis, which can complicate the sampling procedure. Moreover, the method requires an additional analytical method to determine the composition of the liquid phase. Thus, in contrast to visual methods, the determination of the liquidus line is not straightforward. On the other hand, analogous to visual methods, no information about the solidus temperature of the eutectic mixture can be obtained. Thus, the centrifugation method could be only used to determine the SLE in eutectic mixtures of the simple eutectic type. Nevertheless, the SLE phase diagram of the eutectic system might not be of the simple eutectic type, and hence, a more comprehensive method should be employed. In the following section, the DSC analysis technique used to determine the experimental SLE data for eutectic systems of various complexity is discussed in detail.

### 2.3.2 DSC

DSC is a robust thermal analysis method that can be used to obtain the phase diagram of eutectic mixtures.<sup>83</sup> Figure 3 shows a schematic representation of the DSC analysis principle. Two crucibles, one is empty, and the other contains the sample, are placed inside a furnace and subjected to cooling or heating. The temperature of the two crucibles is measured. When the sample undergoes a phase transition, such as melting, crystallization, or solid–solid transition, heat is absorbed by the sample as latent heat, so the temperature of the sample crucible remains constant. The DSC signal represents a measure of the difference between the temperature of the two crucibles, which is proportional to the heat flow. DSC provides information about any phase transition occurring in the mixture, such as melting and solid–solid transition temperatures. In addition to the transition temperature, DSC analysis can be used to determine the phase transition enthalpy.

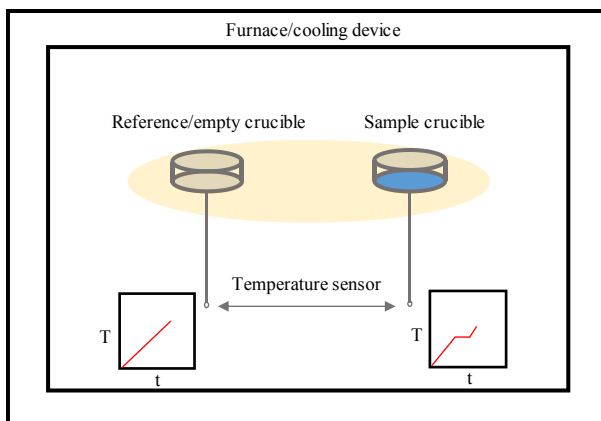


Figure 3. Schematic structure of differential scanning calorimetry chamber.

### 2.3.2.1 Interpretation of DSC curves

In the following, the development of DSC curves of the samples covering the entire composition range of a hypothetical binary eutectic mixture with complex character is discussed. Figure 4 shows a schematic representation of the phase diagram of a hypothetical binary eutectic mixture with the formation of various cocrystals and the observed DSC curve at each labeled point. The DSC curve of *point a* represents the melting temperature of pure component A. The peak corresponding to the melting of a pure substance is usually sharp and symmetrical. By increasing the amount of component B in the mixture, two peaks are observed in the DSC curve at *point b*. The first peak is sharp and symmetrical and corresponds to the decomposition temperature of the incongruently melting cocrystal, while the second peak is asymmetrical and corresponds to the liquidus temperature of the mixture at the composition of *point b*. At *point c*, the observed DSC curve shows three distinct peaks related to the eutectic melting, incongruent melting, and liquidus temperature. At the eutectic point (*point d*), only one sharp and symmetrical peak appears in the DSC curve. The DSC curve of *point e* corresponding to congruently melting cocrystal resembles the DSC curves observed for component A (*point a*) and eutectic melting (*point e*). As seen in Figure 4, component B undergoes a solid–solid transition. Accordingly, the solid–solid transition of component B is observed in the DSC curve at *point f* as a small peak followed by a liquidus peak. Eventually, the DSC curve of component B shows two peaks respective to a solid–solid transition and melting.



## Theory

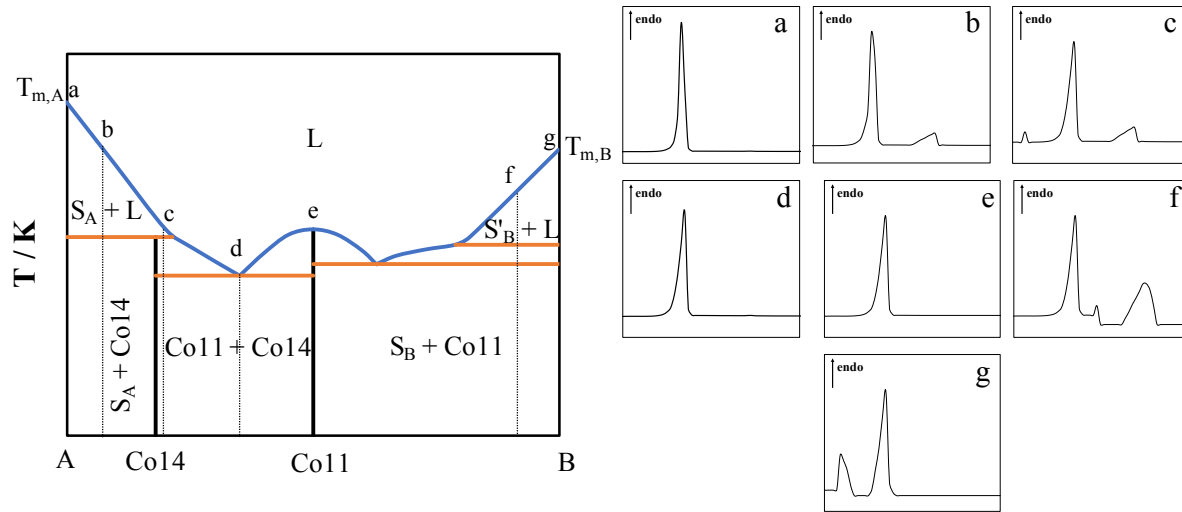


Figure 4. Schematic representation of a phase diagram of a hypothetical binary eutectic mixture and the observed differential scanning calorimetry curve at each labeled point.

Despite the ability of DSC analysis to determine any phase transition temperature and enthalpy, the interpretation of the DSC signal is rather not straightforward. As seen in Figure 4, eutectic, incongruently, and congruently melting peaks are analogous in shape, which can be confusing to assign the peak to the corresponding phase transition. Thus, additional analysis methods, such as X-ray diffraction (XRD), are required to comprehend the crystallized solid phases in each composition region and, accordingly, assign the peaks observed in the DSC curve of the samples to the proper transition.

Figure 5 shows DSC curves of a pure component and a sample in a eutectic system. The phase transition enthalpy  $\Delta h_m$  is determined by the area of the corresponding peak. By definition, the solidus temperature is the temperature at which the first drop of liquid appears (See Section 2.1). Thus, the onset temperature of the corresponding peak well represents the eutectic, incongruent and congruent melting ( $T_m$  and  $T^{\text{solidus}}$  in Figure 5). On the other hand, the liquidus temperature is the temperature at which the last solid disappears. Thus, the peak maximum temperature is commonly used for determining the liquidus temperature (see Figure 5B).<sup>83</sup>

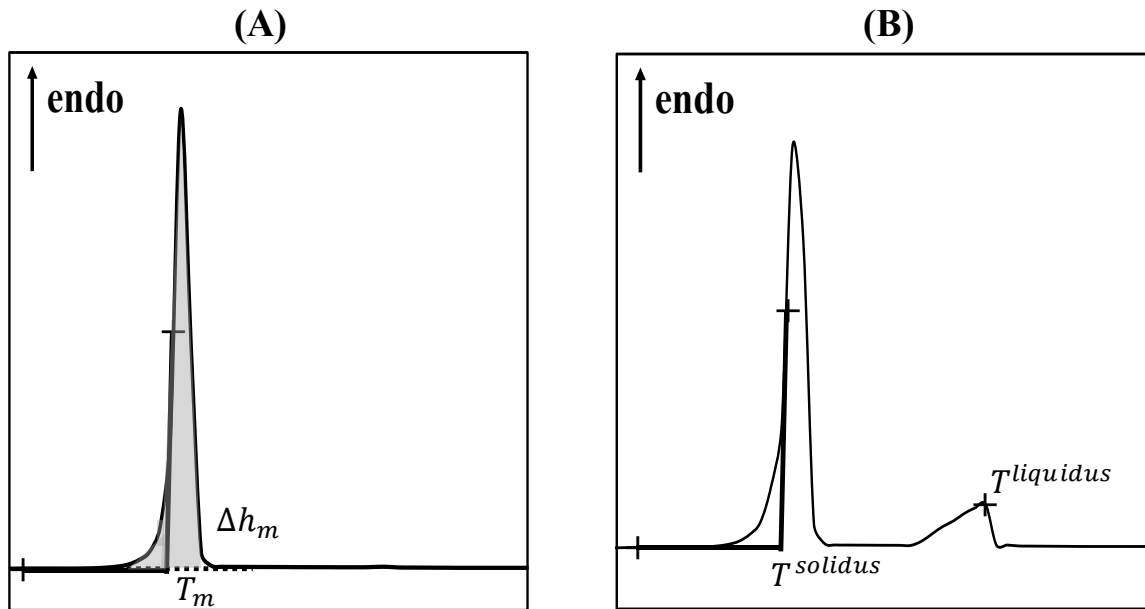


Figure 5. Determining the melting, solidus, and liquidus temperatures and phase transition enthalpy from a differential scanning calorimetry curve.

Tammann's plot can be used to determine the eutectic composition, solubility limit in the solid phase, and the cocrystal stoichiometry experimentally from the DSC analysis. Tammann's diagram is constructed by plotting the eutectic phase transition enthalpy (the area of the solidus peak) as a function of the mole fraction of one of the components.<sup>83</sup> Figure 6 shows a schematic representation of the SLE phase diagram of the simple eutectic type (Figure 6A), a eutectic system with partial miscibility in the solid phase (Figure 6B), and a eutectic system with a cocrystal formation (Figure 6C) along with the corresponding Tammann's plot obtained from the area of the solidus peak. As shown in Figure 6, the eutectic transition enthalpy depends linearly on the mole fraction of the component. For eutectic systems of the simple eutectic type (Figure 6A), the eutectic point can be obtained from the intercept of the two lines regressed to eutectic transition enthalpy in the hypoeutectic (composition range on the left side of the eutectic point) and hypereutectic (composition range on the right side of the eutectic point) regions. For a eutectic system with partial miscibility in the solid phase (Figure 6B), the lines regressed to the eutectic transition enthalpy in the hypoeutectic and hypereutectic regions intercept the x-axis at the solubility limits in the solid phase of component A in B and vice versa. Thus, Tammann's plot does not only provide the solubility limit but can also provide information about the phase diagram type. In the case of cocrystal formation (Figure 6C), the stoichiometry of the cocrystals and the eutectic points of the system can be determined from Tammann's plot. Despite the

valuable information that can be obtained from Tammann's plot, the reliability of the obtained information depends largely on the quality of the determined phase transition enthalpy. In many cases, the peaks corresponding to different phase transitions might overlap, limiting the possibility of constructing Tammann's plot for the eutectic system.<sup>83, 92</sup>

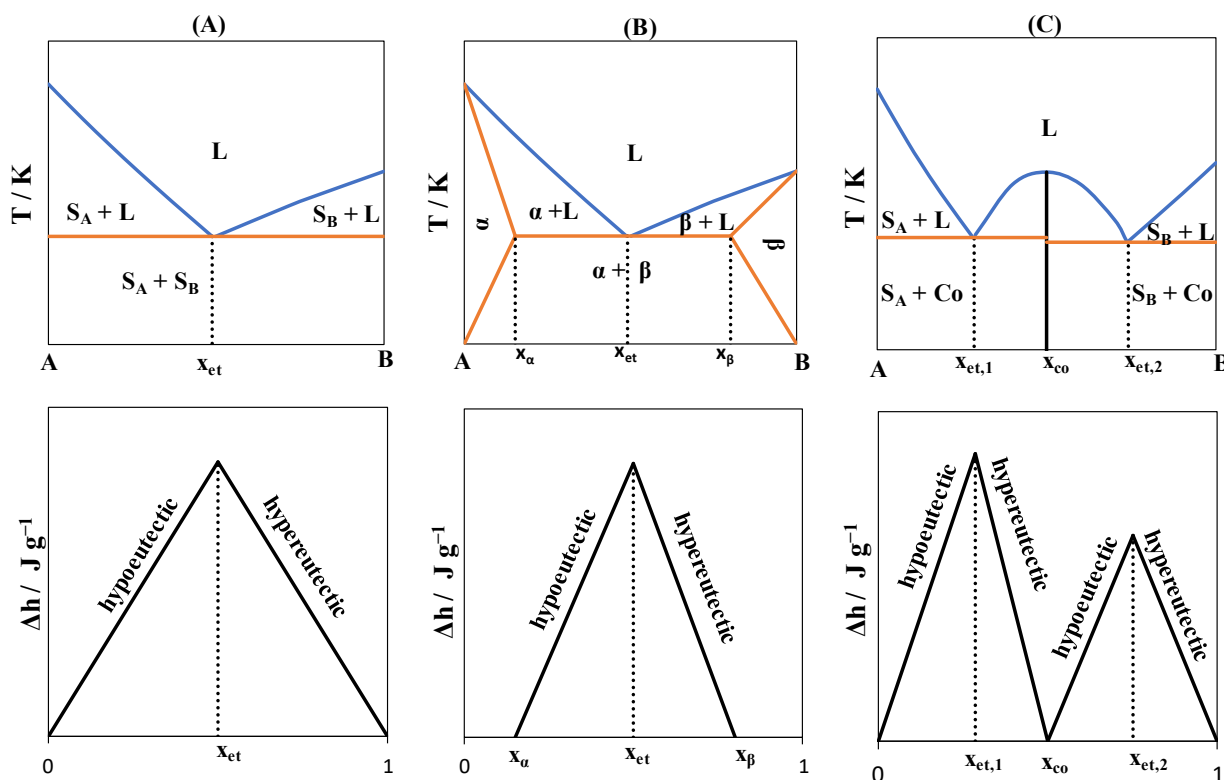


Figure 6. Schematic representation of solid–liquid phase diagrams of different types and the obtained Tammann's plot for each type.

### 2.3.2.2 DSC analysis protocol

The DSC analysis parameters are the heating and cooling rates, sample mass, and measurement temperature range. The heating and cooling rates used in DSC analysis can affect the shape of the solidus and liquidus peaks. Slower heating rates eliminate the effect of heat conductivity of the sample and provide more time for the sample to reach equilibrium. However, slower heating rates affect the sensitivity of the DSC analysis, which might leave out the detection of some transitions, especially those with low transition enthalpy, such as liquidus temperatures near the eutectic point.<sup>93</sup> The commonly used heating rates are between 1–10 K min<sup>-1</sup>. Cooling rates are usually selected based on the capacity of the cooling device as the transition temperature and

## Theory

enthalpy are determined from the heating runs only. However, cooling rates can be critical for substances existing in different polymorphs.<sup>94</sup> Fast cooling might lead to supercooling, glass formation, and crystallization of metastable solid phases.<sup>73, 95</sup>

The DSC instrument is calibrated using standard calibration substances with known phase transition temperature and enthalpy before measurements. The transition enthalpy is used to calibrate the instrument sensitivity, i.e., the area of the observed peak in the DSC curve of the standard material. The onset temperature of the transition peak of the standard materials is used for temperature calibration. The calibration procedure is performed at the same heating rate planned for the measurement. Consequently, pure components, eutectic, incongruently, and congruently melting as well as transition enthalpies are less sensitive to the heating rate, as the heating rate is considered in the calibration procedure. In contrast, the heating rate can affect the measured liquidus temperature. Van den Bruinhorst et al.<sup>96</sup> analyzed the effect of the heating rate on the determined liquidus temperatures and concluded that the inflection point is more suitable for determining the liquidus temperature than the peak maximum temperature. Alternatively, the effect of the heating rate on the determined liquidus temperature can be ruled out by performing the DSC analysis at different heating rates and determining the liquidus temperature as the peak maximum temperature extrapolated to zero heating rate.<sup>97, 98</sup> Nevertheless, the influence of the heating rate on the determined liquidus temperature might be within the uncertainty of the DSC data. Hence, selecting a convenient heating rate, such as 2 or 5 K min<sup>-1</sup>, can be sufficient to determine the SLE phase diagram of most eutectic systems properly.

Saeed et al.<sup>93</sup> showed that the influence of the sample mass is more pronounced on the transition enthalpy than on onset or peak maximum temperatures. Therefore, for SLE measurements, the effects of the sample mass might not be critical. The temperature range should be defined to detect all possible phase transitions occurring in the sample. Hence, the temperature range can be specifically tuned for each sample to ensure time efficiency and convenience only during the experimental analysis.

Figure 7 shows a schematic representation of DSC curves of a sample analyzed by DSC using the typical DSC protocol. The typical DSC analysis protocol involves heating the sample to 10 K above melting temperature, an isothermal run at the final temperature for sufficient time to ensure sample homogeneity, and then a cooling run around 50 K below the crystallization temperature

## Theory

of the sample.<sup>99</sup> The sample is then subjected to second heating run to 10 K above the melting temperature of the sample. The transition temperature and enthalpy are determined from the second run or further heating/cooling cycles.<sup>96-98</sup> This protocol is used to clear the sample history and ensure the homogeneity of the sample. However, in situ crystallization in the DSC (Figure 7A) could lead to metastable polymorphs, metastable solid phases, or glass formation.<sup>73, 95, 100</sup> Corvis et al.<sup>94</sup> overcame the formation of metastable polymorphs in the lidocaine/L-menthol eutectic system by annealing the DSC samples for several months prior to measurements. Moreover, supercooling could occur during the cooling run, and the sample is crystallized during the heating run instead, i.e., cold crystallization.<sup>99, 101</sup> Cold crystallization in the vicinity of the solidus temperature (Figure 7B) can limit the proper determination of the onset temperature of the corresponding peak.<sup>91</sup> In conclusion, the typical DSC protocol can be unsuitable for determining the SLE in eutectic systems showing kinetic limitations in crystallization or the formation of different polymorphs. Therefore, in such a case, methods to aid crystallization and overcome glass formation in eutectic systems should be sought to determine the SLE phase diagram.

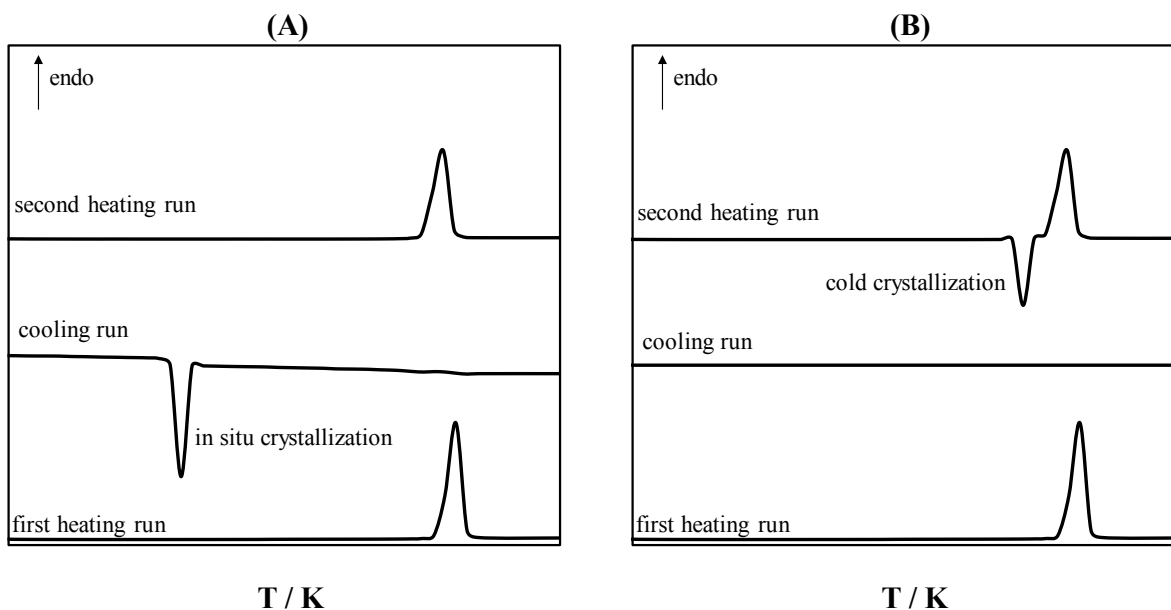


Figure 7. Schematic representation of a differential scanning calorimetry (DSC) curve of a sample analyzed using the typical DSC protocol: first heating, cooling, and second heating runs. In (A), the sample in situ crystallizes in the DSC during the cooling run, while in (B), the sample undergoes cold crystallization, i.e., crystallization during the heating run.

## 2.4 Thermodynamics of SLE

As seen in the previous section, experimental determination of SLE is a tedious task, especially for eutectic systems with complex phase diagrams. Thus, the standard approach to obtaining the SLE phase diagram is to measure the SLE data of the mixture at selected compositions, usually with a mole fraction step of 0.1. The experimental SLE data are then correlated using a thermodynamic model to obtain the phase diagram over the whole composition range.

The equilibrium condition for component  $i$  between the solid (S superscript) and liquid (L superscript) phases is as follows <sup>102</sup>

$$f_i^S = f_i^L \quad (2)$$

$$x_i^S \gamma_i^S f_{0i}^S = x_i^L \gamma_i^L f_{0i}^L \quad (3)$$

where  $f_i$  and is the fugacity,  $f_{0i}$  is the standard state fugacity,  $x_i$  is the mole fraction, and  $\gamma_i$  is the activity coefficient of component  $i$ . The standard states are defined as the pure solid and pure liquid at the liquidus temperature. The ratio between the standard state fugacity of component  $i$  in the liquid and solid phases can be calculated from the thermodynamic cycle shown in Figure 8. First, the pure solid phase is heated from the liquidus temperature  $T$  to its melting temperature  $T_m$ . Second, the pure solid is melted at  $T_m$ . Third, the pure liquid is cooled to the liquidus temperature  $T$ . The Gibbs energy change from point 1 to 4 ( $\Delta g_{1 \rightarrow 4}$ ) is defined as follows

$$\Delta g_{1 \rightarrow 4} = RT \ln \frac{f_{0i}^L}{f_{0i}^S} = \Delta h_{1 \rightarrow 4} - T \Delta s_{1 \rightarrow 4} \quad (4)$$

where  $R$  is the gas constant,  $T$  is the liquidus temperature,  $\Delta h_{1 \rightarrow 4}$  is the enthalpy change, and  $\Delta s_{1 \rightarrow 4}$  is the entropy change.

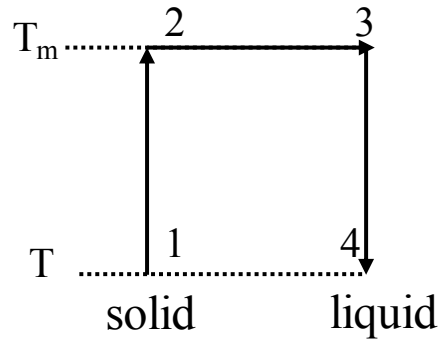


Figure 8. Thermodynamic cycle used to derive the solid–liquid equilibrium equation.

The enthalpy and entropy changes from point 1 to 4 is defined as the sum of the enthalpy and entropy changes along the path as follows

$$\Delta h_{1 \rightarrow 4} = \Delta h_{1 \rightarrow 2} + \Delta h_{2 \rightarrow 3} + \Delta h_{3 \rightarrow 4} \quad (5)$$

$$\Delta s_{1 \rightarrow 4} = \Delta s_{1 \rightarrow 2} + \Delta s_{2 \rightarrow 3} + \Delta s_{3 \rightarrow 4} \quad (6)$$

The enthalpy change from point 1 to 4 is the summation of the enthalpy change upon heating the pure solid from  $T$  to  $T_m$ , the melting enthalpy  $\Delta h_{m,i}$  of pure component  $i$ , and the enthalpy change upon cooling pure liquid from  $T_m$  to  $T$ . In equation form

$$\Delta h_{1 \rightarrow 4} = \int_T^{T_{m,i}} c_{P,i}^S dT + \Delta h_{m,i} + \int_{T_{m,i}}^T c_{P,i}^L dT \quad (7)$$

where  $c_P^S$  and  $c_P^L$  are the constant pressure heat capacity of pure component  $i$  in the solid and liquid states. Similarly, the change in entropy from point 1 to 4 is

$$\Delta s_{1 \rightarrow 4} = \int_T^{T_{m,i}} \frac{c_{P,i}^S}{T} dT + \Delta s_{m,i} + \int_{T_{m,i}}^T \frac{c_{P,i}^L}{T} dT \quad (8)$$

where  $\Delta s_{m,i}$  is the melting entropy of component  $i$ . Substituting equations (7) and (8) in (3) and (4) yields

$$\ln \frac{x_i^L \gamma_i^L}{x_i^S \gamma_i^S} = \ln \frac{f_{0i}^L}{f_{0i}^S} = -\frac{\Delta h_{m,i}}{RT} \left(1 - \frac{T}{T_{m,i}}\right) + \frac{1}{RT} \int_{T_{m,i}}^T \Delta c_{P,i} dT - \frac{1}{R} \int_{T_{m,i}}^T \frac{\Delta c_{P,i}}{T} dT \quad (9)$$

## Theory

where  $\Delta c_p = c_p^L - c_p^S$ . As seen, the ratio between standard state fugacities is determined by the melting properties of pure component  $i$ . Therefore, the activity coefficients of components in the liquid and solid phases are interrelated with the pure components melting properties. As seen in Equation (9), activity coefficients of the component in the liquid and solid phases and its pure melting properties—melting enthalpy, temperature, and the heat capacity of pure solid and liquid states—are the prerequisites for modeling SLE in eutectic systems. The following sections discuss the melting properties and the activity coefficients as well as the modeling procedure for SLE phase diagrams of different patterns (Figure 2).

### 2.4.1 Melting properties of pure components

The right-hand side of Equation (9) can be divided into terms, the first melting enthalpy term and the last two heat capacity terms. The melting enthalpy, entropy, and temperature of a pure component are interrelated by the following simple equation

$$T_m = \frac{\Delta h_m}{\Delta s_m} \quad (10)$$

Based on Equation (10), a high melting temperature of a substance results from high melting enthalpy or low melting entropy. The melting enthalpy of a pure substance is a function of the intermolecular interactions between molecules in the crystal lattice.<sup>103</sup> The intermolecular interactions depend on the type of the interacting groups, i.e., ionic or hydrogen bonding, and the distance between interacting groups. The latter is influenced by the lattice parameters and crystal packing, i.e., crystal structure.<sup>104</sup> High melting enthalpy values indicate strong intermolecular interactions and efficient crystal packing. In the case of unavailable melting enthalpy, the melting enthalpy of pure substances can be predicted using group contribution (GC) methods.<sup>103-107</sup> However, GC methods predictions for melting enthalpy are sometimes unreliable. Moreover, GC methods fail to differentiate between isomers, which can possess significantly different melting enthalpies.<sup>108</sup> The unsuitability of GC methods in predicting the melting enthalpy of pure substances is a direct consequence of the influence of the crystal structure on the melting enthalpy.

In contrast to melting enthalpy, melting entropy is better correlated to the molecular structure.<sup>109</sup> Yalkowsky,<sup>110</sup> Dannenfelser and Yalkowsky,<sup>111</sup> and Jain et al.<sup>112</sup> proposed non-GC methods to estimate the melting entropy of pure substances. The methods are based on calculating the



## Theory

melting entropy from the rotational  $\Delta S_m^{rot}$ , conformational  $\Delta S_m^{conf}$ , and transitional  $\Delta S_m^{expan}$  entropies as follows <sup>104</sup>

$$\Delta S_m = W + \Delta S_m^{rot} + \Delta S_m^{conf} + \Delta S_m^{expan} \quad (11)$$

where  $W$  is Walden's rule constant which is equal to around  $57 \text{ J mol}^{-1} \text{ K}^{-1}$ . <sup>113</sup> The rotational entropy is estimated from the rotational symmetry number  $\sigma$  as follows

$$\Delta S_m^{rot} = -R \ln \sigma \quad (12)$$

The rotational symmetry number is the number of similar structures that the molecule can produce when rotated. The conformational entropy is calculated using the flexibility number  $\Phi$  as follows <sup>103</sup>

$$\Delta S_m^{conf} = R \ln \Phi \quad (13)$$

$$\Phi = 2.435^\tau \quad (14)$$

$$\tau = SP^3 + 0.5SP^2 + 0.5Ring - 1 \quad (15)$$

where  $SP^3$ ,  $SP^2$ , and  $Ring$  are the numbers of non-ring  $SP^3$  atoms, non-ring  $SP^2$  atoms, and single, fused, or conjugated ring systems, respectively. The transitional entropy is calculated from the eccentricity  $\varepsilon$  as follows <sup>104, 105, 114</sup>

$$\Delta S_m^{expan} = R \ln \varepsilon \quad (16)$$

where  $\varepsilon$  is the number of atoms in aromatic and aliphatic rings. Despite the simplicity of these methods, good predictions have been obtained in many cases. <sup>104</sup>

Next, the two heat capacity difference terms are discussed. Several approaches exist to account for the heat capacity difference. <sup>96, 115-117</sup> The simplest case is to neglect the two heat capacity terms on the right-hand side of Equation (9). <sup>115, 118</sup> This approach is usually misunderstood to be based on neglecting the value of  $\Delta C_p$ . However, the approach is based on the fact that the two heat capacity terms in the right-hand side of Equation (9) have opposite signs, which tend to cancel each other in case  $T$  is not far from  $T_m$ . <sup>102, 118</sup> The heat capacity terms are commonly neglected in the absence of experimental data on the heat capacity of pure components.

## Theory

The second approach is to assume a constant heat capacity difference estimated at the melting temperature  $\Delta c_{P,m}$ , which reduces Equation (9) to the following Equation

$$\ln \frac{x_i^L \gamma_i^L}{x_i^S \gamma_i^S} = -\frac{\Delta h_{m,i}}{RT} \left(1 - \frac{T}{T_{m,i}}\right) - \frac{\Delta c_{P,m}}{R} \left(1 - \frac{T_{m,i}}{T} + \ln \frac{T_{m,i}}{T}\right) \quad (17)$$

The value of  $\Delta c_{P,m}$  can be determined from experimental heat capacity data. The pure liquid and solid heat capacities as a function of temperature are linearly extrapolated to the melting temperature of the pure component. However, experimental data on the heat capacity of pure components are scarce. In this case, several methods or approximations have been proposed to estimate the difference in the heat capacity at the melting temperature.<sup>118-125</sup> Hildebrand approximation states that the difference in the heat capacity value can be assumed equal to the melting entropy.<sup>120</sup> Pappa et al.<sup>119</sup>, Růžička and Domalski<sup>124</sup>, and Kolská et al.<sup>125</sup> used GC methods to estimate the heat capacity difference. Wu and Yalkowsky<sup>121</sup> used a simple approach to calculate the heat capacity difference based on the molecular flexibility, molecular symmetry, and hydrogen bond numbers calculated from the molecular structure using simple empirical correlations. However, Mishra and Yalkowsky<sup>115</sup> found that neglecting or considering the heat capacity terms would rather lead to an error within the uncertainty of the solubility measurements. Moreover, unrealistic heat capacity difference values would lead to an unphysical course for the calculated liquidus line.<sup>47</sup> Therefore, in case of unavailable heat capacity data for pure solid and liquid states, it is preferable to assume the simplest approach, i.e., neglecting the two terms on the right-hand side of Equation (9).

The third and most sophisticated approach considers the temperature dependence of the heat capacity of the pure solid and liquid.<sup>96,117</sup> A linear temperature dependence is usually sufficient. However, this approach requires data on pure solid and liquid heat capacities over a wide range of temperatures, which are challenging to obtain experimentally. This approach could be justified in the case of a significant difference between the  $T$  and  $T_m$  and when experimental data for the heat capacity of pure liquid and solid are available.

### 2.4.2 Activity coefficients

The activity coefficients of components represent the intermolecular interactions between unlike molecules in the liquid phase.<sup>102</sup> Activity coefficient values of components equal to one indicate that the system behaves ideally, i.e., similar intermolecular interactions between like and unlike

## Theory

molecules. On the other hand, activity coefficients smaller or larger than one indicate favored or unfavored intermolecular interactions between unlike molecules, respectively. The activity coefficients can be calculated using empirical, semi-empirical, or predictive activity coefficient models.

### 2.4.2.1 Empirical models

The activity coefficients of components in liquid mixtures can be described by a polynomial with empirical parameters that are characteristic of the studied system. Redlich-Kister (RK) polynomial is used to describe the excess Gibbs energy ( $g^E$ ) in any binary mixture as follows <sup>102</sup>

$$g^E = x_1x_2[A + B(x_1 - x_2) + C(x_1 - x_2)^2 + D(x_1 - x_2)^3 + \dots] \quad (18)$$

Accordingly, the activity coefficient can be calculated as follows

$$RT \ln \gamma_1 = a^{(1)}x_2^2 + b^{(1)}x_2^3 + c^{(1)}x_2^4 + d^{(1)}x_2^5 + \dots \quad (19)$$

$$RT \ln \gamma_2 = a^{(2)}x_1^2 + b^{(2)}x_1^3 + c^{(2)}x_1^4 + d^{(2)}x_1^5 + \dots \quad (20)$$

where the parameters in equations (19) and (20) are interrelated by the four empirical parameters in Equation (18) as follows

$$a^{(1)} = A + 3B + 5C + 7D$$

$$a^{(2)} = A - 3B - 5C - 7D$$

$$b^{(1)} = -4(B + 4C + 9D)$$

$$b^{(2)} = 4(B - 4C + 9D)$$

$$c^{(1)} = 12(C + 5D)$$

$$c^{(2)} = 12(C - 5D)$$

$$d^{(1)} = -32D$$

$$d^{(2)} = 32D$$

The simplest empirical activity coefficient model is the two-suffix Margules equation <sup>102</sup>

$$\ln \gamma_i = \frac{A}{RT}(1 - x_i)^2 \quad (21)$$

Because Equation (21) is symmetrical, the two-suffix Margules equation is only suitable for modeling the nonideality in binary mixtures of components with similar size, shape, and chemical nature. Empirical models can describe any liquid mixture regardless of its complexity. However, the availability and quality of fitted experimental data determine the number of empirical

parameters. For nonelectrolyte organic binary mixtures, two parameters are usually sufficient.<sup>102, 126</sup> Empirical activity coefficient models have been successfully used to model SLE data in several nonideal eutectic mixtures.<sup>96, 97</sup>

#### 2.4.2.2 NRTL

In empirical models, the activity coefficients are expressed with a polynomial whose parameters can be obtained by fitting the experimental data. Wilson<sup>127</sup> derived an algebraic function to express the activity coefficients using the local composition concept. A few years later, Renon and Prausnitz<sup>128</sup> used the same concept of local composition to derive the nonrandom two-liquid (NRTL) equations for calculating the activity coefficients of components as follows

$$\gamma_i = x_j^2 \left[ \tau_{ji} \left( \frac{G_{ji}}{x_i + x_j G_{ji}} \right)^2 + \frac{\tau_{ij} G_{ij}}{(x_j + x_i G_{ij})^2} \right] \quad (22)$$

$$G_{ij} = \exp(-\alpha\tau_{ij}) \qquad G_{ji} = \exp(-\alpha\tau_{ji}) \quad (23)$$

$$\tau_{ij} = \frac{g_{ij} - g_{jj}}{RT} \qquad \tau_{ji} = \frac{g_{ji} - g_{ii}}{RT} \quad (24)$$

Unlike the Wilson model, the NRTL model can describe completely miscible and partially miscible liquid systems. The advantage of semi-empirical over empirical models is that the models can be extended to describe the nonideality in multicomponent systems. The binary interaction parameters can then be used to derive the interaction parameters of multicomponent systems.<sup>102</sup> The NRTL model has been shown to describe the SLE in strongly nonideal eutectic mixtures successfully.<sup>87-89, 96, 126</sup>

#### 2.4.2.2 COSMO-RS

Despite the ability of the RK-polynomial and NRTL model to describe the nonideality of the eutectic mixture constituents in the liquid phase, the models are correlative, in which experimental SLE data are needed to fit the model parameters. Therefore, it is desirable to employ predictive thermodynamic models to obtain the SLE phase diagram without the need for experimental SLE data.

The conductor-like screening model for realistic solvation (COSMO-RS)<sup>129-132</sup> has been developed as an efficient tool to predict various thermodynamic properties. The model is based

## Theory

on quantum mechanics and statistical thermodynamic calculations. Density functional theory (DFT) calculations are used to obtain the screening charge surface in an ideal conductor with an infinite dielectric constant. The screening charge surface is discretized into segments with known surface charge density (SCD)  $\sigma_i$ . The pairwise interactions between segments with SCD are used to derive the chemical potential of component  $i$  in the liquid phase by statistical thermodynamics calculations. The calculated chemical potential of component  $i$  is used to calculate various thermodynamic properties.

In the COSMO-RS model, the liquid phase solution is considered an ensemble of packed screened molecules, where the two molecules interact in the contact region. The two types of interactions between segments in the contact regions are: (1) misfit interactions ( $e_{misfit}(\sigma, \sigma')$ ) from the electrostatic interactions (2) hydrogen bonding interactions  $e_{hb}(\sigma, \sigma')$ . The total interaction energy function  $e(\sigma, \sigma')$  in COSMO-RS is

$$e(\sigma, \sigma') = e_{misfit}(\sigma, \sigma') + e_{hb}(\sigma, \sigma') \quad (25)$$

The chemical potential of segment  $\sigma$  in the liquid solution  $\mu_S(\sigma)$  is calculated as follows

$$\mu_S(\sigma) = -\frac{RT}{a_{eff}} \ln \left[ \int p(\sigma') \exp \left( \frac{a_{eff}}{RT} (\mu_S(\sigma') - e(\sigma, \sigma')) \right) d\sigma' \right] \quad (26)$$

where  $a_{eff}$  is the effective contact area and  $p(\sigma')$  is the probability distribution. The probability distribution is the  $\sigma$ -profile obtained from the quantum mechanical calculations.  $\mu_S(\sigma)$  is called the  $\sigma$ -potential, which is a measure of the affinity of the liquid solution to a surface segment of polarity  $\sigma$ . Figure 9 shows the  $\sigma$ -profile and  $\sigma$ -potential of oxalic acid calculated using Turbomole version 6.6 and COSMOtherm X19, respectively.

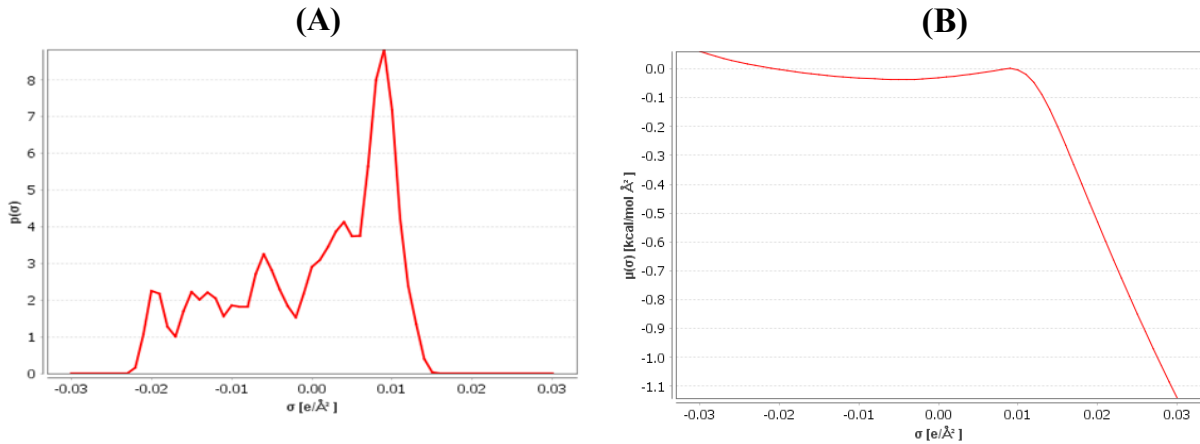


Figure 9. (A)  $\sigma$ -profile and (B)  $\sigma$ -potential of oxalic acid calculated using density functional theory and COSMO-RS, respectively.

The pseudo chemical potential  $\mu_i^{PS}$  of component  $i$  in the liquid solution is calculated from the  $\mu_S(\sigma)$  of its all segments

$$\mu_i^{PS} = \mu_i^{C,S} + \int p_i(\sigma) \mu_S(\sigma) d\sigma \quad (27)$$

where  $\mu_i^{C,S}$  is the combinatorial contribution due to the differences in the molecular size and shape between component  $i$  and the liquid solution molecules. The combinatorial contribution is calculated as follows

$$\mu_i^{C,S} = -RT \{ \lambda_0 \ln A_S^{COSMO} + \lambda_1 L_1^{SG} + \lambda_2 L_2^{SG} \} \quad (28)$$

$$L_1^{SG} = 1 - \frac{A_i^{COSMO}}{A_S^{COSMO}} + \ln \frac{A_i^{COSMO}}{A_S^{COSMO}} \quad (29)$$

$$L_2^{SG} = 1 - \frac{V_i^{COSMO}}{V_S^{COSMO}} \frac{A_i^{COSMO}}{A_S^{COSMO}} + \ln \frac{V_i^{COSMO}}{V_S^{COSMO}} \frac{A_i^{COSMO}}{A_S^{COSMO}} \quad (30)$$

where  $\lambda_0$ ,  $\lambda_1$  and  $\lambda_2$  are adjustable internal model parameters;  $A^{COSMO}$  and  $V^{COSMO}$  are the COSMO molecular surface area and volume, and subscript  $i$  and  $S$  refer to component  $i$  and the solvent, respectively. The liquid solution COSMO molecular surface area and volume are calculated from those of all components in the liquid solution as follows

$$A_S^{COSMO} = \sum_i x_i A_i^{COSMO} \quad (31)$$

$$V_S^{COSMO} = \sum_i x_i V_i^{COSMO} \quad (32)$$

The pseudo-chemical potential in Equation (26) ( $\mu_i^{PS}$ ) is used to calculate the chemical potential (partial molar Gibbs energy) of component  $i$  as follows

$$\mu_i = \mu_i^{PS} + RT \ln x_i \quad (33)$$

As seen, the only input required for COSMO-RS calculations, which allows for predicting many thermodynamic properties, is the molecular geometry obtained from DFT calculations. COSMO-RS has been applied in several studies concerning DESs to predict SLE,<sup>90, 133-136</sup> liquid-liquid equilibria,<sup>137, 138</sup> partitioning and solubility of bioactive compounds,<sup>66, 139, 140</sup> and in gas capture applications.<sup>141, 142</sup>

### 2.4.3 Modeling SLE phase diagram

#### 2.4.3.1 Simple eutectic system

In simple eutectic systems, the pure components crystallize in pure form, i.e.,  $x_i^S \gamma_i^S = 1$  (Figure 2A). In the simple eutectic type, Equation (9) reduces to the following equation

$$\ln x_i^L \gamma_i^L = -\frac{\Delta h_{m,i}}{RT} \left(1 - \frac{T}{T_{m,i}}\right) + \frac{1}{RT} \int_{T_m}^T \Delta c_{P,i} dT - \frac{1}{R} \int_{T_m}^T \frac{\Delta c_{P,i}}{T} dT \quad (34)$$

In case one of the constituents undergoes a solid-solid transition (Figure 2B), the liquidus line of the constituent below its solid-solid transition temperature, neglecting the difference between the heat capacities of the two solids, is calculated as follows

$$\ln x_i^L \gamma_i^L = -\frac{\Delta h_{m,i}}{RT} \left(1 - \frac{T}{T_{m,i}}\right) - \frac{\Delta h_{tr,i}}{RT} \left(1 - \frac{T}{T_{tr,i}}\right) + \frac{1}{RT} \int_{T_m}^T \Delta c_{P,i} dT - \frac{1}{R} \int_{T_m}^T \frac{\Delta c_{P,i}}{T} dT \quad (35)$$

where  $\Delta h_{tr}$  and  $T_{tr}$  are the transition enthalpy and temperature, respectively.

#### 2.4.3.2 solid solution regions

Miscibility in the solid phase is expected when two components of the same chemical nature possess similar molecular and crystal structures.<sup>143</sup> The SLE phase diagram of eutectic systems

with partial miscibility in the solid phase is modeled using Equation (9). In this case, the activity coefficients of components in the solid phase are needed. Empirical models such as the two-suffix Margules or predictive models have been used in the literature to calculate the activity coefficients of alkanes and paraffines in the solid solution.<sup>144-147</sup> However, models for describing the nonideality in the solid solution of salts and substances forming hydrogen bonding networks are yet unavailable.

#### 2.4.3.3 cocrystal formation

The formation of congruently (Figure 2D) or incongruently (Figure 2E) cocrystals with the stoichiometric coefficients  $\vartheta_A$  and  $\vartheta_B$  for components A and B, respectively, can be described via the following chemical reaction



The equilibrium constant  $K_a$  of the chemical reaction in Equation (35) is described as follows

$$K_a = \prod_i a_i^{\vartheta_i} = \frac{(x_A \gamma_A)^{\vartheta_A} (x_B \gamma_B)^{\vartheta_B}}{(x_{AB} \gamma_{AB})} \quad (37)$$

As the cocrystal AB crystallizes in pure form, i.e.,  $x_{AB} \gamma_{AB} = 1$ , Equation (36) is simplified to

$$K_a = (x_A \gamma_A)^{\vartheta_A} (x_B \gamma_B)^{\vartheta_B} \quad (38)$$

To determine the equilibrium constant at different temperatures, the following Gibbs-Helmholtz equation is used

$$\ln K_a = \ln K_a^{ref} + \frac{\Delta h^{ref}}{R} \left( \frac{1}{T^{ref}} - \frac{1}{T} \right) \quad (39)$$

where  $\Delta h^{ref}$  and  $T^{ref}$  are the melting enthalpy and temperature of the cocrystal.  $K_a^{ref}$  is the equilibrium reaction constant determined at  $T^{ref}$  and cocrystal stoichiometry as follows

$$K_a^{ref} = (x_A^{ref} \gamma_A^{ref})^{\vartheta_A} (x_B^{ref} \gamma_B^{ref})^{\vartheta_B} \quad (40)$$

where  $x$  and  $\gamma$  are calculated at the cocrystal stoichiometry. As seen, to model SLE in eutectic systems with cocrystal formation, the melting properties and stoichiometry of the cocrystal as



## Theory

well as the activity coefficients of the components in the liquid phase are required. The melting properties of the cocrystals can be measured by DSC, similar to pure components. In contrast, determining the stoichiometry of the cocrystal is challenging. Powder XRD analysis over the whole composition range can hint at the stoichiometry of the cocrystal. However, the cocrystal stoichiometry can only be verified by single-crystal XRD (SC-XRD) or structure solution from powder XRD data. The latter requires high-quality XRD data and expertise. Moreover, the crystal structure obtained from powder XRD data is usually of poor quality. Thus, in many cases, the SC-XRD technique is inevitable for the proper determination of cocrystal stoichiometry.

### 3. Results

The results of the thesis are presented in six published papers. In Paper I, a parameter study was performed to understand the influence of the melting properties of pure components and their activity coefficients in the liquid solution on the position of the eutectic point. Paper II reports SLE data for six different eutectic systems formed by mixing L-menthol with linear and cyclic monocarboxylic acids to study the influence of the molecular structure of constituents on the eutectic temperature. Paper III investigates glass formation and polymorphism in eutectic systems, which can lead to misinterpretations of the phase diagram and the eutectic temperatures of the eutectic systems. In Paper IV, an efficient sample preparation method was proposed, allowing for measuring the phase diagram of the L-menthol/thymol eutectic system. Paper V highlights cocrystal formation in ChCl-based DES and evaluates the melting properties of ChCl estimated in the literature. Finally, In Paper VI, cocrystal formation in the L-menthol/phenol eutectic system was investigated experimentally and modeled using correlative and predictive thermodynamic models.

### 3.1 Paper I

#### **Modeling of Solid–Liquid Equilibria in Deep Eutectic Solvents: A Parameter Study**

**A. Alhadid, L. Mokrushina and M. Minceva, *Molecules*, 2019, 24, 2334.**

Author contribution: The thesis author conceptualized the paper's idea, performed the calculations, and interpreted the results. He wrote the manuscript draft and completed the editing of the manuscript.

Summary: Paper I aims to investigate the parameters that affect the SLE in binary eutectic mixtures of the simple eutectic type, namely, the melting properties of pure components and the nonideality in the liquid solution, and their interrelation. The parameter study was performed on hypothetical and selected real binary eutectic systems. Although previous works have performed a similar parameter study,<sup>47, 49, 74</sup> Paper I was the first to quantify the influence and provide direct interpretation for each parameter value. The depression at the eutectic point was described as the normalized difference between the eutectic temperature and the melting temperature of the low melting component.

The influence of the melting properties of pure components on the depression at the eutectic point was studied by screening different melting temperatures of components at constant melting entropy and assuming ideal solution behavior. It was found that the depression at the eutectic point decreases as the difference between the melting temperature of both components increases. Therefore, the largest depression at the eutectic point at constant melting entropy is observed when both components possess the same melting temperature. However, the influence of the difference between the melting temperature of both components is relatively insignificant compared to the absolute values of the melting enthalpy and entropy of pure components. Accordingly, ideal eutectic mixtures with large depression at the eutectic point can be formed by mixing constituents possessing low melting enthalpy and entropy values.

Next, the influence of the activity coefficients of components in the liquid phase on the depression at the eutectic point was studied. The activity coefficients in the liquid phase were calculated using the two-suffix Margules equation by screening different binary interaction parameter values. It was found that a large depression at the eutectic temperature cannot result from the substantial negative deviation from ideal behavior only but rather from a combination of low melting enthalpy of components and negative deviation from ideality. The influence of the

### 3.1 Paper I

melting enthalpy and nonideality of the high melting component on the depression at the eutectic point is more prominent than those of the low melting component.

Further, the interrelation between pure components melting properties and their activity coefficients in the liquid phase was studied to evaluate the melting properties of thermally unstable substances estimated in the literature. It was found that any combination of melting enthalpy and the activity coefficient model parameters can describe the SLE data of the thermally unstable salt. However, the calculated activity coefficients of the thermally unstable salt in the liquid phase were different in each case, which lead to a different interpretation of the nonideality of the component in the same liquid solution. Therefore, it was concluded that due to the interrelation between the melting properties of pure components and their activity coefficients, the method for obtaining the melting properties of thermally unstable salts, such as  $\text{ChCl}$ , using the SLE data could be unreasonable.

Article

# Modeling of Solid–Liquid Equilibria in Deep Eutectic Solvents: A Parameter Study

Ahmad Alhadid<sup>1</sup>, Liudmila Mokrushina<sup>2</sup> and Mirjana Minceva<sup>1,\*</sup> 

<sup>1</sup> TUM School of Life and Food Sciences Weihenstephan, Technical University of Munich, Biothermodynamics, Maximus-von-Imhof-Forum 2, 85354 Freising, Germany; ahmad.alhadid@tum.de

<sup>2</sup> Friedrich-Alexander-Universität Erlangen-Nürnberg (FAU), Separation Science & Technology, Egerlandstr. 3, 91058 Erlangen, Germany; liudmila.mokrushina@fau.de

\* Correspondence: mirjana.minceva@tum.de

Academic Editors: Mert Atilhan and John M. Herbert

Received: 5 April 2019; Accepted: 24 June 2019; Published: 25 June 2019



**Abstract:** Deep eutectic solvents (DESs) are potential alternatives to many conventional solvents in process applications. Knowledge and understanding of solid–liquid equilibria (SLE) are essential to characterize, design, and select a DES for a specific application. The present study highlights the main aspects that should be taken into account to yield better modeling, prediction, and understanding of SLE in DESs. The work is a comprehensive study of the parameters required for thermodynamic modeling of SLE—i.e., the melting properties of pure DES constituents and their activity coefficients in the liquid phase. The study is carried out for a hypothetical binary mixture as well as for selected real DESs. It was found that the deepest eutectic temperature is possible for components with low melting enthalpies and strong negative deviations from ideality in the liquid phase. In fact, changing the melting enthalpy value of a component means a change in the difference between solid and liquid reference state chemical potentials which results in different values of activity coefficients, leading to different interpretations and even misinterpretations of interactions in the liquid phase. Therefore, along with reliable modeling of liquid phase non-ideality in DESs, accurate estimation of the melting properties of their pure constituents is of clear significance in understanding their SLE behavior and for designing new DES systems.

**Keywords:** deep eutectic solvents; solid–liquid equilibria; modeling phase equilibria; melting properties; activity coefficient models

## 1. Introduction

Deep eutectic solvents (DESs) are a class of eutectic mixtures of two or more compounds that have a eutectic point far below the melting temperatures of the individual components [1]. The large depression in the melting temperature of the mixture is commonly attributed to strong hydrogen bonding interactions between DES constituents. The recent trend toward green solvents has increased the potential of DESs in many applications [2–5]—e.g., as solvents for active pharmaceutical ingredients [6–8], fuel production [9,10], solid–liquid and liquid–liquid extraction [11–16], and solid–support free liquid–liquid chromatography [17–20].

Similar to ionic liquids (ILs), DESs are considered designer solvents because their properties can be tailored by choosing different combinations of its constituents [2]. However, the ratio of constituents—i.e., the eutectic composition—is not as easy to determine as it is for ILs, in which the ratio of cations and anions is determined by mixture electroneutrality. Many molecular simulation studies can be found in the literature; these aimed to understand DES systems at the molecular level and determine their eutectic composition [21–35]. It should be noted, however, that these studies were mainly performed using DESs of a fixed composition corresponding to a supposed hydrogen bond

complex. Therefore, the studied compositions are not representative of the entire range of possible compositions. Even with fixed ratios between DES constituents, no specific microstructure was found, but rather a network of hydrogen bonding [35]. It has been postulated that the hydrogen bonding network structure could be correlated to eutectic temperature [34]. Molecular simulation studies are a helpful tool in modeling and understanding interactions between DES constituents at a molecular level, but they are so far unable to provide sufficient macroscopic information required for process applications. Although knowledge and understanding of solid–liquid equilibria (SLE) in DES systems are essential to designing and selecting the appropriate system for a particular application, only a small fraction of DES related literature contains information about their SLE [1,36–47].

Eutectic systems are mixtures of two or more components in which the components show complete or partial immiscibility in the solid state at the mixture melting temperature [48]. Although eutectic mixtures have been long studied, no agreement for strict criteria to distinguish between eutectic mixtures and “deep” eutectic mixtures can be found in literature [49]. In recent publications, the term DES or natural DES (NADES) is typically used for any mixture that forms a eutectic mixture with a low freezing temperature. Smith et al. [4] defined DESs as systems that have a large difference between the melting temperature of the mixture at eutectic composition and the weighted sum of the melting temperatures of the pure components. They assumed that the deep eutectic point is associated with the formation of a new complex via hydrogen bonding between DES constituents; therefore, the eutectic composition represents the stoichiometry of this complex. Based on this definition, the search for eutectic compositions has been commonly performed by trial and error using a specific ratio between constituents such as 1:1, 1:2, etc. Despite the fact that in some DES systems the eutectic composition represents a specific molar ratio between the constituents—such as 1 choline chloride ([Ch]Cl):2 urea or 1 [Ch]Cl:1 oxalic acid—the eutectic point of any phase diagram is determined by the intercept of the liquidus lines of the components, even if the solution behaves ideally. Therefore, complex formation might not be the only reason for deep eutectic formation and the eutectic composition may not accord with a specific molar ratio between the constituents.

Martins et al. [49] proposed a more comprehensive definition for DES systems. According to these authors, DES systems are mixtures of two or more components—i.e., not a new compound. At the same time, DES systems should be differentiated from other simple eutectic systems based on their strong negative deviations from ideality—i.e., the eutectic temperature is lower than that of the ideal eutectic. In addition, the term DES should not refer exclusively to eutectic composition but to any composition at which the mixture is liquid at operating temperature. Based on this definition, studying the non-ideality of the liquid phase is essential to determining whether or not a system is a DES. Following this, most recent literature studies on modeling SLE in DESs have focused mainly on modeling non-ideality in the liquid phase as a reason behind the formation of DESs [42–46,49,50]. From a thermodynamic perspective, SLE do not depend only on the intermolecular interactions in the liquid phase but also on a correct estimate of the reference state—i.e., the ratio of the fugacities of the pure components in the solid and subcooled liquid phases at system temperature. Although this was clearly and explicitly stated many years ago in Prausnitz et al. [51], it continues to be overlooked in the literature. Only consideration of the interplay of both pure component melting properties and solution non-ideality can result in reliable modeling of SLE in DESs, which will help in understanding their nature. Moreover, activity coefficients and melting properties are not independent since the value of the reference state chemical potential the activity coefficients refer to is directly related to the melting properties.

Although melting enthalpy and melting temperature can be measured using differential scanning calorimetry, it is still a difficult issue because of polymorphism, possible metastable solid phases, kinetic limitations due to high liquid viscosities close to the melting temperature, etc. For some substances, it is impossible to measure them owing to their thermal instability. These issues result in limited and inaccurate data, especially on the enthalpy of fusion. Despite the fact that the literature reports several

theoretical methods for the estimation of melting properties, these methods usually suffer from many limitations and are hardly applicable to ionic compounds [52].

Recently, Kollau et al. [47] and Martins et al. [49] studied the effect of melting properties and non-ideality on SLE phase diagrams. Defining DES as mixtures with high negative deviation from ideality, they demonstrated that the SLE phase diagram should be known to distinguish DES from other eutectic mixtures and that the non-ideality in DESs can be quantitatively described by the regular solution theory or the PC-SAFT equation of state. However, the focus of these studies was to convince the community that only eutectic mixtures with high negative deviations from ideality should be considered as DES. A number of issues covered in the present study were not discussed or, if considered, then indirectly and not in detail.

The present work presents a systematic study of both melting properties and solution non-ideality, with the goal of understanding DES formation. Consideration is first made based on a hypothetical model eutectic system to find the link between eutectic point properties—eutectic temperature and composition—with both the melting properties and activity coefficients of the components. Then, simplified modeling of [Ch]Cl/ILs eutectic systems is carried out to evaluate the effect of small melting enthalpies on the interpretation of the modeling results. Further, DES systems composed of quaternary ammonium chlorides and fatty acids are modeled to evaluate the effect of overestimation of melting enthalpies of components and to support the initial findings. The only criteria for selecting the activity coefficient model used in this work—namely, Redlich–Kister polynomial—is its simplicity and flexibility in describing curves of different shape and complexity. It should be pointed out that this work does not propose or recommend this model to be used for SLE calculations in DES. The calculations done in this work do not aim at improved modeling of published SLE data; instead, the aim is to encourage discussion and further interpretation of these data.

The general objective of this work is to provide the deeper understanding essential to establishing the basic steps required in defining and designing DES systems based on their SLE behavior. Similar to molecular simulation approaches, thermodynamic modeling of SLE can be a valuable tool to assess the behavior of components in the liquid phase—i.e., intermolecular interactions. Designing DES systems based on their SLE estimated from activity coefficient models or equation of state might have an advantage over molecular simulation approaches owing to the direct estimation of eutectic temperature, eutectic composition, and the composition range at which the DES is a liquid at operating temperature.

## 2. Theory

Most studied DESs have been considered as simple eutectic systems in which pure constituents crystallize in the form of pure components at the mixture liquidus temperature. Figure 1 shows a schematic of a solid–liquid phase diagram of a simple eutectic system. Curve (a') and (a) are the liquidus lines of Component 1 and 2, respectively. They intercept at the eutectic point, which corresponds to the lowest melting temperature—the eutectic temperature ( $T_e$ )—of a mixture of eutectic composition ( $x_e$ ).

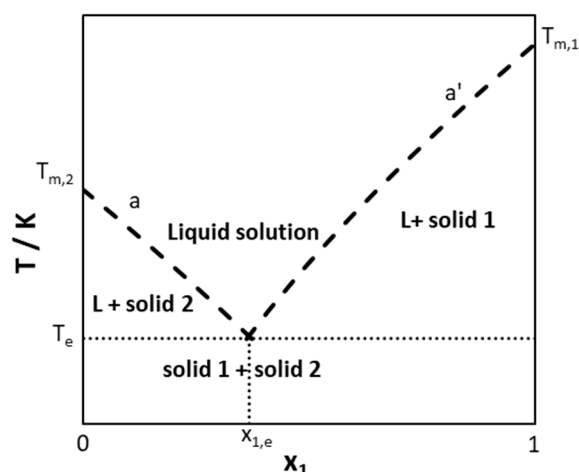


**Figure 1.** Schematic representation of a solid–liquid phase diagram of a simple eutectic system.

The liquidus line of component  $i$  is calculated as [51]

$$\ln x_i^L \gamma_i^L = \frac{\mu_{0i}^S - \mu_{0i}^L}{RT} = \ln \frac{f_{0i}^S}{f_{0i}^L} = -\frac{\Delta h_{m,i}}{RT} \left(1 - \frac{T}{T_{m,i}}\right) - \frac{\Delta c_{p,i}}{R} \left(1 - \frac{T_{m,i}}{T} + \ln \frac{T_{m,i}}{T}\right) \quad (1)$$

where  $x_i^L$  and  $\gamma_i^L$  are the mole fraction and activity coefficient of component  $i$  in the liquid solution, respectively;  $\mu_{0i}^L$  and  $\mu_{0i}^S$  are the reference chemical potentials of pure component  $i$  in the subcooled liquid and solid states at liquidus temperature, respectively;  $f_{0i}^L$  and  $f_{0i}^S$  are the reference fugacities of pure component  $i$  in the subcooled liquid and solid states at liquidus temperature, respectively;  $\Delta h_{m,i}$  and  $T_{m,i}$  are the melting enthalpy and the melting temperature of pure component  $i$ , respectively;  $T$  is the liquidus temperature;  $\Delta c_{p,i}$  is the difference in heat capacity of pure component  $i$  in the solid and liquid states at constant pressure;  $R$  is the universal gas constant.

The  $\Delta c_p$  term on the right-hand side of Equation (1) is typically of low value in comparison with the  $\Delta h_{m,i}$  term. In addition, the  $\Delta c_p$  values are usually unavailable from previous experiments and are difficult to estimate with reasonable accuracy because no liquid exists at temperatures below the melting temperature. As a result, the second term on the right-hand side of Equation (1) has been commonly neglected in literature and the following simplified equation is used to calculate the liquidus lines

$$\ln x_i^L \gamma_i^L = -\frac{\Delta h_{m,i}}{RT} \left(1 - \frac{T}{T_{m,i}}\right) \quad (2)$$

According to Equation (2), the position of the eutectic point, as well as the whole SLE phase diagram, depend on both the melting properties—melting enthalpy and melting temperature—of the pure components and their activity coefficients in solution. When the solution is assumed as ideal ( $\gamma_i^L$ ), the SLE phase diagram can be modeled based on the melting properties of the pure components only. However, if the system deviates from ideal behavior, the activity coefficients of components in the liquid phase can be calculated using well-developed  $g^E$  models or equations of state, which are available in the literature.

### 3. Results and Discussion

#### 3.1. Parameter Study on a Hypothetical Binary System

In the present section, a hypothetical binary DES system is considered. The high melting component is labeled as 1 and the low melting component is labeled as 2.



### 3.1.1. Melting Properties of Pure Components

The melting properties of the pure components—melting enthalpy and melting temperature—are prerequisites for SLE diagram calculations even if the solution is assumed ideal. Melting enthalpy and entropy depend on the molecular arrangement in the crystal lattice—i.e., molecular symmetry, conformational diversity, and intermolecular forces [52]. The melting temperature is the ratio between melting enthalpy and entropy of the component; therefore, a high melting temperature of a compound corresponds to a high melting enthalpy, a low melting entropy, or both [53]. Highly ordered solid structures usually have high melting temperatures as a result of a high melting enthalpy. However, disordered solid structures may also have high melting temperatures as a result of low melting entropy. In this case, the low melting entropy corresponds to association in the liquid phase—as a result of strong hydrogen bonding [54]—or due to a symmetrical and rigid molecular structure [53]. Therefore, it is very difficult to correlate the melting enthalpy values of compounds—or even to obtain an estimate based on melting temperature only—without information relating to (i) their crystal and molecular structures and (ii) interactions between like-molecules in the liquid phase. However, according to Bondi’s observation, melting entropy of components can be better related to the molecular structure [55], although it cannot be measured and is estimated from experimental melting enthalpy and temperature of compounds. Therefore, two cases are considered in this section to represent components of different crystal structures. In the first case, a high melting entropy is assumed of  $54.4 \text{ J mol}^{-1} \text{ K}^{-1}$  ( $\Delta s_m/R \approx 7$ )—also known as the Walden rule (Equation (3))—to represent compounds with ordered crystals of rigid molecules [53]. In the second case, a low melting entropy of  $20.0 \text{ J mol}^{-1} \text{ K}^{-1}$  ( $\Delta s_m/R \approx 2.4$ ) is assumed to represent compounds with disordered crystals of rigid molecules [53]. In this section, the effect of melting properties on the eutectic point properties—eutectic temperature ( $T_e$ ) and composition ( $x_e$ )—of a hypothetical ideal binary system is studied, with the results shown in Figures 2–4. In all cases, SLE are modeled using Equation (2) assuming  $\gamma_i^L = 1$ .

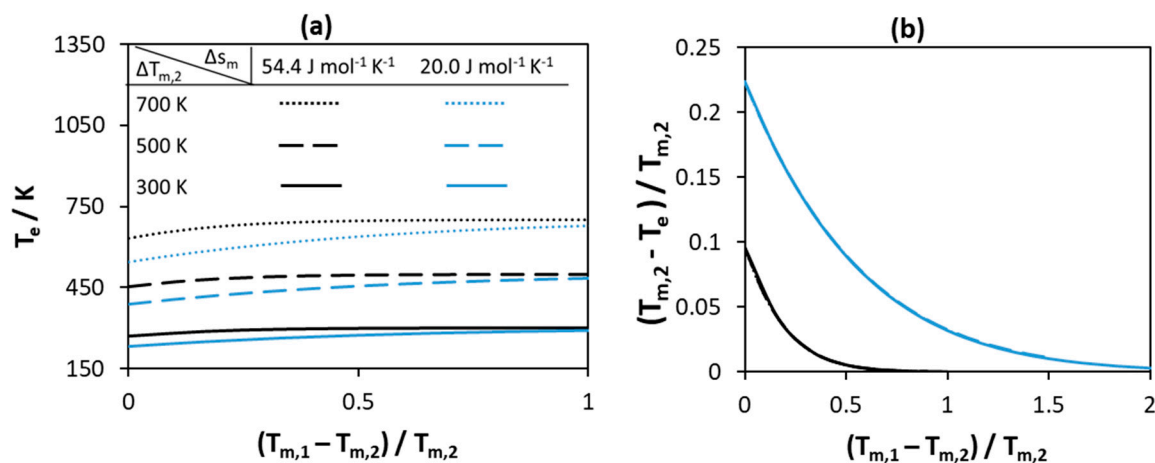


**Figure 2.** Effect of melting temperature of pure components with constant melting entropy on (a) the eutectic temperature (b) the normalized depression at eutectic temperature relative to that of the low melting Component 2.

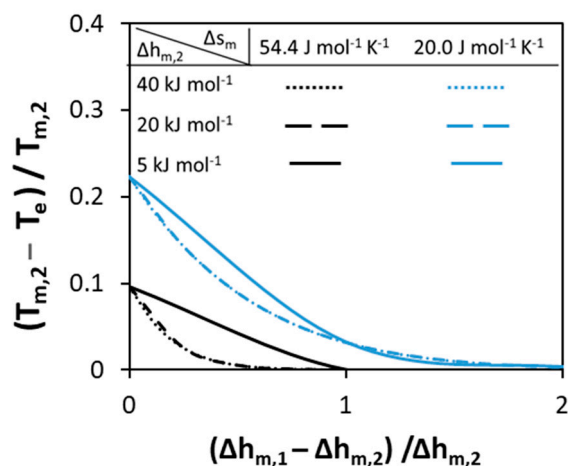


**Figure 3.** Effect of the melting enthalpies of pure components with constant melting entropy on the normalized depression at eutectic temperature relative to that of Component 2.

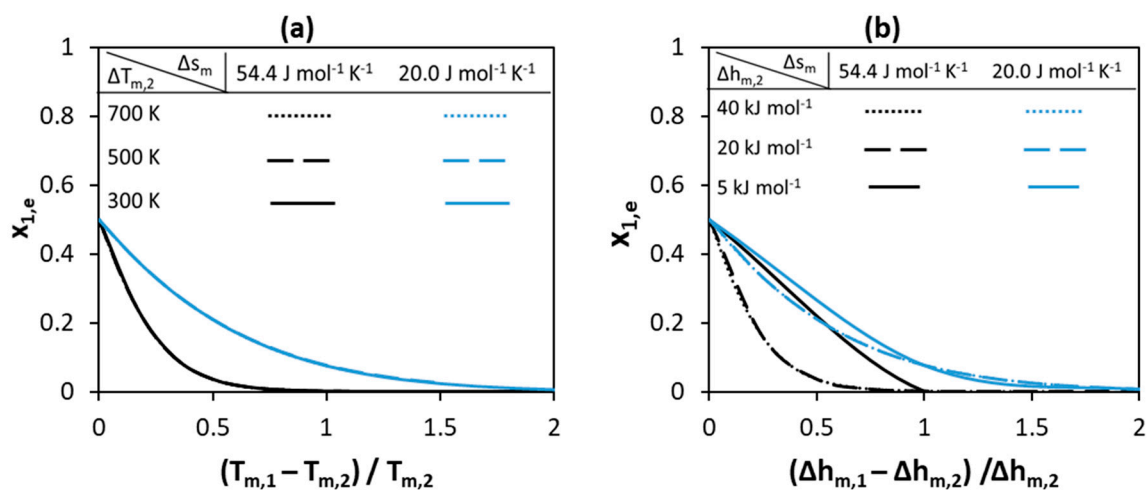


**Figure 4.** Effect of (a) melting temperature (b) melting enthalpy of pure components on the eutectic composition of Component 1.

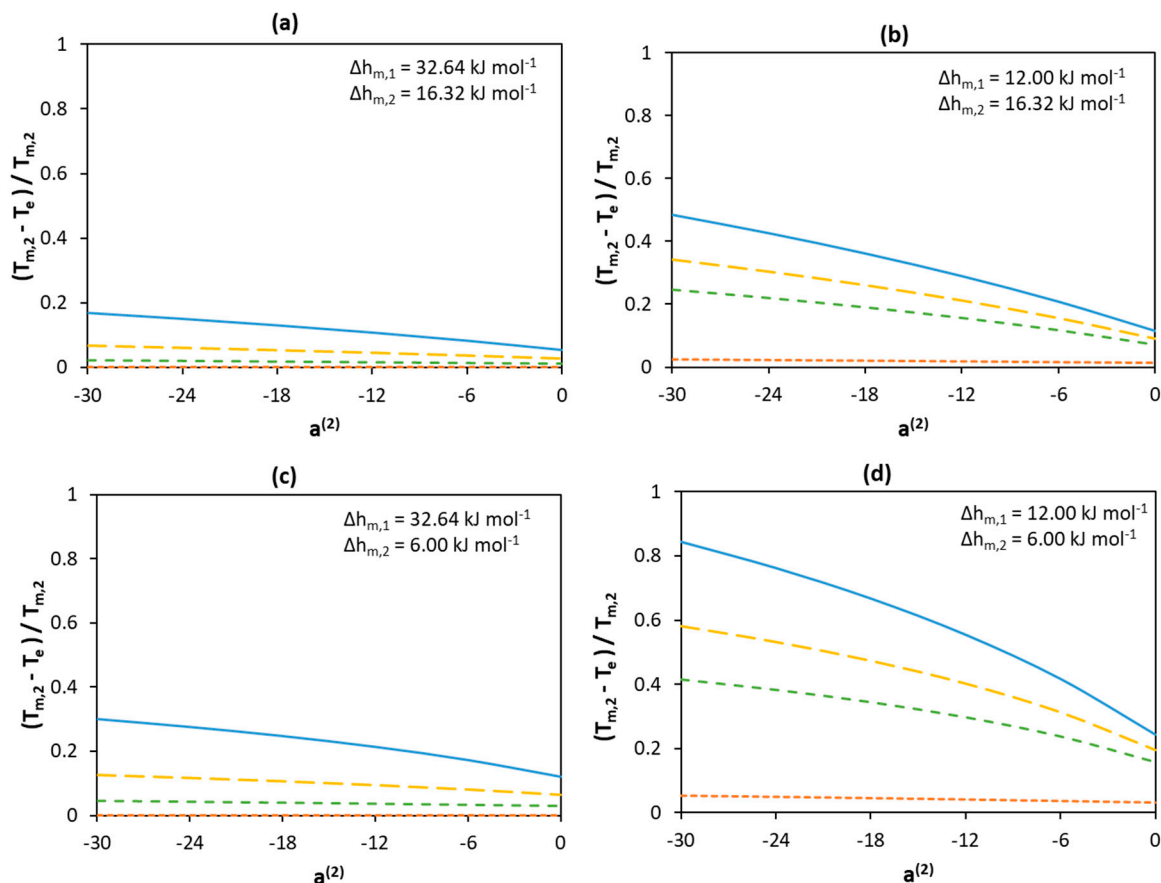
Figure 2 represents the effect of melting temperatures of pure components on the eutectic temperature of the system. As seen from Figure 2a, the absolute value of the eutectic temperatures changes as the melting temperature of the low and the high melting components changes. The higher the values of the melting temperatures of both components, the higher the eutectic point of the system. As the difference between the components increases, the absolute eutectic temperature increases and reaches a constant value that is close to the melting temperature of Component 2. The low value of melting entropy of the components at constant melting temperatures further decreases the eutectic temperature of the system—the blue curves in Figure 2a are always lower than the black curves. As seen in Figure 2b, if the normalized difference between the eutectic temperature and the melting temperature of the low melting component is selected as a measure for the depression at eutectic point, the absolute values of the melting temperatures of both components have no effect on the depression at eutectic point. This effect is a result of fixing the melting entropy of components—increasing the melting temperatures of components at constant melting entropy means an increase in the melting enthalpy of components. Therefore, the effect of melting temperatures of components is negligible if the melting entropy and similarly the melting enthalpy of components is high. Therefore, at constant value of melting entropy, the largest depression is observed if the melting temperatures of both components are equal.

In Figure 3, the effect of the melting enthalpies of pure components on the normalized depression at eutectic point is studied. The different curves correspond to different melting entropy values. In contrast to melting temperatures of pure components, the absolute values of the melting enthalpies of components affect the normalized depression at eutectic point. The lower the values of melting enthalpies, the higher the depression at eutectic point. As can be noticed from Figure 3, if the value of the melting enthalpy of Component 1 is high no depression is observed. In addition, only the low value of melting enthalpy ( $5 \text{ kJ mol}^{-1}$ ) of both components can affect the depression at eutectic point—this can be seen by the shift between solid and dashed lines, while the dotted and the dashed lines are the same. In conclusion, for ideal eutectic systems in which the components possess different melting temperatures, only low value of melting enthalpies of components can lead to deep eutectics.

Figure 4 shows how the eutectic composition depends on melting properties for the systems shown in Figures 2 and 3. As can be seen in Figure 4, an equimolar eutectic composition is possible if both the melting enthalpies and melting temperatures of the components are equal. The eutectic composition is located very close to the pure Component 2 side ( $x_{1,e} = 0$ ) if the difference between components melting temperatures or the melting enthalpy of Component 1 is of a high value. The low melting enthalpy value of Component 1 shifts the eutectic composition to a higher content of Component 1 (toward higher  $x_{1,e}$  values). The change in the absolute values of the melting enthalpies of components shifts the eutectic composition to different values. However, the effect of melting properties on the eutectic composition is lower compared to that on the depression at eutectic point—compare the shift between black and blues curves in Figures 2 and 3 to that in Figure 4.

### 3.1.2. Non-Ideality of Components in Liquid Phase

The effect of both parameters—namely the activity coefficients and melting properties—is demonstrated here for a hypothetical binary system. As shown in the previous section, the absolute values of the melting temperatures of components have no effect on the normalized depression at eutectic point at fixed melting entropies. Therefore, arbitrary melting temperatures of the high melting Component 1 and the low melting Component 2 are set to 600 K and 300 K, respectively. The melting enthalpy and entropy is used to investigate the effect of melting properties. Four cases are present in Figure 5. In the first case, the Walden rule (Equation (3)) is used to calculate the melting enthalpies. In the second case, the melting enthalpy of Component 1 ( $12.0 \text{ kJ mol}^{-1}$ ) is estimated assuming a low value of melting entropy of  $20 \text{ J mol}^{-1} \text{ K}^{-1}$ , whereas the melting enthalpy of Component 2 ( $16.32 \text{ kJ mol}^{-1}$ ) is calculated using the Walden rule. In the third case, the melting enthalpy of Component 2 ( $6.0 \text{ kJ mol}^{-1}$ ) is estimated using a low value of melting entropy of  $20 \text{ J mol}^{-1} \text{ K}^{-1}$ , whereas the melting enthalpy of Component 1 ( $32.64 \text{ kJ mol}^{-1}$ ) is calculated using the Walden rule. In the fourth case, the melting enthalpies of both components are estimated using a low value of melting entropy of  $20 \text{ J mol}^{-1} \text{ K}^{-1}$ . SLE are calculated using Equation (2) with activity coefficients screened using RK-polynomials (Equation (4)). The values of the parameters  $a^{(i)}$  in Equation (4) for each component are varied in the range  $-30$ – $0$  to account for the negative deviation from ideality ( $\ln(\gamma_i^L) < 0$ ). It should be mentioned that these parameters have no significant physical meaning, and they are serving just as a measure for the value of the activity coefficients—i.e., the lower the value of parameter  $a^{(i)}$ , the lower the value of  $\gamma_i^L$  at the eutectic point.



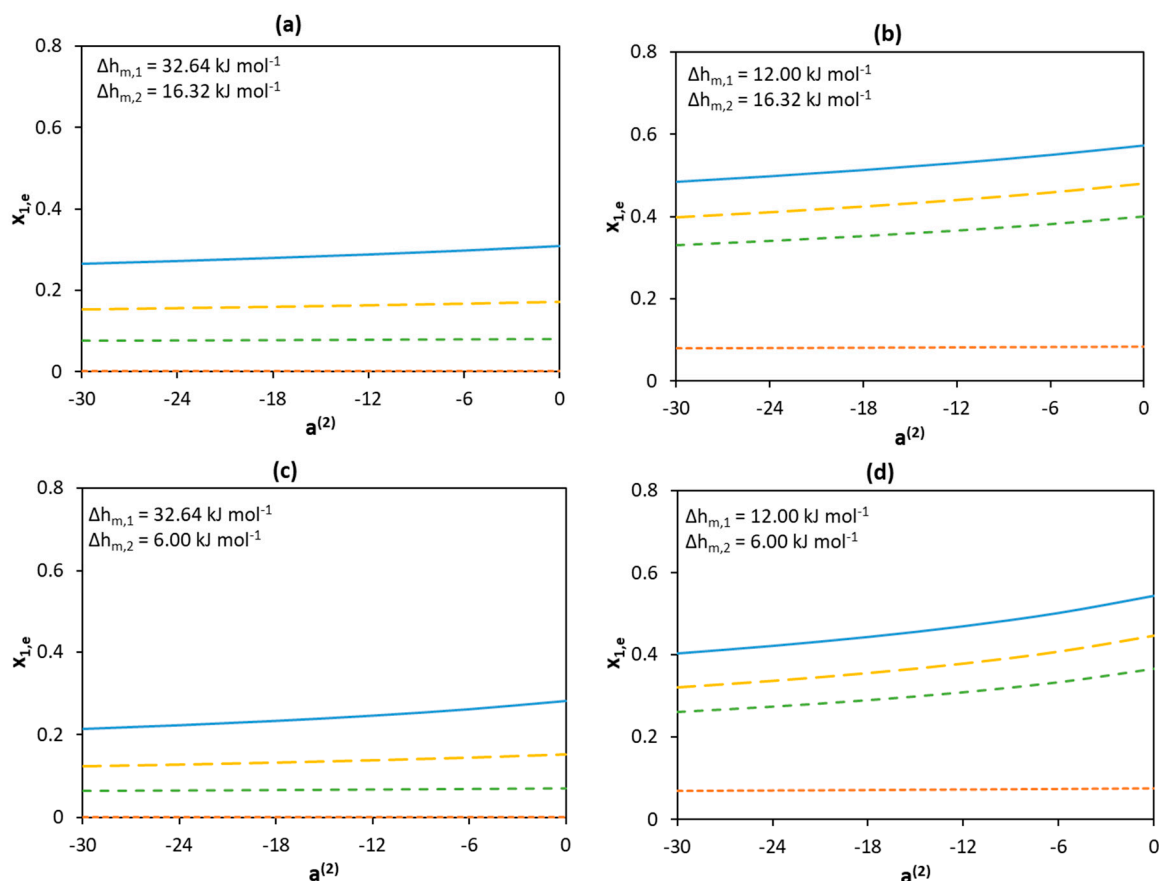
**Figure 5.** Effect of non-ideality of components on the normalized depression at eutectic temperature relative to the melting temperature of Component 2 assuming different melting enthalpy values of components (a)  $\Delta h_{m,1} = 32.64 \text{ kJ mol}^{-1}$  and  $\Delta h_{m,2} = 16.32 \text{ kJ mol}^{-1}$  (b)  $\Delta h_{m,1} = 12.00 \text{ kJ mol}^{-1}$  and  $\Delta h_{m,2} = 16.32 \text{ kJ mol}^{-1}$  (c)  $\Delta h_{m,1} = 32.64 \text{ kJ mol}^{-1}$  and  $\Delta h_{m,2} = 6.00 \text{ kJ mol}^{-1}$  (d)  $\Delta h_{m,1} = 12.00 \text{ kJ mol}^{-1}$  and  $\Delta h_{m,2} = 6.00 \text{ kJ mol}^{-1}$ . The melting temperatures of Components 1 and 2 are set to 600 K and 300 K, respectively. The parameter value is only a measure for non-ideality with no physical significance. Legend: —  $a^{(1)} = -30$ ; - -  $a^{(1)} = -18$ ; ···  $a^{(1)} = -12$ ; - · -  $a^{(1)} = 0$ .

Figure 5 demonstrates how solution non-ideality affects depression at the eutectic temperature for different melting enthalpies of the components. As in the case of the ideal mixture, the lower the melting enthalpy of Component 1, the larger the normalized depression at eutectic temperature. When the melting enthalpy of Component 1 is of a low value—see Figure 5b,d—depression of the melting point occurs, even if Component 1 behaves ideally ( $a^{(1)} = 0$ ; orange curves in Figure 5b,d). However, when the melting enthalpy of Component 1 is of a high value—see Figure 5a,c—depression of the melting temperature is possible only if the activity coefficients of both components deviate considerably from unity—i.e.,  $a^{(1)} < 0$ . Despite the fact that a low melting enthalpy value of Component 2 leads to an even more pronounced decrease in the eutectic temperature—as shown in Figure 5c,d—this occurs only if the activity coefficients of Component 1 are significantly lower than unity.

Generally, low component activity coefficients lead to a significant depression of the eutectic temperature of the mixture, independent of the melting enthalpy values. However, when the melting enthalpy of Component 1 is of a high value, only a small depression is observed when its activity coefficients are equal (or close) to unity ( $a^{(1)} = 0$ , orange curves in Figure 5a,c). In contrast, when Component 1 significantly deviates from ideality, a larger effect can be seen even if Component 2 behaves ideally (compare an orange curve with the lowest point of a blue curve at  $a^{(2)} = 0$ ). In addition, comparing the change in eutectic temperature depression when  $a^{(1)}$  equals  $-30$  and  $0$  at  $a^{(2)} = -30$  (the  $y$ -axis intercepts of the blue and orange curves) and when  $a^{(2)}$  equals  $-30$  and  $0$  at

$a^{(1)} = -30$  (the sides of the blue curves) indicates a weaker contribution of the non-ideality of Component 2 to decreasing the eutectic temperature (as compared with that of Component 1). This shows that compared with Component 2, the non-ideality of Component 1 is more significant in the formation of deeper eutectic mixtures.

Figure 6 shows the effect of the non-ideality of the liquid phase on eutectic composition at different melting enthalpies. The low activity coefficients of Component 1 significantly shift the eutectic point to a higher content of Component 1 (toward higher  $x_{1,e}$  values), whereas an opposite effect is observed for the low activity coefficients of Component 2 (toward lower  $x_{1,e}$  values). However, the effect of the activity coefficients of Component 1 is significantly larger than that of Component 2 (see Figure 5c).



**Figure 6.** Effect of activity coefficients and melting enthalpies of the components on the eutectic mole fraction of Component 1 assuming different melting enthalpy values of components (a)  $\Delta h_{m,1} = 32.64 \text{ kJ mol}^{-1}$  and  $\Delta h_{m,2} = 16.32 \text{ kJ mol}^{-1}$  (b)  $\Delta h_{m,1} = 12.00 \text{ kJ mol}^{-1}$  and  $\Delta h_{m,2} = 16.32 \text{ kJ mol}^{-1}$  (c)  $\Delta h_{m,1} = 32.64 \text{ kJ mol}^{-1}$  and  $\Delta h_{m,2} = 6.00 \text{ kJ mol}^{-1}$  (d)  $\Delta h_{m,1} = 12.00 \text{ kJ mol}^{-1}$  and  $\Delta h_{m,2} = 6.00 \text{ kJ mol}^{-1}$ . The melting temperatures of Components 1 and 2 are set to 600 K and 300 K, respectively. The parameter value is only a measure for non-ideality with no physical significance. Legend: —  $a^{(1)} = -30$ ; - - -  $a^{(1)} = -18$ ; . . .  $a^{(1)} = -12$ ; - . -  $a^{(1)} = 0$ .

To summarize, the melting properties as well as the activity coefficients of the components can affect the position of the eutectic point. Eutectic composition shifts to the side of the component that has lower activity coefficients as well as a lower melting enthalpy. If both components have similar activity coefficients and melting enthalpies, the eutectic composition might occur at a molar ratio of 1:1. Low melting enthalpies and activity coefficients of both components lead to the greatest depression of the eutectic temperature of the mixture. The melting properties and non-ideality of the high melting component have a more pronounced effect on eutectic temperature depression. Therefore, the search

for new deep eutectic mixtures should likely be based on the identification of compounds with low melting enthalpy, especially if they also possess a high melting temperature.

### 3.2. Parameter Study on Real Binary Systems

#### 3.2.1. [Ch]Cl-Based Binary Systems

Choline chloride ([Ch]Cl) is a common constituent (HBA) of DESs. The melting properties of [Ch]Cl are not available experimentally owing to its thermal instability. The decomposition temperature of [Ch]Cl is around 575 K. Recently, Fernandez et al. [56] made an indirect assessment of the melting properties of [Ch]Cl. Experimental SLE data in binary mixtures of [Ch]Cl with different ILs were fitted to the ideal solution model, and the [Ch]Cl melting properties were calculated correspondingly. The values obtained were melting enthalpy = 4.3 kJ mol<sup>-1</sup> and melting temperature = 597 K.

According to Equation (2) applied to an ideal solution ( $\gamma_i^L = 1$ ), the values of  $\ln(x_1)$  plotted as a function of the reciprocal temperature ( $1/T$ ) should fit a straight line with the  $y$ -axis intercept equal to  $(\Delta h_{m,1}/(RT_{m,1}))$  and the slope equal to  $(-\Delta h_{m,1}/R)$ . The corresponding plot for 10 [Ch]Cl/IL systems used for fitting the melting properties of [Ch]Cl is shown in Figure 7a. The points represent the experimental data for all 10 [Ch]Cl/IL systems, and the line is the fitted straight line used for the calculation of the [Ch]Cl melting properties given above. As can be seen from Figure 7a, the value of determination coefficient ( $R^2$ ) indicates a rather good linear regression. However, the points for the individual binaries are systematically distributed to the sides of the fit. For example, all points for [C<sub>2</sub>OHmim]Cl lie above the fit, whereas those for [BzCh]Cl lie below the fit. It is worth noting that the  $y$ -axis shows logarithmic values and the  $x$ -axis reciprocal values; therefore, a small shift from the fitted line corresponds to a significant difference in the calculated  $T$  and  $x$ . As shown in Figure 7b, the lines fitted to five single binaries [Ch]Cl/IL systems have different slopes and intercepts; therefore, they lead to different [Ch]Cl melting properties. The melting temperature is in the range 588.9–630.8 K and melting enthalpy is in the range 3.85–5.63 kJ mol<sup>-1</sup>, being within around 7% and 40% from the mean value, respectively. See Table S1 in supplementary material for detailed results.

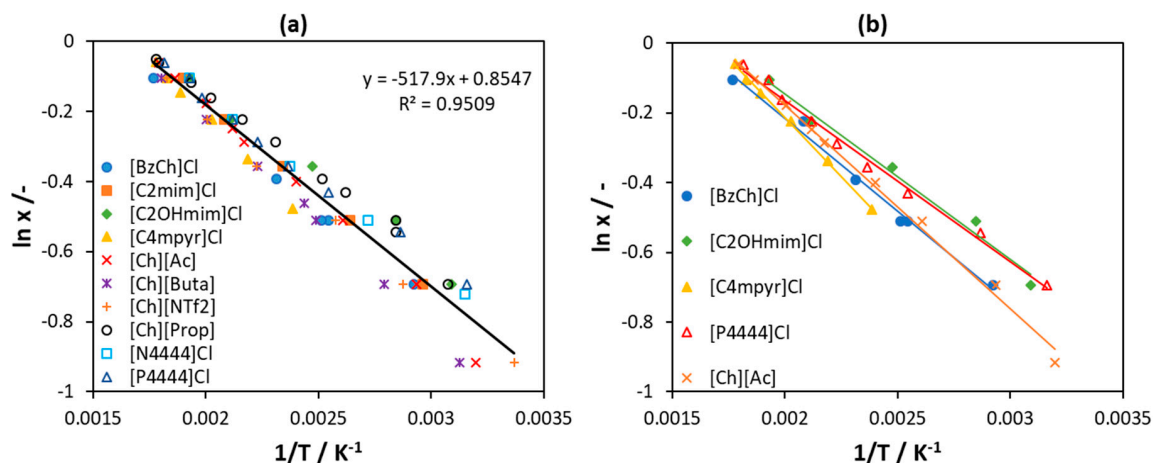


**Figure 7.** (a) Solubility of choline chloride ([Ch]Cl) in several ILs regressed to a linear function. (b) Solubility of [Ch]Cl in selected ILs, each regressed to a linear function. Data are taken from [56].

The ideal solution model accounts for the melting properties of one component only, ignoring any dissimilarity of the second components in the mixture, which can be described by activity coefficients. In order to analyze the possible non-ideality of [Ch]Cl in the liquid phase, SLE of binary mixtures of [Ch]Cl and ILs have been modeled assuming different values of [Ch]Cl melting enthalpy using the RK-polynomial with two parameters to estimate the activity coefficients. The values of [Ch]Cl melting temperature estimated from single [Ch]Cl/IL mixtures scatter within 7% only, and as shown in Section 3.1.1 for the hypothetical ideal system, the absolute values of melting temperatures have on

effect on the eutectic point properties. Hence, the value of 597 K estimated by Fernandes et al. [56] has been used in the present work. Figure 8a shows the obtained results for the [Ch]Cl liquidus line in the [Ch]Cl/choline acetate [Ch][Ac] binary system as an example. Figure 8b represents the corresponding data for activity coefficients of [Ch]Cl, wherein the points correspond to the values calculated from the experimental data using Equation (2) and the lines give the best fit using the RK-polynomial. As shown in Figure 8a, it is possible to model the SLE data with rather good agreement assuming different values of [Ch]Cl melting enthalpy, except in the cases of very low ( $1 \text{ kJ mol}^{-1}$ ) values. However, as seen from Figure 8b, the experimental activity coefficients of [Ch]Cl in the liquid phase change as the melting enthalpy of [Ch]Cl changes. This is because a variation in the melting enthalpy indicates a change in the value of the reference state chemical potential to which the activity coefficients refer. [Ch]Cl shows ideal behavior when the melting enthalpy has a low value of  $5 \text{ kJ mol}^{-1}$ , a value close to that found by Fernandez et al. [56].

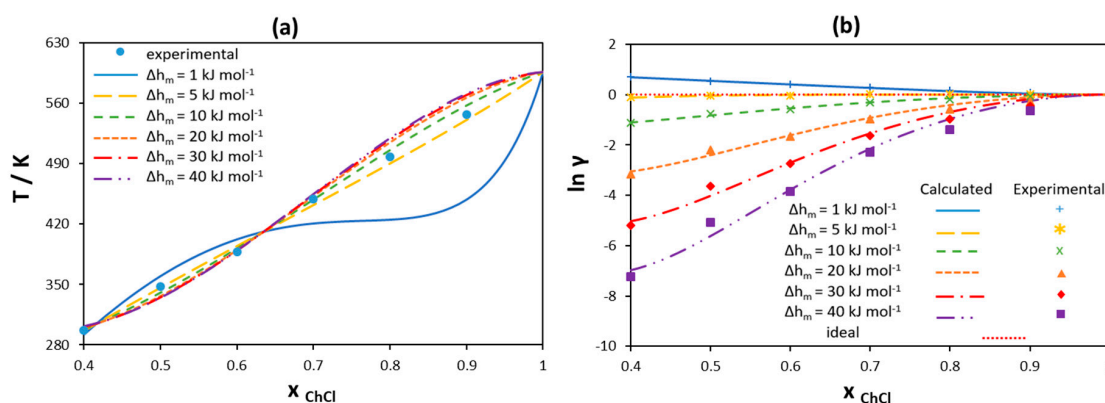


**Figure 8.** (a) Liquidus line of [Ch]Cl in a [Ch]Cl/choline acetate binary mixture modeled using the RK-polynomial assuming different melting enthalpy values. (b) Activity coefficients of [Ch]Cl in the liquid phase calculated using the RK-polynomial assuming different melting enthalpy values. Melting temperature of [Ch]Cl is assumed to be 597 K. Experimental data are taken from [56].

Results for other studied [Ch]Cl/IL systems can be found in Figures S1–S3 in the supplementary material. Figure 9 shows the absolute average deviation (AAD) obtained when screening the melting enthalpy of [Ch]Cl in all studied [Ch]Cl/IL binary mixtures. The high error in modeling the solubility of [Ch]Cl using a very low melting enthalpy ( $1 \text{ kJ mol}^{-1}$ ) indicates that such a value might be unreasonable. At the same time, experimental data can be modeled with low AAD when the value of  $\Delta h_{m,1}$  is in the range  $5\text{--}40 \text{ kJ mol}^{-1}$ .

To further explore [Ch]Cl behavior in the liquid phase, the value of the activity coefficients of [Ch]Cl at the experimental eutectic point can be analyzed (see Figure 10). As seen from the figure, at low melting enthalpy values of [Ch]Cl ( $<5 \text{ kJ mol}^{-1}$ ), the activity coefficients are close to one in all previously studied binary systems (as found by Fernandez et al. [56]). However, at higher [Ch]Cl melting enthalpies ( $>20 \text{ kJ mol}^{-1}$ ), the values of the activity coefficients change (see Figure 10). As seen in Figure 11, the molecular structures of ILs significantly differ from each other and from [Ch]Cl, that would result in different hydrophobicities. Owing to the long alkyl chains in  $[\text{P4444}]^+$  and  $[\text{N4444}]^+$  cations, these cations are more hydrophobic than the  $[\text{Ch}]^+$  cation; hence, the interactions in solution would differ from those of the pure components. At low values of [Ch]Cl melting enthalpy, the difference in the interactions is concealed, leading to quasi-ideal behavior. However, at higher values, the difference in molecular size and hydrophobicity appears obvious.

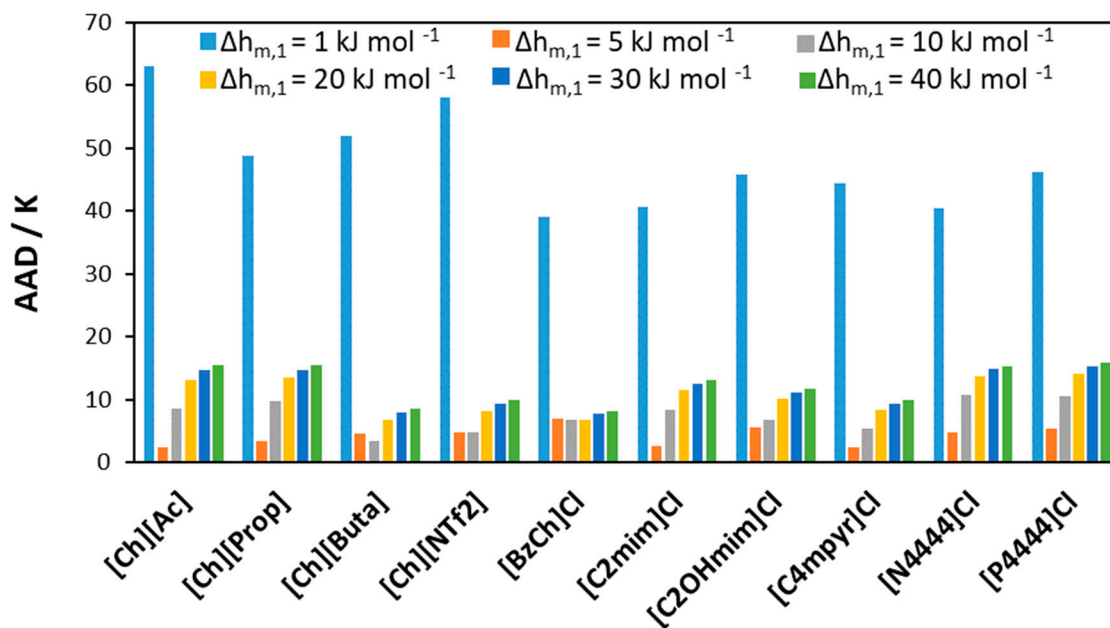


**Figure 9.** AAD between calculated and experimental liquidus temperatures for binary mixtures of [Ch]Cl and ILs assuming different melting enthalpies for [Ch]Cl.

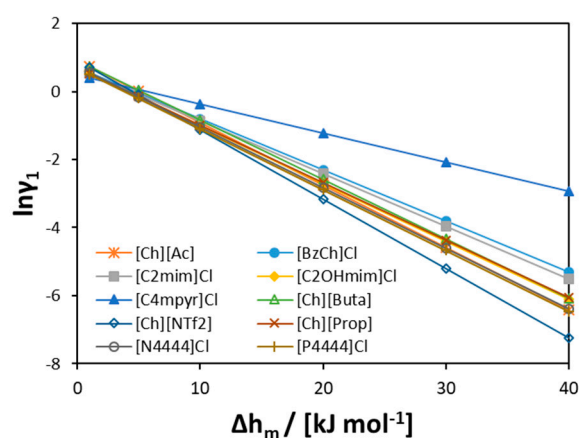


**Figure 10.** The activity coefficients of [Ch]Cl at the experimental eutectic point estimated assuming different melting enthalpies of [Ch]Cl.

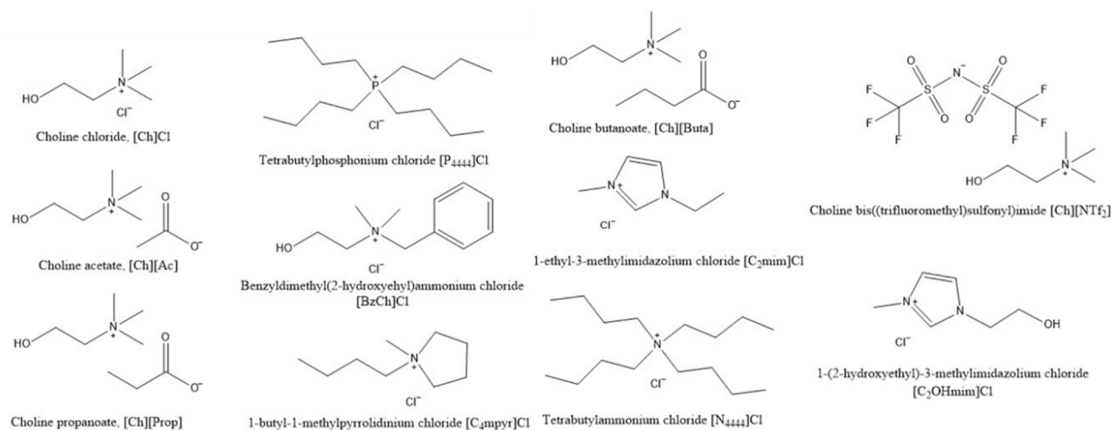


**Figure 11.** Chemical names and structures of the [Ch]Cl and ILs studied.



Despite the fact that predicting [Ch]Cl solubility in ILs is possible by assuming an ideal solubility model with a low melting enthalpy of [Ch]Cl, system-specific information such as the interactions of [Ch]Cl with different ILs can be hidden by the system ideality assumption. Martins et al. [49] also suggested that the deep depression of the eutectic temperature in [Ch]Cl-based mixtures is due to the low value of its melting enthalpy. Assessing these important features of such systems is an advantage of modeling the non-ideality in the liquid phase. An apparent changing of the melting enthalpies of the components leads to different activity coefficients in the liquid phase. This leads to a different conclusion about the intermolecular interactions and the behavior of the components in the system, which might be beneficial in decreasing the complexity of SLE modeling. However, a discussion of SLE results might be impractical based on this empirical approach.

### 3.2.2. Quaternary Ammonium Chloride Salts/Fatty Acids DES

The SLE of binary mixtures of different quaternary ammonium chlorides and fatty acids have been studied in detail [46]. These systems are considered DESs owing to strong negative deviation from ideality in quaternary ammonium chloride liquidus lines. Pontes et al. [46] used PC-SAFT to model liquid phase non-ideality. The modeling results are in good agreement with experimental data. The melting properties of these salts reported in Pontes et al. [46] are summarized in supplementary materials. Pontes et al. [46] confirmed the decomposition of [N<sub>1111</sub>]Cl, and its melting properties were estimated using SLE data and activity coefficients calculated using COSMO-RS. For the other two salts namely, [N<sub>2222</sub>]Cl and [N<sub>3333</sub>]Cl, the melting properties were measured in Büchi apparatus and DSC. However, in earlier literature, these salts were reported to decompose at temperatures below their melting temperatures [57,58]. As a result of decomposition, the melting enthalpy measured by DSC for the salts might represent the heat of decomposition and not the melting enthalpy of these salts.

In this work, the different melting enthalpy values of quaternary ammonium chloride are screened and the activity coefficients are modeled using the Redlich–Kister polynomial with three parameters. The [N<sub>3333</sub>]Cl/palmitic acid system shows the strongest negative deviation from ideality compared with the other systems studied in Pontes et al. [46]; therefore, its SLE data are analyzed here in detail (see Figure 12). Results for the other systems can be found in Figures S5–S7 in supplementary material.

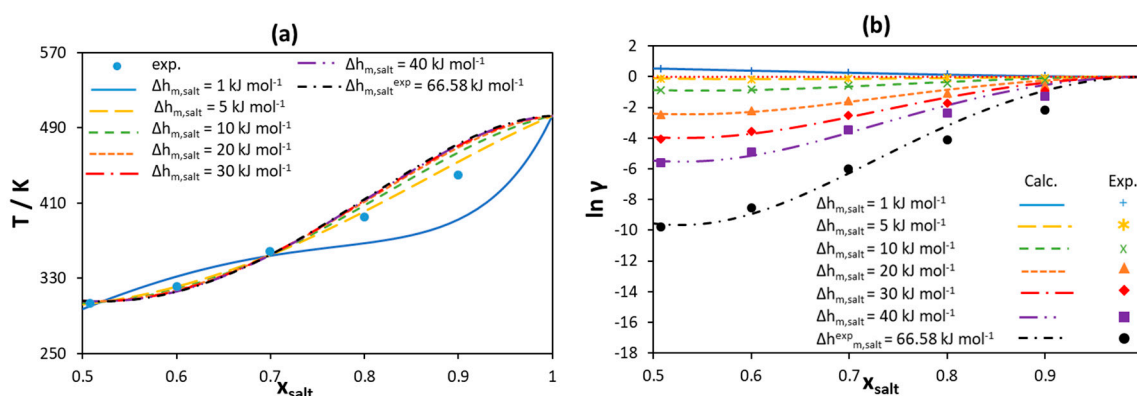


**Figure 12.** (a) [N<sub>3333</sub>]Cl liquidus line for a [N<sub>3333</sub>]Cl/palmitic acid binary mixture modeled using the Redlich–Kister polynomial with three parameters assuming different melting enthalpy values. (b) Activity coefficients of [N<sub>3333</sub>]Cl in the liquid phase calculated using the Redlich–Kister polynomial assuming different melting enthalpy values. Experimental data taken from [46].

As can be seen in Figure 12a, the liquidus lines of [N<sub>3333</sub>]Cl estimated using the RK-polynomials are in good agreement with experimental data for any melting enthalpy assumed, except for the very low melting enthalpy (1 kJ mol<sup>-1</sup>). As for [Ch]Cl/IL systems, the melting enthalpy of 5 kJ mol<sup>-1</sup> leads to ideal solubility for [N<sub>3333</sub>]Cl (see the yellow curve in Figure 12b). However, the larger the value of melting enthalpy, the stronger the negative deviations are from ideality required to reproduce

the experimental data. Therefore, assuming a very high melting enthalpy would overestimate the non-ideality, making it rather difficult to account for using well-established and relatively simple-to-use activity coefficient models.

Table 1 shows the eutectic point properties for all quaternary ammonium chloride/fatty acid binary mixtures studied in [46]. Along with the experimental eutectic composition and temperature ( $x_{e,acid}$  and  $T_e$ ), the table shows the normalized difference between the eutectic temperature predicted by PC-SAFT in [46] and the melting temperature of the acid ( $\Delta T_e$ ). As can be seen from Table 1, the largest depression in melting temperature of the mixture at the eutectic point relative to the melting temperature of the acid is for [N<sub>3333</sub>]Cl/palmitic acid system ( $\Delta T_e = 0.1096$ ). In addition, the [N<sub>3333</sub>]Cl/palmitic acid system has the eutectic composition with the highest salt mole fraction, as compared with any other quaternary ammonium chloride/fatty acid systems ( $x_{e,salt} = 0.517$ ). This seems to be due to the strong interactions between [N<sub>3333</sub>]Cl and palmitic acid, as was shown in [46] (see also the parameter study section for the link between activity coefficients and eutectic composition). As seen from Table 1,  $\Delta T_e$  values show that quaternary ammonium chlorides/ fatty acids DESs do not show deep eutectic behavior based on the normalized depression at eutectic point. However, based on the definition of Kollau et al. [47] and Martins et al. [49] for deep eutectic solvents, these systems would be considered as deep eutectic systems. The small depression at eutectic temperature relative to the acid melting temperature might be a result of the high melting enthalpies of the fatty acids. As shown in the parameter study, melting properties of components affect the depression at eutectic point in a larger extent compared to the eutectic composition. In contrast, activity coefficient values significantly shift the eutectic composition to the side of the component with low activity coefficients. Therefore, the eutectic composition gives an indication for the component with the larger negative deviation from ideality.

**Table 1.** Comparison of eutectic composition, eutectic temperature, and the normalized difference between the eutectic temperature estimated using PC-SAFT and the melting temperature of the acids. Data are taken from [46].

	[N <sub>1111</sub> ]Cl			[N <sub>2222</sub> ]Cl			[N <sub>3333</sub> ]Cl		
	$x_{e,acid}$	$T_e$	$\Delta T_e$	$x_{e,acid}$	$T_e$	$\Delta T_e$	$x_{e,acid}$	$T_e$	$\Delta T_e$
Capric acid	0.808	299.91	0.0161	0.614	297.40	0.0247	0.710	288.46	0.0565
Lauric acid	0.630	303.01	0.0478	0.640	301.44	0.0532	0.644	297.05	0.0688
Myristic acid	0.712	321.65	0.0167	0.658	317.88	0.0288	0.571	304.54	0.0738
Palmitic acid	0.615	328.51	0.0254	0.607	318.78	0.0567	0.483	303.56	0.1096
Stearic acid	0.634	337.89	0.0171	0.556	317.02	0.0841	0.562	322.82	0.0646

To summarize, changing the melting enthalpy value of quaternary ammonium chloride changes the activity coefficient values and thus hides or increases the actual complexity of the systems. Eutectic systems with a high deviation from ideality do not always have a large depression at eutectic temperature; rather, they would have a large shift in the eutectic composition away from pure components sides.

#### 4. Method

To study the effect of melting properties and intermolecular interactions on eutectic point properties, a hypothetical binary system is assumed. The system is considered to be either ideal ( $\gamma_i^L = 1$ ) in order to only study the effect of melting properties, or non-ideal (with negative deviations from ideality;  $\gamma_i^L < 1$ ) to consider the effect of intermolecular interactions. Different values of melting enthalpy and melting temperature are screened for each of the components. In some cases, the melting enthalpy values have been estimated using the Walden rule. The Walden rule states that the melting

entropy of rigid molecules is constant, with a value of  $54.4 \text{ J mol}^{-1}\text{K}^{-1}$  [52]. The melting enthalpy can thus be calculated as

$$\Delta h_m = 54.4 T_m \quad (3)$$

To model the non-ideality of components, the activity coefficients of components in the liquid phase are calculated using Redlich–Kister (RK) polynomial [51]

$$RT \ln \gamma_i = a^{(i)} x_j^2 + b^{(i)} x_j^3 + c^{(i)} x_j^4 \dots \quad (4)$$

When the activity coefficients are screened (Section 3.1.2), only the first term with one parameter is used. In this case, when parameter  $a^{(i)}$  is equal to zero, the ideal case is described; whereas  $a^{(i)} < 0$  describes favored interactions between unlike molecules in the liquid phase—i.e., negative deviation from ideality. Positive deviation from ideality leads to a higher liquidus temperature compared with the ideal case; therefore, values of parameter  $a^{(i)} > 0$  are not considered in this work. The parameters are empirical and do not provide any physical significance. They are just used as a measure of different values of activity coefficients of components.

For modeling the non-ideality in [Ch]Cl/ILs binary systems (Section 3.2.1), two terms with two parameters are used. Binary mixtures of quaternary ammonium chlorides with fatty acids (Section 3.2.2) are more complex; hence, three terms with three parameters are used. In the latter two cases, for a given melting enthalpy value, the RK-parameters are fitted to the SLE experimental data by minimizing the objective function

$$OF = \sum (\gamma_1^{cal} - \gamma_1^{exp})^2 \quad (5)$$

where  $\gamma_1^{cal}$  is the calculated activity coefficient of Component 1 in the liquid phase using the RK-polynomial and  $\gamma_1^{exp}$  is the activity coefficient of Component 1 in the liquid phase estimated using Equation (2) and measured SLE taken from the literature.

To evaluate the quality of the calculated SLE data, the AAD between the calculated ( $T_i^{cal}$ ) and experimental ( $T_i^{exp}$ ) liquidus temperatures is calculated as

$$AAD = \frac{1}{N} \sum_i^N |T_i^{cal} - T_i^{exp}| \quad (6)$$

## 5. Conclusions

The parameter study carried out in the present work shows that (i) obtaining the accurate melting properties of pure constituents and (ii) adequate modeling of non-ideality in the liquid phase are essential for prediction of the SLE in DESs. Deep eutectics can be a result of low melting enthalpies, low activity coefficients, or both. When analyzing the modeled SLE diagrams, the estimate of eutectic composition can provide a better indication of system non-ideality. Components with lower activity coefficient values have a higher mole fraction at the eutectic point. In systems of two components with similar melting enthalpies and similar activity coefficients, the eutectic composition is observed at around a 1:1 molar ratio of the two components. Therefore, designing DES systems should simultaneously take into account melting properties as well as interactions between unlike molecules. However, strong negative deviation from ideality is not the only reason for DES formation; substances with low melting enthalpies could also form rather deep eutectics.

Recent work on the SLE of [Ch]Cl-based DES systems has reported that under an assumption of a low melting enthalpy value ( $4.3 \text{ kJ mol}^{-1}$ ), [Ch]Cl behaves quasi-ideally in most such systems. However, molecular experiments and simulations in the recent literature have revealed that [Ch]Cl-based systems behave in a complex manner. As demonstrated in the present study, the solubility of [Ch]Cl in different ILs can be adequately modeled assuming different melting enthalpy values. Small values lead to a nearly ideal behavior in the liquid phase, whereas it is necessary to account for activity coefficients at higher melting enthalpy values. Owing to the absence of any experimental data on the melting

enthalpy of [Ch]Cl for comparison, it is not possible to determine which of the values is true. However, owing to the differences in size and hydrophobicity of the studied ILs, differences in their interactions with [Ch]Cl should be expected. Thus, the low melting enthalpy value may conceal the complexity of interactions in the liquid phase and should be used with caution. Therefore, modeling the SLE of [Ch]Cl-based DESs remains unclear; more research is necessary to fully understand the behavior of these systems.

For DES systems with strong intermolecular interactions between unlike molecules, the depression in melting temperature at the eutectic point is not related only to activity coefficient values. The studied quaternary ammonium chloride/fatty acid systems show strong negative deviation from ideality with small depression at eutectic point relative to the acid melting temperature. At the same time, the systems show a shift in the eutectic composition to the side of the salt. Therefore, the eutectic composition can provide an indication of strong interactions—e.g., hydrogen bonds—between DES components.

From the application viewpoint when designing a DES, no strict definition of a DES system is necessary; rather, a better understanding of the system behavior and intermolecular interactions, reliable data for the SLE of mixtures and pure components, and an assessment of system suitability for an actual application are required. In fact, any simple eutectic mixture with a large depression in eutectic temperature relative to the melting temperatures of the pure constituents sufficient to form a liquid at operating temperature could be referred to as a DES (or NADES). In searching for new DESs, high melting compounds with low melting enthalpies—which have strong interactions with the second component in the liquid mixture but not in its pure solid state—should be sought. The non-ideality of the liquid phase can thereby be directly estimated using well-developed and easy-to-use thermodynamic tools such as activity coefficient models and equations of state.

**Supplementary Materials:** The following are available online at <http://www.mdpi.com/1420-3049/24/12/2334/s1>. Figure S1: Liquidus line and activity coefficients in the liquid phase of [Ch]Cl in a binary mixture of [Ch]Cl and (a) [Ch][Ac], (b) [Ch][Prop], and (c) [Ch][Buta], modeled using Redlich–Kister polynomial. Figure S2: Liquidus line and activity coefficients in the liquid phase of [Ch]Cl in a binary mixture of [Ch]Cl and (a) [Ch][NTf<sub>2</sub>], (b) [BzCh]Cl, (c) [C<sub>2</sub>mim]Cl, and (d) [C<sub>2</sub>OHmim]Cl, modeled using Redlich–Kister polynomial. Figure S3: Liquidus line and activity coefficients in the liquid phase of [Ch]Cl in a binary mixture of [Ch]Cl and (a) [C<sub>4</sub>mpyr]Cl, (b) [N<sub>4444</sub>]Cl, and (c) [P<sub>4444</sub>]Cl, modeled using Redlich–Kister polynomial. Figure S4: Chemical names and structures of [Ch]Cl and ILs studied. Figure S5: Liquidus line and activity coefficients of [N<sub>1111</sub>]Cl in a binary mixture of [N<sub>1111</sub>]Cl and (a) capric acid, (b) lauric acid, (c) myristic acid, (d) palmitic acid, and (e) stearic acid, modeled using the Redlich–Kister polynomial with three parameters assuming different melting enthalpy values. Figure S6: Liquidus line and activity coefficients of [N<sub>2222</sub>]Cl in a binary mixture of [N<sub>2222</sub>]Cl and (a) capric acid, (b) lauric acid, (c) myristic acid, (d) palmitic acid, and (e) stearic acid, modeled using the Redlich–Kister polynomial with three parameters assuming different melting enthalpy values. Figure S7: Liquidus line and activity coefficients of [N<sub>3333</sub>]Cl in a binary mixture of [N<sub>3333</sub>]Cl and (a) capric acid, (b) lauric acid, (c) myristic acid, (d) palmitic acid, and (e) stearic acid, modeled using the Redlich–Kister polynomial with three parameters assuming different melting enthalpy values. Table S1: Melting properties of [Ch]Cl obtained from linear regression of the solubility of [Ch]Cl in different ILs. Table S2: Empirical parameters of RK-polynomial for calculating activity coefficients of salts in binary mixtures of quaternary ammonium chloride salts and capric acid. Table S3: Empirical parameters of RK-polynomial for calculating activity coefficients of salts in binary mixtures of quaternary ammonium chloride salts and lauric acid. Table S4: Empirical parameters of RK-polynomial for calculating activity coefficients of salts in binary mixtures of quaternary ammonium chloride salts and myristic acid. Table S5: Empirical parameters of RK-polynomial for calculating activity coefficients of salts in binary mixtures of quaternary ammonium chloride salts and palmitic acid. Table S6: Empirical parameters of RK-polynomial for calculating activity coefficients of salts in binary mixtures of quaternary ammonium chloride salts and stearic acid. Table S7: Melting properties of quaternary ammonium chloride and fatty acids.

**Author Contributions:** Conceptualization, generating data, analyzing the results and preparing the manuscript, A.A.; revising and discussing the manuscript, L.M.; supervising, revising and discussing the manuscript, M.M.

**Funding:** This work was supported by the German Research Foundation (DFG) and the Technical University of Munich (TUM) in the framework of the Open Access Publishing Program.

**Conflicts of Interest:** The authors declare no conflict of interest.

## References

1. Abbott, A.P.; Capper, G.; Davies, D.L.; Rasheed, R.K.; Tambyrajah, V. Novel solvent properties of choline chloride/urea mixtures. *Chem. Commun.* **2003**, 70–71. [[CrossRef](#)]
2. Tang, B.; Row, K. Recent developments in deep eutectic solvents in chemical sciences. *Mon. Chem.* **2013**, *144*, 1427–1454. [[CrossRef](#)]
3. Zhang, Q.; De Oliveira Vigier, K.; Royer, S.; Jerome, F. Deep eutectic solvents: Syntheses, properties and applications. *Chem. Soc. Rev.* **2012**, *41*, 7108–7146. [[CrossRef](#)] [[PubMed](#)]
4. Smith, E.L.; Abbott, A.P.; Ryder, K.S. Deep Eutectic Solvents (DESs) and Their Applications. *Chem. Rev.* **2014**, *114*, 11060–11082. [[CrossRef](#)] [[PubMed](#)]
5. Liu, P.; Hao, J.-W.; Mo, L.-P.; Zhang, Z.-H. Recent advances in the application of deep eutectic solvents as sustainable media as well as catalysts in organic reactions. *RSC Adv.* **2015**, *5*, 48675–48704. [[CrossRef](#)]
6. Abbott, A.P.; Ahmed, E.I.; Prasad, K.; Qader, I.B.; Ryder, K.S. Liquid pharmaceuticals formulation by eutectic formation. *Fluid Phase Equilib.* **2017**, *448*, 2–8. [[CrossRef](#)]
7. Aroso, I.M.; Craveiro, R.; Rocha, A.; Dionísio, M.; Barreiros, S.; Reis, R.L.; Paiva, A.; Duarte, A.R.C. Design of controlled release systems for THEDES—Therapeutic deep eutectic solvents, using supercritical fluid technology. *Int. J. Pharm.* **2015**, *492*, 73–79. [[CrossRef](#)] [[PubMed](#)]
8. Aroso, I.M.; Silva, J.C.; Mano, F.; Ferreira, A.S.; Dionísio, M.; Sá-Nogueira, I.; Barreiros, S.; Reis, R.L.; Paiva, A.; Duarte, A.R.C. Dissolution enhancement of active pharmaceutical ingredients by therapeutic deep eutectic systems. *Eur. J. Pharm. Sci.* **2016**, *98*, 57–66. [[CrossRef](#)]
9. Hayyan, A.; Ali Hashim, M.; Mjalli, F.S.; Hayyan, M.; AlNashef, I.M. A novel phosphonium-based deep eutectic catalyst for biodiesel production from industrial low grade crude palm oil. *Chem. Eng. Sci.* **2013**, *92*, 81–88. [[CrossRef](#)]
10. Hayyan, A.; Hashim, M.A.; Hayyan, M.; Mjalli, F.S.; AlNashef, I.M. A novel ammonium based eutectic solvent for the treatment of free fatty acid and synthesis of biodiesel fuel. *Ind. Crop. Prod.* **2013**, *46*, 392–398. [[CrossRef](#)]
11. Hadj-Kali, M.K.; Mulyono, S.; Hizaddin, H.F.; Wazeer, I.; El-Blidi, L.; Ali, E.; Hashim, M.A.; AlNashef, I.M. Removal of Thiophene from Mixtures with n-Heptane by Selective Extraction Using Deep Eutectic Solvents. *Ind. Eng. Chem. Res.* **2016**, *55*, 8415–8423. [[CrossRef](#)]
12. García, A.; Rodríguez-Juan, E.; Rodríguez-Gutiérrez, G.; Rios, J.J.; Fernández-Bolaños, J. Extraction of phenolic compounds from virgin olive oil by deep eutectic solvents (DESs). *Food Chem.* **2016**, *197*, 554–561. [[CrossRef](#)] [[PubMed](#)]
13. Peng, X.; Duan, M.-H.; Yao, X.-H.; Zhang, Y.-H.; Zhao, C.-J.; Zu, Y.-G.; Fu, Y.-J. Green extraction of five target phenolic acids from *Lonicerae japonicae* Flos with deep eutectic solvent. *Sep. Purif. Technol.* **2016**, *157*, 249–257. [[CrossRef](#)]
14. Rodriguez, N.R.; Ferre Guell, J.; Kroon, M.C. Glycerol-Based Deep Eutectic Solvents as Extractants for the Separation of MEK and Ethanol via Liquid-Liquid Extraction. *J. Chem. Eng. Data* **2016**, *61*, 865–872. [[CrossRef](#)]
15. Zhang, H.; Wang, Y.; Xu, K.; Li, N.; Wen, Q.; Yang, Q.; Zhou, Y. Ternary and binary deep eutectic solvents as a novel extraction medium for protein partitioning. *Anal. Methods* **2016**, *8*, 8196–8207. [[CrossRef](#)]
16. Pena-Pereira, F.; Namieśnik, J. Ionic Liquids and Deep Eutectic Mixtures: Sustainable Solvents for Extraction Processes. *Chem. Sus. Chem.* **2014**, *7*, 1784–1800. [[CrossRef](#)] [[PubMed](#)]
17. Roehrer, S.; Bezold, F.; Garcia, E.M.; Minceva, M. Deep eutectic solvents in countercurrent and centrifugal partition chromatography. *J. Chromatogr. A* **2016**, *1434*, 102–110. [[CrossRef](#)]
18. Bezold, F.; Weinberger, M.E.; Minceva, M. Assessing solute partitioning in deep eutectic solvent-based biphasic systems using the predictive thermodynamic model COSMO-RS. *Fluid Phase Equilib.* **2017**, *437*, 23–33. [[CrossRef](#)]
19. Bezold, F.; Weinberger, M.E.; Minceva, M. Computational solvent system screening for the separation of tocopherols with centrifugal partition chromatography using deep eutectic solvent-based biphasic systems. *J. Chromatogr. A* **2017**, *1491*, 153–158. [[CrossRef](#)]
20. Bezold, F.; Minceva, M. A water-free solvent system containing an L-menthol-based deep eutectic solvent for centrifugal partition chromatography applications. *J. Chromatogr. A* **2019**, *1587*, 166–171. [[CrossRef](#)]

21. Atilhan, M.; Aparicio, S. Behavior of Deep Eutectic Solvents under External Electric Fields: A Molecular Dynamics Approach. *J. Phys. Chem. B* **2017**, *121*, 221–232. [[CrossRef](#)] [[PubMed](#)]
22. Das, A.; Das, S.; Biswas, R. Fast fluctuations in deep eutectic melts: Multi-probe fluorescence measurements and all-atom molecular dynamics simulation study. *Chem. Phys. Lett.* **2013**, *581*, 47–51. [[CrossRef](#)]
23. Das, A.; Das, S.; Biswas, R. Density relaxation and particle motion characteristics in a non-ionic deep eutectic solvent (acetamide + urea): Time-resolved fluorescence measurements and all-atom molecular dynamics simulations. *J. Chem. Phys.* **2015**, *142*, 034505. [[CrossRef](#)] [[PubMed](#)]
24. Ferreira, E.S.C.; Voroshylova, I.V.; Pereira, C.M.; Cordeiro, M.N.D.S. Improved Force Field Model for the Deep Eutectic Solvent Ethaline: Reliable Physicochemical Properties. *J. Phys. Chem. B* **2016**, *120*, 10124–10137. [[CrossRef](#)] [[PubMed](#)]
25. García, G.; Atilhan, M.; Aparicio, S. The impact of charges in force field parameterization for molecular dynamics simulations of deep eutectic solvents. *J. Mol. Liq.* **2015**, *211*, 506–514. [[CrossRef](#)]
26. Hammond, O.S.; Bowron, D.T.; Edler, K.J. Liquid structure of the choline chloride-urea deep eutectic solvent (reline) from neutron diffraction and atomistic modelling. *Green Chem.* **2016**, *18*, 2736–2744. [[CrossRef](#)]
27. Morrow, T.I.; Maginn, E.J. Density, local composition and diffusivity of aqueous choline chloride solutions: A molecular dynamics study. *Fluid Phase Equilib.* **2004**, *217*, 97–104. [[CrossRef](#)]
28. Perkins, S.L.; Painter, P.; Colina, C.M. Experimental and computational studies of choline chloride-based deep eutectic solvents. *J. Chem. Eng. Data* **2014**, *59*, 3652–3662. [[CrossRef](#)]
29. Sun, H.; Li, Y.; Wu, X.; Li, G. Theoretical study on the structures and properties of mixtures of urea and choline chloride. *J. Mol. Model.* **2013**, *19*, 2433–2441. [[CrossRef](#)] [[PubMed](#)]
30. Zahn, S. Deep eutectic solvents: Similia similibus solvuntur? *Phys. Chem. Chem. Phys.* **2017**, *19*, 4041–4047. [[CrossRef](#)] [[PubMed](#)]
31. García, G.; Atilhan, M.; Aparicio, S. An approach for the rationalization of melting temperature for deep eutectic solvents from DFT. *Chem. Phys. Lett.* **2015**, *634*, 151–155. [[CrossRef](#)]
32. Gilmore, M.; Moura, L.M.; Turner, A.H.; Swadźba-Kwaśny, M.; Callear, S.K.; McCune, J.A.; Scherman, O.A.; Holbrey, J.D. A comparison of choline:urea and choline:oxalic acid deep eutectic solvents at 338 K. *J. Chem. Phys.* **2018**, *148*, 193823. [[CrossRef](#)] [[PubMed](#)]
33. Ashworth, C.R.; Matthews, R.P.; Welton, T.; Hunt, P.A. Doubly ionic hydrogen bond interactions within the choline chloride-urea deep eutectic solvent. *Phys. Chem. Chem. Phys.* **2016**, *18*, 18145–18160. [[CrossRef](#)] [[PubMed](#)]
34. Stefanovic, R.; Ludwig, M.; Webber, G.B.; Atkin, R.; Page, A.J. Nanostructure, hydrogen bonding and rheology in choline chloride deep eutectic solvents as a function of the hydrogen bond donor. *Phys. Chem. Chem. Phys.* **2017**, *19*, 3297–3306. [[CrossRef](#)] [[PubMed](#)]
35. Mainberger, S.; Kindlein, M.; Bezold, F.; Elts, E.; Minceva, M.; Briesen, H. Deep eutectic solvent formation: A structural view using molecular dynamics simulations with classical force fields. *Mol. Phys.* **2017**, *115*, 1309–1321. [[CrossRef](#)]
36. Fischer, V. Properties and Applications of Deep Eutectic Solvents and Low-Melting Mixtures Dissertation. Ph.D. Thesis, Universität Regensburg, Regensburg, Germany, 2015.
37. Abbott, A.P.; Boothby, D.; Capper, G.; Davies, D.L.; Rasheed, R.K. Deep Eutectic Solvents Formed between Choline Chloride and Carboxylic Acids: Versatile Alternatives to Ionic Liquids. *J. Am. Chem. Soc.* **2004**, *126*, 9142–9147. [[CrossRef](#)] [[PubMed](#)]
38. Morrison, H.G.; Sun, C.C.; Neervannan, S. Characterization of thermal behavior of deep eutectic solvents and their potential as drug solubilization vehicles. *Int. J. Pharm.* **2009**, *378*, 136–139. [[CrossRef](#)]
39. Kareem, M.A.; Mjalli, F.S.; Hashim, M.A.; AlNashef, I.M. Phosphonium-Based Ionic Liquids Analogues and Their Physical Properties. *J. Chem. Eng. Data* **2010**, *55*, 4632–4637. [[CrossRef](#)]
40. Guo, W.; Hou, Y.; Ren, S.; Tian, S.; Wu, W. Formation of Deep Eutectic Solvents by Phenols and Choline Chloride and Their Physical Properties. *J. Chem. Eng. Data* **2013**, *58*, 866–872. [[CrossRef](#)]
41. Meng, X.; Ballerat-Busserolles, K.; Husson, P.; Andanson, J.-M. Impact of water on the melting temperature of urea + choline chloride deep eutectic solvent. *New J. Chem.* **2016**, *40*, 4492–4499. [[CrossRef](#)]
42. Silva, L.P.; Fernandez, L.; Conceição, J.H.F.; Martins, M.A.R.; Sosa, A.; Ortega, J.; Pinho, S.P.; Coutinho, J.A.P. Design and Characterization of Sugar-Based Deep Eutectic Solvents Using Conductor-like Screening Model for Real Solvents. *ACS Sustain. Chem. Eng.* **2018**, *6*, 10724–10734. [[CrossRef](#)]

43. Martins, M.A.R.; Crespo, E.A.; Pontes, P.V.A.; Silva, L.P.; Bülow, M.; Maximo, G.J.; Batista, E.A.C.; Held, C.; Pinho, S.P.; Coutinho, J.A.P. Tunable Hydrophobic Eutectic Solvents Based on Terpenes and Monocarboxylic Acids. *ACS Sustain. Chem. Eng.* **2018**, *6*, 8836–8846. [[CrossRef](#)]
44. Crespo, E.A.; Silva, L.P.; Martins, M.A.R.; Bülow, M.; Ferreira, O.; Sadowski, G.; Held, C.; Pinho, S.P.; Coutinho, J.A.P. The Role of Polyfunctionality in the Formation of [Ch]Cl-Carboxylic Acid-Based Deep Eutectic Solvents. *Ind. Eng. Chem. Res.* **2018**, *57*, 11195–11209. [[CrossRef](#)]
45. Crespo, E.A.; Silva, L.P.; Martins, M.A.R.; Fernandez, L.; Ortega, J.; Ferreira, O.; Sadowski, G.; Held, C.; Pinho, S.P.; Coutinho, J.A.P. Characterization and Modeling of the Liquid Phase of Deep Eutectic Solvents Based on Fatty Acids/Alcohols and Choline Chloride. *Ind. Eng. Chem. Res.* **2017**, *56*, 12192–12202. [[CrossRef](#)]
46. Pontes, P.V.A.; Crespo, E.A.; Martins, M.A.R.; Silva, L.P.; Neves, C.M.S.S.; Maximo, G.J.; Hubinger, M.D.; Batista, E.A.C.; Pinho, S.P.; Coutinho, J.A.P.; et al. Measurement and PC-SAFT modeling of solid–liquid equilibrium of deep eutectic solvents of quaternary ammonium chlorides and carboxylic acids. *Fluid Phase Equilib.* **2017**, *448*, 69–80. [[CrossRef](#)]
47. Kollau, L.J.B.M.; Vis, M.; van den Bruinhorst, A.; Esteves, A.C.C.; Tuinier, R. Quantification of the liquid window of deep eutectic solvents. *Chem. Commun.* **2018**, *54*, 13351–13354. [[CrossRef](#)] [[PubMed](#)]
48. Gamsjäger, H.; Lorimer John, W.; Scharlin, P.; Shaw David, G. Glossary of terms related to solubility (IUPAC Recommendations 2008). *Pure Appl. Chem.* **2008**, *80*, 233–276. [[CrossRef](#)]
49. Martins, M.A.R.; Pinho, S.P.; Coutinho, J.A.P. Insights into the Nature of Eutectic and Deep Eutectic Mixtures. *J. Solut. Chem.* **2018**, 1–21. [[CrossRef](#)]
50. Pyykkö, P. Simple Estimates for Eutectic Behavior. *Chem. Phys. Chem.* **2019**, *20*, 123–127. [[CrossRef](#)]
51. Prausnitz, J.M.; Lichtenthaler, R.N.; Azevedo, E.G.d. *Molecular Thermodynamics of Fluid-Phase Equilibria*; Prentice Hall PTR: Upper Saddle River, NJ, USA, 1999.
52. Katritzky, A.R.; Jain, R.; Lomaka, A.; Petrukhin, R.; Maran, U.; Karelson, M. Perspective on the Relationship between Melting Points and Chemical Structure. *Cryst. Growth Des.* **2001**, *1*, 261–265. [[CrossRef](#)]
53. Brown, R.J.C.; Brown, R.F.C. Melting Point and Molecular Symmetry. *J. Chem. Educ.* **2000**, *77*, 724. [[CrossRef](#)]
54. Gavezzotti, A. Are Crystal Structures Predictable? *Acc. Chem. Res.* **1994**, *27*, 309–314. [[CrossRef](#)]
55. Jain, A.; Yalkowsky, S.H. Estimation of Melting Points of Organic Compounds-II. *J. Pharm. Sci.* **2006**, *95*, 2562–2618. [[CrossRef](#)]
56. Fernandez, L.; Silva, L.P.; Martins, M.A.R.; Ferreira, O.; Ortega, J.; Pinho, S.P.; Coutinho, J.A.P. Indirect assessment of the fusion properties of choline chloride from solid–liquid equilibria data. *Fluid Phase Equilib.* **2017**, *448*, 9–14. [[CrossRef](#)]
57. Sawicka, M.; Storonik, P.; Błażejowski, J.; Rak, J. TG-FTIR, DSC, and Quantum-Chemical Studies on the Thermal Decomposition of Quaternary Ethylammonium Halides. *J. Phys. Chem. A* **2006**, *110*, 5066–5074. [[CrossRef](#)] [[PubMed](#)]
58. Sawicka, M.; Storonik, P.; Skurski, P.; Błażejowski, J.; Rak, J. TG-FTIR, DSC and quantum chemical studies of the thermal decomposition of quaternary methylammonium halides. *Chem. Phys.* **2006**, *324*, 425–437. [[CrossRef](#)]

**Sample Availability:** Samples not available.



© 2019 by the authors. Licensee MDPI, Basel, Switzerland. This article is an open access article distributed under the terms and conditions of the Creative Commons Attribution (CC BY) license (<http://creativecommons.org/licenses/by/4.0/>).

## Supplementary Material

# Modeling of Solid-liquid Equilibria in Deep Eutectic Solvents: A Parameter Study

Ahmad Alhadid <sup>1</sup>, Liudmila Mokrushina <sup>2</sup> and Mirjana Minceva <sup>1,\*</sup>

<sup>1</sup> Technical University of Munich, Biothermodynamics, TUM School of Life and Food Sciences Weißenstephan, Maximus-von-Imhof-Forum 2, 85354 Freising, Germany; [ahmad.alhadid@tum.de](mailto:ahmad.alhadid@tum.de); [mirjana.minceva@tum.de](mailto:mirjana.minceva@tum.de)

<sup>2</sup> Friedrich-Alexander-Universität Erlangen-Nürnberg (FAU), Separation Science & Technology, Egerlandstr. 3, 91058 Erlangen, Germany; [liudmila.mokrushina@fau.de](mailto:liudmila.mokrushina@fau.de)

\* Correspondence: [mirjana.minceva@tum.de](mailto:mirjana.minceva@tum.de)

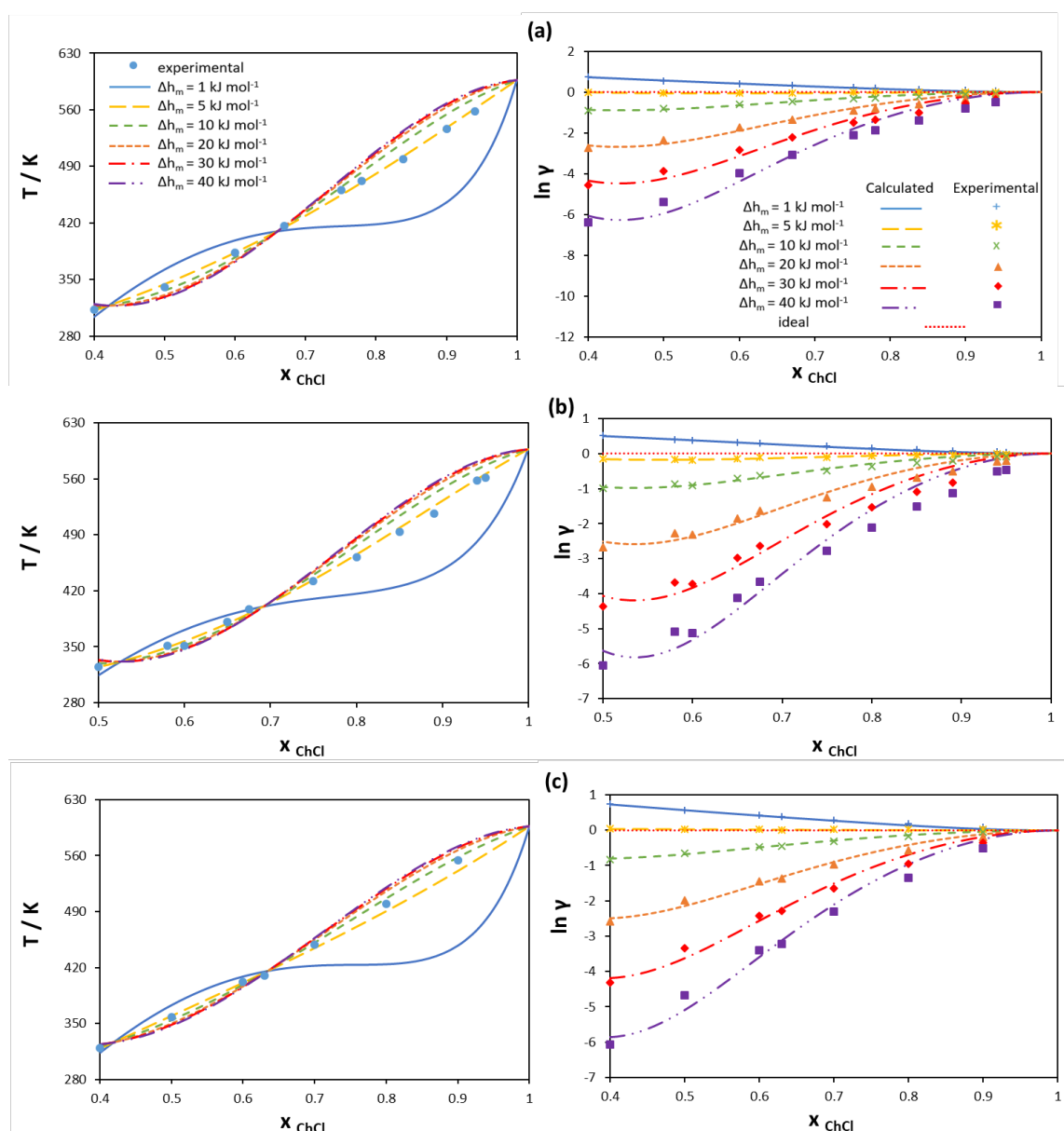


**Figure S1.** Liquidus line (left) and activity coefficients in liquid phase (right) of [Ch]Cl in binary mixture of [Ch]Cl and (a) [Ch][Ac] (b)[Ch][Prop] (c)[Ch][Buta] modeled using Redlich–Kister polynomial. Experimental data are taken from Fernandez et al. [1].



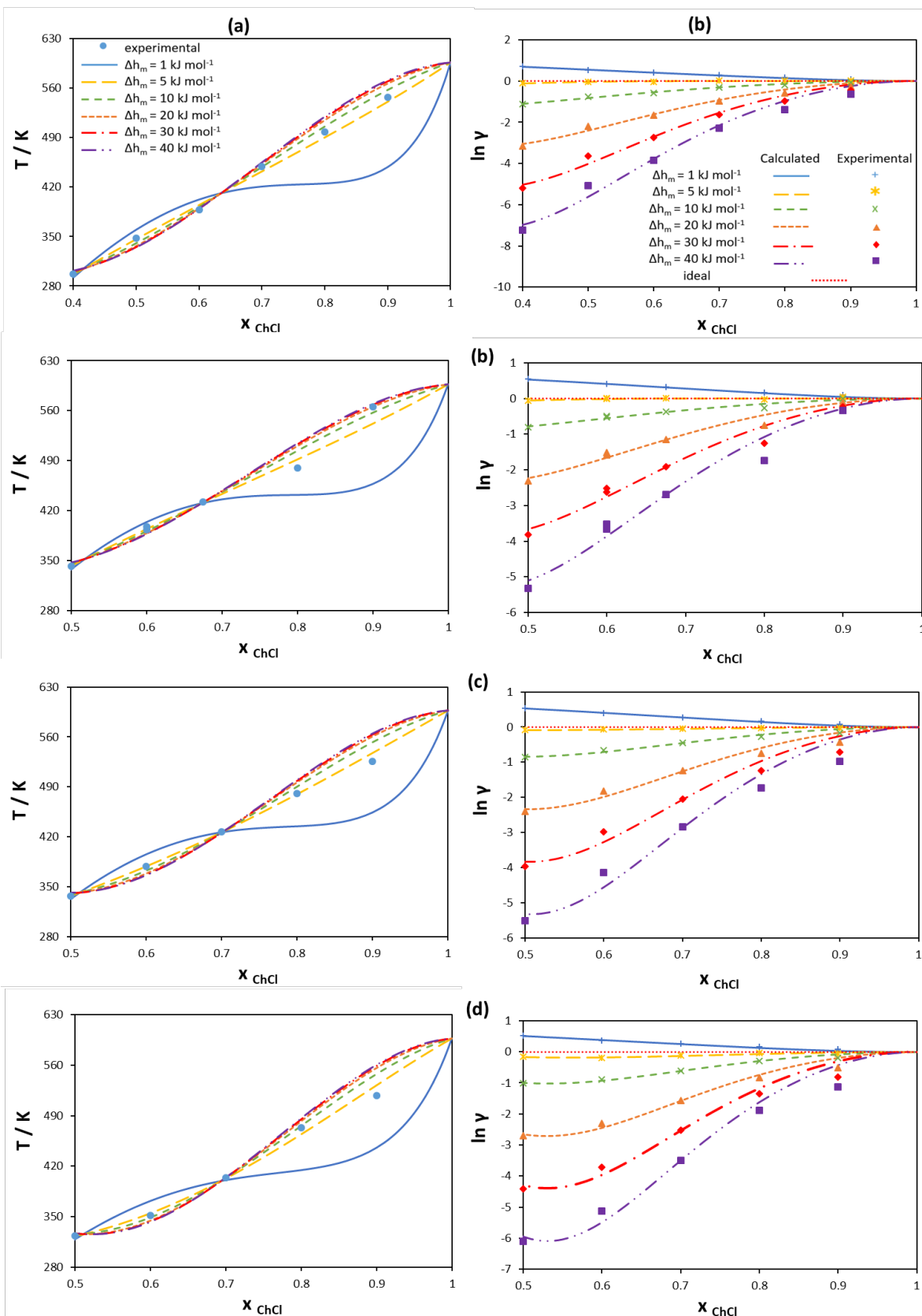


**Figure S2.** Liquidus line (left) and activity coefficients in liquid phase (right) of [Ch]Cl in binary mixture of [Ch]Cl and (a) [Ch][NTf<sub>2</sub>] (b) [BzCh]Cl (c) [C<sub>2</sub>mim]Cl (d) [C<sub>2</sub>OHmim]Cl modeled using Redlich-Kister polynomial. Experimental data are taken from Fernandez et al. [1].

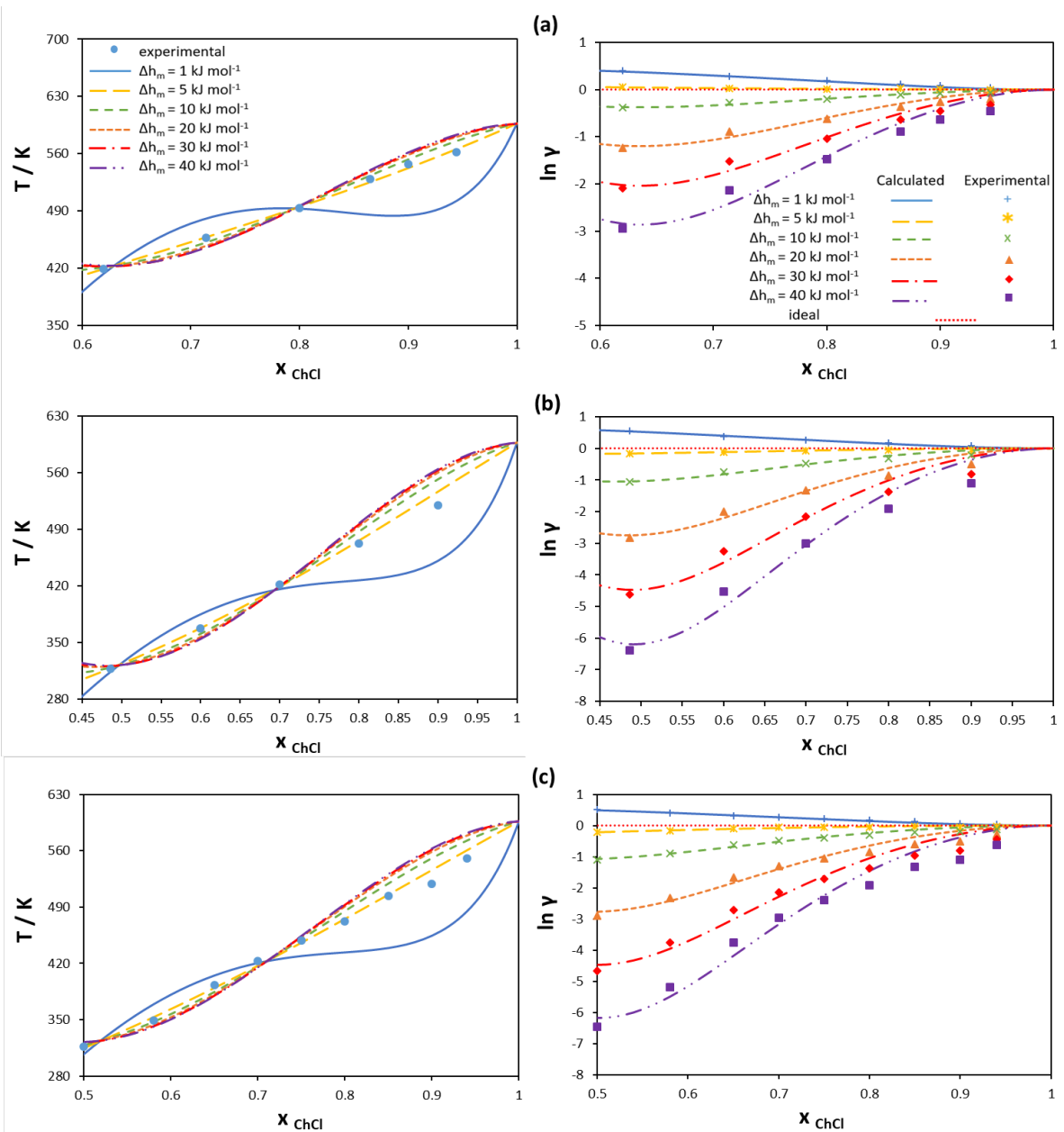


**Figure S3.** Liquidus line (left) and activity coefficients in liquid phase (right) of [Ch]Cl in binary mixture of [Ch]Cl and (a) [Cmpyr]Cl (b) [N<sub>4444</sub>]Cl (c) [P<sub>4444</sub>]Cl modeled using the Wilson equation. Experimental data are taken from Fernandez et al. [1].

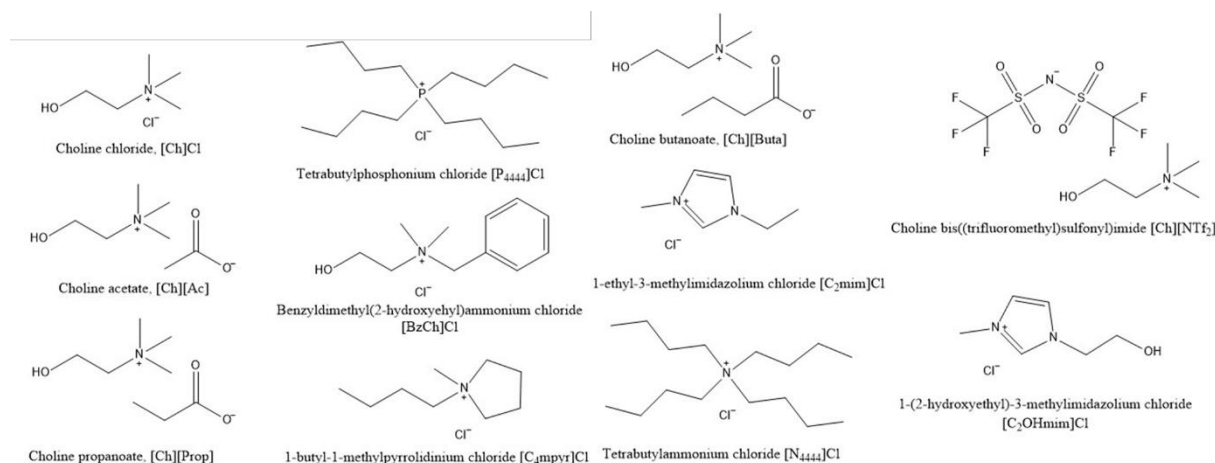


**Figure S4.** Chemical names and structures of [Ch]Cl and ILs studied.

**Table S1.** Melting properties of [Ch]Cl obtained from linear regression of solubility of [Ch]Cl in different ILs.

IL	$T_m / K$	$\Delta h_m / kJ mol^{-1}$
[Ch][Ac]	588.92	4.86
[Ch][Prop]	594.39	3.90
[Ch][Buta]	607.94	5.06
[Ch][NTf <sub>2</sub> ]	630.83	4.34
[BzCh]Cl	628.26	4.41
[C <sub>2</sub> mim]Cl	591.61	4.52
[C <sub>2</sub> OHmim]Cl	589.51	3.95
[C <sub>4</sub> mpyr]Cl	593.32	5.63
[N <sub>4444</sub> ]Cl	594.22	4.11
[P <sub>4444</sub> ]Cl	607.16	3.85
Average	602.61	4.46

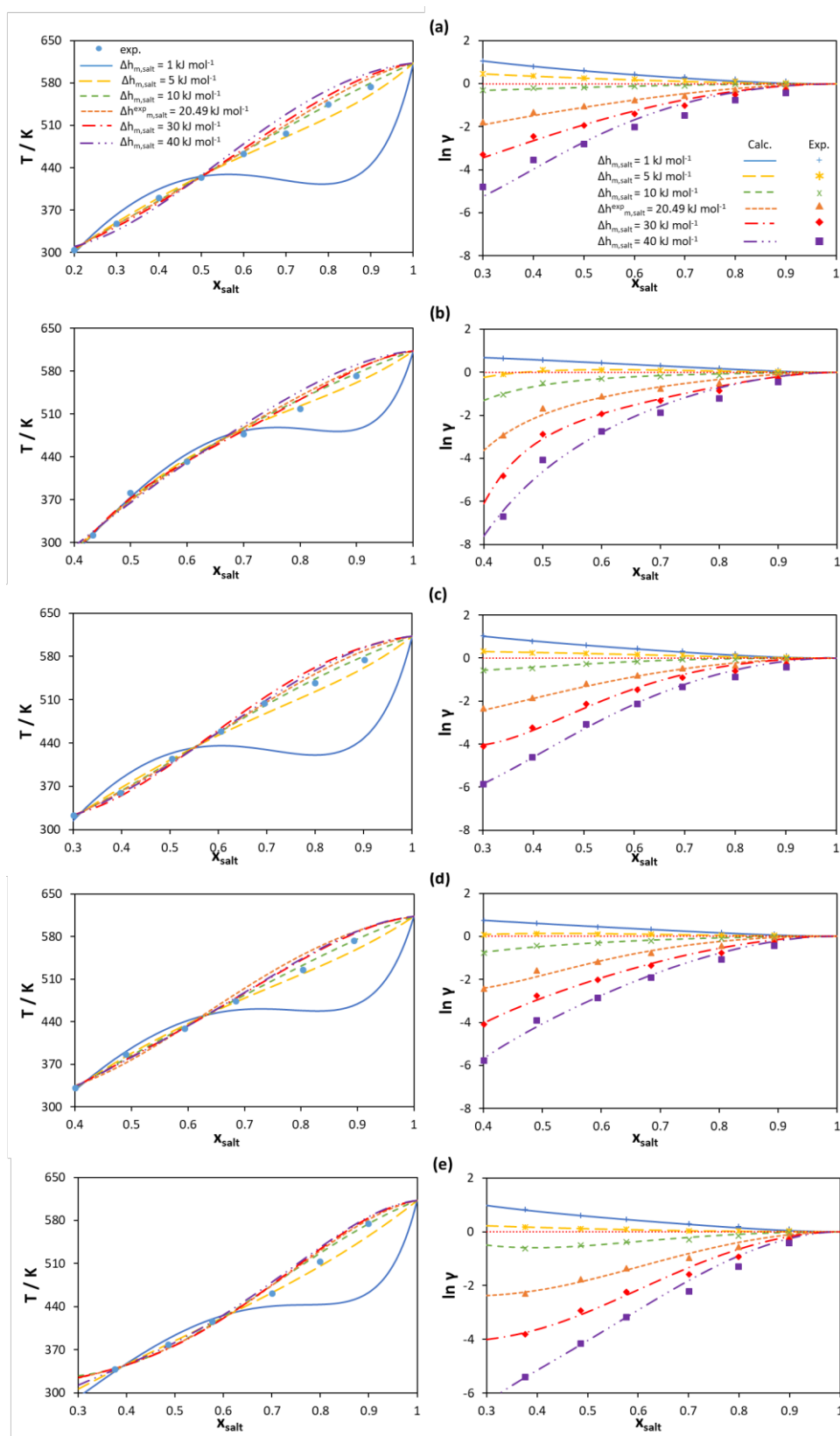


**Figure S5.** Liquidus line (left) and activity coefficients (right) of  $[N_{1111}]Cl$  in binary mixture of  $[N_{1111}]Cl$  and (a) capric acid (b) lauric acid (c) myristic acid (d) palmitic acid (e) stearic acid modeled using Redlich-Kister polynomial with three parameters assuming different melting enthalpy values. Experimental data are taken from [2].

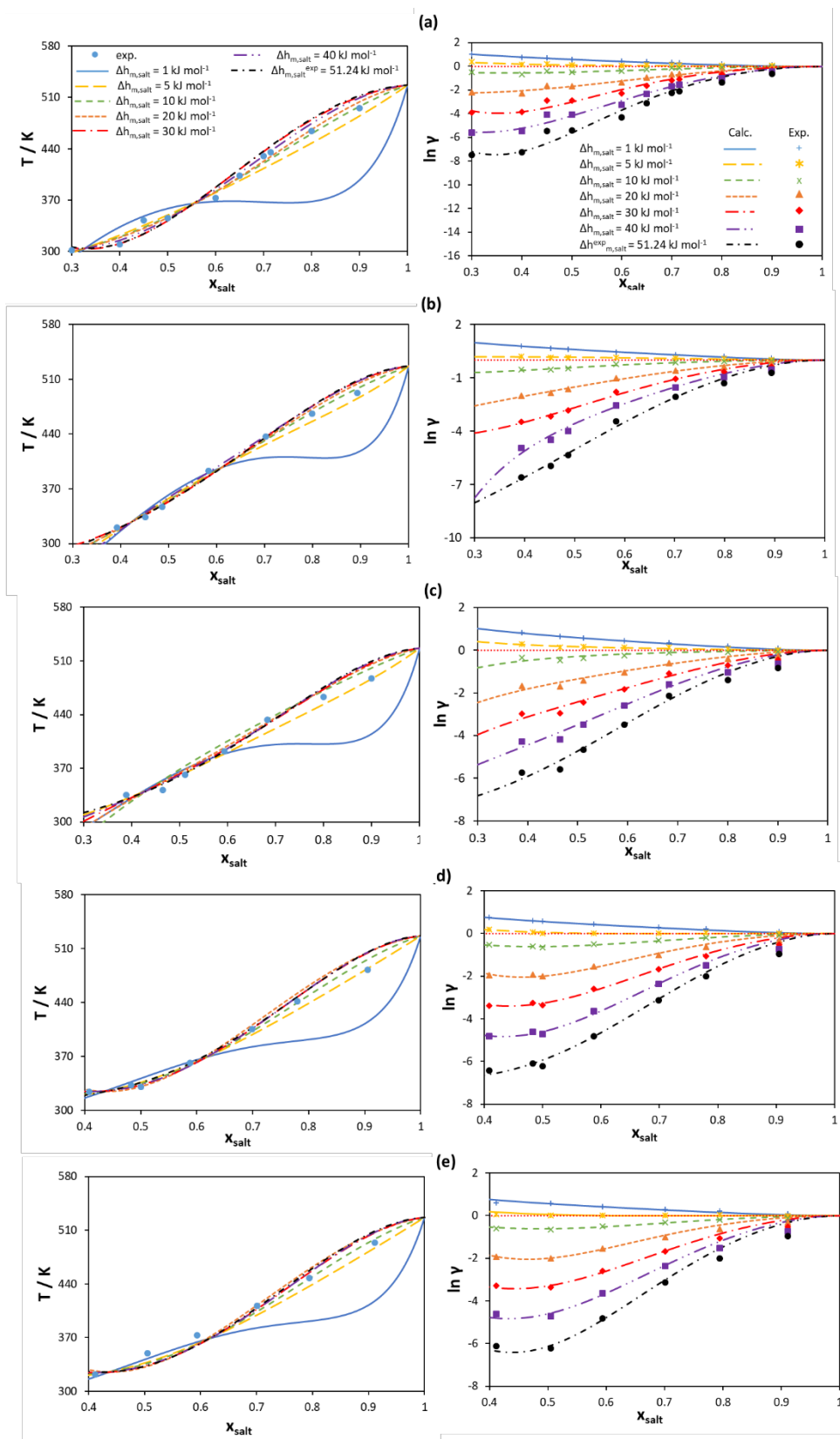


**Figure S6.** Liquidus line (left) and activity coefficients (right) of  $[N_{2222}]Cl$  in binary mixture of  $[N_{2222}]Cl$  and (a) capric acid (b) lauric acid (c) myristic acid (d) palmitic acid (e) stearic acid modeled using Redlich-Kister polynomial with three parameters assuming different melting enthalpy values. Experimental data are taken from [2].

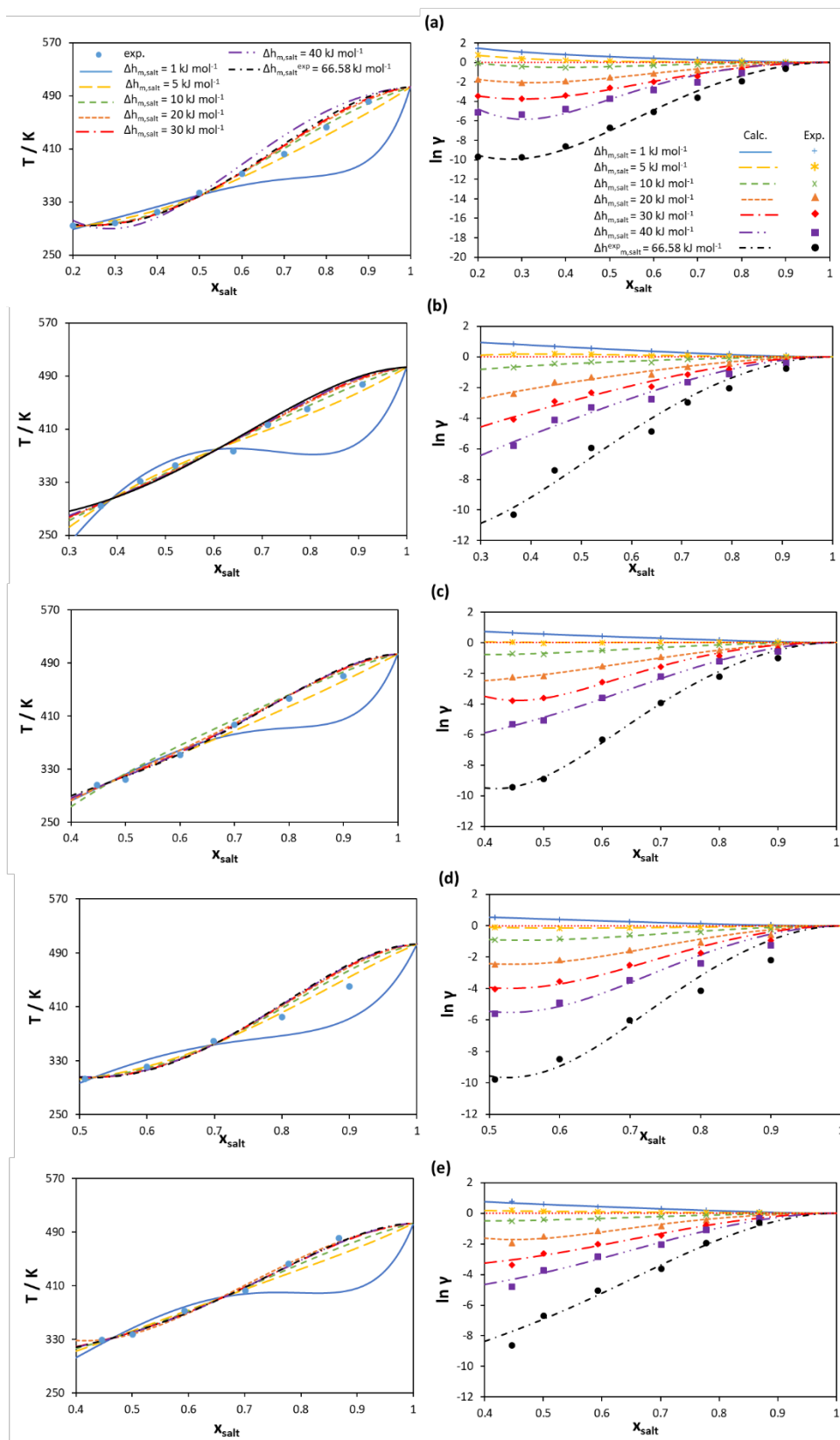


**Figure S7.** Liquidus line (left) and activity coefficients (right) of  $[N_{3333}]Cl$  in binary mixture of  $[N_{3333}]Cl$  and (a) capric acid (b) lauric acid (c) myristic acid (d) palmitic acid (e) stearic acid modeled using Redlich-Kister polynomial with three parameters assuming different melting enthalpy values. Experimental data are taken from [2].

**Table S2.** Empirical parameters of RK-polynomial for calculating activity coefficients of salts in binary mixtures of quaternary ammonium chloride salts and capric acid.

$\Delta h_m / \text{kJ mol}^{-1}$	[N <sub>1111</sub> ]Cl			[N <sub>2222</sub> ]Cl			[N <sub>3333</sub> ]Cl		
	a <sup>(1)</sup>	b <sup>(1)</sup>	c <sup>(1)</sup>	a <sup>(1)</sup>	b <sup>(1)</sup>	c <sup>(1)</sup>	a <sup>(1)</sup>	b <sup>(1)</sup>	c <sup>(1)</sup>
1	12.23	-5.31	-3.97	10.97	-6.66	-2.63	14.91	-24.67	15.95
5	7.93	-10.69	4.71	3.20	-7.56	7.66	3.40	-9.77	11.33
10	-2.70	-0.75	2.88	-13.09	15.14	-0.36	-7.49	-2.29	14.09
20	-	-	-	-49.75	75.31	-29.38	-37.25	38.00	0.19
30	-49.22	51.72	-14.25	-44.63	-16.63	75.13	-66.63	77.13	-12.84
40	-46.00	-5.13	40.13	-98.31	105.69	-8.50	-47.75	-36.63	91.13
Experimental	-32.75	44.56	-19.59	-96.88	18.38	95.00	-170.38	208.75	-51.88

**Table S3.** Empirical parameters of RK-polynomial for calculating activity coefficients of salts in binary mixtures of quaternary ammonium chloride salts and lauric acid.

$\Delta h_m / \text{kJ mol}^{-1}$	[N <sub>1111</sub> ]Cl			[N <sub>2222</sub> ]Cl			[N <sub>3333</sub> ]Cl		
	a <sup>(1)</sup>	b <sup>(1)</sup>	c <sup>(1)</sup>	a <sup>(1)</sup>	b <sup>(1)</sup>	c <sup>(1)</sup>	a <sup>(1)</sup>	b <sup>(1)</sup>	c <sup>(1)</sup>
1	26.33	-48.76	20.49	10	-18	19.5	12.13	-5.17	-9.59
5	8.63	-10.90	-9.88	0	0	4.5	2.68	1.91	-7.20
10	-10.63	23.44	-33.81	0	0	-13.5	-10.48	16.09	-9.34
20	-	-	-	-35.5	62	-48.25	-42.06	65.38	-33.56
30	-124.94	325.88	-305.63	-68.5	116	-76.75	-72.50	110.19	-53.63
40	-108.25	153.25	-98.25	-110.5	205	-138.75	-104.75	161.63	-79.38
Experimental	-54.13	109.53	-99.13	-148.5	269	-173.75	-170.50	219.75	-73.50

**Table S4.** Empirical parameters of RK-polynomial for calculating activity coefficients of salts in binary mixtures of quaternary ammonium chloride salts and myristic acid

$\Delta h_m / \text{kJ mol}^{-1}$	[N <sub>1111</sub> ]Cl			[N <sub>2222</sub> ]Cl			[N <sub>3333</sub> ]Cl		
	a <sup>(1)</sup>	b <sup>(1)</sup>	c <sup>(1)</sup>	a <sup>(1)</sup>	b <sup>(1)</sup>	c <sup>(1)</sup>	a <sup>(1)</sup>	b <sup>(1)</sup>	c <sup>(1)</sup>
1	12.83	-3.81	-9.66	17.84	-28.73	14.94	19.55	-39.47	24.72
5	8.74	-15.07	7.05	6.02	-14.03	12.09	1.45	-6.17	6.78
10	-0.93	-12.67	13.61	-6.00	10.00	-10.00	-17.99	20.95	0.38
20	-	-	-	-41.50	72.00	-43.00	-66.80	120.27	-61.87
30	-31.69	-32.06	65.25	-79.00	139.00	-78.50	-68.44	5.09	111.50
40	-77.50	67.94	-4.25	-108.00	176.00	-88.00	-161.44	305.31	-171.47
Experimental	-30.09	24.00	0.08	-141.50	218.00	-96.50	-230.75	295.00	-35.88

**Table S5.** Empirical parameters of RK-polynomial for calculating activity coefficients of salts in binary mixtures of quaternary ammonium chloride salts and palmitic acid.

$\Delta h_m / \text{kJ mol}^{-1}$	[N <sub>1111</sub> ]Cl			[N <sub>2222</sub> ]Cl			[N <sub>3333</sub> ]Cl		
	a <sup>(1)</sup>	b <sup>(1)</sup>	c <sup>(1)</sup>	a <sup>(1)</sup>	b <sup>(1)</sup>	c <sup>(1)</sup>	a <sup>(1)</sup>	b <sup>(1)</sup>	c <sup>(1)</sup>
1	20.54	-29.42	7.66	17.55	-33.27	22.19	14.81	-24.81	11.25
5	6.47	-9.34	-0.71	0.29	-5.85	12.72	-11.00	23.20	-6.38
10	-11.72	18.42	-13.98	-21.98	31.63	-2.62	-45.94	97.00	-45.47
20	-	-	-	-46.50	23.03	51.75	-116.00	245.31	-124.25
30	-89.75	151.44	-89.13	-109.28	172.75	-53.94	-185.75	392.38	-202.00
40	-126.50	208.69	-117.63	-158.56	267.22	-104.25	-257.00	545.88	-286.00
Experimental	-26.56	-20.25	55.63	-223.00	431.00	-235.25	-441.50	932.50	-488.00

**Table S6.** Empirical parameters of RK-polynomial for calculating activity coefficients of salts in binary mixtures of quaternary ammonium chloride salts and stearic acid.

$\Delta h_m / \text{kJ mol}^{-1}$	[N <sub>1111</sub> ]Cl			[N <sub>2222</sub> ]Cl			[N <sub>3333</sub> ]Cl		
	a <sup>(1)</sup>	b <sup>(1)</sup>	c <sup>(1)</sup>	a <sup>(1)</sup>	b <sup>(1)</sup>	c <sup>(1)</sup>	a <sup>(1)</sup>	b <sup>(1)</sup>	c <sup>(1)</sup>
1	18.97	-29.02	12.78	17.55	-33.27	22.19	19.63	-35.17	18.81
5	1.98	-0.83	-0.48	0.29	-5.85	12.72	5.37	-12.75	10.11
10	-11.47	3.36	12.94	-21.98	31.63	-2.62	-12.38	15.33	-1.19
20	-	-	-	-46.50	23.03	51.75	-32.39	0.12	55.52
30	-101.56	165.25	-73.88	-109.28	172.75	-53.94	-90.22	157.97	-78.78
40	-145.50	259.00	-141.75	-158.56	267.22	-104.25	-130.98	237.61	-126.69
Experimental	-61.25	98.13	-41.81	-196.75	301.19	-87.13	-239.94	452.41	-257.81

**Table S7.** Melting properties of quaternary ammonium chloride and fatty acids. Data are taken from [2]

Compound	T <sub>m</sub> / K	$\Delta h_m / \text{kJ mol}^{-1}$	$\Delta S_m / \text{J mol}^{-1} \text{K}^{-1}$
[N <sub>1111</sub> ]Cl	612.87	20.49	33.43
[N <sub>2222</sub> ]Cl	526.78	51.24	97.27
[N <sub>3333</sub> ]Cl	503.07	66.58	132.35
Capric acid	304.75	27.5	90.24
Lauric acid	317.48	37.83	119.16
Myristic acid	327.03	41.29	126.26
Palmitic acid	336.84	51.02	151.47
Stearic acid	343.67	61.36	178.54

## References

- [1] L. Fernandez, L.P. Silva, M.A.R. Martins, O. Ferreira, J. Ortega, S.P. Pinho, J.A.P. Coutinho, Indirect assessment of the fusion properties of choline chloride from solid-liquid equilibria data, *Fluid Phase Equilib.*, 448 (2017) 9-14.
- [2] P.V.A. Pontes, E.A. Crespo, M.A.R. Martins, L.P. Silva, C.M.S.S. Neves, G.J. Maximo, M.D. Hubinger, E.A.C. Batista, S.P. Pinho, J.A.P. Coutinho, G. Sadowski, C. Held, Measurement and PC-SAFT modeling of solid-liquid equilibrium of deep eutectic solvents of quaternary ammonium chlorides and carboxylic acids, *Fluid Phase Equilib.*, 448 (2017) 69-80.



### 3.2 Paper II

#### **Design of Deep Eutectic Systems: A Simple Approach for Preselecting Eutectic Mixture Constituents**

**A. Alhadid, L. Mokrushina, and M. Minceva, *Molecules*, 2020, 25, 1077.**

Author contribution: The thesis author conceptualized the paper's idea, performed the investigations and formal analysis, interpreted the results, and wrote the manuscript.


Summary: Paper II proposed a simple approach for preselecting eutectic mixture constituents from a pool of substances sharing the same chemical nature using their molecular structure. The approach is based on the conclusion of Paper I by selecting constituents with small melting entropy values. The melting entropy model proposed by Jain et al.<sup>112</sup> was used to calculate the melting entropy of various compounds from their molecular structure.

It was found that constituents with symmetrical and rigid molecular structures possess low melting entropy values. Accordingly, constituents with symmetrical and rigid molecular structures are expected to form eutectic mixtures with lower eutectic temperatures compared to constituents with flexible and asymmetric molecular structures.

To confirm the proposed approach, the SLE phase diagrams of six eutectic systems containing L-menthol and monocarboxylic acids were measured. Pairwise comparison between the eutectic temperature of the studied systems was performed, wherein in each pair of systems, the two acids have the same melting temperature, but the structure of the hydrocarbon chain is either cyclic or linear. The comparison showed that the eutectic temperature of systems containing L-menthol and cyclic acids is lower than that of systems with linear acids. Thus, it was concluded that when substances have the same chemical nature and melting temperature, those with more rigid and symmetrical molecular structures should be selected as constituents to form eutectic mixtures with lower eutectic temperatures.

Article

# Design of Deep Eutectic Systems: A Simple Approach for Preselecting Eutectic Mixture Constituents

Ahmad Alhadid<sup>1</sup>, Liudmila Mokrushina<sup>2</sup> and Mirjana Minceva<sup>1,\*</sup> 

<sup>1</sup> Biothermodynamics, TUM School of Life Sciences Weihenstephan, Technical University of Munich, Maximus-von-Imhof-Forum 2, 85354 Freising, Germany; ahmad.alhadid@tum.de

<sup>2</sup> Separation Science & Technology, Friedrich-Alexander-Universität Erlangen-Nürnberg (FAU), Egerlandstr. 3, 91058 Erlangen, Germany; liudmila.mokrushina@fau.de

\* Correspondence: mirjana.minceva@tum.de

Received: 5 February 2020; Accepted: 25 February 2020; Published: 28 February 2020



**Abstract:** Eutectic systems offer a wide range of new (green) designer solvents for diverse applications. However, due to the large pool of possible compounds, selecting compounds that form eutectic systems is not straightforward. In this study, a simple approach for preselecting possible candidates from a pool of substances sharing the same chemical functionality was presented. First, the melting entropy of single compounds was correlated with their molecular structure to calculate their melting enthalpy. Subsequently, the eutectic temperature of the screened binary systems was qualitatively predicted, and the systems were ordered according to the depth of the eutectic temperature. The approach was demonstrated for six hydrophobic eutectic systems composed of L-menthol and monocarboxylic acids with linear and cyclic structures. It was found that the melting entropy of compounds sharing the same functionality could be well correlated with their molecular structures. As a result, when the two acids had a similar melting temperature, the melting enthalpy of a rigid acid was found to be lower than that of a flexible acid. It was demonstrated that compounds with more rigid molecular structures could form deeper eutectics. The proposed approach could decrease the experimental efforts required to design deep eutectic solvents, particularly when the melting enthalpy of pure components is not available.

**Keywords:** eutectic mixtures; deep eutectic solvents; solid–liquid equilibria; hydrophobic DESs; melting properties

## 1. Introduction

Eutectic systems are mixtures of two or more compounds that exhibit partial immiscibility or negligible mutual solubility in the solid phase [1]. Deep eutectic solvents (DESs) are eutectic mixtures characterized by a large depression of the melting temperature of the mixture at the eutectic point relative to the melting temperature of the pure components [2,3]. DESs are analogous to ionic liquids (ILs) in terms of being designer solvents and possessing low vapor pressure. However, DESs are usually less toxic, easier to prepare, and less expensive than ILs. These advantages have led to the recent increase in applications of DESs, for example, as solvents in diverse separation methods [4–8], media for chemical [9–14], electrochemical [15–19], and biological reactions [20,21], in polymer chemistry [22–24], and for increasing the solubility of active pharmaceutical ingredients [25–28].

Although their preparation may be easier than that of ILs, DESs are more difficult to design. The ratio of the ions in ILs is defined by the electroneutrality of the solution. In contrast, the ratio of DES components is not fixed and can be of any value. One of the first pieces of information required when designing DESs for a specific application is the eutectic temperature and eutectic composition of the system. Thus far, the design of DESs has been performed primarily using a trial and error approach. In

most published works, preselected components are mixed at several fixed molar ratios, such as 1:1 or 1:2, and mixtures that remain liquid at room temperature are selected for further testing [29,30]. To determine the system composition and melting temperature at the eutectic point, the solid–liquid equilibria (SLE) of the eutectic systems should be known. The SLE also provides information about the melting temperature of the system at any specific composition.

The experimental determination of SLE phase diagrams of eutectic systems is non-trivial and is often accompanied by difficulties and limitations. For example, the hygroscopic nature of some DES components [31], the high viscosity and paste-like consistency of some DESs close to their melting temperature [32], the decomposition of DES constituents before melting, and the chemical reaction between DES constituents after storage [33]. Owing to the previously mentioned difficulties, predictive methods are required. Abranches et al. [34] proposed Conductor like Screening Model for Real Solvents (COSMO-RS) to predict the SLE of eutectic mixtures. Wolbert et al. [35] used UNIFAC (Do) to model the activity coefficient of constituents in binary eutectic mixtures.

The SLE of simple eutectic systems, whose components show negligible mutual solubility in the solid phase, is commonly calculated in the literature using the following simplified equation:

$$\ln x_i^L \gamma_i^L = \frac{\Delta h_{m,i}}{R} \left( \frac{1}{T_{m,i}} - \frac{1}{T} \right) \quad (1)$$

where  $x_i^L$  and  $\gamma_i^L$  are the mole fraction and activity coefficient of the component  $i$  in the liquid solution, respectively;  $\Delta h_{m,i}$  and  $T_{m,i}$  are the melting enthalpy and melting temperature of the pure component  $i$ , respectively;  $T$  is the liquidus temperature (i.e., melting temperature of the mixture at the mole fraction  $x_i^L$ ); and  $R$  is the universal gas constant. As seen in Equation (1), SLE calculations require information about the pure components melting properties, namely, the melting enthalpy  $\Delta h_{m,i}$  and temperature  $T_{m,i}$ , as well as information about the behavior of the components in the liquid phase (i.e., activity coefficients  $\gamma_i^L$ ).

Strong intermolecular interactions between unlike molecules in the liquid phase—low activity coefficient values of components—and/or low melting enthalpy values of pure components lead to a deep depression of the melting temperature of the mixture at the eutectic point [35–38]. The melting enthalpy of components is not always easily measured because of polymorphism, kinetic limitations, and/or thermal instability. As a result, the melting enthalpy of many components is unavailable. The aim of this work was to demonstrate the correlation between the molecular structure and melting enthalpy of a component to simplify the selection of components, especially when no experimental data on melting enthalpy is available.

At the melting point of a pure component, the solid and liquid phases are in equilibrium. The melting temperature  $T_m$  of a pure component is the ratio between the melting enthalpy  $\Delta h_m$  and the melting entropy  $\Delta s_m$ :

$$T_m = \frac{\Delta h_m}{\Delta s_m} \quad (2)$$

Melting enthalpy is the energy required to melt solid crystals [39] and depends on the type of interactions between molecules in the lattice structure [39,40]. Melting entropy is the increase in the disorder and randomness upon melting [41] and depends on the molecular symmetry and conformational degrees of freedom of the molecule [41–44]. Despite several attempts to correlate the melting properties of a component with its molecular structure, there is no generic model that can predict the melting properties of pure components [45].

The melting temperature of pure components is difficult to predict [43]; however, unlike the melting enthalpy, experimental data on the melting temperature are, in many cases, available. However, depending on the method of determination as well as the purity of the components, the reported values may deviate by several degrees Celsius from the actual melting temperature. However, as seen from Equation (1), an uncertainty of several degrees Celsius in the melting temperature of pure components would have a small effect on the SLE of the mixture. According to Bondi [46], the melting

entropy of compounds can be better related to the molecular structure than the melting enthalpy. The melting entropy calculated from the molecular structure with the available melting temperature can be used to estimate the melting enthalpy of the components with Equation (2). Using this information, the eutectic temperature can be approximately calculated using Equation (1) under the assumption of ideal behavior ( $\gamma_i^L = 1$ ).

The objective of this study was to test a simple approach that could be used to select potential eutectic system constituents based on their melting enthalpies. It is assumed that mixtures of components with a lower melting enthalpy would result in eutectic mixtures with a larger melting temperature depression, as previously demonstrated [35–38]. This approach aims to reduce the experimental efforts required to measure pure components' melting enthalpy, as well as the SLE of eutectic mixtures. To evaluate the proposed approach, binary eutectic mixtures of L-menthol with six different monocarboxylic acids were considered in this work. The goal was to predict the eutectic temperature of each system relative to other systems. Although the eutectic temperatures were calculated with the unitary activity coefficient, it was not claimed that the components should behave ideally. The proposed approach was based on the assumption that any component in its binary solutions with other components sharing the same type and number of functional groups behaves similarly (i.e., in any binary mixture with monocarboxylic acids, L-menthol behaves in a similar manner). The latter assumption has been validated for many eutectic systems, for example, in [Ch]Cl/sugar [32], [Ch]Cl/dicarboxylic acids [47], [Ch]Cl/fatty acids or alcohols [48], and thymol/fatty acids [49].

## 2. Results and Discussion

### 2.1. Melting Properties of Pure Components

The melting entropy of acids was calculated using the model proposed by Jain et al. [44] (Equations (4)–(6)). The model parameters and calculated melting entropies are presented in Table 1. Linear acids possessed higher melting entropy than cyclic acids. This was a result of the higher flexibility of a linear chain compared to a ring structure. The lowest predicted melting entropy was for cyclohexanecarboxylic acid with a flexibility number  $\Phi$  equal to zero. The model predicted the same melting entropy for 3-phenylpropionic acid and 3-cyclohexylpropionic acid. This was because the model did not differentiate between phenyl and aliphatic ring and predicted the same flexibility number  $\Phi$  for both components. Due to the asymmetry of the carboxylic acid group, the symmetry number  $\sigma$  of all acids tested in this work was one.

**Table 1.** Symmetry number  $\sigma$ , flexibility number  $\Phi$ , and calculated melting entropy  $\Delta s_m$  of components using the model proposed by Jain et al. [44].

Compound	$\sigma$	SP3	SP2	Ring	$\tau$	$\Phi$	$\Delta s_m$ (J mol <sup>-1</sup> K <sup>-1</sup> )
3-cyclohexylpropionic acid	1	2	1	1	2	5.93	64.80
caprylic acid	1	6	1	0	5.5	133.58	90.69
cyclohexanecarboxylic acid	1	0	1	1	0	1	50
capric acid	1	8	1	0	7.5	792.03	105.49
3-phenylpropionic acid	1	2	1	1	2	5.93	64.80
lauric acid	1	10	1	0	9.5	4696.13	120.29

Table 2 presents the melting properties that were experimentally determined in this study using DSC. The obtained values were in good agreement with those reported in the literature. To the best of our knowledge, the melting properties of cyclohexylpropionic acid have not been measured before. As seen in Table 2, the melting enthalpy of L-menthol had a low value, thus making L-menthol a good candidate for designing deep eutectic systems. In general, linear acids have higher melting enthalpies than cyclic acids. The melting enthalpy of linear acids increases by increasing the chain length; for

example, lauric acid > capric acid > caprylic acid. The lowest melting enthalpy was observed for cyclohexanecarboxylic acid, which is the component with the most rigid molecular structure.

**Table 2.** Comparison of melting enthalpies  $\Delta h_m$  and temperatures  $T_m$  measured in this study and reported in the literature.

Compound	$T_m$ (K)		$\Delta h_m$ (kJ mol <sup>-1</sup> )	
	This Work *	Lit.	This Work *	Lit.
L-menthol	314.6 ± 0.1	315.68 [49]	13.74 ± 0.5	12.89 [49]
3-cyclohexylpropionic acid	291.3 ± 0.1	–	16.96 ± 0.5	–
caprylic acid	288.0 ± 0.7	288.20 [49]	21.43 ± 0.3	19.80 [49]
cyclohexanecarboxylic acid	299.4 ± 1.1	301.9 [50]	10.69 ± 0.2	9.20 [50]
capric acid	303.9 ± 0.1	304.75 [51]	28.39 ± 0.7	27.50 [51]
3-phenylpropionic acid	321.6 ± 0.1	321.2 [52]	15.11 ± 0.1	15.68 [52]
lauric acid	316.6 ± 0.1	317.48 [51]	35.81 ± 0.4	37.83 [51]

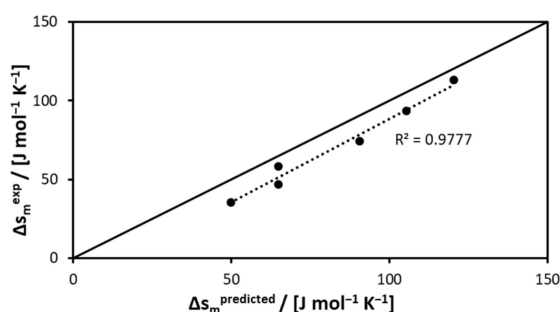
\* Uncertainties are considered as the standard deviation of three measurements.

Table 3 presents a comparison between the melting entropies predicted by the model by Jain et al. [44] (Equations (4)–(6)) and the experimental melting entropies calculated with Equation (2) using the experimentally determined melting enthalpy and melting temperatures of acids. As seen in Table 3, the predicted melting entropy of all acids was overestimated.

**Table 3.** Comparison of predicted  $\Delta s_m^{\text{predicted}}$  and experimental  $\Delta s_m^{\text{experimental}}$  melting entropy of monocarboxylic acids.

Compound	$\Delta s_m^{\text{predicted}}$	$\Delta s_m^{\text{experimental}}$
3-cyclohexylpropionic acid	64.80	58.22
caprylic acid	90.69	74.41
cyclohexanecarboxylic acid	50	35.72
capric acid	105.49	93.44
3-phenylpropionic acid	64.80	46.97
lauric acid	120.29	113.12

Figure 1 depicts the predicted melting entropy values in comparison to the experimental values. The linear correlation between the predicted melting entropies indicated that the model proposed by Jain et al. [44] could provide a reasonably good estimation of the melting entropy of compounds sharing the same chemical functionality.



**Figure 1.** Experimental melting entropies measured in this study in comparison with predicted melting entropies.

## 2.2. Solid–Liquid Equilibria

To validate the proposed approach, the SLE of the six eutectic systems was measured using DSC. Figure 2 presents the measured SLE data for L-menthol with six different monocarboxylic acids. To

simplify the comparison between systems, the systems containing acids of similar melting temperatures are presented next to each other (Figure 2A–F). The approximated melting temperature of acids in each pair increased from Figure 2A,B ( $\approx 15\text{ }^\circ\text{C}$ ) to Figure 2E,F ( $\approx 45\text{ }^\circ\text{C}$ ). Martins et al. [49] measured the SLE of binary eutectic mixtures of L-menthol with caprylic acid, capric acid, and lauric acid. As seen from Figure 2A,C,E, the determined eutectic temperatures were in good agreement with the results reported by Martins et al. [49]. The slightly higher liquidus temperatures measured in this study might be due to the greater heating rate; in this study, a heating rate of  $5\text{ K min}^{-1}$  was used, while in Martins et al. [49],  $1\text{ K min}^{-1}$  was used.

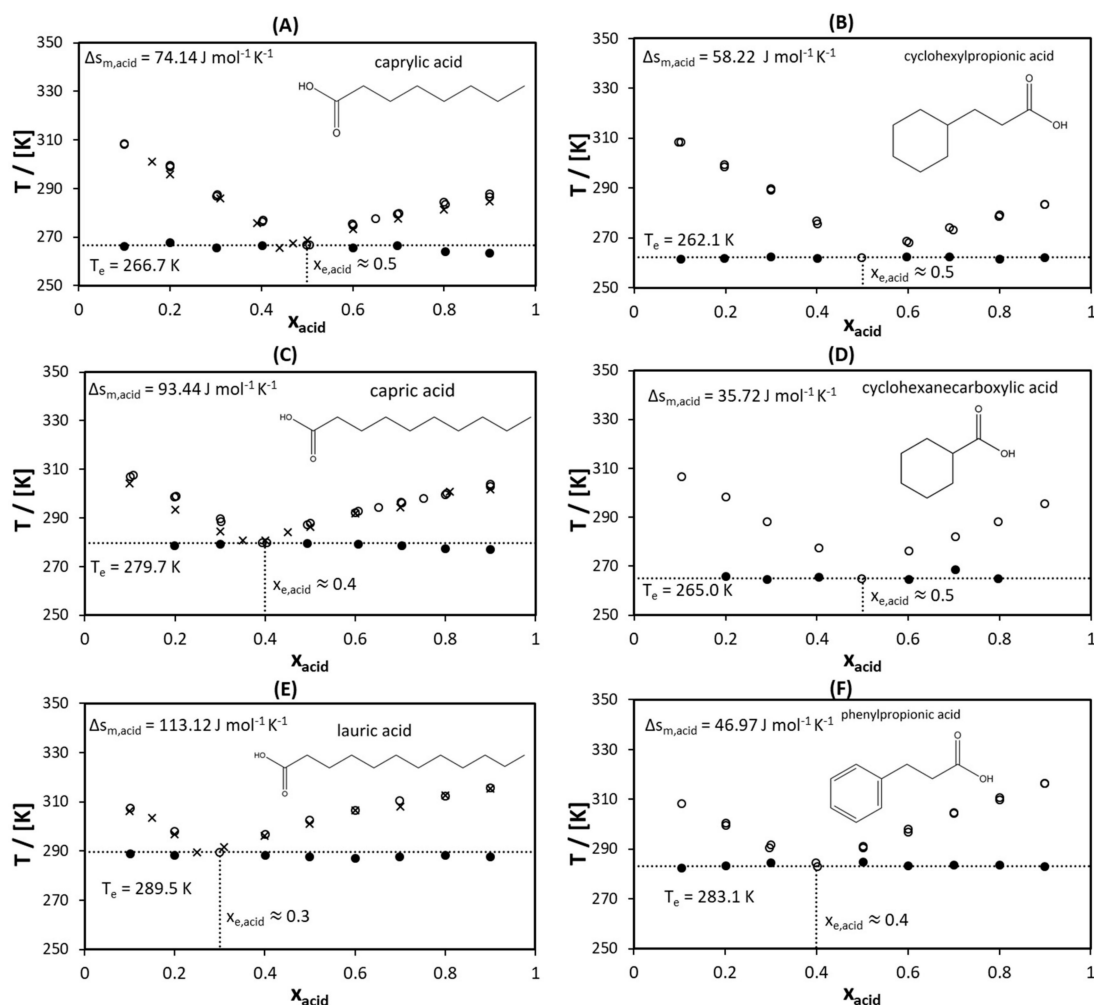


**Figure 2.** Solid–liquid phase diagrams of binary eutectic mixtures consisting of L-menthol and (A) caprylic acid, (B) cyclohexylpropionic acid, (C) capric acid, (D) cyclohexanecarboxylic acid, (E) lauric acid, and (F) phenylpropionic acid. The melting properties presented are experimentally determined values. Legend:  $\circ$  liquidus temperature measured in this study,  $\bullet$  the experimental eutectic temperature measured in this study,  $\times$  Martins et al. [49].

As demonstrated in previous studies [35–38], the lower the melting enthalpy of the pure components, the higher the depression at the eutectic point. This could be confirmed by comparing the eutectic temperatures of eutectic systems formed between L-menthol and acids presented in Figure 2. The molecules with cyclic structures (Figure 2B,D,F) had lower flexibility than molecules with linear structures (Figure 2A,C,E). Therefore, the cyclic compounds possessed lower melting entropies. Because the melting temperatures of each pair of acids were similar (caprylic acid and cyclohexylpropionic acid  $\approx 15\text{ }^\circ\text{C}$ , capric acid and cyclohexanecarboxylic acid  $\approx 30\text{ }^\circ\text{C}$ , and lauric acid and phenylpropionic acid  $\approx 45\text{ }^\circ\text{C}$ ), the melting enthalpy of cyclic compounds was lower than that of

linear ones. As a result, the eutectic temperature of a system formed by a cyclic acid was lower than that of a system formed by a linear acid when both acids had the same melting temperature.

As seen in Figure 2, as the difference in the melting entropy of acids increased, the difference in the eutectic temperature increased. For example, the melting entropy of capric acid was almost three times higher than that of cyclohexanecarboxylic acid (see Figure 2C,D). This resulted in a eutectic temperature for L-menthol/cyclohexanecarboxylic acid (Figure 2C), which was approximately 15 K lower than that of L-menthol/capric acid (Figure 2D). For L-menthol/caprylic acid (Figure 2A) and L-menthol/3-cyclohexylpropionic acid (Figure 2B), the difference between their eutectic temperatures was only 4.5 K. This might be the result of a small difference between the melting entropies of caprylic acid and 3-cyclohexylpropionic acid (see Figure 2A,B). In a previous study [38], it was demonstrated that the eutectic composition was shifted toward the component that had a lower melting enthalpy. Comparing the eutectic composition between the systems revealed that the lower the melting enthalpy compared to that of L-menthol ( $13.74 \text{ kJ mol}^{-1}$ ), the higher the mole fraction of the acid at the eutectic point.

It could be concluded that a lower melting enthalpy of pure components led to a larger melting temperature depression at the eutectic point of all L-menthol/monocarboxylic acid systems studied in this work. The melting enthalpy of components could be correlated with the molecular structure of acids possessing the same melting temperature. Therefore, the eutectic systems formed between L-menthol and cyclic acids exhibited a deeper eutectic point than that of systems formed with linear acids. Because the depression at the eutectic point was related to the difference in the melting entropy of the pure components, the relative depression at the eutectic point between the systems could also be predicted. Thus, the approach of selecting components by assessing the flexibility of their molecular structures could be used to design deeper eutectic systems.

### 3. Materials and Methods

#### 3.1. Prediction of Melting Entropy

The melting entropy of the pure components was calculated as the sum of the rotational  $\Delta s_m^{rot}$ , conformational  $\Delta s_m^{conf}$ , and expansional entropies  $\Delta s_m^{expan}$  as follows [41]:

$$\Delta s_m = W + \Delta s_m^{rot} + \Delta s_m^{conf} + \Delta s_m^{expan} \quad (3)$$

where  $W$  is a constant. In this study, the model proposed by Jain et al. [44] was used to predict the melting entropy of the pure components. The melting entropy in  $\text{J mol}^{-1} \text{K}^{-1}$  was calculated as follows [44]:

$$\Delta s_m = 50 + \Delta s_m^{rot} + \Delta s_m^{conf} \quad (4)$$

$$\Delta s_m^{rot} = -R \ln \sigma \quad (5)$$

$$\Delta s_m^{conf} = R \ln \Phi \quad (6)$$

where  $\sigma$  is the symmetry number,  $\Phi$  is the flexibility number, and  $R$  is the universal gas constant. Readers are directed to the original paper [44] for more information about the determination of the symmetry number  $\sigma$  of the components. The flexibility number  $\Phi$  was calculated as follows [44]:

$$\Phi = 2.435^\tau \quad (7)$$

$$\tau = SP^3 + 0.5SP^2 + 0.5Ring - 1 \quad (8)$$

where  $SP^3$  is the number of non-ring  $SP^3$  atoms ( $\text{CH}_2$ ,  $\text{CH}$ ,  $\text{C}$ ,  $\text{NH}$ ,  $\text{N}$ ,  $\text{O}$ ,  $\text{S}$ ),  $SP^2$  is the number of  $SP^2$  atoms ( $=\text{CH}$ ,  $=\text{C}$ ,  $=\text{N}$ ,  $\text{C}=\text{O}$ ), and  $Ring$  is the number of independent single, fused, or conjugated ring systems. If  $\tau$  is less than zero, the flexibility number  $\Phi$  is set to 1.

In the search for components with low melting enthalpy values, components with low melting entropy were sought. According to Equations (4)–(6), components with symmetrical (large symmetry number  $\sigma$ ) and/or more rigid molecular structures (small flexibility number  $\Phi$ ) should possess lower melting entropy. According to Equations (7) and (8), components with ring systems and double bonds should have a lower flexibility number  $\Phi$  than single bond chains.

### 3.2. Eutectic Mixture Constituents

Binary eutectic mixtures of L-menthol with six different monocarboxylic acids were considered. The acids were sorted into three pairs according to the melting temperatures reported by the suppliers. The acids of each pair had close melting temperatures. The acids pairs were as follows:

- Caprylic acid and 3-cyclohexylpropionic acid with a melting temperature of approximately 15 °C,
- Capric acid and cyclohexanecarboxylic acid with a melting temperature of approximately 30 °C,
- Lauric acid and 3-phenylpropionic acid with a melting temperature of approximately 45 °C.

In each pair, the acid with a more rigid molecular structure was expected to have lower melting entropy, and according to Equation (2), lower melting enthalpy. Therefore, the eutectic systems formed between L-menthol and rigid acids were expected to have a deeper eutectic temperature as a result of their lower melting enthalpy. Figure 3 illustrates the differences in the molecular structures of the acids, paired based on the melting temperatures obtained from the suppliers.

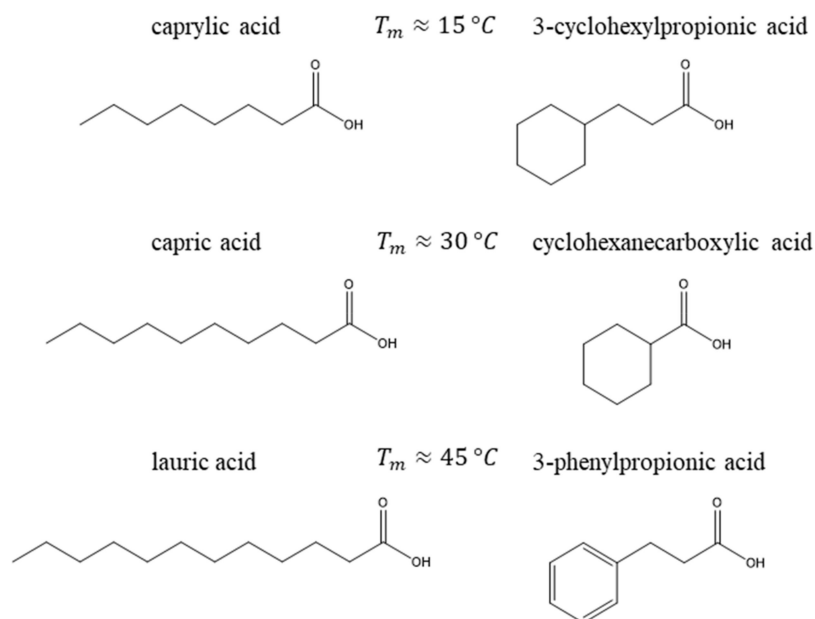


**Figure 3.** Molecular structures of monocarboxylic acids considered in this study. The melting temperatures are approximate values reported by the suppliers used to select each pair of acids.

### 3.3. Eutectic Mixture Preparation

Table 4 lists the chemicals used in this study, along with their purity, as declared by the suppliers. All chemicals were used as received without further purification. The binary eutectic mixtures were prepared by weighing the pure components in a glass vessel. The mixture was heated to 45 °C while stirring with a magnetic stirrer until a homogenous liquid was obtained.



**Table 4.** Chemicals used in this study.

Name	CAS Number	Supplier	Purity *
L-menthol	2216–51–5	Sigma Aldrich Chemie GmbH	≥ 99 %
3-cyclohexylpropionic acid	701–97–3	ThermoFisher (Kandel) GmbH	> 98 %
caprylic acid	124–07–2	Merck KGaA	99 %
cyclohexanecarboxylic acid	98–89–5	ThermoFisher (Kandel) GmbH	98 %
capric acid	334–48–5	Alfa Aesar GmbH	99 %
3-phenylpropionic acid	501–52–0	Alfa Aesar GmbH	99 %
lauric acid	143–07–7	Merck KGaA	99 %

\* As declared by the supplier.

The liquid samples were weighed in aluminum DSC crucibles using a syringe and then sealed by cold welding. Depending on the density of the eutectic mixture, the mass of the samples in the crucibles ranged between 4 and 6 mg.

### 3.4. Differential Scanning Calorimetry

SLE data and the pure components' melting properties were measured using DSC (NETZSCH DSC 200 F3). Temperature and sensitivity calibrations were performed prior to the measurements using five calibration standards with a purity of over 99.999%. The calibration standards included adamantane, bismuth, indium, zinc, and tin. The uncertainties after the temperature and sensitivity calibration were < 0.1 K and < 3%, respectively.

The DSC measurements were performed in an inert nitrogen environment. First, a cooling cycle with a rate of 10 K min<sup>-1</sup> to a final temperature of -80 °C was performed. Then, the sample was heated at a heating rate of 5 K min<sup>-1</sup> up to approximately 10 K above the sample liquidus temperature. The eutectic temperature, as well as the pure components' melting temperature, were determined as the onset temperature of the respective thermal event. The liquidus temperatures were determined as the peak temperature, and the melting enthalpy of the pure components was determined as the peak area of the respective thermal event. The DSC curves of the samples obtained during the heating cycle are shown in Figures S2–S4 in Supplementary Materials.

## 4. Conclusions

In this study, a simple approach was proposed to select constituents for eutectic systems. This approach could be used to select constituents from a pool of substances sharing the same functionality and melting temperature based on their melting enthalpy. If the melting enthalpy is not available, it can be estimated from the melting entropy, which is correlated with the molecular structure, using the simple non-group contribution model proposed by Jain et al. [44].

The proposed approach was used to predict the relative depression of the melting temperature at the eutectic point of L-menthol/monocarboxylic acid systems. It was demonstrated that components with more rigid molecular structures possessed lower melting entropy. For linear and cyclic acids with similar melting temperatures, the cyclic acids possessed lower melting enthalpy due to their lower melting entropy. As a result, deeper eutectic systems could be formed by cyclic acids than by linear acids sharing the same melting temperature. Furthermore, the larger the difference in the melting entropy between the acids in each pair, the higher the relative depression at the eutectic point between the two eutectic systems.

From this study, it could be concluded that in the search for new DES systems, constituents with more rigid and symmetrical structures should be pursued. This could narrow the pool of possible components to be screened for a specific application based on eutectic temperature (i.e., when eutectic mixtures that are liquid at room temperature are investigated). It should be mentioned, however, that for quantitative predictions, experimental melting properties should be used along with activity coefficient modeling, using, for example, excess Gibbs energy models ( $g^E$ ) or equation of states.

**Supplementary Materials:** The following are available online. Figure S1. Solid-liquid phase diagrams of binary eutectic systems consisting of L-menthol and (A) cyclohexylpropionic acid (B) caprylic acid (C) cyclohexanecarboxylic acid (D) capric acid (E) phenylpropionic acid (F) lauric acid. Dashed lines are ideal liquidus lines of components modeled using the Schöder-van-Laar equation and using experimental melting properties. Figure S2. DSC curves of L-menthol/3-cyclohexylpropionic acid and L-menthol/caprylic acid systems. Figure S3. DSC curves of L-menthol/cyclohexanecarboxylic acid and L-menthol/capric acid systems. Figure S4. DSC curves of L-menthol/3-phenylpropionic acid and L-menthol/lauric acid systems.

**Author Contributions:** Designing and performing experiments, analyzing the results, and preparing the manuscript A.A.; revising and discussing the manuscript, L.M.; supervising, revising, and discussing the manuscript, M.M. All authors have read and agreed to the published version of the manuscript.

**Funding:** This work was supported by the German Research Foundation (DFG) and the Technical University of Munich (TUM) in the framework of the Open Access Publishing Program.

**Acknowledgments:** The authors would like to thank Lea Kefalianakis for helping in performing a part of the DSC experiments as a part of her B. Sc. thesis.

**Conflicts of Interest:** The authors declare no conflict of interest.

## References

1. Gamsjäger, H.; Lorimer, J.; Scharlin, P.; Shaw, D.; David, G. Glossary of terms related to solubility (IUPAC Recommendations 2008). *Pure Appl. Chem.* **2008**, *80*, 233.
2. Abbott, A.P.; Boothby, D.; Capper, G.; Davies, D.L.; Rasheed, R.K. Deep Eutectic Solvents Formed between Choline Chloride and Carboxylic Acids: Versatile Alternatives to Ionic Liquids. *J. Am. Chem. Soc.* **2004**, *126*, 9142–9147. [[CrossRef](#)] [[PubMed](#)]
3. Abbott, A.P.; Capper, G.; Davies, D.L.; Rasheed, R.K.; Tambyrajah, V. Novel solvent properties of choline chloride/urea mixtures. *Chem. Commun.* **2003**, 70–71. [[CrossRef](#)] [[PubMed](#)]
4. Abbott, A.P.; Cullis, P.M.; Gibson, M.J.; Harris, R.C.; Raven, E. Extraction of glycerol from biodiesel into a eutectic based ionic liquid. *Green Chem.* **2007**, *9*, 868–872. [[CrossRef](#)]
5. Abbott, A.P.; Harris, R.C.; Ryder, K.S.; D'Agostino, C.; Gladden, L.F.; Mantle, M.D. Glycerol eutectics as sustainable solvent systems. *Green Chem.* **2011**, *13*, 82–90. [[CrossRef](#)]
6. Bezold, F.; Minceva, M. A water-free solvent system containing an L-menthol-based deep eutectic solvent for centrifugal partition chromatography applications. *J. Chromatogr. A* **2019**, *1587*, 166–171. [[CrossRef](#)]
7. Gouveia, A.S.L.; Oliveira, F.S.; Kurnia, K.A.; Marrucho, I.M. Deep Eutectic Solvents as Azeotrope Breakers: Liquid–Liquid Extraction and COSMO-RS Prediction. *ACS Sustain. Chem. Eng.* **2016**. [[CrossRef](#)]
8. Roehrer, S.; Bezold, F.; Garcia, E.M.; Minceva, M. Deep eutectic solvents in countercurrent and centrifugal partition chromatography. *J. Chromatogr. A* **2016**, *1434*, 102–110. [[CrossRef](#)]
9. Alonso, D.A.; Baeza, A.; Chinchilla, R.; Guillena, G.; Pastor, I.M.; Ramón, D.J. Deep Eutectic Solvents: The Organic Reaction Medium of the Century. *Eur. J. Org. Chem.* **2016**, *2016*, 612–632. [[CrossRef](#)]
10. Hayyan, A.; Ali Hashim, M.; Mjalli, F.S.; Hayyan, M.; AlNashef, I.M. A novel phosphonium-based deep eutectic catalyst for biodiesel production from industrial low grade crude palm oil. *Chem. Eng. Sci.* **2013**, *92*. [[CrossRef](#)]
11. Hayyan, A.; Hashim, M.A.; Hayyan, M.; Mjalli, F.S.; AlNashef, I.M. A new processing route for cleaner production of biodiesel fuel using a choline chloride based deep eutectic solvent. *J. Clean. Prod.* **2014**, *65*. [[CrossRef](#)]
12. Khandelwal, S.; Tailor, Y.K.; Kumar, M. Deep eutectic solvents (DESs) as eco-friendly and sustainable solvent/catalyst systems in organic transformations. *J. Mol. Liq.* **2016**, *215*, 345–386. [[CrossRef](#)]
13. Wagle, D.V.; Zhao, H.; Baker, G.A. Deep eutectic solvents: Sustainable media for nanoscale and functional materials. *Acc. Chem. Res.* **2014**, *47*. [[CrossRef](#)] [[PubMed](#)]
14. Liu, P.; Hao, J.-W.; Mo, L.-P.; Zhang, Z.-H. Recent advances in the application of deep eutectic solvents as sustainable media as well as catalysts in organic reactions. *RSC Advances* **2015**, *5*, 48675–48704. [[CrossRef](#)]
15. Abbott, A.P.; Griffith, J.; Nandhra, S.; O'Connor, C.; Postlethwaite, S.; Ryder, K.S.; Smith, E.L. Sustained electroless deposition of metallic silver from a choline chloride-based ionic liquid. *Surf. Coat. Technol.* **2008**, *202*, 2033–2039. [[CrossRef](#)]

16. Boisset, A.; Menne, S.; Jacquemin, J.; Balducci, A.; Anouti, M. Deep eutectic solvents based on N-methylacetamide and a lithium salt as suitable electrolytes for lithium-ion batteries. *PCCP* **2013**, *15*, 20054–20063. [[CrossRef](#)]
17. Chen, Z.; McLean, B.; Ludwig, M.; Stefanovic, R.; Warr, G.G.; Webber, G.B.; Page, A.J.; Atkin, R. Nanostructure of Deep Eutectic Solvents at Graphite Electrode Interfaces as a Function of Potential. *J. Phys. Chem. C* **2016**, *120*, 2225–2233. [[CrossRef](#)]
18. Gómez, E.; Cojocar, P.; Magagnin, L.; Valles, E. Electrodeposition of Co, Sm and SmCo from a Deep Eutectic Solvent. *J. Electroanal. Chem.* **2011**, *658*, 18–24. [[CrossRef](#)]
19. Zaidi, W.; Boisset, A.; Jacquemin, J.; Timperman, L.; Anouti, M. Deep Eutectic Solvents Based on N-Methylacetamide and a Lithium Salt as Electrolytes at Elevated Temperature for Activated Carbon-Based Supercapacitors. *J. Phys. Chem. C* **2014**, *118*, 4033–4042. [[CrossRef](#)]
20. Pätzold, M.; Siebenhaller, S.; Kara, S.; Liese, A.; Syltatk, C.; Holtmann, D. Deep Eutectic Solvents as Efficient Solvents in Biocatalysis. *Trends Biotechnol.* **2019**, *37*, 943–959. [[CrossRef](#)]
21. Oh, Y.; Park, S.; Yoo, E.; Jo, S.; Hong, J.; Kim, H.J.; Kim, K.J.; Oh, K.K.; Lee, S.H. Dihydrogen-bonding deep eutectic solvents as reaction media for lipase-catalyzed transesterification. *Biochem. Eng. J.* **2019**, *142*, 34–40. [[CrossRef](#)]
22. Jablonský, M.; Škulcová, A.; Šima, J. Use of Deep Eutectic Solvents in Polymer Chemistry—A Review. *Molecules* **2019**, *24*, 3978. [[CrossRef](#)] [[PubMed](#)]
23. Roda, A.; Matias, A.A.; Paiva, A.; Duarte, A.R.C. Polymer Science and Engineering Using Deep Eutectic Solvents. *Polymers* **2019**, *11*, 912. [[CrossRef](#)] [[PubMed](#)]
24. Gómez, A.V.; Biswas, A.; Tadini, C.C.; Furtado, R.F.; Alves, C.R.; Cheng, H.N. Use of natural deep eutectic solvents for polymerization and polymer reactions. *J. Braz. Chem. Soc.* **2019**, *30*, 717–726. [[CrossRef](#)]
25. Abbott, A.P.; Ahmed, E.I.; Prasad, K.; Qader, I.B.; Ryder, K.S. Liquid pharmaceuticals formulation by eutectic formation. *Fluid Phase Equilib.* **2017**, *448*, 2–8. [[CrossRef](#)]
26. Aroso, I.M.; Craveiro, R.; Rocha, Â.; Dionísio, M.; Barreiros, S.; Reis, R.L.; Paiva, A.; Duarte, A.R.C. Design of controlled release systems for THEDES—Therapeutic deep eutectic solvents, using supercritical fluid technology. *Int. J. Pharm.* **2015**, *492*, 73–79. [[CrossRef](#)]
27. Aroso, I.M.; Silva, J.C.; Mano, F.; Ferreira, A.S.; Dionísio, M.; Sá-Nogueira, I.; Barreiros, S.; Reis, R.L.; Paiva, A.; Duarte, A.R.C. Dissolution enhancement of active pharmaceutical ingredients by therapeutic deep eutectic systems. *Eur. J. Pharm. Sci.* **2016**, *98*, 57–66. [[CrossRef](#)]
28. Jeong, K.M.; Ko, J.; Zhao, J.; Jin, Y.; Yoo, D.E.; Han, S.Y.; Lee, J. Multi-functioning deep eutectic solvents as extraction and storage media for bioactive natural products that are readily applicable to cosmetic products. *J. Clean. Prod.* **2017**, *151*, 87–95. [[CrossRef](#)]
29. Van Osch, D.J.G.P.; Dietz, C.H.J.T.; van Spronsen, J.; Kroon, M.C.; Gallucci, F.; van Sint Annaland, M.; Tuinier, R. A Search for Natural Hydrophobic Deep Eutectic Solvents Based on Natural Components. *ACS Sustain. Chem. Eng.* **2019**, *7*, 2933–2942. [[CrossRef](#)]
30. Francisco, M.; van den Bruinhorst, A.; Kroon, M.C. New natural and renewable low transition temperature mixtures (LTTMs): Screening as solvents for lignocellulosic biomass processing. *Green Chem.* **2012**, *14*, 2153–2157. [[CrossRef](#)]
31. Van den Bruinhorst, A.; Kollau, L.J.B.M.; Kroon, M.C.; Meuldijk, J.; Tuinier, R.; Esteves, A.C.C. A centrifuge method to determine the solid–liquid phase behavior of eutectic mixtures. *J. Chem. Phys.* **2018**, *149*, 224505. [[CrossRef](#)]
32. Silva, L.P.; Fernandez, L.; Conceição, J.H.F.; Martins, M.A.R.; Sosa, A.; Ortega, J.; Pinho, S.P.; Coutinho, J.A.P. Design and Characterization of Sugar-Based Deep Eutectic Solvents Using Conductor-like Screening Model for Real Solvents. *ACS Sustain. Chem. Eng.* **2018**. [[CrossRef](#)]
33. Rodriguez Rodriguez, N.; van den Bruinhorst, A.; Kollau, L.J.B.M.; Kroon, M.C.; Binnemans, K. Degradation of Deep-Eutectic Solvents Based on Choline Chloride and Carboxylic Acids. *ACS Sustain. Chem. Eng.* **2019**, *7*, 11521–11528. [[CrossRef](#)]
34. Abranches, D.O.; Larriba, M.; Silva, L.P.; Melle-Franco, M.; Palomar, J.F.; Pinho, S.P.; Coutinho, J.A.P. Using COSMO-RS to design choline chloride pharmaceutical eutectic solvents. *Fluid Phase Equilib.* **2019**, *497*, 71–78. [[CrossRef](#)]
35. Wolbert, F.; Brandenbusch, C.; Sadowski, G. Selecting Excipients Forming Therapeutic Deep Eutectic Systems—A Mechanistic Approach. *Mol. Pharm.* **2019**, *16*, 3091–3099. [[CrossRef](#)] [[PubMed](#)]

36. Kollau, L.J.B.M.; Vis, M.; van den Bruinhorst, A.; Esteves, A.C.C.; Tuinier, R. Quantification of the liquid window of deep eutectic solvents. *Chem. Commun.* **2018**, *54*, 13351–13354. [[CrossRef](#)] [[PubMed](#)]
37. Martins, M.A.R.; Pinho, S.P.; Coutinho, J.A.P. Insights into the Nature of Eutectic and Deep Eutectic Mixtures. *J. Solut. Chem.* **2018**. [[CrossRef](#)]
38. Alhadid, A.; Mokrushina, L.; Minceva, M. Modeling of Solid-Liquid Equilibria in Deep Eutectic Solvents: A Parameter Study. *Molecules* **2019**, *24*. [[CrossRef](#)]
39. Williams, D.H.; O'Brien, D.P.; Bardsley, B. Enthalpy/Entropy Compensation as a Competition between Dynamics and Bonding: The Relevance to Melting of Crystals and Biological Aggregates. *J. Am. Chem. Soc.* **2001**, *123*, 737–738. [[CrossRef](#)]
40. Jain, A.; Yalkowsky, S.H. Estimation of Melting Points of Organic Compounds-II. *J. Pharm. Sci.* **2006**, *95*, 2562–2618. [[CrossRef](#)]
41. Yalkowsky, S.H. Carnelley's Rule and the Prediction of Melting Point. *J. Pharm. Sci.* **2014**, *103*, 2629–2634. [[CrossRef](#)] [[PubMed](#)]
42. Dearden, J.C. The QSAR prediction of melting point, a property of environmental relevance. *Sci. Total Environ.* **1991**, *109*, 59–68. [[CrossRef](#)]
43. Brown, R.J.C.; Brown, R.F.C. Melting Point and Molecular Symmetry. *J. Chem. Educ.* **2000**, *77*, 724. [[CrossRef](#)]
44. Jain, A.; Yang, G.; Yalkowsky, S.H. Estimation of Total Entropy of Melting of Organic Compounds. *Ind. Eng. Chem. Res.* **2004**, *43*, 4376–4379. [[CrossRef](#)]
45. Preiss, U.P.; Beichel, W.; Erle, A.M.; Paulechka, Y.U.; Krossing, I. Is universal, simple melting point prediction possible? *Chemphyschem* **2011**, *12*, 2959–2972. [[CrossRef](#)] [[PubMed](#)]
46. Bondi, A. *Physical Properties of Molecular Crystals, Liquids, and Glasses*; John Wiley and Sons: New York, NY, USA, 1968.
47. Crespo, E.A.; Silva, L.P.; Martins, M.A.R.; Bülow, M.; Ferreira, O.; Sadowski, G.; Held, C.; Pinho, S.P.; Coutinho, J.A.P. The Role of Polyfunctionality in the Formation of [Ch]Cl-Carboxylic Acid-Based Deep Eutectic Solvents. *Ind. Eng. Chem. Res.* **2018**, *57*, 11195–11209. [[CrossRef](#)]
48. Crespo, E.A.; Silva, L.P.; Martins, M.A.R.; Fernandez, L.; Ortega, J.; Ferreira, O.; Sadowski, G.; Held, C.; Pinho, S.P.; Coutinho, J.A.P. Characterization and Modeling of the Liquid Phase of Deep Eutectic Solvents Based on Fatty Acids/Alcohols and Choline Chloride. *Ind. Eng. Chem. Res.* **2017**, *56*, 12192–12202. [[CrossRef](#)]
49. Martins, M.A.R.; Crespo, E.A.; Pontes, P.V.A.; Silva, L.P.; Bülow, M.; Maximo, G.J.; Batista, E.A.C.; Held, C.; Pinho, S.P.; Coutinho, J.A.P. Tunable Hydrophobic Eutectic Solvents Based on Terpenes and Monocarboxylic Acids. *ACS Sustain. Chem. Eng.* **2018**, *6*, 8836–8846. [[CrossRef](#)]
50. Domańska, U.; Morawski, P.; Piekarska, M. Solubility of perfumery and fragrance raw materials based on cyclohexane in 1-octanol under ambient and high pressures up to 900MPa. *J. Chem. Thermodyn.* **2008**, *40*, 710–717. [[CrossRef](#)]
51. Pontes, P.V.A.; Crespo, E.A.; Martins, M.A.R.; Silva, L.P.; Neves, C.M.S.S.; Maximo, G.J.; Hubinger, M.D.; Batista, E.A.C.; Pinho, S.P.; Coutinho, J.A.P.; et al. Measurement and PC-SAFT modeling of solid-liquid equilibrium of deep eutectic solvents of quaternary ammonium chlorides and carboxylic acids. *Fluid Phase Equilib.* **2017**, *448*, 69–80. [[CrossRef](#)]
52. Monte, M.J.S.; Hillesheim, D.M. Thermodynamic study on the sublimation of 3-phenylpropionic acid and of three methoxy-substituted 3-phenylpropionic acids. *J. Chem. Thermodyn.* **2001**, *33*, 837–847. [[CrossRef](#)]

**Sample Availability:** Samples of the compounds are no longer available from the authors.



© 2020 by the authors. Licensee MDPI, Basel, Switzerland. This article is an open access article distributed under the terms and conditions of the Creative Commons Attribution (CC BY) license (<http://creativecommons.org/licenses/by/4.0/>).

## Supplementary Material

# Design of Deep Eutectic Systems: A Simple Approach for Preselecting Eutectic Mixture Constituents

Ahmad Alhadid <sup>1</sup>, Liudmila Mokrushina <sup>2</sup> and Mirjana Minceva <sup>1,\*</sup>

<sup>1</sup> Technical University of Munich, Biothermodynamics, TUM School of Life and Food Sciences Weihenstephan, Maximus-von-Imhof-Forum 2, 85354 Freising, Germany; [ahmad.alhadid@tum.de](mailto:ahmad.alhadid@tum.de); [mirjana.minceva@tum.de](mailto:mirjana.minceva@tum.de)

<sup>2</sup> Friedrich-Alexander-Universität Erlangen-Nürnberg (FAU), Separation Science & Technology, Egerlandstr. 3, 91058 Erlangen, Germany; [liudmila.mokrushina@fau.de](mailto:liudmila.mokrushina@fau.de).

\* Correspondence: [mirjana.minceva@tum.de](mailto:mirjana.minceva@tum.de)

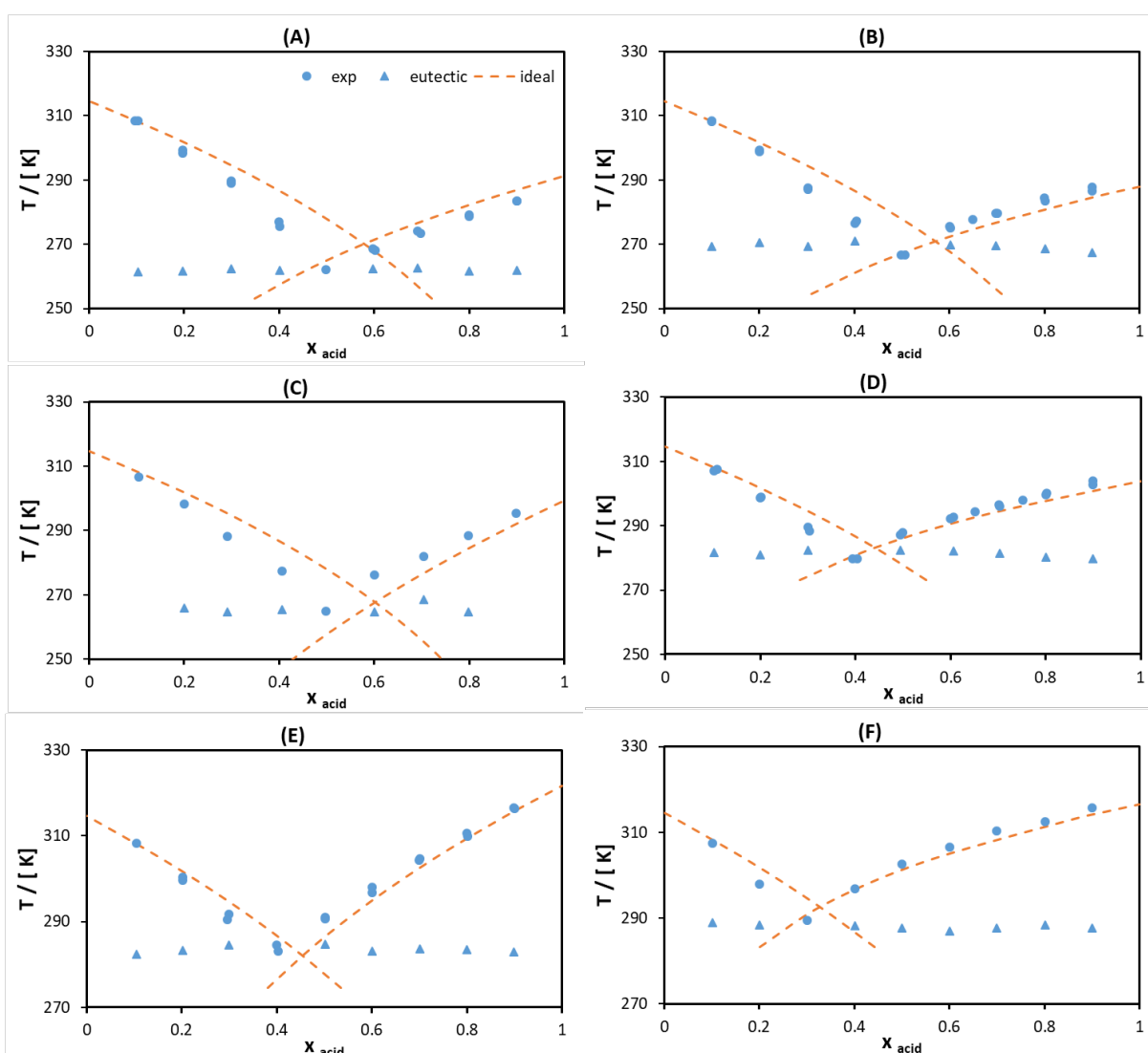


Figure S1. Solid-liquid phase diagrams of binary eutectic systems consist of L-menthol and (A) cyclohexylpropionic acid (B) caprylic acid (C) cyclohexanecarboxylic acid (D) capric acid (E) phenylpropionic acid (F) lauric acid. Dashed lines are ideal liquidus lines of components modeled using the Schöder-van-Laar equation and using experimental melting properties.

L-menthol/3-cyclohexylpropionic acid

L-menthol/caprylic acid

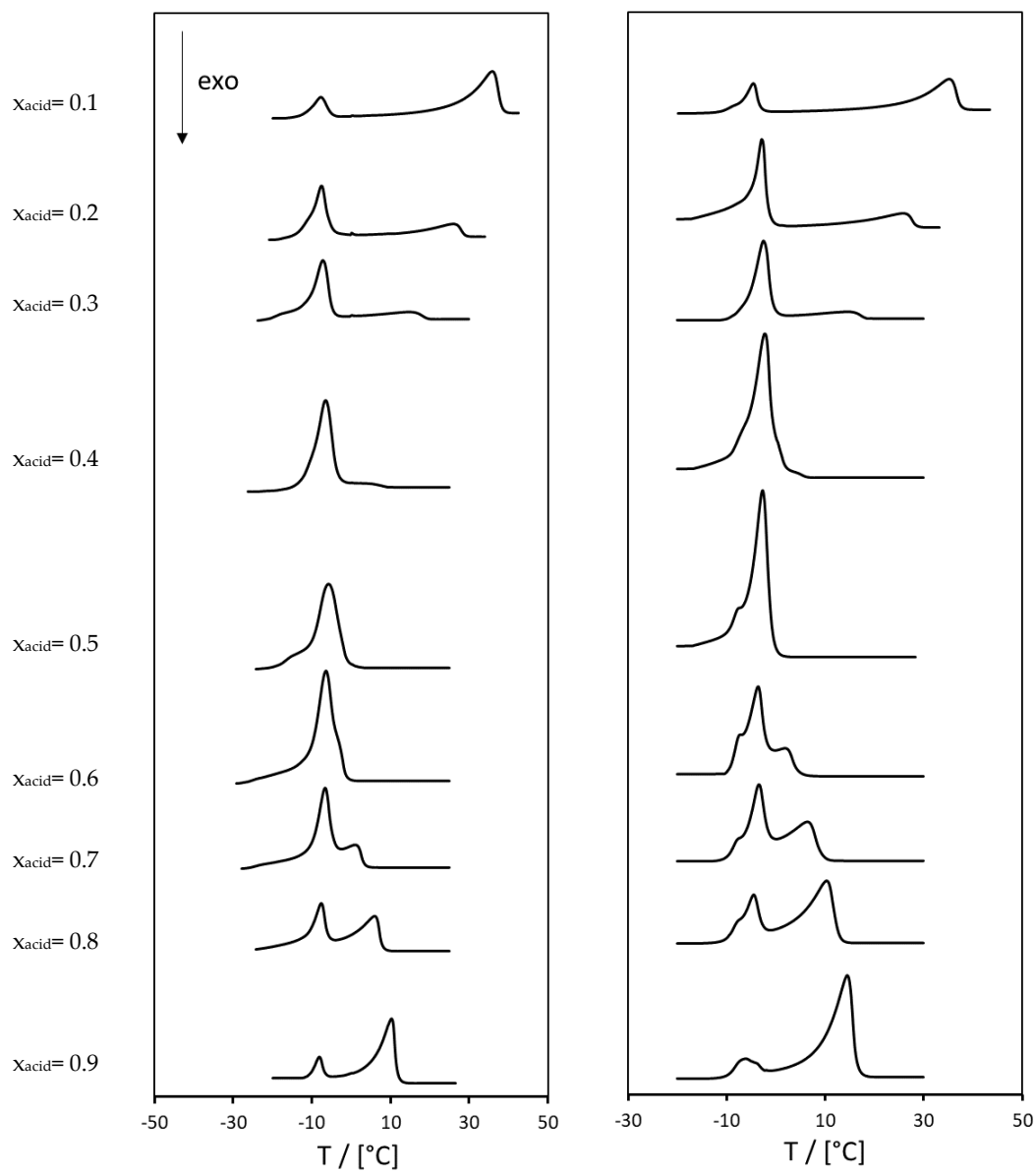


Figure S2. DSC curves of L-menthol/3-cyclohexylpropionic acid and L-menthol/caprylic acid systems

L-menthol/cyclohexanecarboxylic acid

L-menthol/capric acid

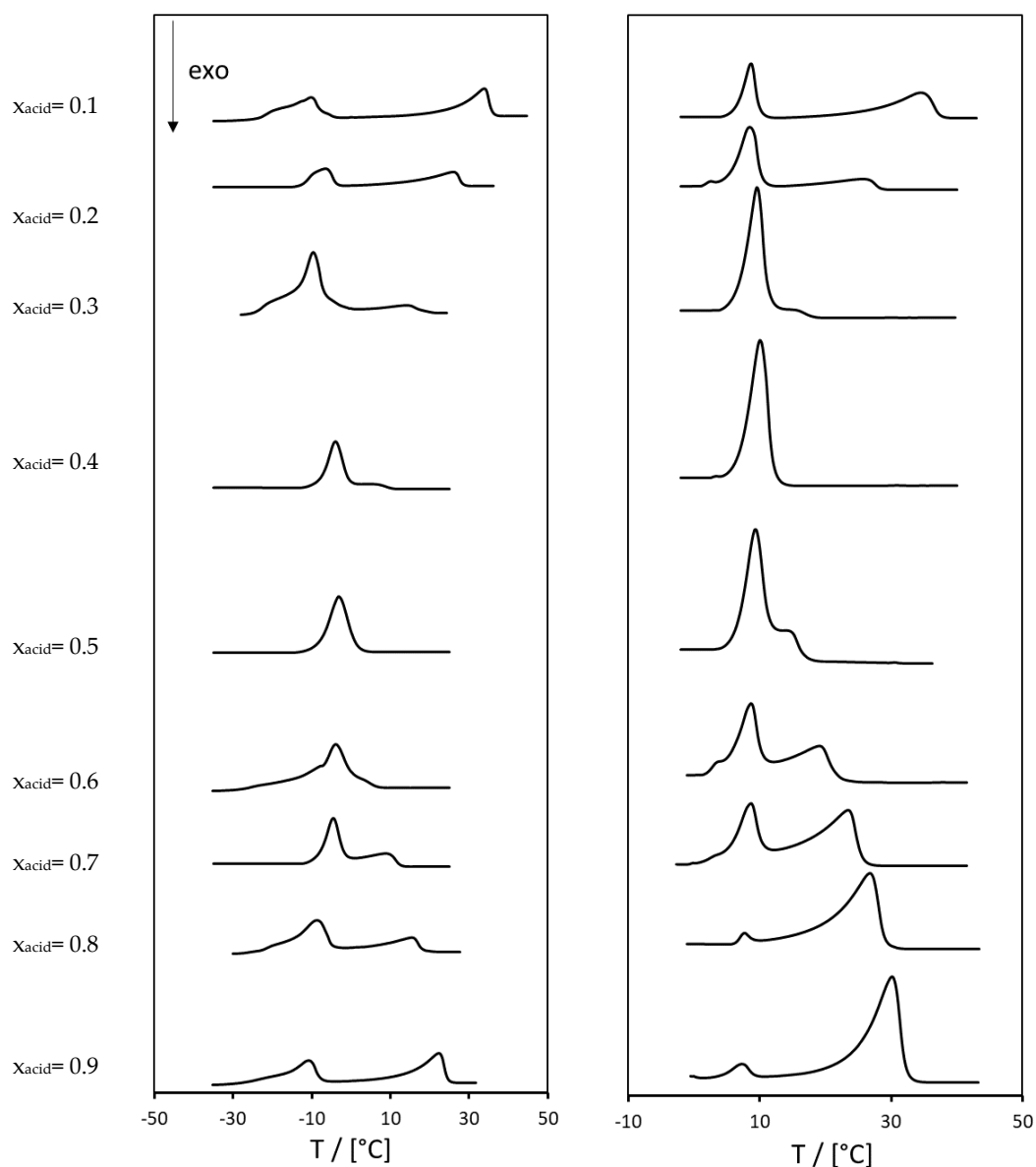


Figure S3. DSC curves of L-menthol/cyclohexanecarboxylic acid and L-menthol/capric acid systems

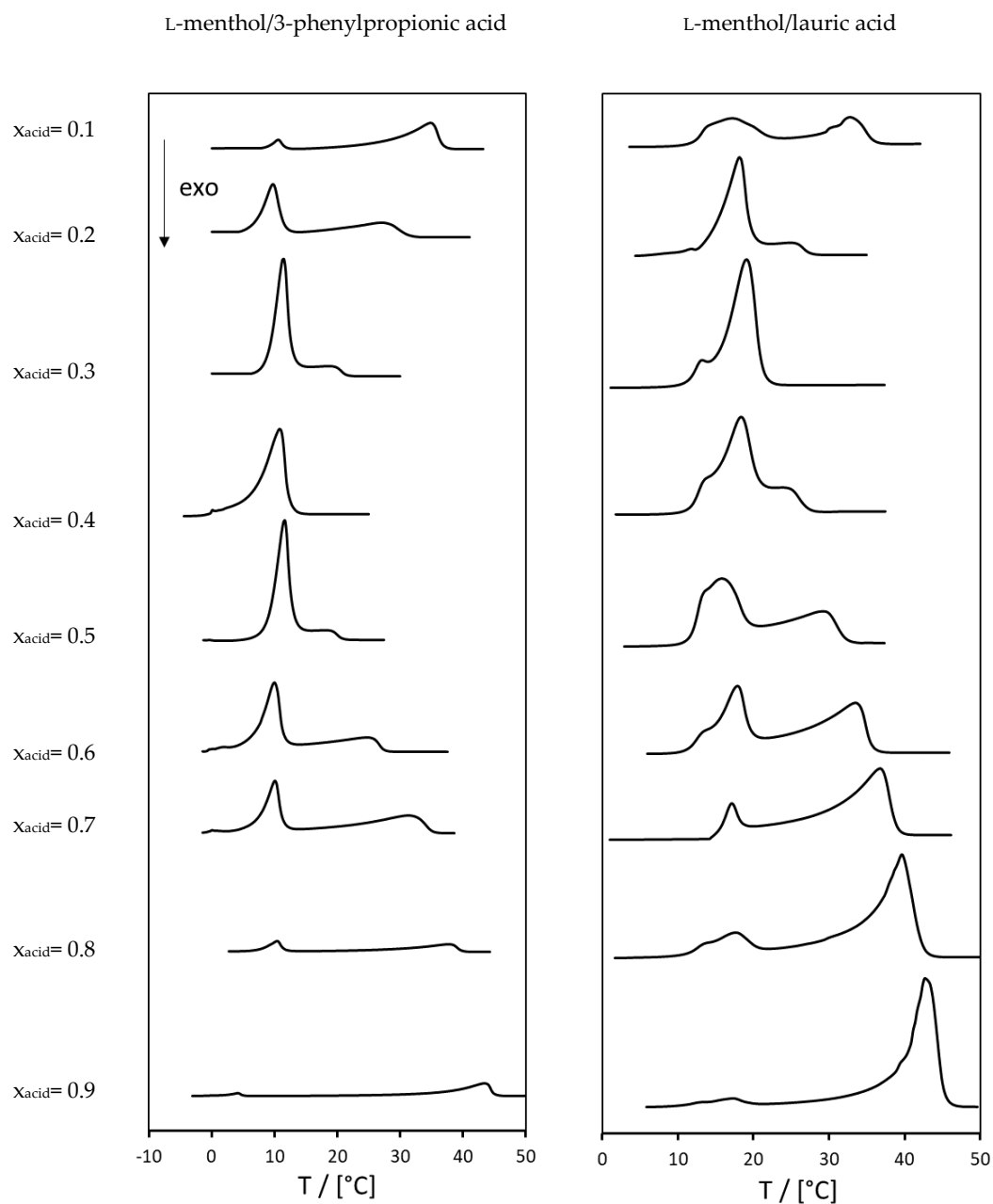


Figure S4. DSC curves of L-menthol/3-phenylpropionic acid and L-menthol/lauric acid systems



### 3.3 Paper III

#### Formation of glassy phases and polymorphism in deep eutectic solvents

**A. Alhadid, L. Mokrushina and M. Minceva, *J. Mol. Liq.*, 2020, 314, 113667.**

Author contribution: The thesis author conceptualized the paper's idea, performed the investigations and formal analysis, interpreted the results, and wrote the manuscript.

Summary: The goal of Paper III is to study and highlight the influence of glass formation and polymorphism on measuring and modeling SLE in binary eutectic systems. L-menthol-based eutectic systems was selected because L-menthol is known to have two main polymorphs, the stable  $\alpha$ -polymorph and the metastable  $\beta$ -polymorph. Moreover, several studies on SLE in L-menthol-based eutectic systems have not reported the eutectic temperature but rather only the glass transition temperature of the mixture.

In Paper III, the SLE data for three eutectic systems containing L-menthol with linear monocarboxylic acids were measured using two different sample preparation methods: in-situ crystallization during the DSC run and annealing the DSC crucibles for one month prior to DSC analysis. A comparison between the experimental data reported in Paper III and the literature showed that in the letter, solidus peaks corresponding to the metastable polymorph were misinterpreted as solidus peaks for the stable polymorph. In Paper III, the observed solidus peaks were assigned to the corresponding polymorph by thermodynamic modeling of the SLE data using the two polymorphs' melting properties. It was concluded that the set of activity coefficients model parameters fitted to the stable polymorph could be used to predict the phase diagram of the metastable polymorph. Next, the glass formation in L-menthol-based eutectic mixtures was studied. Annealing the samples for one month before DSC analysis aided the crystallization, allowing for detecting the solidus peak for the L-menthol/thymol and L-menthol/carvacrol systems. It was found that the observed glass transition temperature of the mixture does not depict the eutectic temperature observed for the system. Moreover, glass formation is not always attributed to strong intermolecular interactions, as glass formation was observed in ideal eutectic mixtures. Further experimental investigations showed that glass transition is attributed to the influence of the cyclohexyl ring in L-menthol and cyclohexyl carboxylic acid as well as the nonideality in the liquid phase, which both contribute to the high viscosity of the mixture. <sup>148</sup>

### 3.3 Paper III

Reprinted with permission from Alhadid et al., *J. Mol. Liq.*, **2020**, 314, 113667. DOI: 10.1016/j.molliq.2020.113667. Copyright 2020 Elsevier.



# Formation of glassy phases and polymorphism in deep eutectic solvents

Ahmad Alhadid<sup>a</sup>, Liudmila Mokrushina<sup>b</sup>, Mirjana Minceva<sup>a,\*</sup>

<sup>a</sup> *Biothermodynamics, TUM School of Life Sciences Weihenstephan, Technical University of Munich, Germany*

<sup>b</sup> *Separation Science & Technology, Friedrich-Alexander-Universität Erlangen-Nürnberg (FAU), Germany*

## ARTICLE INFO

### Article history:

Received 23 April 2020

Received in revised form 15 June 2020

Accepted 22 June 2020

Available online 25 June 2020

### Keywords:

Deep eutectic solvents

Solid–liquid equilibria

Glass-transition temperature

Polymorphism

## ABSTRACT

Deep eutectic solvents (DESs) are a class of eutectic mixtures that have very low melting temperature at the eutectic point, which limits crystallization or lead to formation of metastable polymorphs. This can produce a false estimate of the actual melting temperature of the mixture. The present work focuses on the formation of metastable phases in eutectic systems containing L-menthol. Differential scanning calorimetry (DSC) was applied to measure the solid–liquid equilibria (SLE) of the eutectic mixtures. Two sample-preparation methods were employed, namely annealing and *in situ* crystallization during the DSC run. We found that the eutectic temperature of the stable mixture is much higher than the observed glass-transition temperature of the mixture. Moreover, the eutectic temperature of a mixture with a stable polymorph is different from that of a metastable polymorph. The measured SLE data were correlated through non-ideality modeling using the non-random two-liquid (NRTL) equation. Our results show that SLE modeling is a useful tool for predicting the melting temperatures of stable mixtures without the need for time-consuming annealing methods. This work serves as a guide for reporting stable mixture properties when dealing with eutectic mixtures that form metastable phases.

© 2020 Elsevier B.V. All rights reserved.

## 1. Introduction

Green solvents are sought to replace conventional solvents in chemical and process applications in the modern environmental-protection framework. Eutectic mixtures can be used as solvent systems that comply with the twelve principles of green chemistry [1]. Deep eutectic solvents (DESs) are mixtures of two or more compounds that are capable to form a liquid mixture with a melting temperature considerably lower than that of the pure compounds [2,3]. The DES compounds can be biodegradable, nontoxic, inexpensive, and possess a very low vapor pressure. Eutectic solvents have been used as solvents in separation methods [4–8] and in chemical and biochemical reactions [9–16].

Knowledge of the solid–liquid equilibria (SLE) of eutectic mixtures is essential in order to design DESs for specific applications [17–20]. SLE data of eutectic mixtures are usually obtained through visual methods such as a melting point device, or by thermal analysis methods such as differential scanning calorimetry (DSC). Other techniques have been proposed in the literature, such as the centrifuge method for determining the solid–liquid behavior in eutectic mixtures [21]. However, all these methods are time consuming and/or require special equipment. Therefore, the amount of available SLE data for eutectic systems is low compared to the number of eutectic mixtures studied, proposed, or potentially useful.

SLE measurements in eutectic systems are not always straightforward. In many cases, no crystallization but a glass transition is observed on the DSC curve of a eutectic mixture near the eutectic point [22]. Such eutectic mixtures are sometimes called *Low-Transition Temperature Mixtures (LTTM)* [23,24]. However, the glass-transition temperature is not a first-order transition that occurs at a specific temperature [25]. The glass transition is the transition of the amorphous solid to a subcooled liquid with increasing temperature. Amorphous solids and subcooled liquids are both metastable phases; upon further cooling or heating, transformation to a stable crystalline solid or a stable liquid, respectively, occurs. When a glass phase is formed near the eutectic point, measuring the eutectic temperature of the mixture is not a straightforward task.

Polymorphism refers to the existence of a pure component in different solid forms under different conditions [26]. Different polymorphs have different melting properties. Transformation from one polymorph to another can occur under certain conditions. L-menthol, which has been used to form eutectic mixtures, offers an interesting example in this respect. L-menthol has four identified polymorphs:  $\alpha$ ,  $\beta$ ,  $\gamma$ , and  $\delta$  [27,28]. Corvis et al. [29] showed that the metastable  $\beta$ -polymorph of L-menthol can exist for sufficiently long time, so that its melting properties can be measured.

In this work, we investigate eutectic mixtures that show kinetic limitations in crystallization, polymorphism, and the formation of metastable phases. The goal is to show that proper sample preparation and careful analysis of SLE data are essential in order

\* Corresponding author.

E-mail address: [mirjana.minceva@tum.de](mailto:mirjana.minceva@tum.de) (M. Minceva).

to avoid reporting metastable mixture properties. We use DSC to measure the SLE of selected eutectic mixtures using appropriate methods of sample preparation. Furthermore, the non-ideality of the mixture components in the liquid phase is modeled using the non-random two-liquid (NRTL) equation on the measured SLE data.

## 2. Materials and method

### 2.1. Sample preparation

The chemicals used to prepare the eutectic mixtures in this work are listed in Table 1. L-menthol (purity  $\geq 99\%$ ) and carvacrol (purity 99%) were purchased from Sigma Aldrich. Caprylic acid (purity 99%) and lauric acid (purity 99%) were purchased from Merck. Thymol (purity  $> 99\%$ ) was purchased from VWR International. Capric acid (purity 99%) was purchased from Alfa Aesar. All chemicals were used as received without further purification. The water content of pure components was measured in triplicates using Karl-Fischer coulometric titrator (Hanna instrument, USA). The results are listed in Table 1. In the same table, the measured melting properties are compared with data from the literature.

Each eutectic mixture was prepared by weighing the pure components in a glass vessel using a balance with a precision of  $1 \times 10^{-4}$  g (Sartorius, Germany). The vessel was closed directly after introducing the components to avoid possible sublimation/evaporation and moisture absorption. The sample was heated to 318.15 K under continuous stirring until a homogenous clear liquid was obtained. At least nine samples were prepared for each eutectic mixture, covering the mole fraction range from 0.1 to 0.9. The liquid mixtures were introduced into DSC aluminum crucibles using syringes. The DSC samples were prepared in triplicates for each mixture composition. The DSC samples of all eutectic systems were then transferred directly to 193.15 K and kept at this temperature overnight. The DSC samples were stored for at least one month at constant temperature, *i.e.*, annealing. The annealing temperature for the DSC samples of the acid-based eutectic mixtures, namely L-menthol/caprylic acid, L-menthol/capric acid, and L-menthol/lauric acid, was 253.15 K, whereas for the L-menthol/thymol and L-menthol/carvacrol systems, it was 193.15 K.

### 2.2. Differential scanning calorimetry

Thermal characterization was carried out using DSC (NETZSCH DSC 200 F3, Germany). The device was calibrated with five calibration standards: adamantane, bismuth, indium, zinc, and tin. The measurements were done under a continuous nitrogen flow of  $150 \text{ ml min}^{-1}$ .

The DSC chamber was precooled to around 50 K below the eutectic temperature of the mixture. Then, the annealed samples were introduced into the DSC chamber. A heating cycle with a rate of  $5 \text{ K min}^{-1}$  was conducted until we achieved a temperature of approximately 10 K higher than the liquidus temperature of the sample. Next, a cooling cycle with a cooling rate of  $5 \text{ K min}^{-1}$  was run until 193.15 K on the same sample, followed by a second heating

cycle. The DSC curves of the annealed samples were obtained in the first heating cycle. The DSC curves of the second heating cycle represented the *in situ* crystallized samples (common practice in DSC measurements).

The DSC curves were analyzed using the NETZSCH Proteus software, version 6.1. The pure components' melting temperatures and the eutectic temperatures were determined as the onset temperature of the associated peak. The liquidus temperatures were taken as the maximum temperature of the peak associated with the respective liquidus thermal event. The reported values for each eutectic mixture with a specific composition were the average values of the three DSC samples. The standard uncertainties of the DSC were 0.1 K and 3% for the measured temperatures and the transition enthalpies, respectively.

### 2.3. Thermodynamic modeling

The SLE phase diagram of a simple eutectic system, *i.e.*, whose components show negligible mutual solubility in the solid phase, can be calculated as follows [32].

$$\ln x_i^L \gamma_i^L = -\frac{\Delta h_{m,i}}{RT} \left(1 - \frac{T}{T_{m,i}}\right) - \frac{\Delta c_p}{R} \left(1 - \frac{T_{m,i}}{T} + \ln \frac{T_{m,i}}{T}\right) \quad (1)$$

where  $x_i^L$  and  $\gamma_i^L$  are the mole fraction and the activity coefficient of component  $i$  in the liquid solution, respectively;  $\Delta h_{m,i}$  and  $T_{m,i}$  are the melting enthalpy and the melting temperature of pure component  $i$ , respectively;  $R$  is the universal gas constant;  $T$  is the liquidus temperature; and  $\Delta c_p$  is the difference in heat capacities of the pure component  $i$  between the solid state and the liquid state at constant pressure. The second term on the right-hand side of this equation is usually of a low value compared to the first term, and it therefore is usually neglected [33]. Hence, the following simplified equation is typically used to calculate the SLE

$$\ln x_i^L \gamma_i^L = -\frac{\Delta h_{m,i}}{RT} \left(1 - \frac{T}{T_{m,i}}\right) \quad (2)$$

The activity coefficients can be calculated using excess Gibbs energy ( $g^E$ ) models or the thermal equation of state. In this work, the NRTL equation was used to calculate the activity coefficients of component  $i$  in the liquid phase as follows [32].

$$\ln \gamma_i = x_j^2 \left[ \tau_{ji} \left( \frac{G_{ji}}{x_i + x_j G_{ji}} \right)^2 + \frac{\tau_{ij} G_{ij}}{(x_i + x_j G_{ij})^2} \right] \quad (3)$$

$$G_{ij} = \exp(-\alpha \tau_{ij}) \quad G_{ji} = \exp(-\alpha \tau_{ji}) \quad (4)$$

$$\tau_{ij} = \frac{g_{ij} - g_{ji}}{RT} \quad \tau_{ji} = \frac{g_{ji} - g_{ii}}{RT} \quad (5)$$

The value of the non-randomness parameter  $\alpha$  was set to 0.3. The binary interaction parameters ( $g_{ij} - g_{ji}$ ) and ( $g_{ji} - g_{ii}$ ) were fitted to

**Table 1**  
Chemicals used to prepare the eutectic mixtures, including their water content, and their melting temperatures and enthalpies measured in this work and available from the literature.

Name	Water content/mg g <sup>-1</sup>	T <sub>m</sub> /K		Δh <sub>m</sub> /kJ mol <sup>-1</sup>	
		This work	Lit.	This work	Lit.
L-Menthol	0.328 ± 0.035	–	314.6 [30]	–	13.74 [30]
Thymol	0.0749 ± 0.0093	322.70 ± 0.10	323.9 [31]	20.64 ± 0.41	19.65 [31]
Carvacrol	4.158 ± 0.011	274.20 ± 0.20	–	11.49 ± 0.29	–
Caprylic acid	1.253 ± 0.019	–	288.0 [30]	–	21.43 [30]
Capric acid	0.167 ± 0.028	–	303.9 [30]	–	28.39 [30]
Lauric acid	0.084 ± 0.010	–	316.6 [30]	–	35.81 [30]

experimental liquidus temperatures by minimizing the following objective function

$$F(T) = \sum \left( \frac{(T_i^{exp} - T_i^{cal})^2}{n} \right)^{\frac{1}{2}} \quad (6)$$

where  $T_i^{exp}$  and  $T_i^{cal}$  are the experimental and calculated liquidus temperatures, respectively; and  $n$  is the number of experimental points. The model was used to calculate the eutectic composition as the intercept of the two liquidus lines, since it is impossible to construct Tammann plots for systems with metastable phases.

### 3. Results and discussion

We investigate the formation of metastable phases, either glassy phases or metastable polymorphs, in several eutectic mixtures. Two sample-preparation methods were applied: annealing for a long time at a temperature below the eutectic temperature of the mixture, and *in situ* crystallization in the DSC run. The measured DSC curves and eutectic temperatures of annealed and *in situ* crystallized DSC samples were compared in each case. Next, the non-ideality of the components in the liquid phase was modeled using the NRTL equation, and the liquidus curves of the components were calculated using Eq. (2). The eutectic point was estimated from the intersection of the calculated liquidus lines.

#### 3.1. Glass formation

Several eutectic mixtures with very low glass-transition temperatures have been reported in literature. Abranches et al. [22] reported the glass-transition temperature of *l*-menthol/thymol near the eutectic composition, which is between  $x_{thymol} = 0.4$  and  $0.5$ , since no melting transition could be observed as a result of kinetic limitations. In this work, the *l*-menthol/thymol system was studied in detail. To measure the melting temperature of the mixture near the eutectic point, the samples were annealed before the DSC experiment. Fig. 1 shows the DSC curves of the annealed (blue line) and the *in situ* crystallized (dashed orange line) samples for the *l*-menthol/thymol system at  $x_{thymol} = 0.5000$  (Fig. 1A) and  $x_{thymol} = 0.4008$  (Fig. 1B). The *in situ* crystallized samples show only a glass transition at around 217 K. On the other hand, an endothermic broad peak is observed in the annealed samples, which indicates the transition of several metastable phases [34]. The kinetic hindrance during the crystallization of *l*-menthol and thymol near the eutectic point is the reason for the glassy phase formation. There have been reports in the literature on the kinetic hindrance of other eutectic mixtures containing thymol [31,35]. In the *l*-

menthol/thymol system, the eutectic peak can only be observed if the samples have been annealed before the DSC measurements. As seen in Fig. 1, the difference between the glass-transition peak and the onset of the eutectic peak is around 30 K. Moreover, the difference between the onset temperature and the peak maximum temperature is around 22 K. Fig. 2 shows the SLE data of the annealed samples measured in this work compared to the data reported in Abranches et al. [22]. The liquidus temperatures measured in this work are in good agreement with those reported by Abranches et al. [22].

The experimental eutectic composition can be determined from the Tammann plot. However, it is impossible to make the Tammann plot if metastable phases occur in the eutectic thermal event [34]. Alternatively, the eutectic composition can be determined by modeling the activity coefficients of the components in the liquid phase. In this work, we used the NRTL model (Eqs. (3)–(5)) to model the activity coefficients of the components in the liquid phase, and the SLE was calculated according to Eq. (2). Fig. 3 shows the experimental and calculated SLE data of the *l*-menthol/thymol eutectic system. The eutectic mixture shows a strong negative deviation from the ideal behavior. The NRTL model with two fitted parameters provides a good representation of the measured SLE data of the *l*-menthol/thymol system. Moreover, the eutectic temperature predicted by the NRTL model (241.46 K) is in good agreement with the eutectic temperature determined from the onset of the eutectic peak of the annealed samples (241.45 K). The eutectic composition predicted by the NRTL model is  $x_{e,thymol}^{NRTL} = 0.4326$ , slightly shifted toward *l*-menthol that has the lower melting enthalpy compared to thymol [18]. Abranches et al. [22] determined the eutectic

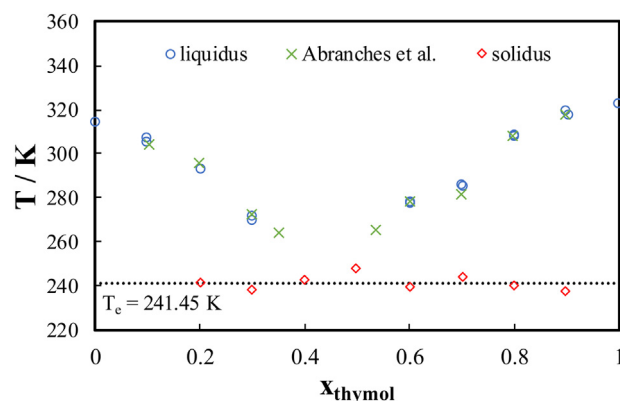


Fig. 2. Measured solid-liquid equilibria (SLE) data of the *l*-menthol/thymol system in comparison to SLE data reported in Abranches et al. [22]. The eutectic temperature ( $T_e = 241.45$  K) presented is an average value of temperatures determined at different composition.

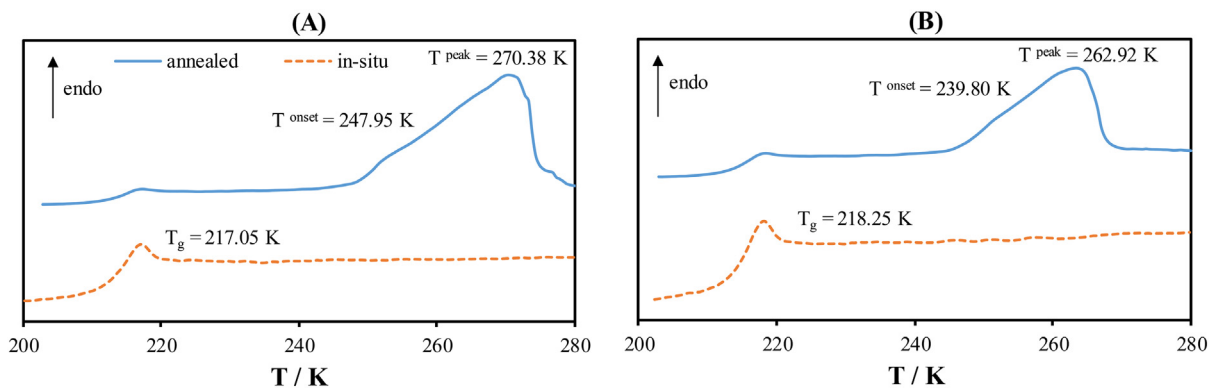


Fig. 1. Differential scanning calorimetry (DSC) curves of the *l*-menthol/thymol system at (A)  $x_{thymol} = 0.5000$  and (B)  $x_{thymol} = 0.4008$ . The DSC curves are shifted for clarity. The DSC curves of *in situ* samples are scaled by a factor of five for clarity. (For interpretation of the references to color in this figure, the reader is referred to the web version of this article.)

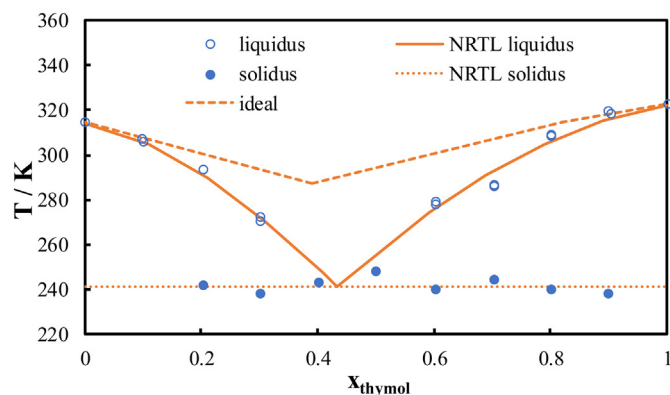


Fig. 3. Measured solid-liquid equilibria (SLE) data of the L-menthol/thymol eutectic system modeled assuming the ideal solution model and using the NRTL equation.

temperature by modeling the SLE data using the COSMO-RS model, which predicted a very low eutectic temperature (226.90 K) with an eutectic composition of  $x_{e, thymol}^{COSMO} = 0.4654$ . Although the liquidus temperatures predicted by COSMO-RS were in good agreement with the experimental data, the model underestimated the eutectic temperature of the system.

To investigate whether or not the kinetic limitation of the L-menthol/thymol system depends only on its strong negative deviation from the ideal behavior, we studied the SLE of the L-menthol/carvacrol eutectic mixture. Fig. 4 shows the chemical structures and melting properties of carvacrol and thymol, which were measured in this work. Although carvacrol and thymol are isomers, their melting properties are very different. Carvacrol is liquid at room temperature with a melting temperature of 274.20 K. Moreover, the melting enthalpy of carvacrol is almost half that of thymol. The lower melting enthalpy and melting entropy might indicate a disordered crystal structure of carvacrol. To the best of our knowledge, no crystallographic information is available on carvacrol in the literature to confirm this.

Fig. 5 shows the DSC curves of the annealed samples of L-menthol/carvacrol systems with different molar compositions. The top five DSC curves in the orange box correspond to the mixtures that are rich in carvacrol, while the bottom two DSC curves correspond to mixtures that are rich in L-menthol. As seen in Fig. 5, the eutectic peak is broad, similar to that observed in the L-menthol/thymol system. Moreover, a glass transition is observed at around  $T_g = 217.85$  K. However, in mixtures with a mole fraction of carvacrol lower than 0.8, the liquidus peak of carvacrol cannot be properly distinguished because of its overlapping with the eutectic peak. In contrast, a melting peak corresponding to a crystalline phase of pure L-menthol is observed in the DSC curves of the mixtures rich in L-menthol (the DSC curves inside the green box in Fig. 5).

Fig. 6 shows the measured SLE data for the annealed samples as well as the calculated liquidus lines using the ideal solution model and the

	thymol	carvacrol
<chem>CC(C)C1=CC=C(O)C=C1</chem>	<chem>CC(C)C1=CC=C(O)C=C1</chem>	<chem>CC(C)C1=CC=C(O)C=C1</chem>
$T_m$ [K]	322.68	274.2
$\Delta h_m$ [kJ mol <sup>-1</sup> ]	20.63	11.49
$\Delta s_m$ [J mol <sup>-1</sup> K <sup>-1</sup> ]	63.95	41.89

Fig. 4. Chemical structures and melting properties of thymol and carvacrol measured in this work.

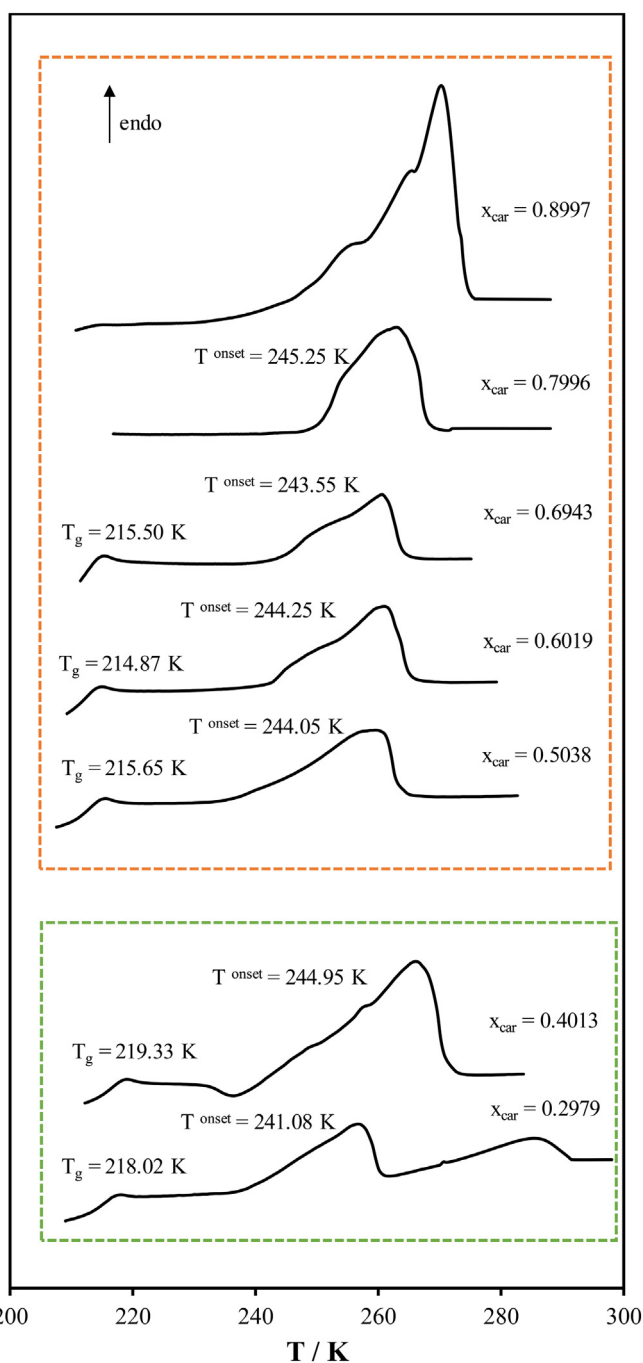
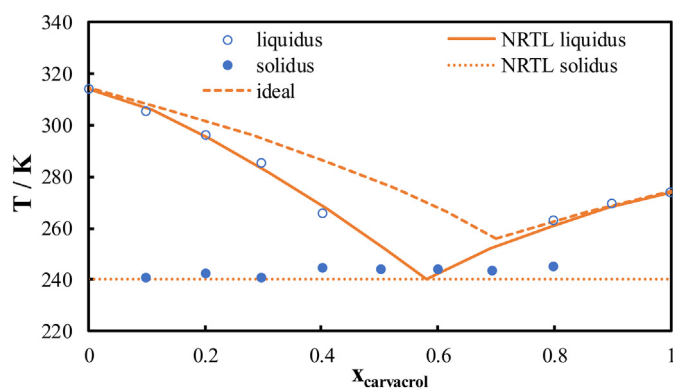


Fig. 5. Differential scanning calorimetry (DSC) curves of the annealed L-menthol/carvacrol mixtures with different mole fractions of carvacrol. The DSC curves in the orange and the green boxes correspond to mixtures rich in carvacrol and L-menthol, respectively. The DSC curves are shifted for clarity. (For interpretation of the references to color in this figure legend, the reader is referred to the web version of this article.)

NRTL model. The NRTL model provides a good representation of the measured SLE data of the L-menthol/carvacrol eutectic mixture. The eutectic temperature predicted by the NRTL model (240.15 K) is in good agreement with the onset of the eutectic peak in the annealed mixtures (243.35 K). The eutectic composition predicted by the NRTL model is  $x_{e, carvacrol}^{NRTL} = 0.5804$ . This shows that the eutectic composition is shifted toward the component that possesses the lowest melting enthalpy, i.e., carvacrol ( $\Delta h_m = 11.49$  and  $13.74$  kJ mol<sup>-1</sup> for carvacrol and L-menthol, respectively).

The L-menthol/thymol and L-menthol/carvacrol systems have similar eutectic temperatures (Figs. 3 and 6). The deviation from the ideal



**Fig. 6.** Measured solid-liquid equilibria (SLE) data of the L-menthol/carvacrol eutectic system modeled assuming an ideal solution and using the NRTL equation.

liquidus line of L-menthol in L-menthol/thymol (Fig. 3) is larger compared to that in L-menthol/carvacrol (Fig. 6). The thymol liquidus line in the L-menthol/thymol system shows a negative deviation from the ideal behavior (Fig. 3). In contrast, the carvacrol liquidus line shows a quasi-ideal behavior (Fig. 6). This emphasizes that eutectic mixtures with very low eutectic temperatures can be formed when their components possess low melting enthalpies, even if these components behave ideally. As noticed from the DSC curves inside the orange box in Fig. 5, a glass transition ( $T_g \approx 215.50$  K) is observed in the mixtures rich in carvacrol, even if the liquidus line deviates from the ideal liquidus line only slightly.

Kinetic hindrance during crystallization has also been noticed in other eutectic systems containing L-menthol [30]. Fig. 7 shows the DSC curves of annealed samples (blue curves) and *in situ* crystallized samples (orange dashed curves) of L-menthol/3-cyclohexylpropionic acid and L-menthol/cyclohexanecarboxylic acid near the eutectic composition of each eutectic system. Crystallization at the eutectic point is hindered in both systems. Although the glass transition is observed at lower temperatures (around 205 K) compared to those required in the L-menthol/thymol and L-menthol/carvacrol systems (around 217 K), the eutectic temperatures of L-menthol/3-cyclohexylpropionic acid ( $T_e = 262.10$  K) and L-menthol/cyclohexanecarboxylic acid ( $T_e = 265.50$  K) are higher than those of L-menthol/thymol ( $T_e = 241.45$  K) and L-menthol/carvacrol ( $T_e = 243.35$  K) systems. The SLE phase diagrams for both eutectic systems are shown in Fig. S1 of the Supplementary material. In L-menthol/3-cyclohexylpropionic acid, the L-menthol and 3-cyclohexylpropionic acid liquidus lines deviate negatively from the ideal liquidus line. In contrast, the cyclohexanecarboxylic acid liquidus line deviate positively from the ideal behavior.

Strong negative deviations from the ideal behavior can surely lead to a large temperature drop at the eutectic point and thus to kinetic hindrance at low temperatures. In L-menthol/thymol, the strong negative

deviation from ideality justifies the observed low glass-transition temperature. On the other hand, crystallization at low temperatures can lead to inefficient crystal packing in the crystalline phase of pure constituents. In order to build the crystal lattice, molecules should adapt a proper conformation that can be hindered at low temperatures. Substances with low melting enthalpies can also form deep eutectics. Thus, the combined effect of the attraction between unlike molecules and the inefficient crystal packing in the crystal structure of a pure component can lead to the formation of glassy states. The latter case is observed in the L-menthol/carvacrol, L-menthol/3-cyclohexylpropionic, and L-menthol/cyclohexanecarboxylic acid systems. It can be concluded that the formation of glassy phases at very low temperatures occurs not only due to the strong negative deviations from the ideal behavior, *i.e.*, strong attraction between unlike molecules, but also due to the crystal structure and melting properties of the pure components. Besides, the value of the glass transition temperature does not give a factual estimate of the value of the eutectic temperature. However, in case of kinetic limitation during crystallization near the eutectic point, the position of the latter can be estimated by SLE modeling using well-established thermodynamic models.

### 3.2. Polymorphism

As previously mentioned, L-menthol has four polymorphs. The melting properties of L-menthol, which are reported in the literature and measured using common DSC practice, are for stable  $\alpha$ -polymorph [28,36]. However, Corvis et al. [29] showed that crystallization of L-menthol in the metastable  $\beta$ -polymorph is also possible, if the molten L-menthol is quenched at temperatures below 288.15 K. The  $\beta$ -polymorph was stable for more than 8 h at 193.15 K, and all the  $\beta$ -polymorph transformed into the stable  $\alpha$ -polymorph after 80 min at 288.15 K [29]. The melting properties measured by Corvis [29] were  $\Delta h_m = 14.1$  and  $11.0$  kJ mol $^{-1}$ , and  $T_m = 316.05$  and  $308.45$  K for the  $\alpha$ -polymorph and the  $\beta$ -polymorph, respectively. In eutectic mixtures, the mixture has a lower melting temperature than its pure components. Therefore, when *in situ* crystallization of the samples is performed in the DSC run, and if the eutectic temperature of the mixture is lower than 288.15 K, L-menthol crystallizes at temperatures below its pure melting temperature. As a result, part of the solid L-menthol may crystallize in the form of the metastable  $\beta$ -polymorph.

The SLE of several binary eutectic mixtures based on L-menthol can be found in the literature [36–38]. Corvis et al. [38] reported the phase diagram of L-menthol/lidocaine, where L-menthol crystallized as the  $\beta$ -polymorph. The eutectic temperatures of mixtures of L-menthol as  $\alpha$ -polymorph and  $\beta$ -polymorph differ by 12 K [38] due to different melting properties of the two polymorphs.

In the L-menthol/thymol and L-menthol/carvacrol systems, the metastable polymorphs cannot be observed explicitly in the *in situ* or

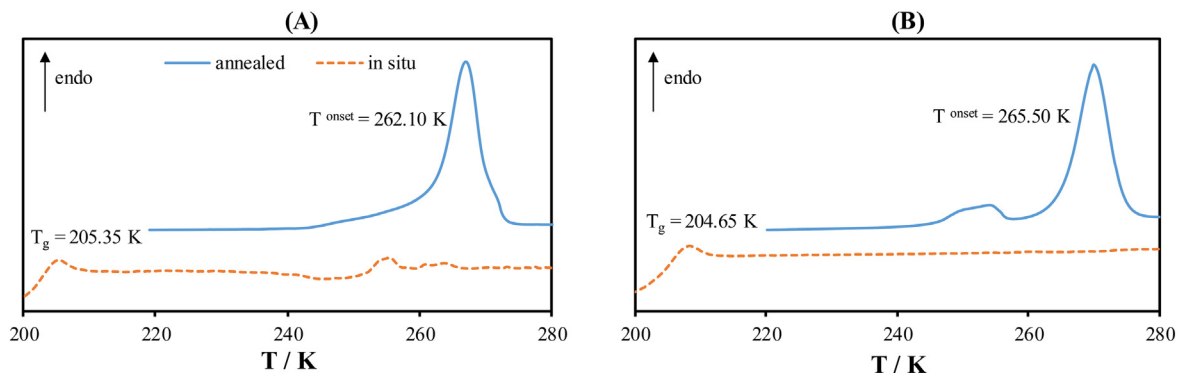


**Fig. 7.** Differential scanning calorimetry (DSC) curves of (A) the L-menthol/3-cyclohexylpropionic acid and (B) the L-menthol/cyclohexanecarboxylic acid at  $x_{acid} = 0.5000$ . The DSC curves are shifted for clarity. The DSC curves of the *in situ* samples are scaled by a factor of five for clarity.

the annealed samples. In the *in situ* measurements, only the glass transition can be found near the eutectic point. Annealing leads to formation of the stable polymorph mostly. Thus, to study polymorphism, eutectic systems without kinetic limitations should be considered. In the present study, we targeted the *L*-menthol eutectic systems with caprylic acid, capric acid, and lauric acid. The DSC experiments were carried out for the *in situ* crystallized samples as well as for the samples annealed in advance for at least one month at 253.15 K.

Fig. 8 shows the DSC curves of the annealed (blue curve) and the *in situ* crystallized (orange dashed curve) samples of *L*-menthol/caprylic acid (Fig. 8A), *L*-menthol/capric acid (Fig. 8B), and *L*-menthol/lauric acid (Fig. 8C) systems near their respective eutectic points ( $x_{\text{acid}}$ ,  $e \approx 0.5$ , 0.4, and 0.3 for *L*-menthol/caprylic acid, *L*-menthol/capric acid, and *L*-menthol/lauric acid, respectively) [30]. The annealed and *in situ* crystallized samples of the same mixture produce different DSC curves. Annealed samples (blue curves) show one large peak (peak maximum at  $T = 270.80$  K, 283.15 K, and 292.84 K for *L*-menthol/caprylic acid, *L*-menthol/capric acid and *L*-menthol/lauric acid, respectively), whereas *in situ* crystallized samples (orange dashed curve) show two peaks (peak maximum at  $T = 266.45$  K and 269.80 K, 278.08 K and 282.30 K, 287.45 K and 292.22 K, for *L*-menthol/caprylic acid, *L*-menthol/capric acid and *L*-menthol/lauric acid, respectively). Annealing leads to almost complete disappearance of the first peak (Fig. 8), indicating that the first peak is related to a metastable polymorph of *L*-menthol, supposedly the  $\beta$ -polymorph. Furthermore, the two peaks are much closer in *L*-menthol/caprylic acid (Fig. 8A) compared to *L*-menthol/capric acid (Fig. 8B) and *L*-menthol/lauric acid (Fig. 8C). In addition, the area of the first peak in Fig. 8A in *L*-menthol/caprylic acid is larger compared to the second peak, whereas, the area of the two peaks are almost the same in the *L*-menthol/capric acid (Fig. 8B) and *L*-menthol/lauric acid (Fig. 8C) systems. This indicates that the amount of the metastable polymorph related to the first peak is greater in *L*-menthol/caprylic acid. Corvis et al. [29] showed that the ratio between the stable and metastable polymorphs in *L*-menthol depends on the quenching temperature. This justifies the relative position of the peaks and the ratio between the peak areas observed in the present study, as the eutectic temperature of *L*-menthol/caprylic acid ( $T_e = 265.84$  K) is lower compared to *L*-menthol/capric acid ( $T_e = 278.64$  K) and *L*-

menthol/lauric acid ( $T_e = 291.12$  K) [30,37]. Therefore, we conclude that, in eutectic systems containing *L*-menthol, *L*-menthol can crystallize in the metastable  $\beta$ -polymorph if the samples are *in situ* crystallized in a conventional DSC run.

Fig. 9 shows the SLE data of the annealed and *in situ* crystallized samples measured in this work in comparison to the SLE data reported by Martins et al. [37]. We observe that the eutectic temperature of the *in situ* crystallized samples is lower than that of the annealed samples of the same mixture. The liquidus temperatures on the acid side are not expected to differ between the *in situ* crystallized samples and the annealed samples, because the liquidus line of the acid depends on the melting properties of the acid and the activity coefficient of the acid in the liquid phase (see Eq. (2)). However, this should not be the case for the liquidus temperatures on the *L*-menthol side, as the melting properties of  $\alpha$ - and  $\beta$ -polymorphs are different. The liquidus temperatures of the *in situ* crystallized samples are different from that of the annealed samples only for *L*-menthol/caprylic acid (Fig. 9A) and *L*-menthol/capric acid (Fig. 9B) at around  $x_{\text{acid}} = 0.1000$ . The metastable polymorph can only be detected for the *in situ* crystallized samples at the eutectic point or for the mixtures rich in *L*-menthol (Fig. 9). In Martins et al. [37], the samples were *in situ* crystallized, and the eutectic points reported in Martins et al. [37] were closer to those of the *in situ* crystallized samples measured in the present study (Fig. 9). The liquidus temperatures measured in this work are in good agreement with those reported in Martins et al. [37]. As can be seen in Fig. 9, the eutectic temperatures of stable polymorph (annealed samples) are higher than those of metastable polymorph (*in situ* crystallized samples). Thus, different sample preparation leads to different values of eutectic temperatures related either to the metastable polymorph, in case of the *in-situ* measurements, or to the stable polymorph, if the samples are annealed prior to the DSC run.

To confirm that the first peaks in Fig. 8 are the transition peaks at the eutectic point corresponding to metastable  $\beta$ -polymorph, *x*-ray diffraction measurements are needed. Alternatively, thermodynamic modeling can be used. The values of the activity coefficients depend on the composition and temperature of the solution and the latter is different for the stable and metastable polymorphs at liquidus conditions. The binary interaction parameters of activity coefficient models, such as NRTL,

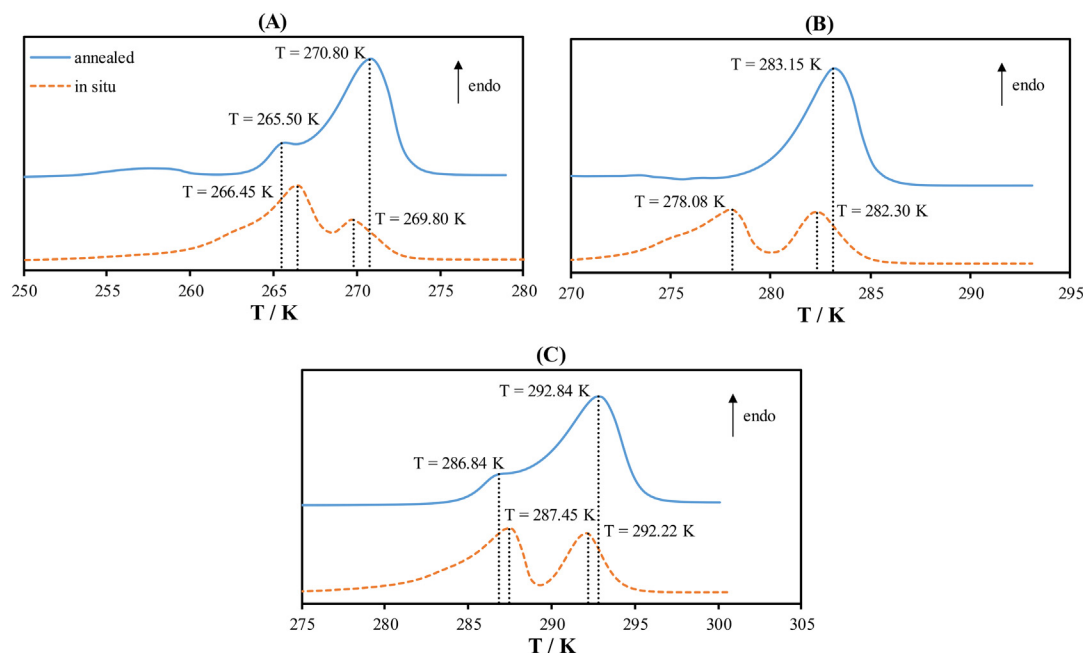
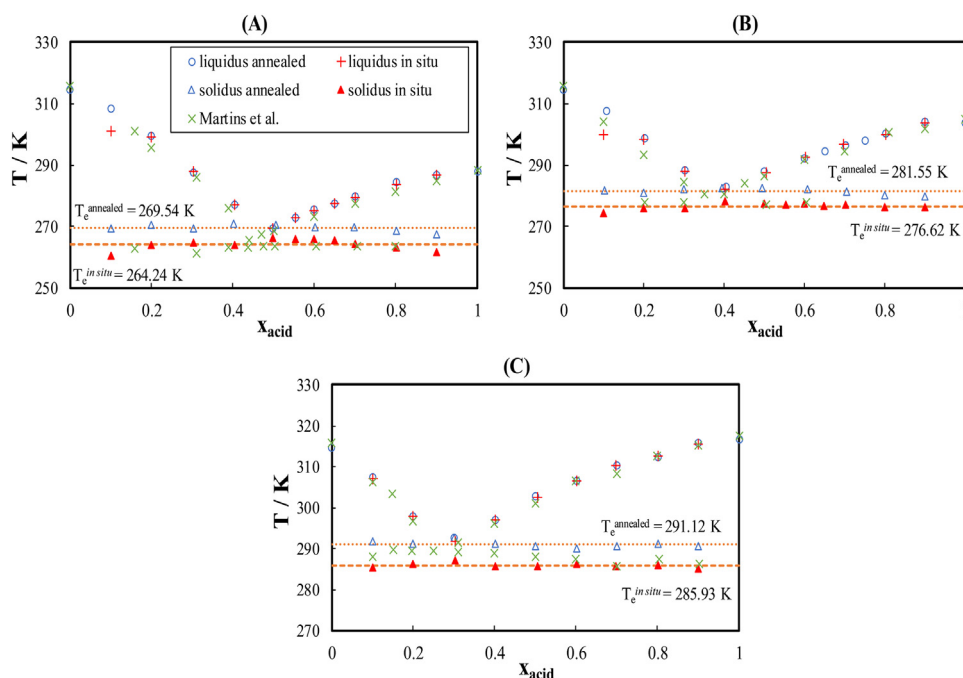


Fig. 8. Differential scanning calorimetry (DSC) curves of the (A) *L*-menthol/caprylic acid at  $x_{\text{acid}} = 0.5058$  (B) *L*-menthol/capric acid at  $x_{\text{acid}} = 0.3939$  (C) *L*-menthol/lauric acid  $x_{\text{acid}} = 0.3002$ . The DSC curves are shifted for clarity.





**Fig. 9.** Solid-liquid equilibria (SLE) in of (A) L-menthol/caprylic acid, (B) L-menthol/capric acid, and (C) L-menthol/lauric acid measured in this work for annealed and *in situ* crystalized samples in comparison with SLE data reported by Martins et al. [37]. The eutectic temperature of annealed samples ( $T_e^{annealed}$ ) and *in situ* crystalized samples ( $T_e^{in situ}$ ) presented are the average values of temperatures determined at different compositions.

provide the values of activity coefficients of its components in the liquid phase in the whole composition range and in the appropriate range of temperatures (used for fitting the binary interaction parameters) [32], independent of whether such a solution is or is not in equilibrium with one or another phase. Therefore, the NRTL binary interactions parameters (Eqs. (3)–(5)) fitted to the liquidus temperatures of the  $\alpha$ -polymorph, *i.e.*, the liquidus temperatures of the annealed samples, can be used to calculate the activity coefficients of L-menthol in the liquid phase. Then, using Eq. (2) and the melting properties of the  $\beta$ -

polymorph, the metastable SLE phase diagram corresponding to the  $\beta$ -polymorph can be calculated. Fig. 10 shows the calculated SLE of L-menthol/caprylic acid (Fig. 10A), L-menthol/capric acid (Fig. 10B), and L-menthol/lauric acid (Fig. 10C) eutectic systems modeled using the NRTL equation and the melting properties of L-menthol in  $\alpha$ - and  $\beta$ -polymorphs, in comparison to the measured SLE data for the annealed and *in situ* crystalized samples. We observe that the eutectic temperature measured for the *in situ* crystalized samples can be predicted from the melting properties of the  $\beta$ -polymorph and the activity

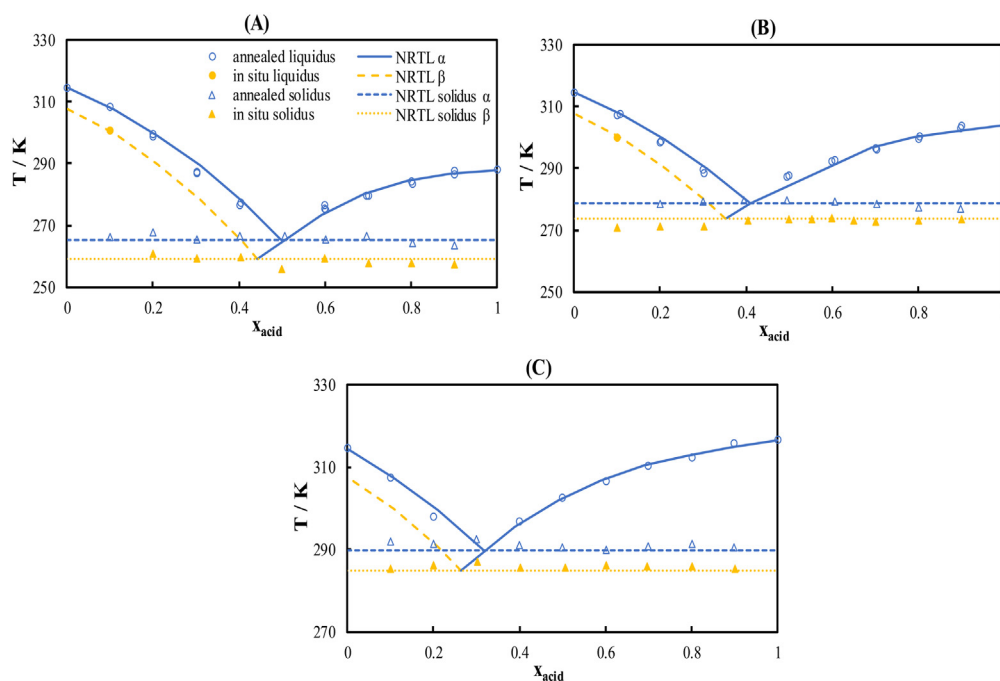


**Fig. 10.** Measured solid-liquid equilibria (SLE) in eutectic mixtures containing L-menthol with (A) caprylic acid, (B) capric acid, and (C) lauric acid compared to those modeled using the NRTL equation.

coefficients calculated using the binary interaction parameters fitted to the  $\alpha$ -polymorph liquidus temperatures. This confirms that the first transition peak measured for the *in situ* crystallized samples corresponds to the eutectic phase of the mixture with the metastable  $\beta$ -polymorph. Moreover, the liquidus temperatures determined at around  $x_{\text{acid}} = 0.1$  in *l*-menthol/caprylic acid (Fig. 10A) and *l*-menthol/capric acid (Fig. 10B) are predicted well. It can be concluded that SLE modeling is a useful tool for predicting the SLE of components having different polymorphs.

#### 4. Conclusions

In this work, the formation of metastable phases in several eutectic systems was studied in detail. SLE data were obtained using DSC with two different samples preparation methods, annealing and *in situ* crystallization in the DSC run. For the *in situ* crystallized samples, glass transition or formation of metastable polymorphs was observed. The SLE data were correlated by modeling the non-ideality of the components in the liquid phase using the NRTL equation.

The eutectic temperature peak was not detected in the *l*-menthol/thymol and *l*-menthol/carvacrol systems by applying DSC on the *in situ* crystallized samples. However, the samples annealed in advance for a sufficient amount of time showed a eutectic peak. We propose that a possible reason for the low glass-transition temperature of the *in situ* crystallized samples may be the very low eutectic temperature of the system or the inefficient crystal packing in the crystalline phase of the pure constituents. The low eutectic temperature can be a result of strong negative deviations from the ideal behavior or low melting enthalpy values. The latter can also indicate inefficient crystal packing of the pure constituents.

Modeling of activity coefficients of components in the liquid phase using NRTL equations provides good estimates of the eutectic temperatures and compositions of eutectic systems that show glass-transition temperatures near their eutectic points. Therefore, in case no crystallized eutectic phase can be detected, thermodynamic modeling offers an easier and more time-efficient option for estimating the position of the eutectic point compared to the time-consuming annealing method.

In case one of the eutectic system constituents possesses several polymorphic phases, care should be taken when analyzing the DSC curves. Eutectic peaks can be misinterpreted as liquidus peaks. Metastable and stable polymorphs have different melting properties that result in different phase diagrams. However, we demonstrated that the binary interaction parameters of activity coefficient models fitted to the SLE data measured for the stable polymorph can be used to predict the SLE in the corresponding system with the metastable polymorph.

We showed here that prior to designing process applications using DES, it is necessary to establish a better understanding of polymorphism and the formation of metastable phases in DES systems. This is essential to ensure the recyclability of the solvent as well as the reproducibility of the reported properties of DES.

#### CRedit authorship contribution statement

**Ahmad Alhadid:** Investigation, Formal analysis, Writing - original draft. **Liudmila Mokrushina:** Writing - review & editing. **Mirjana Minceva:** Writing - review & editing, Supervision.

#### Declaration of competing interest

The authors declare no conflict of interest.

#### Appendix A. Supplementary data

Supplementary data to this article can be found online at <https://doi.org/10.1016/j.molliq.2020.113667>.

#### References

- [1] P. Anastas, N. Eghbali, Green chemistry: principles and practice, Chem. Soc. Rev. 39 (2010) 301–312, <https://doi.org/10.1039/B918763B>.
- [2] Q. Zhang, K. De Oliveira Vigier, S. Royer, F. Jerome, Deep eutectic solvents: syntheses, properties and applications, Chem. Soc. Rev. 41 (2012) 7108–7146, <https://doi.org/10.1039/C2CS35178A>.
- [3] E.L. Smith, A.P. Abbott, K.S. Ryder, Deep eutectic solvents (DESs) and their applications, Chem. Rev. 114 (2014) 11060–11082, <https://doi.org/10.1021/cr300162p>.
- [4] T. Cai, H. Qiu, Application of deep eutectic solvents in chromatography: a review, TrAC Trends Anal. Chem. 120 (2019) 115623, <https://doi.org/10.1016/j.trac.2019.115623>.
- [5] J. Huang, X. Guo, T. Xu, L. Fan, X. Zhou, S. Wu, Ionic deep eutectic solvents for the extraction and separation of natural products, J. Chromatogr. A 1598 (2019) 1–19, <https://doi.org/10.1016/j.chroma.2019.03.046>.
- [6] X. Li, K.H. Row, Development of deep eutectic solvents applied in extraction and separation, J. Sep. Sci. 39 (2016) 3505–3520, <https://doi.org/10.1002/jssc.201600633>.
- [7] I. Wazeer, M. Hayyan, M.K. Hadj-Kali, Deep eutectic solvents: designer fluids for chemical processes, J. Chem. Technol. Biotechnol. 93 (2018) 945–958, <https://doi.org/10.1002/jctb.5491>.
- [8] H.F. Hizaddin, M. Sarwono, M.A. Hashim, I.M. Alnashef, M.K. Hadj-Kali, Coupling the capabilities of different complexing agents into deep eutectic solvents to enhance the separation of aromatics from aliphatics, J. Chem. Thermodyn. 84 (2015) 67–75, <https://doi.org/10.1016/j.jct.2014.12.024>.
- [9] P. Xu, G.W. Zheng, M.H. Zong, N. Li, W.Y. Lou, Recent progress on deep eutectic solvents in biocatalysis, Bioresources Bioprocess. 4 (2017) 34, <https://doi.org/10.1186/s40643-017-0165-5>.
- [10] B.L. Gadilohar, G.S. Shankarling, Choline based ionic liquids and their applications in organic transformation, J. Mol. Liq. 227 (2017) 234–261, <https://doi.org/10.1016/j.molliq.2016.11.136>.
- [11] S. Khandelwal, Y.K. Tailor, M. Kumar, Deep eutectic solvents (DESs) as eco-friendly and sustainable solvent/catalyst systems in organic transformations, J. Mol. Liq. 215 (2016) 345–386, <https://doi.org/10.1016/j.molliq.2015.12.015> (Review).
- [12] D.A. Alonso, A. Baeza, R. Chinchilla, G. Guillena, I.M. Pastor, D.J. Ramón, Deep eutectic solvents: the organic reaction medium of the century, Eur. J. Org. Chem. 2016 (2016) 612–632, <https://doi.org/10.1002/ejoc.201501197>.
- [13] J. García-Álvarez, Deep eutectic mixtures: promising sustainable solvents for metal-catalysed and metal-mediated organic reactions, Eur. J. Inorg. Chem. 2015 (2015) 5147–5157, <https://doi.org/10.1002/ejic.201500892>.
- [14] P. Liu, J.W. Hao, L.P. Mo, Z.H. Zhang, Recent advances in the application of deep eutectic solvents as sustainable media as well as catalysts in organic reactions, RSC Adv. 5 (2015) 48675–48704, <https://doi.org/10.1039/c5ra05746a>.
- [15] M. Pätzold, S. Siebenhaller, S. Kara, A. Liese, C. Syladat, D. Holtmann, Deep eutectic solvents as efficient solvents in biocatalysis, Trends Biotechnol. 37 (2019) 943–959, <https://doi.org/10.1016/j.tibtech.2019.03.007>.
- [16] A. Hayyan, M.A. Hashim, M. Hayyan, F.S. Mjalli, I.M. AlNashef, A new processing route for cleaner production of biodiesel fuel using a choline chloride based deep eutectic solvent, J. Clean. Prod. 65 (2014) 246–251, <https://doi.org/10.1016/j.jclepro.2013.08.031>.
- [17] M.A.R. Martins, S.P. Pinho, J.A.P. Coutinho, Insights into the nature of eutectic and deep eutectic mixtures, J. Solut. Chem. 48 (2019) 962–982, <https://doi.org/10.1007/s10953-018-0793-1>.
- [18] A. Alhadid, L. Mokrushina, M. Minceva, Modeling of solid–liquid equilibria in deep eutectic solvents: a parameter study, Molecules 24 (2019) 2334, <https://doi.org/10.3390/molecules24122334>.
- [19] I.I. Alkhatib, D. Bahamon, F. Llovel, M.R.M. Abu-Zahra, L.F. Vega, Perspectives and guidelines on thermodynamic modelling of deep eutectic solvents, J. Mol. Liq. 298 (2020) <https://doi.org/10.1016/j.molliq.2019.112183>.
- [20] L.J.B.M. Kollau, M. Vis, A. van den Bruinhorst, G. de With, R. Tuinier, Activity modelling of the solid–liquid equilibrium of deep eutectic solvents, Pure Appl. Chem. 91 (2019) 1341–1349, <https://doi.org/10.1515/pac-2018-1014>.
- [21] A. van den Bruinhorst, L.J.B.M. Kollau, M.C. Kroon, J. Meuldijk, R. Tuinier, A.C.C. Esteves, A centrifuge method to determine the solid–liquid phase behavior of eutectic mixtures, J. Chem. Phys. 149 (2018) 224505, <https://doi.org/10.1063/1.5051515>.
- [22] D.O. Abranches, M.A.R. Martins, L.P. Silva, N. Schaeffer, S.P. Pinho, J.A.P. Coutinho, Phenolic hydrogen bond donors in the formation of non-ionic deep eutectic solvents: the quest for type V DES, Chem. Commun. (Camb.) 55 (2019) 10253–10256, <https://doi.org/10.1039/c9cc04846d>.
- [23] E. Durand, J. Lecomte, P. Villeneuve, From green chemistry to nature: the versatile role of low transition temperature mixtures, Biochimie 120 (2016) 119–123, <https://doi.org/10.1016/j.biochi.2015.09.019>.
- [24] M. Francisco, A. van den Bruinhorst, M.C. Kroon, Low-transition-temperature mixtures (LTTMs): a new generation of designer solvents, Angew. Chem. Int. Ed. 52 (2013) 3074–3085, <https://doi.org/10.1002/anie.201207548>.
- [25] T. Koop, J. Bookhold, M. Shiraiwa, U. Posch, Glass transition and phase state of organic compounds: dependency on molecular properties and implications for secondary organic aerosols in the atmosphere, Phys. Chem. Chem. Phys. 13 (2011) 19238–19255, <https://doi.org/10.1039/c1cp22617g>.
- [26] U.P. Preiss, W. Beichel, A.M. Erle, Y.U. Paulechka, I. Krossing, Is universal, simple melting point prediction possible? Chemphyschem 12 (2011) 2959–2972, <https://doi.org/10.1002/cphc.201100522>.
- [27] F.E. Wright, The crystallization of menthol, J. Am. Chem. Soc. 39 (1917) 1515–1524, <https://doi.org/10.1021/ja02253a001>.

- [28] Y. Corvis, A. Wurm, C. Schick, P. Espeau, New menthol polymorphs identified by flash scanning calorimetry, *CrystEngComm* 17 (2015) 5357–5359, <https://doi.org/10.1039/C5CE00697J>.
- [29] Y. Corvis, P. Négrier, S. Massip, J.-M. Leger, P. Espeau, Insights into the crystal structure, polymorphism and thermal behavior of menthol optical isomers and racemates, *CrystEngComm* 14 (2012) 7055–7064, <https://doi.org/10.1039/C2CE26025E>.
- [30] A. Alhadid, L. Mokrushina, M. Minceva, Design of deep eutectic systems: a simple approach for preselecting eutectic mixture constituents, *Molecules* 25 (2020) 1077, <https://doi.org/10.3390/molecules25051077>.
- [31] F. Wolbert, C. Brandenbusch, G. Sadowski, Selecting excipients forming therapeutic deep eutectic systems—a mechanistic approach, *Mol. Pharm.* 16 (2019) 3091–3099, <https://doi.org/10.1021/acs.molpharmaceut.9b00336>.
- [32] J.M. Prausnitz, R.N. Lichtenthaler, E.G.d. Azevedo, *Molecular Thermodynamics of Fluid-phase Equilibria*, Prentice Hall PTR, Upper Saddle River, NJ, 1999.
- [33] S.H. Yalkowsky, M. Wu, Estimation of the ideal solubility (crystal–liquid fugacity ratio) of organic compounds, *J. Pharm. Sci.* 99 (2010) 1100–1106, <https://doi.org/10.1002/jps.21897>.
- [34] L. Rycerz, Practical remarks concerning phase diagrams determination on the basis of differential scanning calorimetry measurements, *J. Therm. Anal. Calorim.* 113 (2013) 231–238, <https://doi.org/10.1007/s10973-013-3097-0>.
- [35] F. Bezold, M. Minceva, Liquid-liquid equilibria of n-heptane, methanol and deep eutectic solvents composed of carboxylic acid and monocyclic terpenes, *Fluid Phase Equilib.* 477 (2018) 98–106, <https://doi.org/10.1016/j.fluid.2018.08.020>.
- [36] M.A.R. Martins, L.P. Silva, N. Schaeffer, D.O. Abranches, G.J. Maximo, S.P. Pinho, J.A.P. Coutinho, Greener terpene–terpene eutectic mixtures as hydrophobic solvents, *ACS Sustain. Chem. Eng.* 7 (2019) 17414–17423, <https://doi.org/10.1021/acssuschemeng.9b04614>.
- [37] M.A.R. Martins, E.A. Crespo, P.V.A. Pontes, L.P. Silva, M. Bülow, G.J. Maximo, E.A.C. Batista, C. Held, S.P. Pinho, J.A.P. Coutinho, Tunable hydrophobic eutectic solvents based on terpenes and monocarboxylic acids, *ACS Sustain. Chem. Eng.* 6 (2018) 8836–8846, <https://doi.org/10.1021/acssuschemeng.8b01203>.
- [38] Y. Corvis, P. Négrier, M. Lazerges, S. Massip, J.-M. Léger, P. Espeau, Lidocaine/l-menthol binary system: cocrystallization versus solid-state immiscibility, *J. Phys. Chem. B* 114 (2010) 5420–5426, <https://doi.org/10.1021/jp101303j>.

## Supplementary Materials

### Formation of Glassy Phases and Polymorphism in Deep Eutectic Systems

Ahmad Alhadid <sup>1</sup>, Liudmila Mokrushina <sup>2</sup>, and Mirjana Minceva <sup>1\*</sup>

<sup>1</sup> Biothermodynamics, TUM School of Life Sciences Weihenstephan, Technical University of Munich, Germany

<sup>2</sup> Separation Science & Technology, Friedrich-Alexander-Universität Erlangen-Nürnberg (FAU), Germany

\*Corresponding author e-mail: [mirjana.minceva@tum.de](mailto:mirjana.minceva@tum.de)

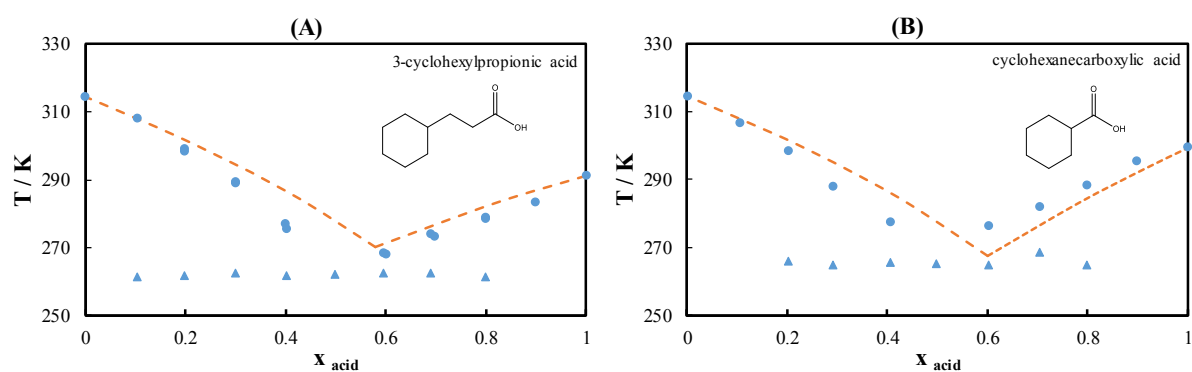


Figure S1. Solid-liquid equilibria data for eutectic mixture containing L-menthol with (A) 3-cyclohexylpropionic acid and (B) cyclohexanecarboxylic acid. Data are taken from [1]. Legend: ● liquidus temperature; ▲ solidus temperature; --- ideal liquidus line

Table S1. Experimental liquidus temperatures  $T^{\text{exp}}$ , onset temperature of eutectic peak  $T^{\text{onset}}$ , and calculated liquidus temperatures  $T^{\text{cal}}$  using NRTL model for L-menthol/thymol eutectic system.

$x_{\text{thymol}}$	$T^{\text{exp}} / \text{K}$	$T^{\text{onset}} / \text{K}$	$T^{\text{cal}} / \text{K}$
0.8978	319.55	237.80	316.15
0.8003	308.15	239.90	306.19
0.7032	285.65	244.15	292.51
0.6015	278.55	239.80	276.52
0.5000	–	247.95	–
0.4008	–	242.55	–
0.3010	269.90	238.00	272.43
0.2019	293.30	241.45	291.35
0.1000	305.70	–	305.68
0.9035	317.95	–	316.61
0.8009	309.00	239.25	306.29
0.7011	286.30	237.50	292.26
0.6012	277.80	239.80	276.40
0.3011	271.80	241.85	272.58
0.0987	307.15	238.00	305.81

Table S2. Experimental liquidus temperatures  $T^{\text{exp}}$ , onset temperature of eutectic peak  $T^{\text{onset}}$ , and calculated liquidus temperatures  $T^{\text{cal}}$  using NRTL model for L-menthol/carvacrol eutectic system.

$x_{\text{carvacrol}}$	$T^{\text{exp}} / \text{K}$	$T^{\text{onset}} / \text{K}$	$T^{\text{cal}} / \text{K}$
0.8997	270.05	–	267.66
0.7996	263.05	245.25	260.51
0.6943	–	243.55	–
0.6019	–	244.25	–
0.5038	–	244.05	–
0.4013	266.25	244.95	267.88
0.2979	285.58	241.08	283.67
0.2030	296.35	242.70	295.80
0.0998	305.85	240.95	306.82

Table S3. Experimental liquidus temperatures  $T^{\text{exp}}$ , onset temperature of eutectic peak  $T^{\text{onset}}$ , and calculated liquidus temperatures  $T^{\text{cal}}$  using NRTL model for L-menthol/caprylic acid eutectic system.

$x_{\text{acid}}$	$T^{\text{exp}} / \text{K}$	$T^{\text{onset}} / \text{K}$	$T^{\text{cal}} / \text{K}$
0.9000	287.70	263.35	286.64
0.8021	283.55	264.15	284.90
0.6974	279.55	266.65	280.55
0.6013	275.00	265.55	274.29
0.5058	–	266.75	–
0.4019	276.40	266.65	278.55
0.3025	286.90	265.60	290.07
0.1996	298.75	267.65	300.02
0.0997	308.50	266.20	307.99
0.9002	286.65	266.65	286.65
0.8001	284.35	265.60	284.84
0.7012	279.65	267.65	280.75
0.5999	275.60	266.20	274.22
0.4989	–	266.45	–
0.4035	277.15	263.90	278.39
0.3030	287.75	264.85	290.04
0.2001	299.40	263.95	299.98
0.0998	308.20	260.65	307.99

Table S4. Experimental liquidus temperatures  $T^{\text{exp}}$ , onset temperature of eutectic peak  $T^{\text{onset}}$ , and calculated liquidus temperatures  $T^{\text{cal}}$  using NRTL model for L-menthol/capric acid eutectic system.

$x_{\text{acid}}$	$T^{\text{exp}} / \text{K}$	$T^{\text{onset}} / \text{K}$	$T^{\text{cal}} / \text{K}$
0.8990	302.85	276.95	302.14
0.8007	299.55	277.25	300.35
0.7039	296.10	278.55	297.35
0.6066	292.65	279.20	292.86
0.4937	287.20	279.55	285.76
0.3939	–	279.75	–
0.3003	289.55	279.25	290.88
0.1997	298.60	278.65	300.21
0.1015	307.10	–	307.91
0.8995	303.95	276.35	302.14
0.8025	300.15	276.50	300.40
0.7014	296.60	277.00	297.26
0.5995	292.30	277.50	292.47
0.4998	287.85	277.70	286.22
0.4037	–	278.10	–
0.3023	288.40	275.90	290.88
0.2016	298.85	275.85	300.06
0.1082	307.65	–	307.42



Table S5. Experimental liquidus temperatures  $T^{\text{exp}}$ , onset temperature of eutectic peak  $T^{\text{onset}}$ , and calculated liquidus temperatures  $T^{\text{cal}}$  using NRTL model for L-menthol/lauric acid eutectic system.

$x_{\text{acid}}$	$T^{\text{exp}} / \text{K}$	$T^{\text{onset}} / \text{K}$	$T^{\text{cal}} / \text{K}$
0.8997	315.68	290.58	314.80
0.8010	312.45	291.35	313.14
0.6996	310.38	290.68	310.65
0.6007	306.58	289.95	307.15
0.4998	302.65	290.58	302.39
0.4007	296.88	291.18	296.33
0.3002	–	292.52	–
0.1999	297.88	291.35	300.49
0.1014	307.45	291.85	307.98

Table S6. NRTL binary interaction parameters and root-mean-square deviation (RMSD) between experimental liquidus temperatures and calculated liquidus temperatures.

NRTL binary interaction parameters			
Eutectic system	$(g_{12} - g_{22})$	$(g_{21} - g_{11})$	RMSD* / K
L-menthol/thymol	-4.3333	-4.0648	3.5
L-menthol/carvacrol	3.1532	-4.5610	1.9
L-menthol/caprylic acid	-4.3718	11.1196	1.5
L-menthol/capric acid	-4.2923	9.7161	1.2
L-menthol/lauric acid	-4.0097	8.5889	1.2

$$* RMSD / K = \sqrt{\frac{\sum(T^{exp} - T^{cal})^2}{n-2}}$$

Table S7. Glass transition temperature  $T_g$ , average onset temperature of eutectic peak  $T^{\text{onset}}$ , as well as eutectic temperature  $T_e^{\text{NRTL}}$  and eutectic composition  $x_{e,2}^{\text{NRTL}}$  calculated by NRTL of studied systems.

Eutectic system	$T_g$ / K	$T^{\text{onset}}$ / K	$T_e^{\text{NRTL}}$ / K	$x_{e,2}^{\text{NRTL}}$
L-menthol/thymol	217.55	241.45	241.46	0.4326
L-menthol/carvacrol	217.85	243.35	240.15	0.5804
L-menthol/3-cyclohexylpropionic acid	205.35	262.10 [1]	–	–
L-menthol/cyclohexanecarboxylic acid	204.65	265.00 [1]	–	–
L-menthol/caprylic acid	$\alpha$ -polymorph	265.84	265.08	0.4992
	–			
	$\beta$ -polymorph	258.53	259.05	0.4431
L-menthol/capric acid	$\alpha$ -polymorph	278.64	278.82	0.4091
	–			
	$\beta$ -polymorph	272.67	273.53	0.3531
L-menthol/lauric acid	$\alpha$ -polymorph	291.12	289.91	0.3173
	–			
	$\beta$ -polymorph	285.93	285.02	0.2637

## References

1. Alhadid, A.; Mokrushina, L.; Minceva, M. Design of Deep Eutectic Systems: A Simple Approach for Preselecting Eutectic Mixture Constituents. *Molecules* **2020**, *25*, 1077, doi:10.3390/molecules25051077.

### 3.4 Paper IV

#### **Experimental Investigation and Modeling of Cocrystal Formation in L-Menthol/Thymol Eutectic System**

**A. Alhadid, C. Jandl, L. Mokrushina and M. Minceva**, *Cryst. Growth Des.*, **2021**, *21*, 6083-6091.

Author contribution: The thesis author conceptualized the paper's idea, performed the investigations and formal analysis (excluding powder and SC-XRD), interpreted the results, and wrote the manuscript.

Summary: Paper IV objective is to investigate cocrystal formation in the L-menthol/thymol eutectic systems. The system was selected for two reasons. First, it is one of the most studied nonionic DES in the literature. Second, the observed solidus peaks for the system in Paper III were broad and asymmetric, hinting at the formation of several metastable phases. To overcome glass and metastable phases formation and allow for combined DSC and powder XRD analyses, an efficient sample preparation method was proposed. The liquid solutions obtained by mixing and heating pure constituents in different ratios were quenched at 193 K for several hours, and later stored at 253 K for several days until complete crystallization was observed. The obtained solid was ground to a fine powder within a cold room at 253 K using mortar and pestle. DSC and powder XRD analyses were performed on samples covering the entire composition range of the mixture to obtain the SLE phase diagram and investigate cocrystal formation.

Paper IV showed that the phase diagram of the L-menthol/thymol eutectic system is more complicated than previously anticipated, whether in Paper III or the literature.<sup>100</sup> The formation of two cocrystals and two solid solution regions was observed.

The heat capacity terms are usually neglected in the literature when modeling SLE in DES, mainly due to unavailable data for the heat capacity of pure liquid and solid. To test this assumption in the studied system, the three common approaches to account for the heat capacity terms were evaluated. It was found that assuming a constant difference between pure liquid and solid heat capacities calculated at the melting temperature provided the lowest deviation between calculated and experimental liquidus data of pure constituents. Nevertheless, the influence of the approach used to account for the heat capacity difference on the obtained NRTL interaction parameters was insignificant. Therefore, if no experimental data are available on the heat

### 3.4 Paper IV

capacity of pure components in the solid and liquid states, neglecting the heat capacity terms could be sufficient for modeling of SLE.

The SLE data were correlated using the NRTL model and considering the two cocrystals and the partial miscibility in the solid phase. The two calculated eutectic temperatures using the NRTL model were in good agreement with the experimentally observed ones, which demonstrates the postulated stoichiometries and the melting properties of the two cocrystals as well as the ability of the NRTL model to describe the nonideality of the components in the liquid solution.

### 3.4 Paper IV

Reprinted with permission from Alhadid et al., *Cryst. Growth Des.*, **2021**, *21*, 6083-6091.

DOI:10.1021/acs.cgd.1c00306. Copyright 2021 American Chemical Society.

Article full text: <http://pubs.acs.org/articlesonrequest/AOR-3FTJ2S7WIHUD5KXIKNZ2>

# Experimental Investigation and Modeling of Cocrystal Formation in L-Menthol/Thymol Eutectic System

Ahmad Alhadid,\* Christian Jandl, Liudmila Mokrushina, and Mirjana Minceva

Cite This: *Cryst. Growth Des.* 2021, 21, 6083–6091

Read Online

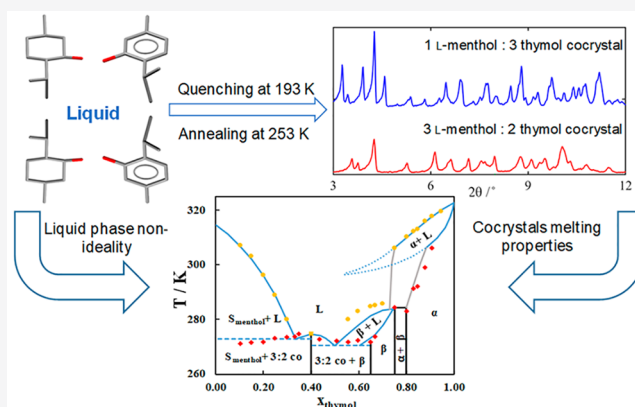
ACCESS |

Metrics & More

Article Recommendations

Supporting Information

**ABSTRACT:** Solid–liquid equilibria (SLE) of the L-menthol/thymol eutectic system were studied in detail using a combination of differential scanning calorimetry (DSC) and powder X-ray diffraction (XRD). The existence of two cocrystals with stoichiometric ratios 1:3 and 3:2 for L-menthol:thymol was monitored by performing XRD on samples of different compositions. Moreover, the existence of two solid solution regions of L-menthol in thymol and L-menthol in the 1:3 cocrystal was observed. The nonrandom two-liquid (NRTL) and two-suffix Margules models were applied to model the measured SLE data. The two eutectic points of the system were determined at  $T_{e1}^{cal} = 271.7$  K,  $x_{thymol,e1}^{cal} = 0.48$  and  $T_{e2}^{cal} = 273.1$  K,  $x_{thymol,e2}^{cal} = 0.33$ . The complex character of the obtained phase diagram of the system shows that not all deep eutectic systems can be assumed to be of a simple eutectic type with immiscible solid phases. For the accurate determination of the SLE of eutectic systems, a combination of several experimental techniques and thermodynamic modeling is needed.



## 1. INTRODUCTION

Deep eutectic solvents (DES) have emerged as a new class of designer solvents. Prepared from natural, nontoxic, and sustainable components, they have been considered a greener alternative to ionic liquids.<sup>1,2</sup> Several studies have shown that DES can be used in several applications such as drug delivery,<sup>3,4</sup> liquid chromatography,<sup>5,6</sup> and reaction media.<sup>7</sup> A considerable amount of research has been dedicated to studying intermolecular interactions in the liquid phase using molecular simulation or thermodynamic models.<sup>8,9</sup> The motivation for exclusively studying the liquid phase in DES is the assumption that strong hydrogen bonding in the liquid phase is the reason for the depression of the mixture melting temperature.<sup>10,11</sup>

A knowledge of solid–liquid equilibria (SLE) in DES is essential to the design of eutectic mixtures.<sup>12,13</sup> Studying SLE in DES requires measuring the melting temperature of the mixture at different compositions. The mixture melting temperature can be measured by visual methods or by differential scanning calorimetry (DSC). The main advantage of DSC is the possibility to identify different phase transitions, such as the solid–solid transition and the glass transition, which is not possible with visual methods.<sup>14–16</sup> To generate the phase diagram over the full composition range, the obtained SLE data are modeled using the equation<sup>17</sup>

$$\ln x_i^L \gamma_i^L = -\frac{\Delta h_{m,i}}{RT} \left(1 - \frac{T}{T_{m,i}}\right) - \frac{1}{RT} \int_{T_m}^T \Delta c_p(T) dT + \frac{1}{R} \int_{T_m}^T \frac{\Delta c_p(T)}{T} dT \quad (1)$$

where  $x_i^L$  and  $\gamma_i^L$  are the mole fraction and activity coefficient of component  $i$  in the liquid solution, respectively,  $\Delta h_{m,i}$  and  $T_{m,i}$  are the melting enthalpy and melting temperature of pure component  $i$ , respectively,  $R$  is the universal gas constant;  $T$  is the liquidus temperature, and  $\Delta c_{p,i}$  is the difference between the liquid and solid state heat capacities of pure component  $i$  at constant pressure. Several approaches can be found in the literature considering the treatment of the heat capacity term.<sup>18</sup> However, due to the opposite signs of the last two terms in eq 1, their contribution is insignificant if  $T_m/T < 1.4$ . Further, the difference between the liquid and solid states heat capacities is difficult to obtain experimentally and is only available for a

Received: March 19, 2021  
Revised: October 11, 2021  
Published: October 25, 2021



limited number of substances. As a result, the heat capacity term is usually neglected in modeling SLE.

In eq 1, the primary assumption is that the components crystallize as pure solids in their most stable polymorph: i.e., a simple eutectic mixture. Although this assumption might be applicable to many DES, experimental investigations to prove its validity are lacking. It has been shown that polymorphism can be observed in many eutectic systems.<sup>19–22</sup> Corvis et al.<sup>20</sup> reported the formation of a 1:1 molar ratio cocrystal in the lidocaine/L-menthol binary eutectic system. Recently, Hall et al.<sup>23</sup> used synchrotron X-ray powder diffraction (XRD) and DSC to prove the formation of several metastable solid phases in different eutectic systems. Polymorphism and the formation of congruently or incongruently melting compounds will affect the measured melting temperature of the mixture and thus the phase diagram.

The L-menthol/thymol eutectic system has attracted much attention in the literature because of its very low eutectic temperature, low viscosity at room temperature, and poor miscibility with water.<sup>24–28</sup> The SLE data for this system are available in the literature.<sup>19,24</sup> In a previous work,<sup>19</sup> it was shown that the peaks observed in the DSC curves of the L-menthol/thymol eutectic system, which were interpreted as eutectic peaks, were broad, indicating a possibility of several thermal events. The present study investigates the SLE of the L-menthol/thymol eutectic system in detail to comprehend these thermal events and characterize the formed solid phases. For this purpose, DSC measurements were coupled with low-temperature XRD experiments. The nonrandom two-liquid (NRTL) and the two-suffix Margules equations were applied to model the nonideality in the liquid and solid phases, respectively, to generate the phase diagram in the whole composition range and determine the eutectic points.

## 2. METHODS

**2.1. Solid–Liquid Equilibria.** L-menthol (purity  $\geq 99\%$ , Sigma-Aldrich) and thymol (purity  $\geq 99\%$ , Sigma-Aldrich) were weighed (precision  $1 \times 10^{-4}$  g, Sartorius, Germany) in various ratios in glass vials. Then, the vials were tightly closed, and the mixtures were gently heated with continuous stirring until a homogeneous clear liquid was obtained.

Two sample preparation methods were used. The first sample preparation method—later referred to as slow crystallization because the samples crystallized after long storage—the samples were introduced in DSC crucible pans as a liquid. The DSC pans were hermetically sealed and stored at a temperature below their freezing temperature observed previously in the literature.<sup>19</sup> For samples with  $x_{\text{thymol}} \geq 0.70$ , crystallization was observed at 277 K after a few days or weeks, depending on the sample composition. However, due to kinetic limitations, no crystallization was observed in samples with  $x_{\text{thymol}} < 0.70$  even at 253 K. The second preparation method—later referred to as rapid crystallization since the crystallization was observed shortly after annealing at 253 K—included quenching the liquid samples inside plastic tubes at 193 K and then keeping them at this temperature for several hours. Then, the tubes were transferred to a freezer at 253 K. Crystallization was observed after a few hours or days, depending on the sample composition. Later, the solid was ground inside a cold room at 253 K using a mortar and pestle. The samples were introduced into DSC aluminum crucible pans as a fine powder, and the DSC crucibles were hermetically sealed.

SLE data were measured using DSC (NETZSCH DSC 200 F3, Germany). The instrument was calibrated before measurements using the standard procedure based on the onset temperature of the transition of six calibration standards at a heating rate of 5 K min<sup>-1</sup>: adamantane, bismuth, cesium chloride, indium, tin, and zinc. Measurements were performed under nitrogen with a flow rate of

150 mL min<sup>-1</sup>. The standard uncertainties of the temperature and sensitivity measurements were 0.1 K and 0.3%, respectively.

The DSC chamber was precooled to 243 K before introducing the sample. Then, a cooling run with a rate of 5 K min<sup>-1</sup> down to 193 K was performed. Finally, a heating run up to 323 K was conducted. The solidus phase transition temperatures were determined as the onset temperatures at a heating rate of 5 K min<sup>-1</sup>. To determine the liquidus temperatures, the DSC measurements were performed at three different heating rates: namely, 1, 2, and 5 K min<sup>-1</sup>. The liquidus temperatures at zero heating rate were determined by extrapolation of peak maximum temperature to the zero heating rate. Figure S1 in the Supporting Information shows the extrapolation procedure for selected samples. DSC experiments were performed in duplicate for the same mixture. The difference in the determined temperatures for different samples of the same mixture was less than 1 K (the average absolute deviation is 0.5 K).

**2.2. X-ray Diffraction.** Powder XRD experiments were performed using a Stadi P diffractometer (Stoe & Cie, Germany) with Debye–Scherrer geometry equipped with a Mo fine-focus sealed tube, a curved Ge monochromator selecting  $K\alpha_1$  radiation ( $\lambda = 0.70930$  Å), and a Mythen 2 R 1K detector (Dectris, Switzerland). The data were collected with a step size of  $0.015^\circ$   $2\theta$  per data point. For measurements performed at 253 K, a cryostream (Oxford 800 series, UK) was used. The samples were prepared by grinding using a mortar and pestle in a cold room (at a temperature of 253 K) and then filled into a glass capillary (Hilgenberg, Germany) with a 1.0 mm diameter.

For single-crystal XRD (SC-XRD) measurements, a single crystal with the approximate dimensions  $0.442$  mm  $\times$   $0.528$  mm  $\times$   $0.547$  mm was used for analysis. The X-ray intensity data were measured on a D8 Venture Duo IMS system (Bruker, USA) equipped with a Helios optic monochromator and a Mo IMS microsource ( $\lambda = 0.71073$  Å). The measurements were performed at 100 K. Details of the structure and refinement can be found in the Supporting Information.

**2.3. Thermodynamic Modeling.** In this work, SLE data were modeled by considering the miscibility in the solid phase. Thus, the activities of components in the solid phase should be considered. The following equation was used to calculate the liquidus temperature at different mole fractions of components<sup>17</sup>

$$\ln \frac{x_i^L \gamma_i^L}{x_i^S \gamma_i^S} = -\frac{\Delta h_{m,i}}{RT} \left(1 - \frac{T}{T_{m,i}}\right) - \frac{1}{RT} \int_{T_m}^T \Delta c_p(T) dT + \frac{1}{R} \int_{T_m}^T \frac{\Delta c_p(T)}{T} dT \quad (2)$$

where  $x_i^S$  and  $\gamma_i^S$  are the composition and the activity coefficient of component  $i$  in the solid phase, respectively. The activity coefficients of components in the liquid phase  $\gamma_i^L$  were calculated using the NRTL model as follows:<sup>17</sup>

$$\ln \gamma_i^L = x_j^2 \left[ \tau_{ji} \left( \frac{G_{ji}}{x_i + x_j G_{ji}} \right)^2 + \frac{\tau_{ij} G_{ij}}{(x_j + x_i G_{ij})^2} \right] \quad (3)$$

$$G_{ij} = \exp(-\alpha \tau_{ij}), \quad G_{ji} = \exp(-\alpha \tau_{ji}) \quad (4)$$

$$\tau_{ij} = \frac{g_{ij} - g_{jj}}{RT}, \quad \tau_{ji} = \frac{g_{ji} - g_{ii}}{RT} \quad (5)$$

The value of the nonrandomness parameter ( $\alpha$ ) was set to 0.3. The activity coefficients of components in the solid phase  $\gamma_i^S$  were calculated using the two-suffix Margules equation as follows:<sup>17</sup>

$$\ln \gamma_i^S = \frac{A_{ij}}{RT} (x_j^S)^2 \quad (6)$$

The binary interaction parameters  $A_{ij}$ ,  $g_{ij} - g_{jj}$ , and  $g_{ji} - g_{ii}$  were fitted to experimental liquidus data ( $T_i^{\text{exp}}$ ) by minimizing the objective function



$$F(T) = \sum_{i=1}^n \left( \frac{(T_i^{\text{exp}} - T_i^{\text{cal}})^2}{n} \right)^{1/2} \quad (7)$$

where  $T_i^{\text{cal}}$  is the calculated liquidus temperature and  $n$  is the number of data points. The liquidus and solidus curves can be calculated similarly to dew and bubble curve calculations.<sup>29</sup>

In a binary system with a cocrystal, the formation of a cocrystal between component A and component B can be described using the chemical reaction<sup>30,31</sup>



where  $\vartheta_A$  and  $\vartheta_B$  are the stoichiometric coefficients of components A and B in the cocrystal, respectively. The equilibrium constant ( $K_a$ ) of the chemical reaction in eq 2 is defined via activities ( $a_i$ ) as

$$K_a = \prod_i a_i^{\vartheta_i} = \frac{(x_A^L \gamma_A^L)^{\vartheta_A} (x_B^L \gamma_B^L)^{\vartheta_B}}{(x_{AB}^S \gamma_{AB}^S)} \quad (9)$$

In the case where the melting temperature of the cocrystal is close to the eutectic temperature, the effect of the temperature on the melting enthalpy of the cocrystal can be neglected, and the equilibrium constant of the chemical reaction at different temperatures can be calculated using the Gibbs–Helmholtz equation

$$\ln K_a = \ln K_a^{\text{ref}} + \frac{\Delta h^{\text{ref}}}{R} \left( \frac{1}{T^{\text{ref}}} - \frac{1}{T} \right) \quad (10)$$

where  $T^{\text{ref}}$  is a reference temperature,  $K_a^{\text{ref}}$  is the equilibrium constant at  $T^{\text{ref}}$ , and  $\Delta h^{\text{ref}}$  is the melting enthalpy of the cocrystal at  $T^{\text{ref}}$ . In this work,  $T^{\text{ref}}$  was considered to be the maximum temperature at which the cocrystal is stable.  $T^{\text{ref}}$  and  $\Delta h^{\text{ref}}$  were measured using DSC. The equilibrium constant at  $T^{\text{ref}}$  was calculated as

$$K_a^{\text{ref}} = \frac{(x_A^{\text{ref}} \gamma_A^{\text{ref}})^{\vartheta_A} (x_B^{\text{ref}} \gamma_B^{\text{ref}})^{\vartheta_B}}{(x_{AB}^{\text{ref}} \gamma_{AB}^{\text{ref}})} \quad (11)$$

where  $x^{\text{ref}}$  and  $\gamma^{\text{ref}}$  are the mole fraction and the activity coefficient of the component at which  $T^{\text{ref}}$  and  $\Delta h^{\text{ref}}$  were measured, respectively.

### 3. RESULTS AND DISCUSSION

**3.1. Experimental Solid–Liquid Equilibria.** For the sake of simplicity, the discussion of the measured phase diagram is divided below into two parts: first, the thymol-rich region ( $x_{\text{thymol}}$  from 0.70 to 1.0) is considered, and then, the *L*-menthol-rich region ( $x_{\text{thymol}} \leq 0.67$ ).

Figure 1 shows the measured SLE data compared to those found in the literature along with the DSC curves for samples in the composition range  $x_{\text{thymol}}$  from 0.70 to 1.0. In this composition range, samples were prepared using two different methods: (i) slow crystallization or (ii) rapid crystallization. As shown in Figure 1, the liquidus temperatures of samples prepared by slow crystallization (yellow circles) or rapid crystallization (blue circles) are similar and are in good agreement with data found in the literature (black star and cross symbols). For samples prepared by slow or rapid crystallization with  $x_{\text{thymol}} < 0.80$ , the solidus temperatures do not change with composition. In contrast, in samples with  $x_{\text{thymol}} > 0.80$  prepared by rapid crystallization, the solidus temperatures depend strongly on the composition. As can be seen in Figure 1, the DSC curves of the sample with  $x_{\text{thymol}} = 0.88$  prepared by slow crystallization (yellow curve) and rapid crystallization (blue curve) are similar. However, the DSC curves of the sample with  $x_{\text{thymol}} < 0.80$  prepared by rapid crystallization and slow crystallization are different. The solidus temperature of the samples with  $x_{\text{thymol}} < 0.80$  prepared by rapid crystallization is lower than that of samples prepared by

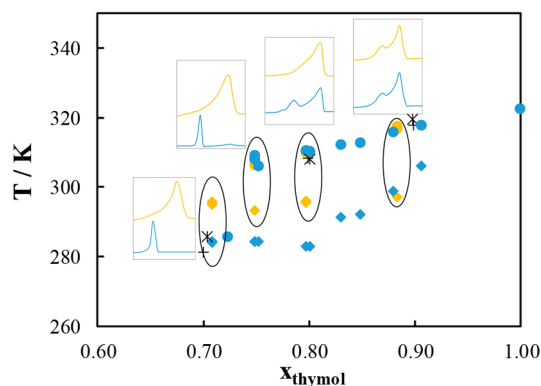


**Figure 1.** Solid–liquid equilibria of the *L*-menthol/thymol system measured in this work (filled symbols) for samples prepared using two different methods compared to literature data (cross symbols), with the corresponding differential scanning calorimetry curves for slow crystallization (yellow curves) and rapid crystallization (blue curves) samples. Literature data were taken from Abranches et al.<sup>24</sup> and Alhadid et al.<sup>19</sup> Legend: slow crystallization liquidus (yellow circles); rapid crystallization liquidus (blue circles); slow crystallization solidus (yellow diamonds); rapid crystallization solidus (blue diamond); Alhadid et al. (black star); Abranches et al. (black cross).

slow crystallization. It is worth mentioning that a glass transition at 217 K was observed for samples with  $x_{\text{thymol}} = 0.75$  and 0.70 prepared by slow crystallization (the DSC curves are shown in Figure S2 in the Supporting Information). This can be attributed to incomplete crystallization in the samples with a lower thymol content prepared by the slow crystallization method due to their high viscosity.<sup>26</sup>

To better understand the DSC curves and the phase diagram, powder XRD measurements are needed. For samples with  $x_{\text{thymol}} = 0.70$  prepared by slow crystallization, it was impossible to obtain a completely crystallized sample to perform powder XRD. Therefore, single-crystal XRD (SC-XRD) analysis was performed on crystals isolated from the liquid phase during storage at 277 K. The obtained crystal structure, shown in Figure S5 and Table S5 in the Supporting Information, corresponds to the reported crystal structure for thymol at room temperature, thus confirming that the solid obtained by slow crystallization consists of pure thymol crystals.<sup>32</sup> Therefore, the solidus and liquidus temperatures of slow crystallization samples correspond to thymol liquidus and solidus lines.

Powder XRD was performed on several mixtures of different compositions in the range  $x_{\text{thymol}} > 0.67$ . The samples were prepared by rapid crystallization. Figure 2 presents the SLE data and the powder XRD pattern at 253 K of the samples marked with circles in Figure 2A. As shown in Figure 2B, the powder XRD pattern of pure thymol (point a) matches that of the sample with  $x_{\text{thymol}} = 0.83$  (point b). The absence of the pure *L*-menthol solid phase indicates that it is dissolved in the solid phase of thymol, forming a solid solution ( $\alpha$  solid phase). Therefore, the solidus temperatures in Figure 2A for samples with  $x_{\text{thymol}} > 0.83$  correspond to the  $\alpha$  solid phase. When the thymol mole fraction is decreased further, a different solid phase appears at  $x_{\text{thymol}} = 0.80$  (point c). This solid phase does not correspond to pure *L*-menthol, as seen in Figure 2B (bottom black powder XRD pattern). On comparison of the powder XRD patterns at  $x_{\text{thymol}} = 0.75$  (point d) and 0.80 (point c), it becomes clear that the solid phase at  $x_{\text{thymol}} = 0.80$  is a mixture of the  $\alpha$  solid phase and the solid phase of the

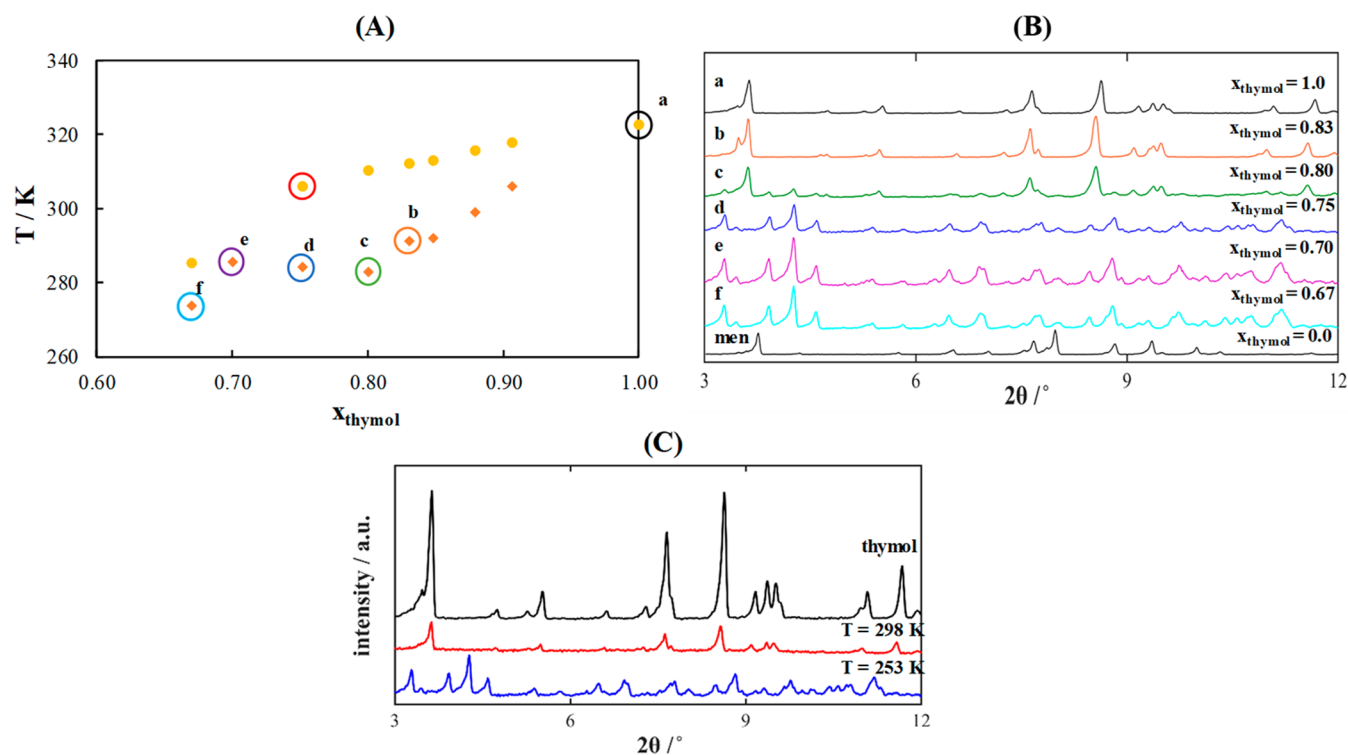


**Figure 2.** (A) Solid–liquid equilibria of the L-menthol/thymol system and (B) powder X-ray diffraction pattern obtained at 253 K for the solid formed by rapid crystallization. (C) Powder X-ray diffraction patterns of the sample with  $x_{\text{thymol}} = 0.75$  obtained at 253 and 298 K in comparison to that of pure thymol. The intensities are shifted for a better comparison.

sample  $x_{\text{thymol}} = 0.75$ . As can be seen in Figure 2B, the same powder XRD patterns are observed for samples with  $x_{\text{thymol}} = 0.75$ , 0.70, and 0.67. The absence of pure L-menthol indicates the formation of a second solid solution ( $\beta$  solid phase). The solidus temperatures in the range  $0.67 < x_{\text{thymol}} < 0.80$  correspond to the  $\beta$  solid phase.

Although the solid phases of samples with  $x_{\text{thymol}} = 0.75$ , 0.70, and 0.67 are similar, a liquidus peak is only observed at  $x_{\text{thymol}} = 0.75$ , as seen in Figure 1. To further investigate which solid phase the liquidus peak corresponds to, powder XRD was performed on samples with  $x_{\text{thymol}} = 0.75$  at 253 K (below the solidus temperature) and 298 K (above the solidus temperature). As seen in Figure 2C, the powder XRD pattern of the sample with  $x_{\text{thymol}} = 0.75$  at 298 K corresponds to pure thymol: i.e.,  $\alpha$  solid phase. This indicates that the solid formed in the composition range of  $0.67 < x_{\text{thymol}} < 0.80$  is unstable, and above the solidus temperature, it decomposes to an  $\alpha$  solid phase and a liquid phase. Indexing of powder data at  $x_{\text{thymol}} = 0.75$ , 0.70, and 0.67 showed that the number of molecules per unit cell is approximately 16 (results for  $x_{\text{thymol}} = 0.67$  are shown in Table S4 in the Supporting Information). The number matches a cocrystal with a stoichiometric ratio of 1:3 for L-menthol:thymol (1:3 cocrystal). As seen in Figure 2A, the cocrystal melts incongruently at around 285 K. Moreover, the  $\beta$  solid phase is a solid solution of L-menthol and the 1:3 cocrystal.

In the following, the second part of the phase diagram in the L-menthol-rich region, i.e.,  $x_{\text{thymol}} \leq 0.67$ , is discussed. As already mentioned, it was impossible to crystallize the L-menthol-rich samples by slow crystallization due to the high viscosity of the mixture close to its melting temperature.<sup>26</sup> Therefore, only the second preparation method, i.e., rapid crystallization, was considered. Figure 3 shows SLE data

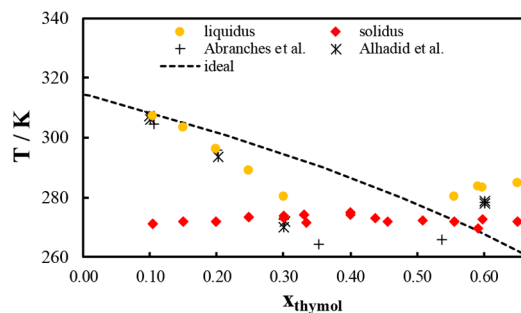


**Figure 3.** Solid–liquid equilibria data of L-menthol/thymol for samples prepared by rapid crystallization after quenching the liquid mixture at 193 K (filled symbols) compared to literature data (cross symbols). Literature data were taken from Abranches et al.<sup>24</sup> and Alhadid et al.<sup>19</sup>

measured in this work compared to published literature data. As can be noticed, a significant negative deviation from the ideal behavior (dashed line) is observed in the part of the phase diagram rich in L-menthol. The liquidus temperatures of the L-menthol liquidus line measured in this work are in good agreement with the data found in the literature.

As seen in Figure 3, in the region  $0.33 < x_{\text{thymol}} \leq 0.50$ , only solidus temperatures are observed. The DSC curves in this region are discussed in the following to understand the phase diagram better. Figure 4A shows the DSC curves of samples with different thymol mole fractions. The DSC curve of the sample with  $x_{\text{thymol}} = 0.67$  shows the liquidus peak of the 1:3 cocrystal and the solidus peak of the  $\beta$  solid phase as discussed above. As the mole fraction of thymol decreases, the solidus and liquidus peaks shift slightly to lower temperatures. At  $x_{\text{thymol}} = 0.50$ , only a solidus peak is observed. Although at

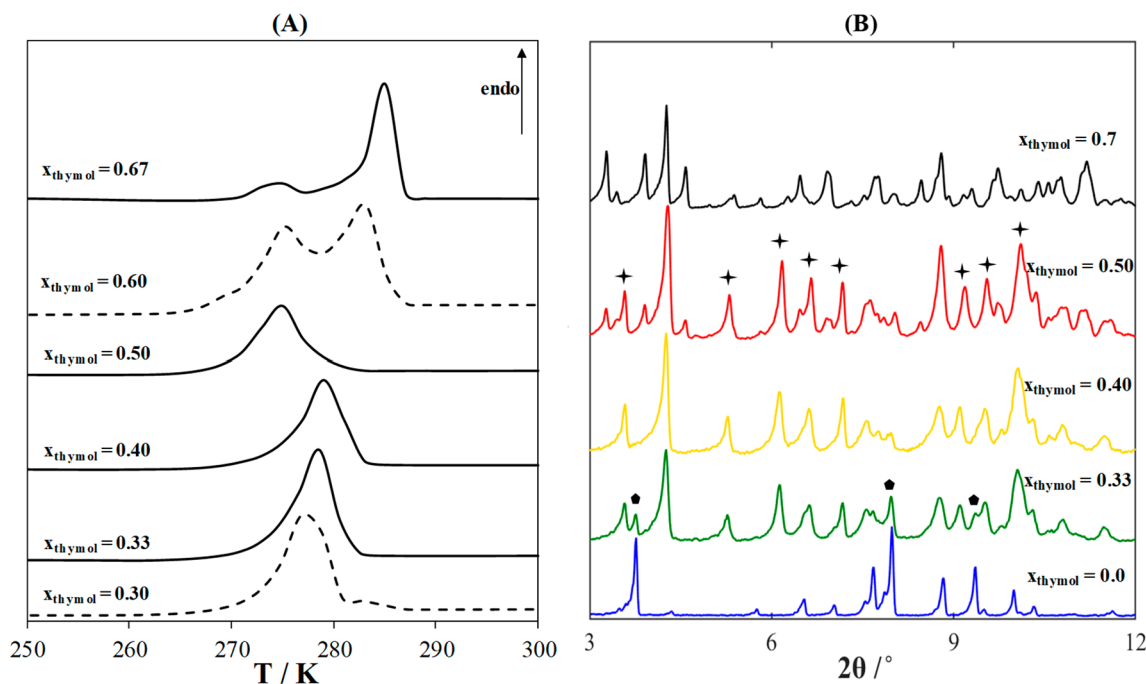


**Figure 4.** (A) DSC curves of samples with different thymol mole fractions. Powder X-ray diffraction was performed on samples shown by solid curves. (B) Powder X-ray diffraction patterns of samples with different mole fractions and of pure L-menthol.

**Table 1.** Melting Properties Used to Model the Solid–Liquid Equilibria of the L-Menthol:Thymol System

substance	$\Delta h_m$ (kJ mol <sup>-1</sup> )	$T_m$ (K)	$\Delta c_p = a + bT$ (J mol <sup>-1</sup> K <sup>-1</sup> )			
			a		b	
			liquid	solid	liquid	solid
L-menthol	13.74 <sup>36</sup>	314.6 <sup>36</sup>	-195.20 <sup>37</sup>	-68.0 <sup>37</sup>	1.795 <sup>37</sup>	1.092 <sup>37</sup>
thymol	20.64 <sup>19</sup>	322.7 <sup>19</sup>	147.50 <sup>38</sup>	12.739 <sup>38</sup>	0.571 <sup>38</sup>	0.767 <sup>38</sup>
3:2 cocrystal	44.90 ± 1.50 <sup>a,b</sup>	274.7 ± 0.10 <sup>a</sup>				
		$\Delta h^{\text{ref}}$ (kJ mol <sup>-1</sup> )			$T^{\text{ref}}$ (K)	
1:3 cocrystal		45.0 ± 0.20 <sup>a</sup>			285.7 ± 0.10 <sup>a</sup>	

<sup>a</sup>Measured in this work using DSC. <sup>b</sup>Uncertainties are the standard deviation of three samples.

$x_{\text{thymol}} = 0.40$  only a solidus peak is observed, it is different from that observed at  $x_{\text{thymol}} = 0.50$ . At a lower thymol mole fraction, a solidus peak with a similar onset temperature is observed with no obvious liquidus peaks. At  $x_{\text{thymol}} = 0.30$ , a small liquidus peak appears.

To help understand the different solidus peaks observed in different samples in Figure 4A, powder XRD was performed on samples showing only one solidus peak. Figure 4B shows the powder XRD patterns of mixtures with  $x_{\text{thymol}} = 0.67$ , 0.50, 0.40, and 0.33 and pure L-menthol. The powder XRD patterns of samples with  $x_{\text{thymol}} = 0.67$  (black curve) and  $x_{\text{thymol}} = 0.50$  (red curve) have several similar peaks. However, additional peaks (marked with crosses in Figure 4B) are observed for the sample with  $x_{\text{thymol}} = 0.50$ , indicating the presence of a different solid phase. By a comparison of the powder XRD pattern of the sample with  $x_{\text{thymol}} = 0.50$  (red curve) with those of  $x_{\text{thymol}} = 0.67$  (black curve) and  $x_{\text{thymol}} = 0.40$  (yellow curve), it can be seen that the solid phase of the sample with  $x_{\text{thymol}} = 0.50$  is a mixture of the  $\beta$  solid phase and the solid phase of the sample with  $x_{\text{thymol}} = 0.40$ . At  $x_{\text{thymol}} = 0.40$ , the  $\beta$  solid phase and pure L-menthol are not observed.

By a comparison of the powder XRD pattern of the samples with  $x_{\text{thymol}} = 0.40$  (yellow curve) and 0.33 (green curve),

additional peaks (marked with pentagons in Figure 4B) are observed in the sample with  $x_{\text{thymol}} = 0.33$ . As shown in Figure 4B, these additional peaks are related to pure L-menthol (blue curve). This implies that the sample with  $x_{\text{thymol}} = 0.33$  is a mixture of the solid phase observed at  $x_{\text{thymol}} = 0.40$  and pure L-menthol.

In conclusion, the formation of a second solid phase was observed in samples rich in L-menthol prepared by rapid crystallization after quenching the liquid mixture at 193 K. The XRD pattern of the sample with  $x_{\text{thymol}} = 0.40$  depicted the absence of a  $\beta$  solid phase and of pure L-menthol. According to the DSC curves shown in Figure 4A, it is highly probable that the second solid is a cocrystal with a stoichiometric ratio of 3:2 for L-menthol:thymol (3:2 cocrystal). An analysis of the powder XRD patterns and the DSC curves in Figure 4 shows that the solidus peaks at  $x_{\text{thymol}} = 0.50$  and 0.33 with onset temperatures of 271.6 and 272.7 K, respectively, represent the two eutectic points of the system.<sup>33–35</sup>

The melting properties of the 3:2 cocrystal and the reference temperature and enthalpy for the 1:3 cocrystal were measured by DSC. Liquid mixtures with molar ratios of 3:7 and 3:2 L-menthol:thymol were quenched at 193 K for 1 day and then annealed at 253 K for 1 week. Then, the samples were ground

using a mortar and pestle in a cold room at 253 K. The samples were then filled in DSC crucibles in triplicate. The melting temperatures and enthalpies of the 3:2 cocrystal were determined as the onset temperatures and the areas of the corresponding peaks, respectively. The reference temperature and enthalpy of the 1:3 cocrystal were determined as the peak maximum temperature and the area of the corresponding peak, respectively. The melting properties of the 3:2 cocrystal, pure thymol, and L-menthol, as well as the reference temperature and enthalpy of the 1:3 cocrystal, are presented in Table 1.

**3.2. Thermodynamic Modeling.** The measured SLE data were correlated to obtain the phase diagram of the mixture over the whole composition range. eq 2 was used to calculate the liquidus temperatures at different thymol mole fractions. The activity coefficients of components in the liquid solution were calculated using the NRTL model. The solid solution was considered either ideal or nonideal, and in the latter case, the two-suffix Margules equation was used to calculate the activity coefficients of components in the solid phase. Thymol liquidus temperatures (measured in the range  $x_{\text{thymol}} = 0.75\text{--}1.0$ ) and L-menthol liquidus temperatures (measured in the range  $x_{\text{thymol}} = 0.0\text{--}0.30$ ) were used to obtain the binary interaction parameters of the NRTL and two-suffix Margules equations.

Three approaches were applied on consideration of the heat capacity term, namely,  $\Delta c_p = 0$ , constant  $\Delta c_p$  calculated at the melting temperature of pure components, and linear temperature dependence of  $\Delta c_p$  using the coefficients in Table 1. The binary interaction parameters and RMSDs obtained using the three different approaches are shown in Table 2. Considering

**Table 2. Binary Interaction Parameters and Root-Mean-Square Deviation (RMSD) Obtained Using Different Approaches Considering the Heat Capacity Term**

	$g_{12} - g_{22}$ (kJ mol <sup>-1</sup> )	$g_{21} - g_{11}$ (kJ mol <sup>-1</sup> )	$A_{ij}^a$ (kJ mol <sup>-1</sup> )	RMSD (K)
$\Delta c_p = 0$	-4.7068	-2.4656	-3.9724	0.6
constant $\Delta c_p$	-4.6067	-1.5759	-2.3691	0.4
temperature-dependent $\Delta c_p$	-4.6548	-1.6443	-2.1716	2.7

or neglecting the heat capacity term leads to slightly different binary interaction parameters. The small difference between

the binary interaction parameters in each case can be attributed to the small value of  $T_m/T$  for the system. The obtained RMSD was smaller when a constant heat capacity term was considered. In contrast, the highest RMSD was obtained assuming a temperature-dependent  $\Delta c_p$ . Therefore, the constant heat capacity term was considered for further calculations.

The liquidus lines of thymol ( $x_{\text{thymol}} > 0.67$ ) and L-menthol ( $x_{\text{thymol}} < 0.33$ ) were calculated using eq 2 and their melting properties from Table 1. Because no solid solution region is formed in the L-menthol-rich region, the liquidus line can be calculated as a simple eutectic system: i.e.,  $x_i^S \gamma_i^S = 1$ . In contrast, calculating the thymol liquidus line should consider the composition and activity coefficients of components in the solid phase.

The liquidus and solidus lines in the middle range of composition ( $0.33 < x_{\text{thymol}} < 0.67$ ), corresponding to the crystallization of the two cocrystals, were calculated using eqs 8–11 and the measured melting properties from Table 1, and the activity coefficients in the liquid phase were calculated using eqs 3–5. The  $x_{\text{thymol}}^{\text{ref}}$  values for the 1:3 cocrystal and 3:2 cocrystal are 0.70 and 0.40, respectively. The  $K_a^{\text{ref}}$  values for the two cocrystals calculated using eq 11 are reported in Table S3 in the Supporting Information. In the case of 3:2 cocrystal liquidus lines,  $x_{\text{AB}}^S/\gamma_{\text{AB}}^S = 1$  because the 3:2 cocrystal is immiscible with L-menthol and the 1:3 cocrystal in the solid state. In contrast, the composition and the activity coefficients of the 1:3 cocrystal in the solid phase should be considered in calculating the liquidus and solidus lines. The  $\beta$  solid phase was assumed to be ideal to avoid fitting additional experimental data.

The results of the SLE modeling are discussed in the following to depict the SLE behavior of the system and attain the position of the eutectic points. Figure 5 shows the complete phase diagram of the L-menthol/thymol eutectic system modeled considering an ideal (Figure 5A) and nonideal (Figure 5B)  $\alpha$  solid solution. The points correspond to experimental data from the present study obtained by rapid crystallization, and the solid blue lines represent the results of the SLE modeling. As seen, the calculated liquidus lines of pure thymol and L-menthol are in good agreement with experimental data. Moreover, the SLE data in the middle

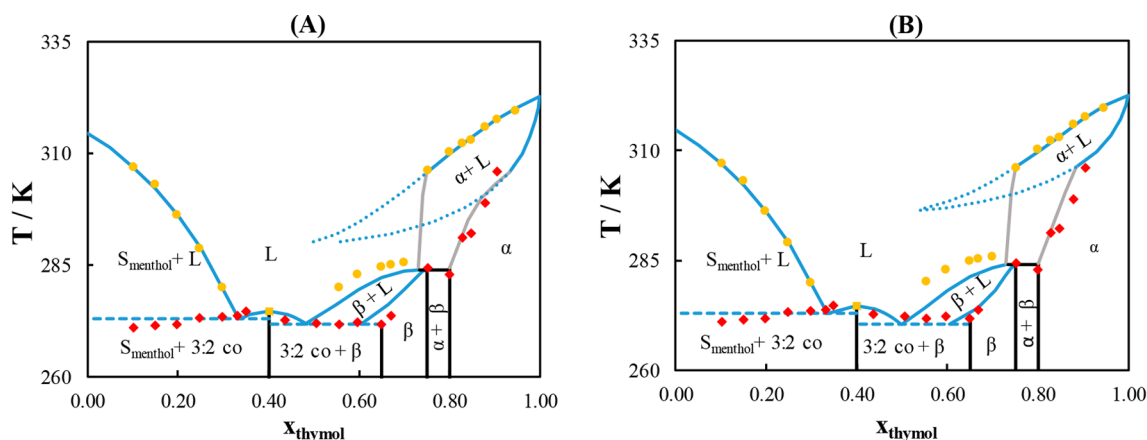


**Figure 5.** Solid–liquid equilibria data of the L-menthol/thymol mixture modeled using the NRTL equation considering cocrystal formation and (A) ideal solid solution and (B) nonideal solution. Legend: (yellow ●) liquidus temperatures; (red ◆) solidus temperatures; (yellow ■) 3:2 cocrystal melting temperature; (blue line) modeled lines; (blue dashed line) predicted eutectic temperature; (dotted blue line) extension of modeled thymol liquidus and solidus lines; (gray line) expected liquidus and solidus lines.

composition range corresponding to the liquidus lines of the two cocrystals as well as the two eutectic points of the system are well predicted. This further supports the stoichiometric ratio of the cocrystals and the presence of a solid solution region between L-menthol and the 1:3 cocrystal ( $\beta$  solid phase).<sup>31,39</sup> Additionally, this indicates the reliability of the NRTL equation to capture the nonideality in the liquid phase. The two eutectic temperatures estimated by SLE modeling are  $T_{e1}^{\text{cal}} = 271.7$  K,  $x_{\text{thymol},e1}^{\text{cal}} = 0.48$  and  $T_{e2}^{\text{cal}} = 273.1$  K,  $x_{\text{thymol},e2}^{\text{cal}} = 0.33$ .

The dotted blue lines are extrapolations of the thymol liquidus and solidus lines wherein the formation of the 1:3 cocrystal is not considered. These liquidus and solidus lines do not describe the system behavior in the middle range of composition, and their use would lead to an incorrect estimation of the eutectic point. The gray lines represent a possible course of the liquidus and solidus lines if cocrystal formation is considered. Obviously, because of the extreme change in the liquidus temperature within a very narrow range of system compositions corresponding to the gray lines, it is hardly possible to verify the course of the gray lines by measurements.

Due to the small solid solubility limit and similarity between thymol and L-menthol, it is reasonable to assume the solid solution ( $\alpha$  solid phase) as an ideal solution, i.e.,  $\gamma_{\text{thymol}}^{\text{S}} = 1$ . Nevertheless, the phase diagram was modeled by assuming ideal or nonideal solid phases. The obtained binary interaction parameters and RMSDs are shown in Table S3 in the Supporting Information. Although a significant difference was observed in the binary interaction parameters when the nonideality in the solid phase was considered, the RMSD was similar in each case. As seen in Figure 5, the predictions for the solidus lines of  $\alpha$  and  $\beta$  solid phases could not be improved by considering the nonideality in the solid phase.

#### 4. CONCLUSION

In this work, detailed SLE data of the L-menthol/thymol eutectic system were obtained using DSC. Different sample preparation methods were applied to comprehend the SLE behavior of the studied system. Due to kinetic limitations, the complete phase diagram of the system could only be obtained if samples were prepared by quenching the liquid mixture at 193 K, followed by annealing at 253 K. DSC measurements were coupled with XRD measurements to characterize the formed solid phases. The SLE diagram was found to have a character more complex than that previously reported.

The formations of an incongruently melting cocrystal of 1:3 menthol:thymol and a congruently melting cocrystal of 3:2 L-menthol:thymol were observed. The melting properties of the two cocrystals were measured in this work using DSC. Additionally, the presence of two solid solution regions was confirmed by DSC analysis and powder XRD measurements.

The obtained SLE data were modeled by considering the formation of the two cocrystals and the solid solution regions. The activity coefficients of the components in the solid and liquid phases were calculated by the two-suffix Margules and NRTL models, respectively. The data obtained on the liquidus and solidus lines of the pure components and the two cocrystals are in good agreement with the measured data. Further, the two eutectic points of the system are in good agreement with the solidus temperatures measured in the middle composition range. This supports the stoichiometric ratio of the cocrystals and the formation of the solid solution

regions and indicates the reliability of the NRTL equation to capture the nonideality in the liquid phase. The two eutectic points of the system obtained by SLE modeling are  $T_{e1}^{\text{cal}} = 271.7$  K,  $x_{\text{thymol},e1}^{\text{cal}} = 0.48$  and  $T_{e2}^{\text{cal}} = 273.1$  K,  $x_{\text{thymol},e2}^{\text{cal}} = 0.33$ .

In general, this study shows that immiscibility in the solid phase cannot always be assumed in measuring and modeling SLE in DES. The actual behavior of the system can be obtained from detailed studies of samples prepared by different methods. DSC measurements should be coupled with XRD when possible to acquire information regarding the solid phases formed. Thermodynamic modeling is a useful tool to generate and understand the solid–liquid phase diagram in the whole range of compositions and can provide the position of eutectic points that can often be difficult to obtain experimentally.

To determine the exact type of crystalline phases and their stoichiometry, more specific techniques such as 3D electron diffraction and SC-XRD are recommended. Nevertheless, the sample preparation methods required to form the cocrystals of the L-menthol/thymol system, i.e., quenching and annealing, are not suitable for obtaining samples for SC-XRD.

#### ■ ASSOCIATED CONTENT

##### SI Supporting Information

The Supporting Information is available free of charge at <https://pubs.acs.org/doi/10.1021/acs.cgd.1c00306>.

Solid–liquid equilibria data, models of binary interaction parameters, calculated eutectic point properties, and RMSD between experimental and calculated liquidus temperatures, DSC curves of samples with  $x_{\text{thymol}} = 0.7$  and 0.75 prepared by different methods, DSC curves of samples with a 1:1 molar ratio mixture prepared by different methods, DSC curves of samples with different thymol mole fractions, indexing of powder data of a sample with  $x_{\text{thymol}} = 0.67$ , and single-crystal X-ray diffraction data (PDF)

#### Accession Codes

CCDC 2069355 contains the supplementary crystallographic data for this paper. These data can be obtained free of charge via [www.ccdc.cam.ac.uk/data\\_request/cif](http://www.ccdc.cam.ac.uk/data_request/cif), or by emailing [data\\_request@ccdc.cam.ac.uk](mailto:data_request@ccdc.cam.ac.uk), or by contacting The Cambridge Crystallographic Data Centre, 12 Union Road, Cambridge CB2 1EZ, UK; fax: +44 1223 336033.

#### ■ AUTHOR INFORMATION

##### Corresponding Author

Ahmad Alhadid – *Biothermodynamics, TUM School of Life Sciences, Technical University of Munich (TUM), 85354 Freising, Germany*; [orcid.org/0000-0003-1443-1517](https://orcid.org/0000-0003-1443-1517); Email: [ahmad.alhadid@tum.de](mailto:ahmad.alhadid@tum.de)

##### Authors

Christian Jandl – *Catalysis Research Center, Department Chemie, Technical University of Munich (TUM), 85748 Garching bei München, Germany*

Liudmila Mokrushina – *Separation Science & Technology, Friedrich-Alexander-Universität Erlangen-Nürnberg (FAU), 91058 Erlangen, Germany*

Mirjana Minceva – *Biothermodynamics, TUM School of Life Sciences, Technical University of Munich (TUM), 85354 Freising, Germany*

Complete contact information is available at:

<https://pubs.acs.org/10.1021/acs.cgd.1c00306>

### Author Contributions

A.A.: conceptualization, methodology, formal analysis, and writing—original draft. C.J.: single-crystal and powder XRD experiments and writing—review and editing. L.M.: writing—review and editing. M.M.: writing—review, editing, and supervision.

### Notes

The authors declare no competing financial interest.

## REFERENCES

- (1) van Osch, D. J. G. P.; Dietz, C. H. J. T.; van Spronsen, J.; Kroon, M. C.; Gallucci, F.; van Sint Annaland, M.; Tuinier, R. A search for natural hydrophobic deep eutectic solvents based on natural components. *ACS Sustainable Chem. Eng.* **2019**, *7* (3), 2933–2942.
- (2) Perna, F. M.; Vitale, P.; Capriati, V. Deep eutectic solvents and their applications as green solvents. *Curr. Opin. Green Sustain. Chem.* **2020**, *21*, 27–33.
- (3) Emami, S.; Shayanfar, A. Deep eutectic solvents for pharmaceutical formulation and drug delivery applications. *Pharm. Dev. Technol.* **2020**, *25* (7), 779–796.
- (4) Álvarez, M. S.; Zhang, Y. Sketching neoteric solvents for boosting drugs bioavailability. *J. Controlled Release* **2019**, 311–312, 225–232.
- (5) Olives, A. I.; González-Ruiz, V.; Martín, M. A. Sustainable and eco-friendly alternatives for liquid Chromatographic Analysis. *ACS Sustainable Chem. Eng.* **2017**, *5* (7), 5618–5634.
- (6) Cai, T.; Qiu, H. Application of deep eutectic solvents in chromatography: A review. *TrAC, Trends Anal. Chem.* **2019**, *120*, 115623.
- (7) Hooshmand, S. E.; Afshari, R.; Ramón, D. J.; Varma, R. S. Deep eutectic solvents: cutting-edge applications in cross-coupling reactions. *Green Chem.* **2020**, *22* (12), 3668–3692.
- (8) González de Castilla, A.; Bittner, J. P.; Müller, S.; Jakobtorweihen, S.; Smirnova, I. Thermodynamic and transport properties modeling of deep eutectic solvents: A review on gE-models, equations of state, and molecular dynamics. *J. Chem. Eng. Data* **2020**, *65* (3), 943–967.
- (9) Alkhatib, I. I. I.; Bahamon, D.; Llovel, F.; Abu-Zahra, M. R. M.; Vega, L. F. Perspectives and guidelines on thermodynamic modelling of deep eutectic solvents. *J. Mol. Liq.* **2020**, *298*, 112183.
- (10) Smith, E. L.; Abbott, A. P.; Ryder, K. S. Deep eutectic solvents (DESs) and their applications. *Chem. Rev.* **2014**, *114* (21), 11060–11082.
- (11) Martins, M. A. R.; Pinho, S. P.; Coutinho, J. A. P. Insights into the nature of eutectic and deep eutectic mixtures. *J. Solution Chem.* **2019**, *48* (7), 962–982.
- (12) Alhadid, A.; Mokrushina, L.; Minceva, M. Modeling of solid-liquid equilibria in deep eutectic solvents: A parameter study. *Molecules* **2019**, *24* (12), 2334.
- (13) Wolbert, F.; Brandenbusch, C.; Sadowski, G. Selecting excipients forming therapeutic deep eutectic systems—A mechanistic approach. *Mol. Pharmaceutics* **2019**, *16* (7), 3091–3099.
- (14) Abdallah, M. M.; Müller, S.; González de Castilla, A.; Gurikov, P.; Matias, A. A.; Bronze, M. D.; Fernández, N. Physicochemical characterization and simulation of the solid-liquid equilibrium phase diagram of terpene-based eutectic solvent systems. *Molecules* **2021**, *26* (6), 1801.
- (15) Trache, D.; Khimeche, K.; Benelmir, R.; Dahmani, A. DSC measurement and prediction of phase diagrams for binary mixtures of energetic materials' stabilizers. *Thermochim. Acta* **2013**, *565*, 8–16.
- (16) Benziane, M.; Khimeche, K.; Dahmani, A.; Nezar, S.; Trache, D. Experimental determination and prediction of (solid + liquid) phase equilibria for binary mixtures of heavy alkanes and fatty acids methyl esters. *J. Therm. Anal. Calorim.* **2013**, *112* (1), 229–235.
- (17) Prausnitz, J. M.; Lichtenthaler, R. N.; Azevedo, E. G. d. *Molecular Thermodynamics of Fluid-Phase Equilibria*; Prentice-Hall: 1999.
- (18) Do, H. T.; Chua, Y. Z.; Habicht, J.; Klinksiek, M.; Hallermann, M.; Zaitsau, D.; Schick, C.; Held, C. Melting properties of peptides and their solubility in water. Part 1: dipeptides based on glycine or alanine. *RSC Adv.* **2019**, *9* (56), 32722–32734.
- (19) Alhadid, A.; Mokrushina, L.; Minceva, M. Formation of glassy phases and polymorphism in deep eutectic solvents. *J. Mol. Liq.* **2020**, *314*, 113667.
- (20) Corvis, Y.; Négrier, P.; Lazerges, M.; Massip, S.; Léger, J.-M.; Espeau, P. Lidocaine/l-menthol binary system: Cocrystallization versus solid-state immiscibility. *J. Phys. Chem. B* **2010**, *114* (16), 5420–5426.
- (21) Hamilton, V.; Andrusenko, I.; Potticary, J.; Hall, C.; Stenner, R.; Mugnaioli, E.; Lanza, A. E.; Gemmi, M.; Hall, S. R. Racemic conglomerate formation via crystallization of metaxalone from volatile deep eutectic solvents. *Cryst. Growth Des.* **2020**, *20* (7), 4731–4739.
- (22) Potticary, J.; Hall, C.; Hamilton, V.; McCabe, J. F.; Hall, S. R. Crystallization from volatile deep eutectic solvents. *Cryst. Growth Des.* **2020**, *20* (5), 2877–2884.
- (23) Hall, C. L.; Potticary, J.; Hamilton, V.; Gaisford, S.; Buanz, A.; Hall, S. R. Metastable crystalline phase formation in deep eutectic systems revealed by simultaneous synchrotron XRD and DSC. *Chem. Commun.* **2020**, *56*, 10726.
- (24) Abranches, D. O.; Martins, M. A. R.; Silva, L. P.; Schaeffer, N.; Pinho, S. P.; Coutinho, J. A. P. Phenolic hydrogen bond donors in the formation of non-ionic deep eutectic solvents: the quest for type V DES. *Chem. Commun.* **2019**, *55* (69), 10253–10256.
- (25) Martins, M. A. R.; Silva, L. P.; Schaeffer, N.; Abranches, D. O.; Maximo, G. J.; Pinho, S. P.; Coutinho, J. A. P. Greener terpene-terpene eutectic mixtures as hydrophobic solvents. *ACS Sustainable Chem. Eng.* **2019**, *7* (20), 17414–17423.
- (26) Alhadid, A.; Mokrushina, L.; Minceva, M. Influence of the molecular structure of constituents and liquid phase non-ideality on the viscosity of deep eutectic solvents. *Molecules* **2021**, *26* (14), 4208.
- (27) Rodríguez-Llorente, D.; Cañada-Barcala, A.; Álvarez-Torrellas, S.; Agueda, V. I.; García, J.; Larriba, M. A review of the use of eutectic solvents, terpenes and terpenoids in liquid-liquid extraction processes. *Processes* **2020**, *8* (10), 1220.
- (28) Lemaoui, T.; Darwish, A. S.; Attoui, A.; Abu Hatab, F.; Hammoudi, N. E. H.; Benguerba, Y.; Vega, L. F.; Alnashef, I. M. Predicting the density and viscosity of hydrophobic eutectic solvents: towards the development of sustainable solvents. *Green Chem.* **2020**, *22*, 8511.
- (29) Domanska, U.; Groves, F. R.; McLaughlin, E. Solid-liquid phase equilibria of binary and ternary mixtures of benzene and polynuclear aromatic compounds. *J. Chem. Eng. Data* **1993**, *38* (1), 88–94.
- (30) Lange, L.; Sadowski, G. Polymorphs, hydrates, cocrystals, and cocrystal hydrates: Thermodynamic modeling of theophylline systems. *Cryst. Growth Des.* **2016**, *16* (8), 4439–4449.
- (31) Lange, L.; Sadowski, G. Thermodynamic modeling for efficient cocrystal formation. *Cryst. Growth Des.* **2015**, *15* (9), 4406–4416.
- (32) Thozet, A.; Perrin, M. Structure of 2-isopropyl-5-methylphenol (thymol). *Acta Crystallogr., Sect. B: Struct. Crystallogr. Cryst. Chem.* **1980**, *36* (6), 1444–1447.
- (33) Chelouche, S.; Trache, D.; Pinho, S. P.; Khimeche, K. Experimental and modeling studies of binary organic eutectic systems to be used as stabilizers for nitrate esters-based energetic materials. *Fluid Phase Equilib.* **2019**, *498*, 104–115.
- (34) Chelouche, S.; Trache, D.; Neves, C. M. S. S.; Pinho, S. P.; Khimeche, K.; Benziane, M. Solid + liquid equilibria and molecular structure studies of binary mixtures for nitrate ester's stabilizers: Measurement and modeling. *Thermochim. Acta* **2018**, *666*, 197–207.
- (35) Chelouche, S.; Trache, D.; Pinho, S. P.; Khimeche, K.; Mezroua, A.; Benziane, M. Solid-liquid phase equilibria, molecular interaction and microstructural studies on (N-(2-ethanol)-p-nitroaniline + N-(2-acetoxyethyl)-p-nitroaniline) binary mixtures. *Int. J. Thermophys.* **2018**, *39* (11), 129.

- (36) Alhadid, A.; Mokrushina, L.; Minceva, M. Design of deep eutectic systems: A simple approach for preselecting eutectic mixture constituents. *Molecules* **2020**, *25* (5), 1077.
- (37) Corvis, Y.; Espeau, P. Interpretation of the global heat of melting in eutectic binary systems. *Thermochim. Acta* **2018**, *664*, 91–99.
- (38) Zhu, P.; Chen, Y.; Fang, J.; Wang, Z.; Xie, C.; Hou, B.; Chen, W.; Xu, F. Solubility and solution thermodynamics of thymol in six pure organic solvents. *J. Chem. Thermodyn.* **2016**, *92*, 198–206.
- (39) Tumakaka, F.; Prikhodko, I. V.; Sadowski, G. Modeling of solid-liquid equilibria for systems with solid-complex phase formation. *Fluid Phase Equilib.* **2007**, *260* (1), 98–104.

## Supporting Information

### Experimental Investigation and Modeling of Cocrystal Formation in L-Menthol/Thymol Eutectic System

Ahmad Alhadid\*<sup>1</sup>, Christian Jandl<sup>2</sup>, Liudmila Mokrushina<sup>3</sup>, and Mirjana Minceva<sup>1</sup>

<sup>1</sup> Biothermodynamics, TUM School of Life Sciences, Technical University of Munich (TUM), Germany

<sup>2</sup> Catalysis Research Center, Department Chemie, Technical University of Munich (TUM), Germany

<sup>3</sup> Separation Science & Technology, Friedrich-Alexander-Universität Erlangen-Nürnberg (FAU), Germany

\*Corresponding author e-mail: [ahmad.alhadid@tum.de](mailto:ahmad.alhadid@tum.de)

---

Table S1. Solid–liquid equilibria data of L-menthol/thymol mixture for samples prepared by rapid crystallization.

$x_{\text{thymol}}$	$T_e / \text{K}$	$T / \text{K}$
0.94	–	319.6
0.91	306.1	317.7
0.88	299.0	315.8
0.85	292.1	312.9
0.83	291.2	312.2
0.80	282.9	310.2
0.75	284.4	306.1
0.70	285.7	–
0.67	272.7	285.2
0.65	271.7	284.7
0.60	272.3	282.9
0.59	272.3	282.9
0.55	271.7	280.1
0.51	272.1	–
0.50	271.6	–
0.46	271.2	–
0.44	272.7	–
0.40	274.8	–
0.35	274.6	–

---



$x_{\text{thymol}}$	$T_e / \text{K}$	$T / \text{K}$
0.33	273.7	–
0.32	273.3	–
0.30	273.5	280.0
0.25	273.1	288.9
0.20	271.7	296.2
0.15	271.5	303.1
0.10	271.1	307.0

Table S2. Solid–liquid equilibria data of L-menthol/thymol mixture for samples prepared by slow crystallization.

$x_{\text{thymol}}$	$T_e / \text{K}$	$T / \text{K}$
0.88	297.2	317.4
0.80	295.7	309.9
0.75	293.2	307.5
0.70	295.4	–

Table S3. Binary interaction parameters, calculated eutectic point properties, and root-mean-square deviation (RMSD) between experimental and calculated liquidus temperatures obtained in this work compared to data reported in the literature.

	Non-ideal solid	Ideal solid	Alhadid et al. <sup>1</sup>
$(g_{12} - g_{22}) / \text{kJ mol}^{-1}$	-4.6067	-3.8712	-4.3333
$(g_{21} - g_{11}) / \text{kJ mol}^{-1}$	-1.5759	-1.7768	-4.0648
$A_{ij}^{\alpha} / \text{kJ mol}^{-1}$	-2.3691	0	-
$K_a^{ref}$ (1:3 cocrystal)	$8.60 \times 10^{-3}$	$1.27 \times 10^{-2}$	-
$K_a^{ref}$ (3:2 cocrystal)	$7.06 \times 10^{-4}$	$1.10 \times 10^{-3}$	-
$x_e$	0.50 0.34	0.48 0.33	0.43
$T_e / \text{K}$	270.4 272.9	271.7 273.0	241.5
RMSD / K	0.4	0.5	3.5

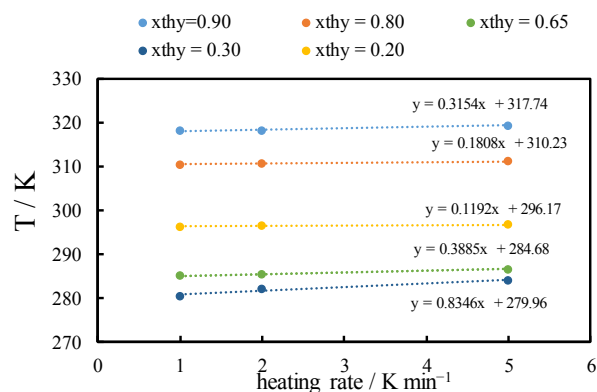


Figure S1. Determination of the liquidus temperature by extrapolating the peak maximum to zero heating rate.

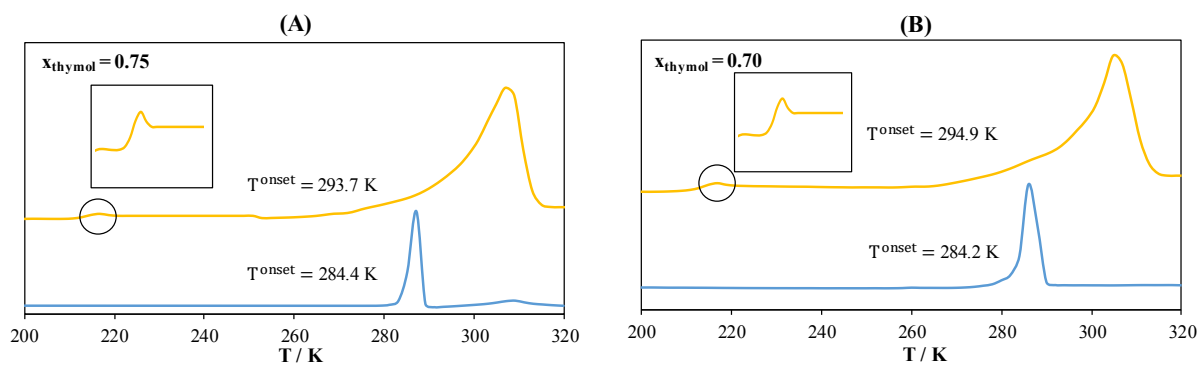


Figure S2. Differential scanning calorimetry curves of samples with (a)  $x_{\text{thymol}} = 0.75$  and (b)  $x_{\text{thymol}} = 0.70$  prepared by slow crystallization (yellow curve) and rapid crystallization (blue curve). The circles mark the glass transition temperature. Curves are shifted and scaled for clarity.

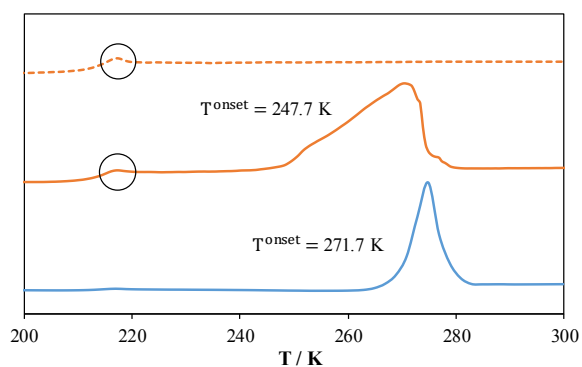


Figure S3. Differential scanning calorimetry curve of samples with 1:1 L-menthol:thymol molar ratio obtained by different conditions. Curves are shifted and scaled for clarity. Legend: (orange dashed line) *in-situ* crystallized at the DSC; (orange line) samples stored at 193 K for more than one month; (blue line) samples quenched at 193 K and annealed at 253 K.

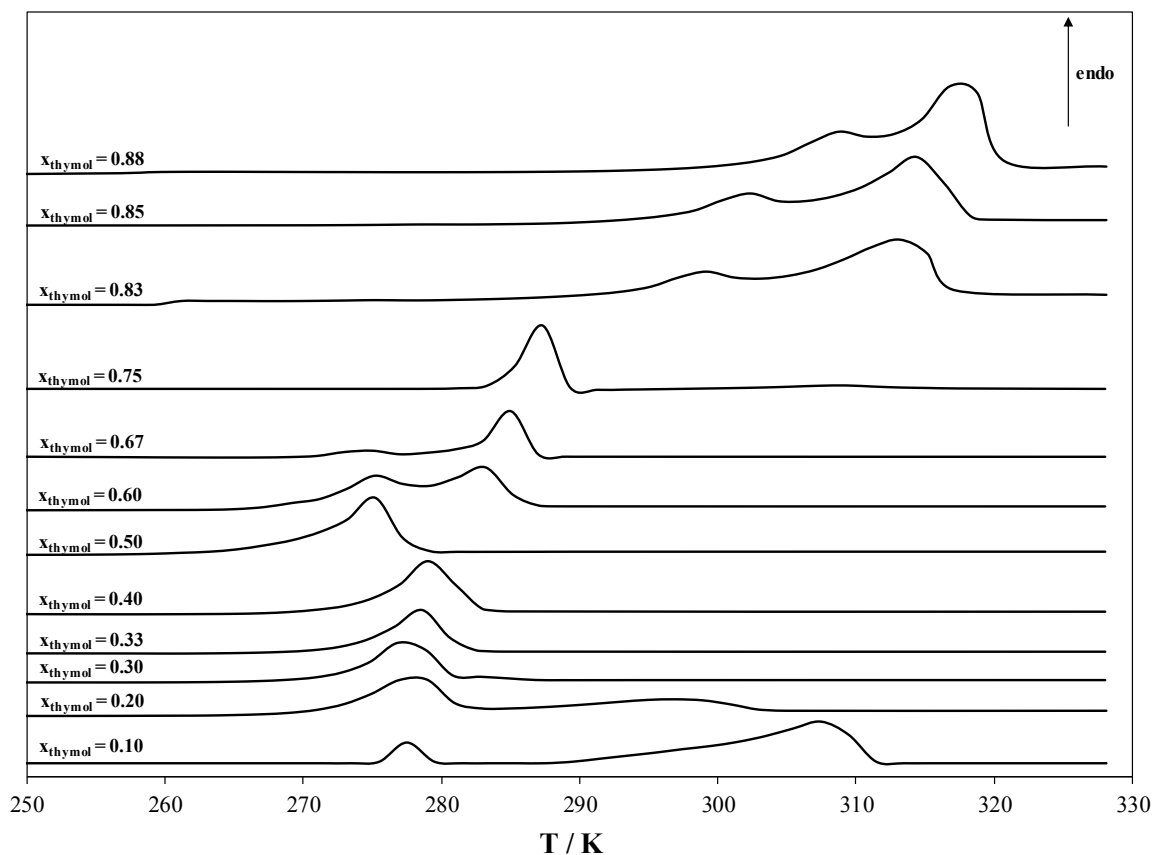


Figure S4. Differential scanning calorimetry curves of samples with different thymol mole fractions.

Table S4. Cell parameters from indexing and Pawley refinement of a powder X-ray diffraction pattern of a sample with  $x_{\text{thymol}} = 0.67$

Monoclinic P	
a	11.9451 Å
b	19.1600 Å
c	16.7199 Å
$\beta$	99.428°
V	3774.96 Å <sup>3</sup>
Z	ca. 16

### X-ray Crystallographic Details

Data were collected on a Bruker D8 Venture single crystal x-ray diffractometer equipped with a CPAD detector (Bruker Photon II), an IMS micro source with MoK $\alpha$  radiation ( $\lambda = 0.71073$  Å) and a Helios optic using the APEX3 software package.<sup>2</sup> Measurements were performed on single crystals coated with perfluorinated ether. The crystals were fixed on top of a Kapton micro sampler and frozen under a stream of cold nitrogen. A matrix scan was used to determine the initial lattice parameters. Reflections were corrected for Lorentz and polarisation effects, scan speed, and background using SAINT.<sup>3</sup> Absorption correction, including odd and even ordered spherical harmonics, was performed using SADABS.<sup>3</sup> Space

group assignments were based upon systematic absences, E statistics, and successful refinement of the structures. The structures were solved using SHELXT with the aid of successive difference Fourier maps and were refined against all data using SHELXL in conjunction with SHELXLE.<sup>4,5,6</sup> Hydrogen atoms except on heteroatoms were calculated in ideal positions as follows: Methyl H atoms were refined as part of rigid rotating groups, with a C–H distance of 0.98 Å and  $U_{\text{iso}}(\text{H}) = 1.5 \cdot U_{\text{eq}}(\text{C})$ . Non-methyl H atoms were placed in calculated positions and refined using a riding model, with methylene, aromatic, and other C–H distances of 0.99 Å, 0.95 Å and 1.00 Å, respectively, and  $U_{\text{iso}}(\text{H}) = 1.2 \cdot U_{\text{eq}}(\text{C})$ . Non-hydrogen atoms were refined with anisotropic displacement parameters. Full-matrix least-squares refinements were carried out by minimizing  $\sum w(F_o^2 - F_c^2)^2$  with the SHELXL weighting scheme.<sup>4</sup> Neutral atom scattering factors for all atoms and anomalous dispersion corrections for the non-hydrogen atoms were taken from *International Tables for Crystallography*.<sup>7</sup> Images of the crystal structure were generated with PLATON.<sup>8</sup> CCDC 2069355 contains the supplementary crystallographic data for this paper. These data are provided free of charge by The Cambridge Crystallographic Data Centre.

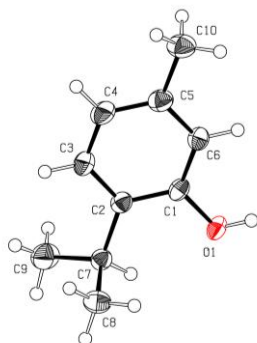


Figure S5. Molecular structure of thymol in the solid state at 100 K as obtained from single-crystal x-ray diffraction data with ellipsoids at the 50% probability level (disorder of the C10-methyl group is omitted). The structure is analogous to a previously published structure at room temperature.<sup>9</sup>

Table S5. Structure and refinement data

Deposition number	CCDC 2069355	
Chemical formula	$\text{C}_{10}\text{H}_{14}\text{O}$	
Crystal description	colourless fragment	
Formula weight	150.21	
Temperature	$100 \pm 2$ K	
Wavelength	0.71073 Å	
Crystal size	$0.442 \times 0.528 \times 0.547$ mm	
Crystal system	trigonal	
Space group	R $\bar{3}$	
Unit cell dimensions	$a = 14.4552 \pm 4$ Å	$a = 90^\circ$
	$b = 14.4552 \pm 4$ Å	$b = 90^\circ$
	$c = 23.0330 \pm 10$ Å	$c = 120^\circ$
Volume	$4168.0 \pm 3$ Å <sup>3</sup>	
Z	18	
Density (calculated)	$1.077$ g cm <sup>-3</sup>	

Absorption coefficient	0.067 mm <sup>-1</sup>
F(000)	1476
θ range	2.4–26.7°
Absorption correction	multi-scan (SADABS)
T <sub>min</sub> , T <sub>max</sub>	0.712, 0.745
Reflections measured	41260
Independent reflections	1971
Reflections I > 2σ(I)	1909
R <sub>int</sub>	0.021
Refinement method	full matrix least squares on F <sup>2</sup>
Data, restraints, parameters	1971, 0, 108
R1 [I > 2σ(I)]	0.045
wR2 (all data)	0.112
Goodness of fit	1.06
Weighting scheme	$W = 1/[\Sigma^2(F_o^2) + (0.0449P)^2 + 5.2473P]$ where $P = (F_o^2 + 2F_c^2)/3$
Largest difference peak and hole	0.27 and -0.21 eÅ <sup>-3</sup>

## References

1. Alhadid, A.; Mokrushina, L.; Minceva, M., *J. Mol. Liq.* **2020**, *314*, 113667.
2. *APEX suite of crystallographic software*, APEX 3, Version 2019-1.0, Bruker AXS Inc., Madison, Wisconsin, USA, 2016.
3. *SAINTE*, Version 8.40A and *SADABS*, Version 2016/2, Bruker AXS Inc., Madison, Wisconsin, USA, 2016/2019.
4. Sheldrick, G. M. *Acta Crystallogr. Sect. A* **2015**, *71*, 3–8.
5. Sheldrick, G. M. *Acta Crystallogr. Sect. C* **2015**, *71*, 3–8.
6. Hübschle, C. B.; Sheldrick, G. M.; Dittrich, B. *J. Appl. Cryst.* **2011**, *44*, 1281–1284.
7. *International Tables for Crystallography, Vol. C* (Ed.: A. J. Wilson), Kluwer Academic Publishers, Dordrecht, The Netherlands, **1992**, Tables 6.1.1.4 (pp. 500–502), 4.2.6.8 (pp. 219–222), and 4.2.4.2 (pp. 193–199).
8. Spek, A. L. *Acta Crystallogr. Sect. D* **2009**, *65*, 148–155.
9. Thozet, A.; Perrin, M. *Acta Crystallogr. Sect. B* **1980**, *36*, 1444–1447. Deposition number: CCDC 1180630.

### 3.5 Paper V

#### Cocrystal Formation in Choline Chloride Deep Eutectic Solvents

**A. Alhadid, C. Jandl, L. Mokrushina, and M. Minceva**, *Cryst. Growth Des.*, **2022**, 22, 3, 1933–1942.

Author contribution: The thesis author conceptualized the paper's idea, performed the investigations and formal analysis (excluding powder and SC-XRD), interpreted the results, and wrote the manuscript.

Summary: ChCl is one of the most studied HBA in the DES literature. Because ChCl is thermally unstable, its melting properties are unavailable. As shown in Paper I, modeling of the nonideality of thermally unstable salts is implausible. The objectives of Paper V are to highlight cocrystal formation in ChCl-based DES and examine the melting properties and nonideality of ChCl. ChCl was mixed with two cofomers (dihydroxybenzenes) to form ChCl-based cocrystals. DSC and powder XRD analyses were employed to obtain the SLE data of the two systems. The investigations revealed the formation of two cocrystals in ChCl/catechol and one cocrystal in ChCl/hydroquinone. The cocrystals' stoichiometry and structure were obtained by the SC-XRD technique. It was concluded that not all ChCl-based eutectic systems could be assumed to be of the simple eutectic type, and extensive experimental investigations are needed to detect cocrystal formation.

Next, the SLE data of the cofomers and cocrystals liquidus lines were used to obtain the NRTL binary interaction parameters. The activity coefficients of ChCl in the liquid phase and the SLE data of its liquidus line were used to assess the melting properties of ChCl. Surprisingly, no liquidus temperature could be observed in the DSC curves of the samples in the ChCl-rich region above the solid–solid transition temperature up to the decomposition temperature of the mixture. The presence of the ChCl solid phase in the samples above the solid–solid transition temperature was confirmed by variable temperature XRD (VT-XRD). Without liquidus data for pure ChCl above the solid–solid transition temperature, no distinctive melting properties could be determined for ChCl. However, the estimated ChCl melting properties estimated in the literature are not within the range of possible values estimated in this work, indicating that those found in the literature could be unreasonable.

### 3.5 Paper V

Paper V confirmed that the unique character of ChCl to form nonideal eutectic mixtures with a large depression at the eutectic point is its small melting entropy. The small melting entropy of ChCl is attributed to the symmetrical and disordered crystal structure of the high-temperature polymorph of ChCl. Therefore, Paper V provided evidence for the conclusions drawn in Paper I that DES are nonideal eutectic mixtures formed by mixing constituents with low melting enthalpy and entropy values.



### 3.5 Paper V

Reprinted with permission from Alhadid et al., *Cryst. Growth Des.*, **2022**, *21*, 6083-6091. DOI: 10.1021/acs.cgd.1c01477. Copyright 2022 American Chemical Society.

Article full text: <http://pubs.acs.org/articlesonrequest/AOR-UVXRX3M2KU4DDTIVN2MA>

## Cocrystal Formation in Choline Chloride Deep Eutectic Solvents

Ahmad Alhadid, Christian Jandl, Liudmila Mokrushina, and Mirjana Minceva\*

Cite This: *Cryst. Growth Des.* 2022, 22, 1933–1942

Read Online

ACCESS |



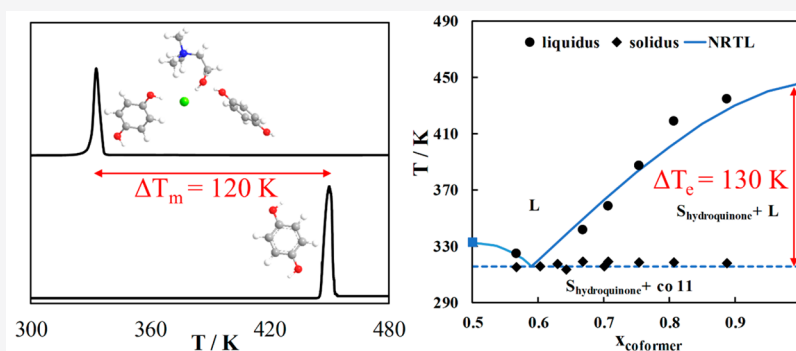
Metrics &amp; More



Article Recommendations



Supporting Information



**ABSTRACT:** Deep eutectic solvents (DESs) are eutectic mixtures representing a new generation of tunable solvents. The majority of the DESs studied in the literature contains choline chloride (ChCl). The knowledge of solid–liquid equilibria (SLE) in the DESs is crucial for the identification of the composition range in which the mixture is liquid below process-relevant temperatures. ChCl-based DES phase diagrams are usually assumed to be simple eutectics with no cocrystal formation. However, the simple eutectic assumption is questionable without a detailed characterization of the crystallized solid phases. This study investigates the formation of cocrystals in ChCl-based DESs. The SLE in ChCl/catechol and ChCl/hydroquinone eutectic mixtures were studied using powder X-ray diffraction (XRD) and differential scanning calorimetry (DSC). The research demonstrated the formation of two cocrystals in the ChCl/catechol system and one cocrystal in the ChCl/hydroquinone system; the crystal structures were obtained using single-crystal XRD. The solid–solid transition of ChCl in the mixture was observed by DSC and variable-temperature XRD. The SLE data were correlated using the nonrandom two-liquid (NRTL) model and the melting properties of the pure components and cocrystals. Modeling the SLE data enabled one to evaluate the melting properties of ChCl estimated in the literature.

## 1. INTRODUCTION

Recently, eutectic mixtures have been used to form tunable and green solvents, often called deep eutectic solvents (DESs).<sup>1,2</sup> DESs are prepared by mixing hydrogen bond acceptors (HBAs) with hydrogen bond donors (HBDs).<sup>3</sup> The eutectic temperature of the mixture is considerably lower than the melting temperature of the pure constituents. The reasons for the low eutectic temperature of the DESs are the negative deviation from the ideality in the liquid phase and the low melting enthalpy value of the constituents.<sup>4</sup>

A prerequisite for using a DES as a solvent is that the melting temperature of the mixture is below the process temperature. The melting temperature of the mixture at any composition is obtained from the solid–liquid equilibria (SLE) phase diagram.<sup>4</sup> Hence, the knowledge of SLE is essential for the selection of the DES constituents and their molar ratios. Recently, the SLE phase diagram of numerous binary eutectic mixtures has become available in the literature to aid in the design of the DES for a certain application.<sup>5–12</sup> However, experimental determination of SLE data over the entire composition range is not a straightforward task. The most commonly used approach for the determination of the complete SLE phase diagram is to measure

the melting temperature for a few mixture compositions and then correlate the SLE data assuming that the system is of the simple eutectic type, i.e., the components crystallize as pure solids.<sup>13,14</sup> However, the simple eutectic assumption should be verified. In various eutectic systems, polymorphism, the formation of metastable solid phases, and cocrystal formation have been identified by the characterization of the crystallized solid phases.<sup>15–19</sup> Therefore, the crystallized solid phases should be analyzed to determine and model the SLE phase diagram properly.

Choline chloride (ChCl) was the first HBA used in DESs and the one present in over half of the DESs reported in the literature.<sup>1,20–23</sup> The distinctive character of ChCl in forming DESs with a considerably low eutectic temperature has not been well-explored so far. ChCl has been shown to undergo a solid–

Received: December 17, 2021

Revised: January 24, 2022

Published: February 8, 2022



solid transition at around 352 K.<sup>24</sup> However, the solid–solid transition of ChCl in its eutectic mixtures was indirectly observed only in a few cases as the change in the slope of the ChCl liquidus line.<sup>10,25</sup> Accordingly, it was argued that the ChCl low-temperature polymorph is stabilized, and thus, the solid–solid transition cannot be observed in most ChCl-based DESs, relying only on the measurements of the liquidus temperature of ChCl.<sup>9</sup> However, it is hardly probable that the liquid phase could stabilize ChCl low- or high-temperature polymorphs because the liquid phase is only in contact with the surface but not with the bulk of the solid ChCl. Therefore, it is required to directly examine the solid–solid transition of ChCl in ChCl-based DESs by analysis methods such as X-ray diffraction (XRD).

The formation of cocrystals in ChCl-based DESs has not been thoroughly disclosed.<sup>26–30</sup> Various HBDs used in ChCl-based DESs, such as urea, thiourea, catechol, and hydroquinone, are known to be cocrystal formers.<sup>31</sup> However, without systematical characterization of the crystallized solid phases in ChCl-based DES, the formation of cocrystals can be ruled out. This study presents a detailed investigation of SLE in two ChCl-based DESs, namely, ChCl/catechol and ChCl/hydroquinone, with an extensive analysis of the crystallized solid phases. The crystallized solids were characterized by performing powder XRD on samples of different compositions. The SLE data of the two eutectic systems were measured using differential scanning calorimetry (DSC) over the entire composition range. The obtained SLE data were modeled using the nonrandom two-liquid (NRTL) equation.

## 2. METHODS

**2.1. Sample Preparation.** Figure 1 shows the molecular structure of the pure substances. Before the eutectic mixtures were prepared,

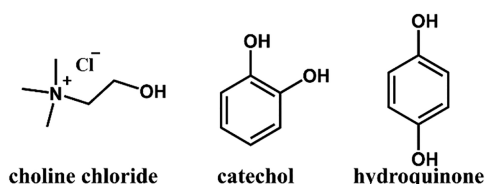


Figure 1. Molecular structure of the studied pure substances.

ChCl (Alfa Aesar, <98%) was dried overnight under vacuum at 343 K, and its water content after drying was measured using a Karl Fischer Coulometer (Hanna Instrument, USA) and found to be <1000 ppm. The eutectic mixtures were prepared by mixing ChCl with catechol (Acros Organics, <99%, water content ~ 500 ppm) or hydroquinone (Merck, <98%, water content ~ 700 ppm) in different ratios. The pure components were weighed (Sartorius, Germany, precision  $1 \times 10^{-4}$  g) and introduced into glass vials. The vials were directly sealed, and the mixture was gently heated under continuous stirring until a clear liquid was formed. To aid sample crystallization, the liquid solutions were quenched at 193 K and annealed for 1 day at 253 K. Using a mortar and pestle, the solid was ground to a fine powder inside a cold room at 253 K. The water content of the powder was measured after grinding and found to be less than 500 ppm.

**2.2. XRD.** Powder XRD was used to characterize the crystalline solid phases across the entire composition range. The powder XRD samples were prepared by grinding the powder at 253 K and directly adding it into a glass capillary (Hilgenberg, Germany) with a 1.0 mm diameter. The powder XRD experiments were performed using a Stadi P diffractometer (Stoe & Cie, Germany) with Debye–Scherrer geometry equipped with a Mo fine-focus sealed tube, curved Ge monochromator selecting for  $K\alpha_1$  radiation ( $\lambda = 0.70930 \text{ \AA}$ ), and a Mythen2 R 1K detector (Dectris, Switzerland). The data were collected with a step size

of  $0.015^\circ 2\theta$  per data point. Due to ChCl radiation sensitivity, the measurements were performed at 253 K to avoid the decomposition of ChCl. A cryostream (Oxford 800 series, UK) was used to perform measurements at various temperatures.

The cocrystal's stoichiometry and structure were determined by single-crystal XRD (SC-XRD) analysis. Single crystals with sufficient size and quality for SC-XRD were obtained by dissolving the cocrystal powder in acetonitrile at 318 K in a 1:1 mass ratio, and the solution was stored at 253 K for around 1 week until suitable crystals appeared. Details regarding the SC-XRD method can be found in the Supporting Information.

**2.3. DSC.** DSC analysis was used to get the SLE data for the two eutectic systems. Before measurement, the DSC instrument (NETZSCH DSC 200 F3, Germany) was calibrated using six calibration standards, namely, adamantane, bismuth, cesium chloride, indium, tin, and zinc, at a heating rate of  $5 \text{ K min}^{-1}$ . Measurements were performed in an inert environment using nitrogen with a flow rate of  $150 \text{ mL min}^{-1}$ . The standard uncertainties of the temperature and sensitivity measurements were 0.3 K and 0.4%, respectively.

After filling the DSC crucible pans with the ground powder in triplicates, they were hermetically sealed. Before adding the sample, the DSC chamber was precooled to 253 K. Then, a heating run with a heating rate of  $5 \text{ K min}^{-1}$  was conducted until 373 K for ChCl/catechol and 443 K for ChCl/hydroquinone systems. The solidus phase transition and the liquidus temperatures were determined as the onset and peak maximum temperatures. DSC experiments were performed in triplicate for each mixture composition being studied. The average standard deviation of the obtained liquidus and solidus temperatures was found to be 0.5 K.

**2.4. Thermodynamic Modeling.** The SLE data obtained from the DSC analysis were modeled to obtain the complete solid–liquid phase diagram and the eutectic points. The pure constituent liquidus line was modeled using the following equation<sup>32</sup>

$$\ln x_i^L \gamma_i^L = -\frac{\Delta h_{m,i}}{RT} \left( 1 - \frac{T}{T_{m,i}} \right) \quad (1)$$

where  $x_i^L$  and  $\gamma_i^L$  are the mole fraction and the activity coefficient of the component  $i$  in the liquid phase,  $\Delta h_{m,i}$  and  $T_{m,i}$  are the melting enthalpy and temperature of pure component  $i$ ,  $R$  is the gas constant, and  $T$  is the liquidus temperature. Since ChCl undergoes a solid–solid transition,<sup>24</sup> the ChCl liquidus line below the solid–solid transition temperature was calculated as follows<sup>33</sup>

$$\ln x_i^L \gamma_i^L = -\frac{\Delta h_{m,i}}{RT} \left( 1 - \frac{T}{T_{m,i}} \right) - \frac{\Delta h_{tr,i}}{RT} \left( 1 - \frac{T}{T_{tr,i}} \right) \quad (2)$$

where  $\Delta h_{tr,i}$  and  $T_{tr,i}$  are the solid–solid transition enthalpy and temperature, respectively. The formation of a cocrystal containing component A with a stoichiometric coefficient of  $\vartheta_A$  and component B with a stoichiometric coefficient of  $\vartheta_B$  in a binary eutectic mixture was described as a chemical reaction.<sup>34</sup>



The equilibrium constant of the chemical reaction ( $K_a$ ) in eq 3 was defined as

$$K_a = \prod_i a_i^{\vartheta_i} = \frac{(x_A^L \gamma_A^L)^{\vartheta_A} (x_B^L \gamma_B^L)^{\vartheta_B}}{(x_{AB}^S \gamma_{AB}^S)} \quad (4)$$

The solid phase is a pure cocrystal; hence,  $x_{AB}^S \gamma_{AB}^S = 1$ . The temperature effect on the melting enthalpy of the cocrystal was neglected in a narrow temperature range, and  $K_a$  at different temperatures was calculated using the Gibbs–Helmholtz equation

$$\ln K_a = \ln K_a^{\text{ref}} + \frac{\Delta h^{\text{ref}}}{R} \left( \frac{1}{T^{\text{ref}}} - \frac{1}{T} \right) \quad (5)$$

where  $T^{\text{ref}}$  is a reference temperature,  $K_a^{\text{ref}}$  is the equilibrium constant at  $T^{\text{ref}}$ , and  $\Delta h^{\text{ref}}$  is the melting enthalpy of the cocrystal at  $T^{\text{ref}}$ .  $T^{\text{ref}}$  and

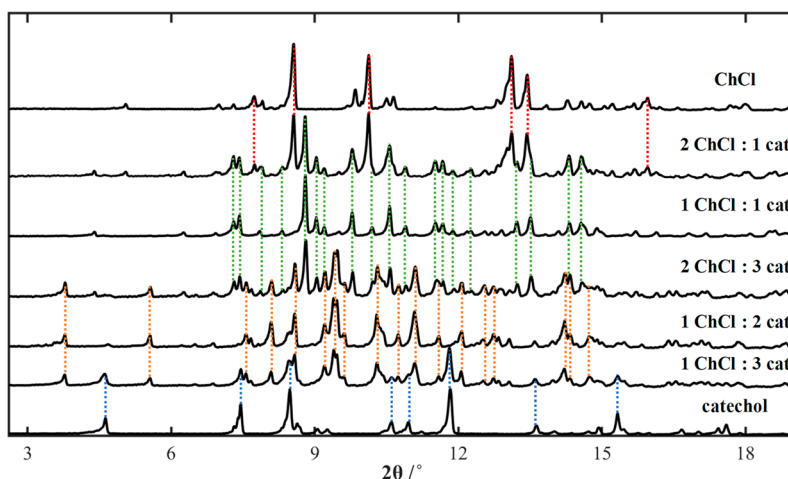


**Figure 2.** X-ray diffraction patterns of choline chloride (ChCl) and catechol (cat) binary eutectic mixtures for samples of different ratios. The measurements were performed at 253 K. Characteristic peaks are marked as follows: catechol (blue dotted lines), 1:2 cocrystal (orange dotted lines), 1:1 cocrystal (green dotted lines), and ChCl (red dotted lines).

$\Delta h^{\text{ref}}$  are the melting temperature and enthalpy of the cocrystals measured in this work using DSC. The equilibrium constant at  $T^{\text{ref}}$  was calculated as follows

$$K_a^{\text{ref}} = (x_A^{\text{ref}} \gamma_A^{\text{ref}})^{\theta_A} (x_B^{\text{ref}} \gamma_B^{\text{ref}})^{\theta_B} \quad (6)$$

where  $x^{\text{ref}}$  and  $\gamma^{\text{ref}}$  are the mole fraction and the activity coefficient of the component at which  $T^{\text{ref}}$  and  $\Delta h^{\text{ref}}$  were measured, i.e., at the cocrystal stoichiometry. Equations 4–6 were solved simultaneously to obtain the liquidus lines of the cocrystal.

The activity coefficients of the components in the liquid phase ( $\gamma_i^{\text{L}}$ ) are prerequisites in calculating the pure components (eqs 1 and 2) and cocrystal (eqs 4–6) liquidus lines. The activity coefficients of the components in the liquid phase were calculated using the NRTL model as follows<sup>32</sup>

$$\ln \gamma_i^{\text{L}} = x_j^2 \left[ \tau_{ji} \left( \frac{G_{ji}}{x_i + x_j G_{ji}} \right)^2 + \frac{\tau_{ij} G_{ij}}{(x_i + x_j G_{ij})^2} \right] \quad (7)$$

$$G_{ij} = \exp(-\alpha \tau_{ij}) \quad G_{ji} = \exp(-\alpha \tau_{ji}) \quad (8)$$

$$\tau_{ij} = \frac{g_{ij} - g_{jj}}{RT} \quad \tau_{ji} = \frac{g_{ji} - g_{ii}}{RT} \quad (9)$$

The nonrandom parameter  $\alpha$  was set to 0.3, and the binary interaction parameters ( $g_{ij} - g_{jj}$ ) and ( $g_{ji} - g_{ii}$ ) were fitted to the experimental liquidus data ( $T_i^{\text{exp}}$ ) by minimizing the following objective function

$$F(T) = \sum_{i=1}^n \left( \frac{(T_i^{\text{exp}} - T_i^{\text{cal}})^2}{n} \right)^{1/2} \quad (10)$$

where  $T_i^{\text{cal}}$  is the calculated liquidus temperature by the NRTL model and  $n$  is the number of experimental data points.

The SLE data on the mixtures rich in ChCl were used to determine the melting properties of thermally unstable ChCl. For this, eq 2 was rearranged as follows<sup>33</sup>

$$\ln x_i^{\text{L}} \gamma_i^{\text{L}} = \left( -\frac{\Delta h_{m,i}}{R} - \frac{\Delta h_{\text{tr},i}}{R} \right) \times \frac{1}{T} + \left( \frac{\Delta h_{m,i}}{RT_{m,i}} + \frac{\Delta h_{\text{tr},i}}{RT_{\text{tr},i}} \right) \quad (11)$$

Given that the NRTL model is available for the calculation of the activity coefficients of ChCl in the liquid phase, experimental  $\ln x_i^{\text{L}} \gamma_i^{\text{L}}$  values were plotted as a function of  $1/T$ . Accordingly, the melting enthalpy and temperature of ChCl were determined from the slope  $\left( -\frac{\Delta h_{m,i}}{R} - \frac{\Delta h_{\text{tr},i}}{R} \right)$  and intercept  $\left( \frac{\Delta h_{m,i}}{RT_{m,i}} + \frac{\Delta h_{\text{tr},i}}{RT_{\text{tr},i}} \right)$ .

### 3. RESULTS

**3.1. XRD.** The formation of cocrystals was monitored by powder XRD analysis. Figure 2 shows the powder XRD pattern obtained at 253 K for pure catechol, ChCl, and a ChCl/catechol mixture of different ratios. Starting with the bottom curves, which depict catechol-rich samples, the XRD pattern of the 1:3 ratio sample shows the main peaks of the catechol XRD pattern (blue dotted lines) with additional peaks that do not correspond to the peaks of the pure ChCl XRD pattern. When the XRD patterns of the 1:3 and 1:2 ratio samples were compared, the additional peaks observed in the 1:3 ratio sample match with those in the 1:2 ratio sample XRD pattern (orange dotted lines), indicating that the crystallized solid of the 1:3 ratio sample consists of pure catechol and the solid phase of the 1:2 ratio sample. The absence of pure catechol peaks in the XRD pattern of the 1:2 ratio sample indicates the formation of a cocrystal with a 1:2 ratio. SC-XRD analysis was performed on a single crystal obtained from the 1:2 ratio sample to confirm the formation of a 1:2 cocrystal according to the procedure described in Section 2.2. The cocrystal formation with a stoichiometric ratio of 1:2 for ChCl/catechol was confirmed by SC-XRD analysis; the crystal structure details are shown in Figures S1 and S2 and Table S3.

When one moves toward the middle composition range, a comparison between the XRD patterns of the 1:2 and 2:3 ratio samples reveals additional peaks in the 2:3 ratio sample XRD pattern (green dotted lines), which again do not match with the peaks of pure catechol or ChCl. These additional peaks correspond to the 1:1 ratio sample XRD pattern (green dotted lines). Thus, the crystallized solid of the 2:3 ratio sample consists of the 1:2 cocrystal and the solid phase of the 1:1 ratio sample. The powder XRD pattern of the 1:1 ratio does not match or contain any peaks corresponding to pure catechol, ChCl, or the 1:2 cocrystal, which may indicate the formation of a second cocrystalline phase at the 1:1 ratio. Accordingly, SC-XRD analysis was performed on a single crystal obtained from the 1:1 ratio sample. The results confirmed the formation of a cocrystal with a stoichiometric ratio of 1:1 for ChCl/catechol; the crystal structure details are shown in Figures S3 and S4 and Table S4. Finally, the peaks of the pure ChCl XRD pattern (red dotted lines) can be seen in the 2:1 ratio sample XRD pattern, showing that the crystallized solid of the 2:1 ratio sample consists of pure ChCl and the 1:1 cocrystal. We could perform quantitative

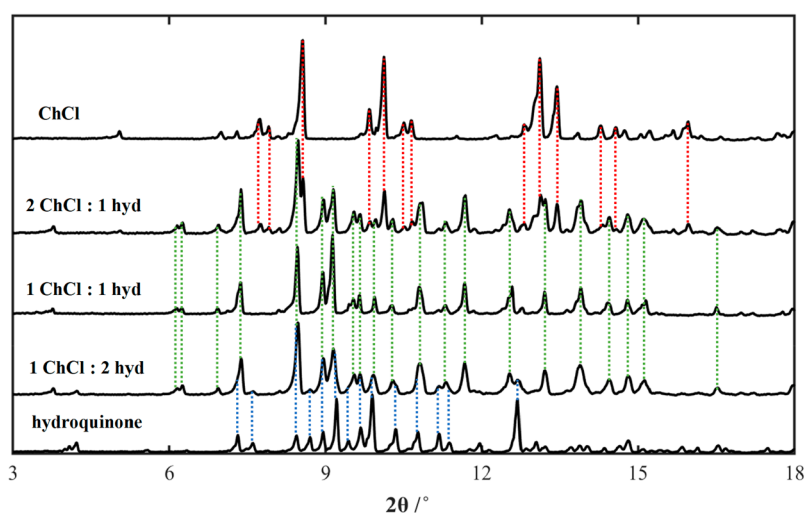


**Figure 3.** X-ray diffraction pattern of choline chloride (ChCl) and hydroquinone (hyd) binary eutectic mixture for samples of different ratios. The measurements were performed at 253 K. Characteristic peaks are marked as follows: hydroquinone (blue dotted lines), 1:1 cocrystal (green dotted lines), and ChCl (red dotted lines).

phase analysis via Rietveld refinement of the powder XRD data for the samples shown in Figure 2 within the ChCl/catechol system (see Tables S6 and S7) because we had determined the crystal structures of the 1:2 and 1:1 cocrystals, which confirmed the above assignments.

Next, powder XRD investigations were performed on the ChCl/hydroquinone eutectic system samples covering the entire composition range. Figure 3 shows the powder XRD pattern obtained at 253 K for pure hydroquinone, ChCl, and ChCl/hydroquinone samples of varying ratios showing distinct powder XRD patterns. Starting with hydroquinone-rich samples, the XRD pattern of the 1:2 ratio sample shows the peaks corresponding to the pure hydroquinone XRD pattern (blue dotted lines). Conversely, the additional peaks in the 1:2 ratio sample XRD pattern do not correspond to the peaks seen in the pure ChCl XRD pattern. These peaks correspond to the XRD pattern of the 1:1 ratio sample. Thus, the crystallized solid phase of the 1:2 ratio sample consists of pure hydroquinone and the solid phase of the 1:1 ratio sample. As seen, no hydroquinone or ChCl peaks were observed in the 1:1 ratio sample XRD pattern, hinting at the possibility of a cocrystal formation at the 1:1 ratio. Thus, SC-XRD analysis was performed on a single crystal obtained from the 1:1 ratio sample. The formation of a cocrystal with a stoichiometric ratio of 1:1 for ChCl/hydroquinone (Figure S5 and Table S5) was confirmed by the SC-XRD results. When one refers to Figure 3, the 2:1 sample ratio XRD pattern contains the peaks of pure ChCl and the 1:1 cocrystal, which indicates that the crystallized solid phase of the 2:1 ratio sample consists of pure ChCl and the 1:1 cocrystal. Consequently, one cocrystal can be identified in the ChCl/hydroquinone eutectic system. Finally, quantitative phase analysis by Rietveld refinement of the powder XRD data of the samples shown in Figure 3 within the ChCl/hydroquinone system confirmed the above assignments (see Tables S6 and S8).

**3.2. DSC.** The powder XRD analysis revealed the formation of two cocrystals in the ChCl/catechol (1:2 and 1:1 cocrystals) and one cocrystal in the ChCl/hydroquinone (1:1 cocrystal) eutectic systems. Thus, the phase diagram is not of a simple eutectic type, and the melting properties of the cocrystals are needed for adequate modeling of the SLE in the two eutectic

systems. The melting properties of catechol, hydroquinone, and the three cocrystals as well as the solid–solid transition enthalpy and temperature of ChCl were measured using DSC. The corresponding DSC curves can be found in Figure S7. Table 1

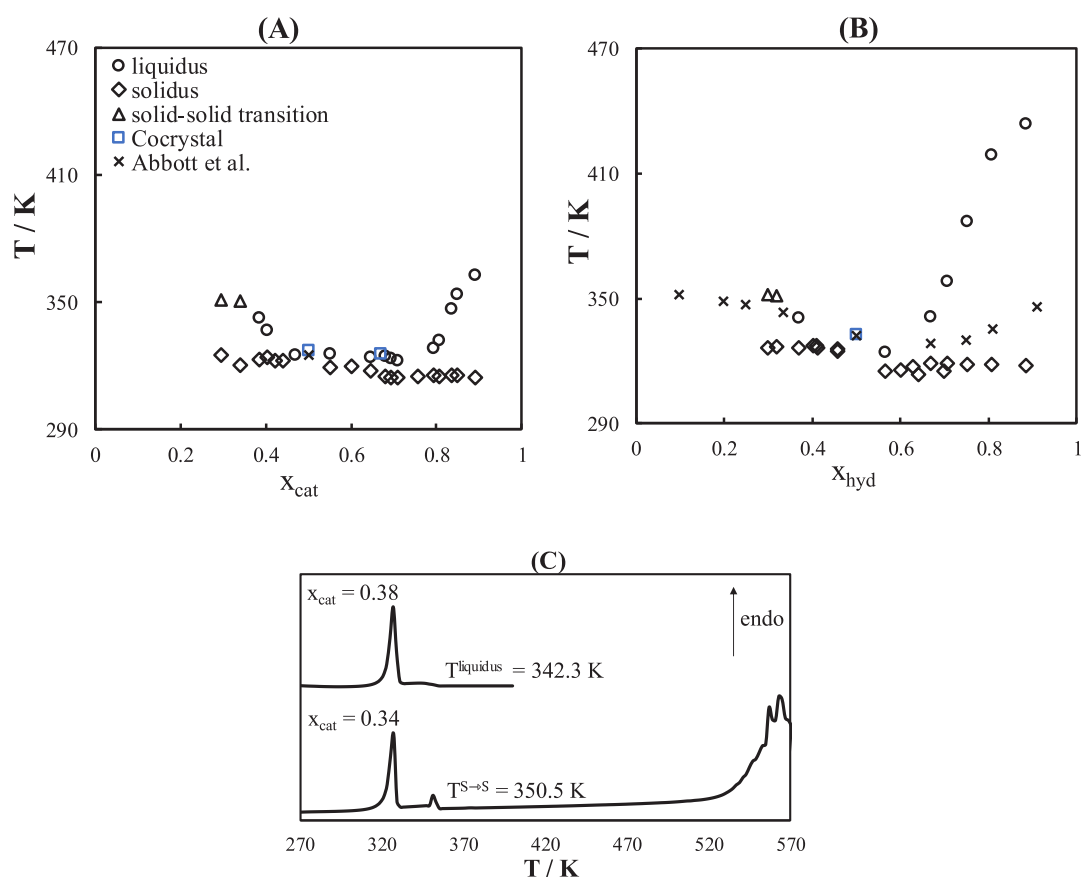
**Table 1.** Pure Constituents and Cocrystal Melting Properties Measured in This Work Compared to the Data Found in the Literature

solid phase	$\Delta h_m/\text{kJ mol}^{-1}$		$T_m/\text{K}$	
	this work	literature	this work	literature
catechol	$21.99 \pm 0.61$	22.87 <sup>36</sup>	$377.1 \pm 0.1$	377.6 <sup>36</sup>
1:2 ChCl:cat	$39.54 \pm 0.61$		$325.7 \pm 0.1$	
1:1 ChCl:cat	$34.15 \pm 0.11$		$327.4 \pm 0.4$	325.2 <sup>35</sup>
hydroquinone	$28.73 \pm 0.15$	27.23 <sup>36</sup>	$445.7 \pm 0.1$	445.1
1:1 ChCl:hyd	$31.97 \pm 0.38$		$332.7 \pm 0.1$	332.2 <sup>35</sup>
solid–solid transition				
	$\Delta h_{tr}/\text{kJ mol}^{-1}$		$T_{tr}/\text{K}$	
	this work	literature	this work	literature
choline chloride	$16.35 \pm 0.67$	16.53 <sup>37</sup>	$352.3 \pm 0.1$	351 <sup>37</sup>

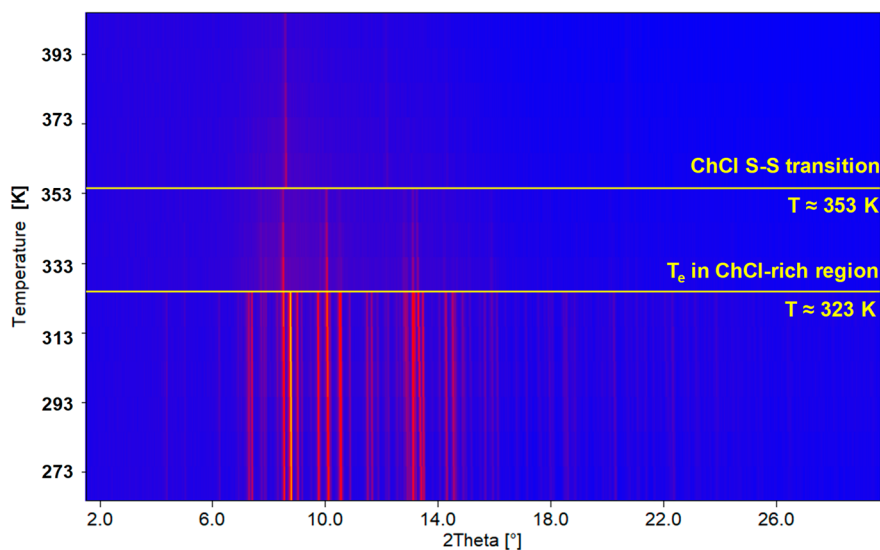
shows the measured melting properties compared to those reported in the literature. As seen, the melting temperatures of the pure components measured in the present work agree with the literature values. Abbott et al.<sup>35</sup> reported the melting temperatures of the 1:1 molar ratio mixture in the two eutectic systems as eutectic temperatures. The reported values match well with the melting temperatures of the 1:1 cocrystals obtained in the present work but were misinterpreted as eutectic points.

Figure 4 shows SLE data of the two eutectic systems over the whole composition range measured using DSC in this work compared to the data found in the literature (indicated by crosses). As seen in Figure 4A, the ChCl/catechol eutectic system shows three solidus temperatures ( $\sim 314$ ,  $319$ , and  $323$  K) attributed to the formation of two cocrystals. As shown in Figure 4B, the ChCl/hydroquinone eutectic system shows the formation of one cocrystal and two different solidus temperatures ( $\sim 318$  and  $326$  K).

For mixtures rich in ChCl, no liquidus temperature could be observed above a certain temperature value. This temperature



**Figure 4.** Measured solid–liquid equilibria data for (A) choline chloride (ChCl)/catechol (cat) and (B) ChCl/hydroquinone (hyd). Literature data were taken from Abbott et al.<sup>35</sup> (C) Differential scanning calorimetry curves of samples from the ChCl/catechol eutectic system with  $x_{cat} = 0.38$  and 0.34. The curves were shifted for clarity.



**Figure 5.** Variable temperature powder X-ray diffraction for the sample with  $x_{cat} = 0.34$  from choline chloride (ChCl)/catechol. The solid–solid (S–S) transition and eutectic temperature ( $T_e$ ) in the ChCl-rich region are shown.

( $T = 352.3$  K) corresponds to the solid–solid transition of ChCl. The DSC curves of the samples with  $x_{cat} = 0.38$  and 0.34 are shown in Figure 4C. Although the liquidus temperature of the sample with  $x_{cat} = 0.38$  is 342.3 K, no liquidus temperature at  $x_{cat} = 0.34$  could be measured above the solid–solid transition temperature of ChCl up to the decomposition temperature of

the mixture ( $T > 550$  K). The same behavior was observed for all samples with  $x_{ChCl} > 0.66$  in the ChCl/catechol and ChCl/hydroquinone eutectic systems. The data found in the literature for the ChCl/hydroquinone eutectic system (cross symbols in Figure 4B) hint at the observed behavior, but the solid–solid transition temperature of ChCl has been misinterpreted as

liquidus temperatures. The variable temperature XRD (VT-XRD) experiment carried out on pure ChCl (Figure S8) confirmed the fact of the solid–solid transition.

Further investigations were performed to validate the DSC observations. VT-XRD was performed on a sample from the ChCl/catechol eutectic system with  $x_{\text{cat}} = 0.34$  in the temperature range from 263 to 403 K; the results are shown in Figure 5. As seen in Figure 5, the XRD pattern remains the same from 263 to around 323 K. At 323 K, several peaks in the XRD pattern disappear while the remaining peaks fade slightly. The vanishing and fading of the XRD pattern peaks indicate partial melting of the solid phase of the sample. Thus, this temperature corresponds to the eutectic temperature observed in the ChCl-rich region, i.e., the melting of the 1:1 cocrystal and part of pure ChCl. At temperatures higher than 323 K, only the XRD peaks corresponding to pure ChCl are observed. The solid–solid transition of ChCl can be observed as a change in the XRD pattern at around 353 K. Above the solid–solid transition temperature, no vanishing of the peaks of the high-temperature polymorph of ChCl is observed, indicating that pure ChCl remains as a solid in the sample.

Nevertheless, liquidus temperatures for ChCl above its solid–solid transition temperature were reported for other ChCl-based DESs.<sup>5,7–10,38</sup> However, the reported data were obtained by a melting-point device and not by DSC. This method relies on visual determination of the mixture melting temperature, and thus, some of the phase transitions, such as solid–solid solidus (eutectic) transitions, cannot be captured or can be misinterpreted. We recommend the detailed reinvestigation of the crystallized solid phases in ChCl-based DESs to confirm that ChCl undergoes the solid–solid transition and does not melt above its solid–solid transition temperature regardless of the HBD.

**3.3. Thermodynamic Modeling.** The correlation of experimental SLE data is a valuable tool to obtain the complete solid–liquid phase diagram and determine the position of the eutectic points. As the melting properties of ChCl are unknown, the correlation of the liquidus line SLE data ( $x_{\text{ChCl}} > 0.6$ ) to obtain the NRTL binary interaction parameters is not possible. Thus, for each system being studied, the experimental data obtained for the liquidus lines of catechol, hydroquinone, and the cocrystals were correlated using the NRTL model and based on the melting properties of the pure components and the cocrystals from Table 1. Table 2 displays the obtained binary interaction parameters, the RMSD between experimental and estimated liquidus temperatures, and the calculated eutectic

compositions and temperatures for the two eutectic systems. The binary interaction parameters with negative values indicate a significant negative deviation from the ideal behavior, i.e., strong intermolecular interactions between unlike molecules in the liquid phase ( $\gamma_i < 1$ ). Figure 6 shows the calculated liquidus (solid blue lines) and solidus lines (dashed blue lines) compared to the measured data (points). The calculated liquidus and solidus lines are in good agreement with the experimental data, as seen in Figure 6. The model can adequately describe the formation of the cocrystals and determine the position of the eutectic points.

As shown in the previous section, the liquidus temperatures of ChCl above its solid–solid transition temperature could not be measured. Nevertheless, the activity coefficients of ChCl in the ChCl-rich liquid phase can be calculated by the NRTL model using the binary interaction parameters from Table 2. Thus, the ChCl liquidus line above the solid–solid transition could be, in principle, modeled if the melting properties of ChCl were known. However, the melting properties of ChCl are not available experimentally due to its thermal instability. Fernandez et al.<sup>38</sup> estimated the melting properties of ChCl as  $T_m = 597$  K and  $\Delta h_m = 4.3$  kJ mol<sup>-1</sup>. The estimation was made based on the SLE data of ten binary eutectic mixtures containing ChCl with various ionic salts and assuming an ideal solution behavior of ChCl in the liquid solutions, i.e.,  $\gamma_{\text{ChCl}} = 1$ . Vilas-Boas et al.<sup>39</sup> used ChCl water solubility data and the PC-SAFT or COSMO-RS models to estimate the melting enthalpy of ChCl as  $\Delta h_m = 7.67$  kJ mol<sup>-1</sup>, assuming the melting temperature estimated in Fernandez et al.<sup>38</sup> In both studies, the systems were assumed to be of the simple eutectic type without accounting for the solid–solid transition of ChCl.

Figure 7 shows the ChCl-rich region ( $x_{\text{ChCl}} > 0.5$ ) in the phase diagram of ChCl/catechol (Figure 7A) and ChCl/hydroquinone (Figure 7B) eutectic mixtures. The blue lines in the figure represent the liquidus lines of the 1:1 cocrystals as correlated with the NRTL model. The red and orange lines indicate the liquidus lines of ChCl calculated using the literature values of the melting properties of ChCl found in Fernandez et al.<sup>38</sup> ( $\Delta h_m = 4.30$  kJ mol<sup>-1</sup>,  $T_m = 597$  K) and Vilas-Boas et al. ( $\Delta h_m = 7.67$  kJ mol<sup>-1</sup>,  $T_m = 597$  K),<sup>39</sup> respectively. As seen, none of the published melting properties of ChCl can adequately describe the measured data in the composition range of  $x_{\text{ChCl}} > 0.60$ . Therefore, the reported ChCl melting properties seem inadequate for modeling its liquidus line accurately in the ChCl/catechol and ChCl/hydroquinone eutectic systems.

Although the melting properties of ChCl are unknown, its crystal structure may provide a premise about its melting properties. ChCl has a highly disordered crystal structure above the solid–solid transition.<sup>24</sup> The solid–solid transition entropy of ChCl ( $\Delta s_{\text{tr}} = \frac{\Delta h_{\text{tr}}}{T_{\text{tr}}} = 46.41$  J mol<sup>-1</sup> K<sup>-1</sup>) resembles the melting entropy of many other solids, indicating the high entropy of the high-temperature ChCl solid phase. Thus, the entropy values of the solid and the liquid phases at the melting temperature should be similar, and therefore, the melting entropy should be of a low value. The melting entropy of substances with highly disordered crystal structure ranges between 0.5 and 2 R (4.16 to 16.63 J mol<sup>-1</sup> K<sup>-1</sup>).<sup>40</sup> The melting temperature is the ratio between the melting enthalpy and entropy of the component, and thus, the melting properties are interrelated.

To estimate the melting properties of ChCl, the experimental SLE data on the ChCl liquidus line below the solid–solid

**Table 2. NRTL Binary Interaction Parameters, RMSD, Estimated Eutectic Point from Solid–Liquid Equilibria Correlation, and the Absolute Difference between Measured and Calculated Eutectic Temperatures**

	ChCl/catechol	ChCl/hydroquinone
$(g_{ij} - g_{ji})/\text{kJ mol}^{-1}$	-9.8501	-11.4683
$(g_{ji} - g_{ii})/\text{kJ mol}^{-1}$	-9.3442	-10.8958
RMSD/K	2.0	9.6
$\alpha_c$	0.74	0.59
	0.60	
$T_e/\text{K}$	312.1	315.5
	316.0	
$ T_e^{\text{exp}} - T_e^{\text{cal}} /\text{K}$	3.0	1.7
	2.9	

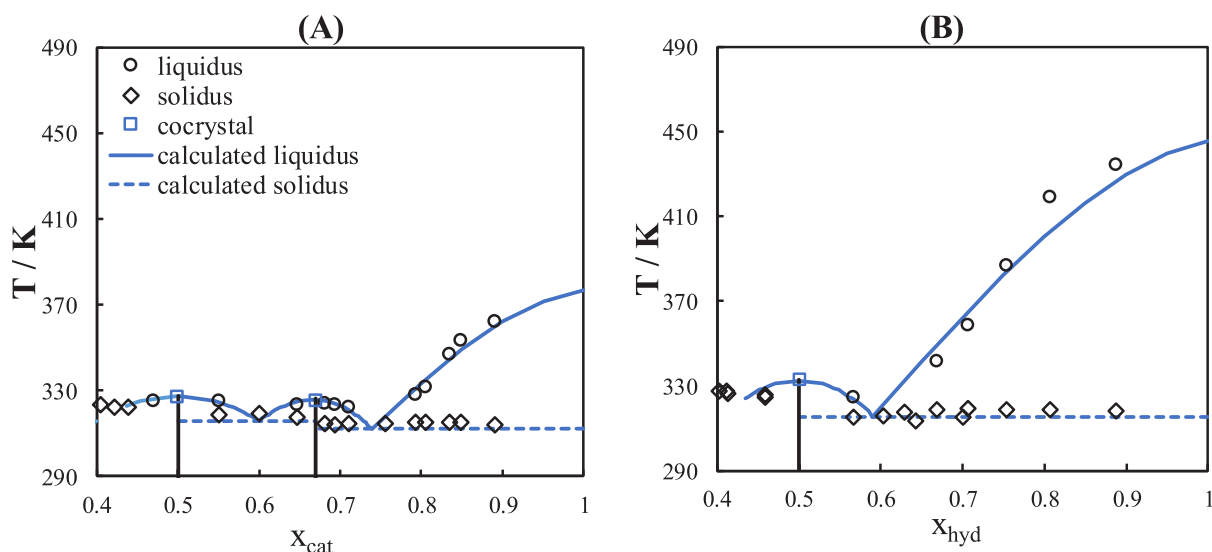


**Figure 6.** Solid–liquid phase diagram of (A) choline chloride (ChCl)/catechol (cat) and (B) ChCl/hydroquinone (hyd) eutectic systems in the hydrogen bond donor-rich region. The liquidus and solidus lines were calculated using the NRTL model.

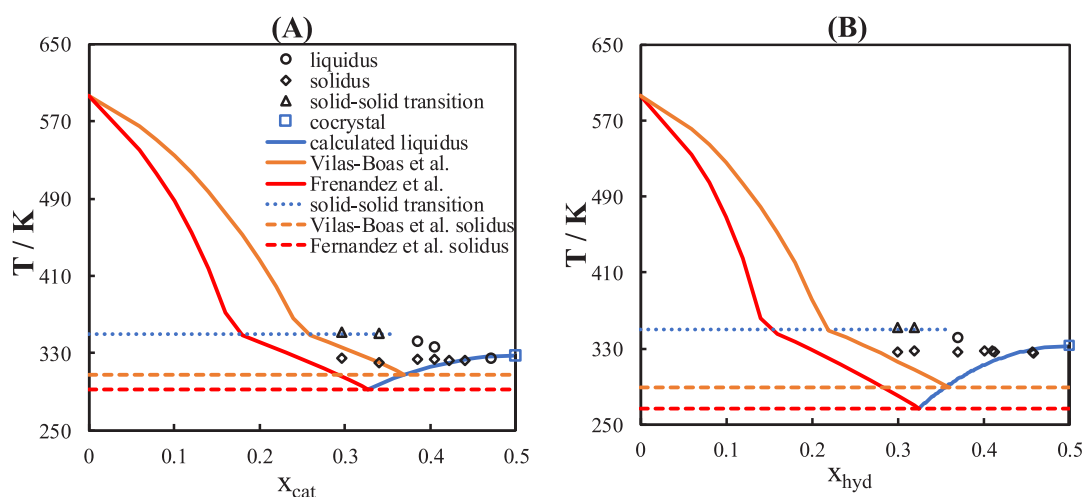


**Figure 7.** Solid–liquid phase diagram of (A) choline chloride (ChCl)/catechol and (B) ChCl/hydroquinone. The ChCl liquidus line was calculated using the nonrandom two-liquid (NRTL) model and the melting properties determined in Fernandez et al.<sup>38</sup> ( $\Delta h_m = 4.30 \text{ kJ mol}^{-1}$ ,  $T_m = 597 \text{ K}$ ) or Vilas-Boas et al.<sup>39</sup> ( $\Delta h_m = 7.67 \text{ kJ mol}^{-1}$ ,  $T_m = 597 \text{ K}$ ).

transition in each eutectic system were fitted by eq 11 at various melting entropy values in the range from 0.5 to 2 R; the results are shown in Figure 8. Each value of the predicted melting entropy yields a pair of melting temperature and enthalpy values due to a lack of experimental evidence regarding the liquidus temperatures of the high-temperature polymorph of ChCl. As shown in Figure 8A,B, any of these pairs adequately describe the liquidus lines of the low-temperature polymorph of ChCl, but as expected, they lead to distinct courses of a high-temperature polymorph's liquidus line. Thus, the estimation of any definite values of the ChCl melting properties without the experimental SLE data for the high-temperature polymorph seems unattainable. However, the obtained data allow one to analyze the melting properties of the high-temperature polymorph.

As seen in Figure 8C,D, the obtained melting enthalpy increases with an increase in the melting entropy, while the melting temperature, on the contrary, decreases. As shown in Figure 8C, the minimum feasible value of melting enthalpy of ChCl, i.e., at  $\Delta s_m \rightarrow 0$ , is about 6.26 or 5.58  $\text{kJ mol}^{-1}$ , which is still higher than that estimated by Fernandez et al.<sup>38</sup>

Simultaneously, these values would correspond to high values of melting temperatures. Furthermore, the melting temperature of ChCl at the highest possible value for the melting entropy of substances with a disordered crystal structure like ChCl (2 R) is 675.1 and 717.9 K, which are higher than the melting temperature reported by Fernandez et al.<sup>38</sup> ( $T_m = 597 \text{ K}$ ) and correspond to the melting enthalpy of 11.22 and 11.94  $\text{kJ mol}^{-1}$ . Thus, the reported values of the melting properties of ChCl seem unreasonable. Hence, it is necessary to find another approach to estimate the melting properties of ChCl.

#### 4. CONCLUSION

This work presents a detailed study of the SLE in ChCl/catechol and ChCl/hydroquinone eutectic systems. The SLE data of the two binary eutectic systems were measured over the whole composition range by DSC analysis. Two cocrystals with stoichiometric ratios of 1:2 and 1:1 in the ChCl/catechol eutectic system and one cocrystal with a stoichiometric ratio of 1:1 in the ChCl/hydroquinone eutectic system were observed.



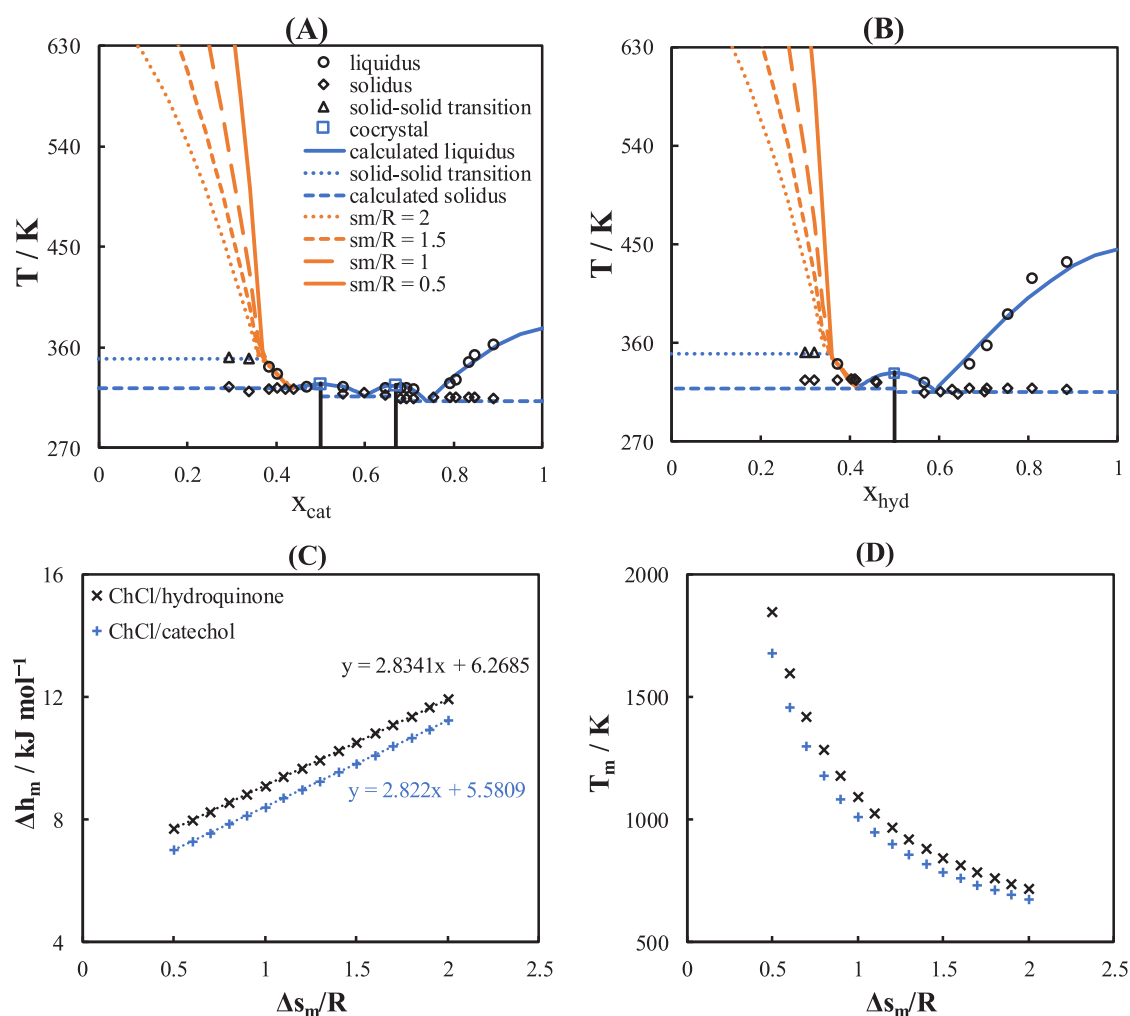


**Figure 8.** Solid–liquid phase diagram of (A) choline chloride (ChCl)/catechol and (B) ChCl/hydroquinone. Obtained (C) melting enthalpy and (D) temperature of choline chloride from its solid–liquid equilibria data assuming different melting entropy values.

Solid ChCl was shown to undergo the solid–solid transition at 352 K in the two studied systems. The formation and structure of the cocrystals and the ChCl solid–solid transition were confirmed by SC-XRD and VT-XRD analysis, respectively.

The experimental data were correlated with the NRTL model for both studied systems. Substantial negative deviation from the ideal behavior was observed for both constituents in both systems. Due to the lack of experimental data on the liquidus lines of the ChCl high-temperature polymorph, the melting properties of ChCl could not be estimated on the basis of the measured SLE data. However, the close analysis of the ChCl crystal structure could show that the values of its melting properties estimated in the literature could not be considered reasonable.

It was found in this study that the prevalent assumption that all ChCl-based DESs are of the simple eutectic type should be examined. The quest to model the phase diagram of DESs should be based on reliable melting properties of pure constituents and on verified SLE data of the system. The latter could be obtained by a combination of DSC analysis with a rigorous XRD characterization of the formed solid phases. To conclude, we encourage the reinvestigation of the SLE data of ChCl-based DESs available in the literature guided by the procedure of the present study.

## ■ ASSOCIATED CONTENT

### Supporting Information

The Supporting Information is available free of charge at <https://pubs.acs.org/doi/10.1021/acs.cgd.1c01477>.

Single crystal X-ray diffraction (SC-XRD) details, solid–liquid equilibria data of choline chloride/catechol, details on SC-XRD, solid–liquid equilibrium data of the ChCl/catechol and ChCl/hydroquinone eutectic system, SC-XRD data for the ChCl/catechol cocrystal with ratios of 1:1 and 1:2, SC-XRD data for the ChCl/hydroquinone cocrystal with a ratio of 1:1, DSC curves of cocrystals and pure components of ChCl/catechol and ChCl/hydroquinone eutectic systems, Rietveld refinement results for powder X-ray data, and VT-XRD study of ChCl (PDF)

### Accession Codes

CCDC 2125060–2125062 contain the supplementary crystallographic data for this paper. These data can be obtained free of charge via [www.ccdc.cam.ac.uk/data\\_request/cif](http://www.ccdc.cam.ac.uk/data_request/cif), or by emailing [data\\_request@ccdc.cam.ac.uk](mailto:data_request@ccdc.cam.ac.uk), or by contacting The Cambridge Crystallographic Data Centre, 12 Union Road, Cambridge CB2 1EZ, UK; fax: +44 1223 336033.

## AUTHOR INFORMATION

## Corresponding Author

Mirjana Minceva – Biothermodynamics, TUM School of Life Sciences, Technical University of Munich (TUM), Freising 85354, Germany; Email: [mirjana.minceva@tum.de](mailto:mirjana.minceva@tum.de)

## Authors

Ahmad Alhadid – Biothermodynamics, TUM School of Life Sciences, Technical University of Munich (TUM), Freising 85354, Germany; [orcid.org/0000-0003-1443-1517](https://orcid.org/0000-0003-1443-1517)

Christian Jandl – Catalysis Research Center, Department Chemie, Technical University of Munich (TUM), Garching 85748, Germany

Liudmila Mokrushina – Separation Science & Technology, Friedrich-Alexander-Universität Erlangen-Nürnberg (FAU), Erlangen 91058, Germany

Complete contact information is available at:

<https://pubs.acs.org/10.1021/acs.cgd.1c01477>

## Author Contributions

Conceptualization: A.A. Formal analysis: A.A. and C.J. Writing, original draft: A.A. and C.J. Writing, review and editing: L.M. and M.M. Supervision: M.M.

## Notes

The authors declare no competing financial interest.

## REFERENCES

- (1) Abbott, A. P.; Capper, G.; Davies, D. L.; Rasheed, R. K.; Tambyrajah, V. Novel solvent properties of choline chloride/urea mixtures. *Chem. Commun. (Camb)* **2003**, 70–71.
- (2) Smith, E. L.; Abbott, A. P.; Ryder, K. S. Deep Eutectic Solvents (DESs) and Their Applications. *Chem. Rev.* **2014**, *114* (21), 11060–11082.
- (3) Zhang, Q.; De Oliveira Vigier, K.; Royer, S.; Jerome, F. Deep eutectic solvents: syntheses, properties and applications. *Chem. Soc. Rev.* **2012**, *41* (21), 7108–7146.
- (4) Alhadid, A.; Mokrushina, L.; Minceva, M. Modeling of Solid–Liquid Equilibria in Deep Eutectic Solvents: A Parameter Study. *Molecules* **2019**, *24* (12), 2334.
- (5) Silva, L. P.; Martins, M. A. R.; Conceição, J. H. F.; Pinho, S. P.; Coutinho, J. A. P. Eutectic Mixtures Based on Polyalcohols as Sustainable Solvents: Screening and Characterization. *ACS Sustain. Chem. Eng.* **2020**, *8* (40), 15317–15326.
- (6) Martins, M. A. R.; Silva, L. P.; Schaeffer, N.; Abranches, D. O.; Maximo, G. J.; Pinho, S. P.; Coutinho, J. A. P. Greener Terpene–Terpene Eutectic Mixtures as Hydrophobic Solvents. *ACS Sustain. Chem. Eng.* **2019**, *7* (20), 17414–17423.
- (7) Silva, L. P.; Araújo, C. F.; Abranches, D. O.; Melle-Franco, M.; Martins, M. A. R.; Nolasco, M. M.; Ribeiro-Claro, P. J. A.; Pinho, S. P.; Coutinho, J. A. P. What a difference a methyl group makes – probing choline–urea molecular interactions through urea structure modification. *Phys. Chem. Chem. Phys.* **2019**, *21* (33), 18278–18289.
- (8) Silva, L. P.; Fernandez, L.; Conceição, J. H. F.; Martins, M. A. R.; Sosa, A.; Ortega, J.; Pinho, S. P.; Coutinho, J. A. P. Design and Characterization of Sugar-Based Deep Eutectic Solvents Using Conductor-like Screening Model for Real Solvents. *ACS Sustain. Chem. Eng.* **2018**, *6* (8), 10724–10734.
- (9) Crespo, E. A.; Silva, L. P.; Martins, M. A. R.; Bülow, M.; Ferreira, O.; Sadowski, G.; Held, C.; Pinho, S. P.; Coutinho, J. A. P. The Role of Polyfunctionality in the Formation of [Ch]Cl-Carboxylic Acid-Based Deep Eutectic Solvents. *Ind. Eng. Chem. Res.* **2018**, *57* (32), 11195–11209.
- (10) Abranches, D. O.; Silva, L. P.; Martins, M. A. R.; Pinho, S. P.; Coutinho, J. A. P. Understanding the Formation of Deep Eutectic Solvents: Betaine as a Universal Hydrogen Bond Acceptor. *ChemSusChem* **2020**, *13* (18), 4916–4921.
- (11) Kollau, L. J. B. M.; Tuinier, R.; Verhaak, J.; den Doelder, J.; Filot, I. A. W.; Vis, M. Design of Nonideal Eutectic Mixtures Based on Correlations with Molecular Properties. *J. Phys. Chem. B* **2020**, *124* (25), 5209–5219.
- (12) Kollau, L. J. B. M.; Vis, M.; van den Bruinhorst, A.; Tuinier, R.; de With, G. Entropy models for the description of the solid–liquid regime of deep eutectic solutions. *J. Mol. Liq.* **2020**, *302*, 112155.
- (13) González de Castilla, A.; Bittner, J. P.; Müller, S.; Jakobtorweihen, S.; Smirnova, I. Thermodynamic and Transport Properties Modeling of Deep Eutectic Solvents: A Review on gE-Models, Equations of State, and Molecular Dynamics. *J. Chem. Eng. Data* **2020**, *65* (3), 943–967.
- (14) Alkhatib, I. I. L.; Bahamon, D.; Llovel, F.; Abu-Zahra, M. R. M.; Vega, L. F. Perspectives and guidelines on thermodynamic modelling of deep eutectic solvents. *J. Mol. Liq.* **2020**, *298*, 112183.
- (15) Alhadid, A.; Mokrushina, L.; Minceva, M. Formation of glassy phases and polymorphism in deep eutectic solvents. *J. Mol. Liq.* **2020**, *314*, 113667.
- (16) Alhadid, A.; Jandl, C.; Mokrushina, L.; Minceva, M. Experimental Investigation and Modeling of Cocrystal Formation in L-Menthol/Thymol Eutectic System. *Cryst. Growth Des.* **2021**, *21* (11), 6083–6091.
- (17) Hamilton, V.; Andrusenko, I.; Potticary, J.; Hall, C.; Stenner, R.; Mugnaioli, E.; Lanza, A. E.; Gemmi, M.; Hall, S. R. Racemic Conglomerate Formation via Crystallization of Metaxalone from Volatile Deep Eutectic Solvents. *Cryst. Growth Des.* **2020**, *20* (7), 4731–4739.
- (18) Potticary, J.; Hall, C.; Hamilton, V.; McCabe, J. F.; Hall, S. R. Crystallization from Volatile Deep Eutectic Solvents. *Cryst. Growth Des.* **2020**, *20* (5), 2877–2884.
- (19) Hall, C. L.; Potticary, J.; Hamilton, V.; Gaisford, S.; Buanz, A.; Hall, S. R. Metastable crystalline phase formation in deep eutectic systems revealed by simultaneous synchrotron XRD and DSC. *Chem. Commun. (Camb)* **2020**, *56* (73), 10726–10729.
- (20) Martins, M. A. R.; Pinho, S. P.; Coutinho, J. A. P. Insights into the Nature of Eutectic and Deep Eutectic Mixtures. *J. Solution Chem.* **2019**, *48* (7), 962–982.
- (21) Che Zain, M. S.; Yeoh, J. X.; Lee, S. Y.; Shaari, K. Physicochemical Properties of Choline Chloride-Based Natural Deep Eutectic Solvents (NaDES) and Their Applicability for Extracting Oil Palm Flavonoids. *Sustainability* **2021**, *13* (23), 12981.
- (22) Abbasi, N. M.; Farooq, M. Q.; Anderson, J. L. Investigating the Variation in Solvation Interactions of Choline Chloride-Based Deep Eutectic Solvents Formed Using Different Hydrogen Bond Donors. *ACS Sustain. Chem. Eng.* **2021**, *9* (35), 11970–11980.
- (23) Golgoun, S.; Mokhtarpour, M.; Shekaari, H. Solubility Enhancement of Betamethasone, Meloxicam and Piroxicam by Use of Choline-Based Deep Eutectic Solvents. *Pharm. Sci.* **2021**, *27* (1), 86–101.
- (24) Shanley, P.; Collin, R. L. The crystal structure of the high temperature form of choline chloride. *Acta Crystallogr.* **1961**, *14* (1), 79–80.
- (25) Crespo, E. A.; Silva, L. P.; Lloret, J. O.; Carvalho, P. J.; Vega, L. F.; Llovel, F.; Coutinho, J. A. P. A methodology to parameterize SAFT-type equations of state for solid precursors of deep eutectic solvents: the example of cholinium chloride. *Phys. Chem. Chem. Phys.* **2019**, *21* (27), 15046–15061.
- (26) Zahn, S. Deep eutectic solvents: similia similibus solvuntur? *Phys. Chem. Chem. Phys.* **2017**, *19* (5), 4041–4047.
- (27) García, G.; Atilhan, M.; Aparicio, S. An approach for the rationalization of melting temperature for deep eutectic solvents from DFT. *Chem. Phys. Lett.* **2015**, *634*, 151–155.
- (28) Abranches, D. O.; Silva, L. P.; Martins, M. A. R.; Coutinho, J. A. P. Differences on the impact of water on the deep eutectic solvents betaine/urea and choline/urea. *J. Chem. Phys.* **2021**, *155* (3), 034501.
- (29) Morrison, H. G.; Sun, C. C.; Neervannan, S. Characterization of thermal behavior of deep eutectic solvents and their potential as drug solubilization vehicles. *Int. J. Pharm.* **2009**, *378* (1–2), 136–139.

(30) van den Bruinhorst, A.; Kollau, L. J. B. M.; Kroon, M. C.; Meuldijk, J.; Tuinier, R.; Esteves, A. C. C. A centrifuge method to determine the solid–liquid phase behavior of eutectic mixtures. *J. Chem. Phys.* **2018**, *149* (22), 224505.

(31) Kitaigorodskii, A. I. *Mixed crystals*; Springer-Verlag: Berlin, 1984.

(32) Prausnitz, J. M.; Lichtenthaler, R. N.; Azevedo, E. G. d. *Molecular Thermodynamics of Fluid-Phase Equilibria*; Prentice Hall PTR: Upper Saddle River, NJ, 1999.

(33) Lohmann, J.; Joh, R.; Gmehling, J. Estimation of Enthalpies of Fusion, Melting Temperatures, Enthalpies of Transition, and Transition Temperatures of Pure Compounds from Experimental Binary Solid–Liquid Equilibrium Data of Eutectic Systems. *J. Chem. Eng. Data* **1997**, *42* (6), 1176–1180.

(34) Lange, L.; Sadowski, G. Polymorphs, Hydrates, Cocrystals, and Cocrystal Hydrates: Thermodynamic Modeling of Theophylline Systems. *Cryst. Growth Des.* **2016**, *16* (8), 4439–4449.

(35) Abbott, A. P.; Ahmed, E. I.; Prasad, K.; Qader, I. B.; Ryder, K. S. Liquid pharmaceuticals formulation by eutectic formation. *Fluid Phase Equilib.* **2017**, *448*, 2–8.

(36) Verevkin, S. P.; Kozlova, S. A. Di-hydroxybenzenes: Catechol, resorcinol, and hydroquinone: Enthalpies of phase transitions revisited. *Thermochim. Acta* **2008**, *471* (1), 33–42.

(37) Petrouleas, V.; Lemmon, R. M. Calorimetric studies of choline chloride, bromide, and iodide. *J. Chem. Phys.* **1978**, *69* (3), 1315.

(38) Fernandez, L.; Silva, L. P.; Martins, M. A. R.; Ferreira, O.; Ortega, J.; Pinho, S. P.; Coutinho, J. A. P. Indirect assessment of the fusion properties of choline chloride from solid-liquid equilibria data. *Fluid Phase Equilib.* **2017**, *448*, 9–14.

(39) Vilas-Boas, S. M.; Abranches, D. O.; Crespo, E. A.; Ferreira, O.; Coutinho, J. A. P.; Pinho, S. P. Experimental solubility and density studies on aqueous solutions of quaternary ammonium halides, and thermodynamic modelling for melting enthalpy estimations. *J. Mol. Liq.* **2020**, *300*, 112281.

(40) Brown, R. J. C.; Brown, R. F. C. Melting Point and Molecular Symmetry. *J. Chem. Educ.* **2000**, *77* (6), 724.

## Supporting Information

### Cocrystal Formation in Choline Chloride Deep Eutectic Solvents

Ahmad Alhadid,<sup>a</sup> Christian Jandl,<sup>b</sup> Liudmila Mokrushina<sup>c</sup> and Mirjana Minceva<sup>\* a</sup>

<sup>a</sup> Biothermodynamics, TUM School of Life Sciences, Technical University of Munich (TUM), Germany

<sup>b</sup> Catalysis Research Center, Department Chemie, Technical University of Munich (TUM), Germany

<sup>c</sup> Separation Science & Technology, Friedrich-Alexander-Universität Erlangen-Nürnberg (FAU),  
Germany

\*Corresponding author e-mail: [mirjana.minceva@tum.de](mailto:mirjana.minceva@tum.de)

---

#### Single-crystal X-ray diffraction

Crystals suitable for SC-XRD were prepared by dissolving the cocrystal powder in hot acetonitrile in a 1:1 mass ratio. The solution was stored at 253 K until suitable crystals appeared. The average time to obtain suitable crystals was around one week.

Data were collected on a Bruker D8 Venture single crystal x-ray diffractometer equipped with a CMOS detector (Bruker Photon-100), a TXS rotating anode with MoK $\alpha$  radiation ( $\lambda = 0.71073 \text{ \AA}$ ) and a Helios optic using the APEX3 software package.<sup>1</sup> Measurements were performed on single crystals coated with perfluorinated ether. The crystals were fixed on top of a Kapton micro sampler and frozen under a stream of cold nitrogen. A matrix scan was used to determine the initial lattice parameters. Reflections were corrected for Lorentz and polarisation effects, scan speed, and background using SAINT.<sup>2</sup> Absorption correction, including odd and even ordered spherical harmonics, was performed using SADABS.<sup>2</sup> Space group assignments were based upon systematic absences, E statistics, and successful refinement of the structures. The structures were solved using SHELXT with the aid of successive difference Fourier maps and were refined against all data using SHELXL in conjunction with SHELXLE.<sup>3,4,5</sup> Hydrogen atoms except on heteroatoms were calculated in ideal positions as follows: Methyl H atoms were refined as part of rigid rotating groups, with a C–H distance of 0.98 Å and  $U_{\text{iso}}(\text{H}) = 1.5 \cdot U_{\text{eq}}(\text{C})$ . Non-methyl H atoms were placed in calculated positions and refined using a riding model, with methylene, aromatic, and other C–H distances of 0.99 Å, 0.95 Å and 1.00 Å, respectively, and  $U_{\text{iso}}(\text{H}) = 1.2 \cdot U_{\text{eq}}(\text{C})$ . Non-hydrogen atoms were refined with anisotropic displacement parameters. Full-matrix least-squares refinements were carried out by minimizing  $\sum w(F_o^2 - F_c^2)^2$  with the SHELXL weighting scheme.<sup>4</sup> Neutral atom scattering factors for all atoms and anomalous dispersion corrections for the non-hydrogen atoms were taken from *International Tables for Crystallography*.<sup>6</sup> Images of the crystal structures were generated with PLATON and Mercury.<sup>7,8</sup> CCDC 2125060-2125062 contains the supplementary crystallographic data for this paper. These data are provided free of charge by The Cambridge Crystallographic Data Centre.

Table S1 Solid–liquid equilibria data of choline chloride/catechol eutectic system.

catechol mole fraction	$T^{\text{liq}} / \text{K}$	$T_e / \text{K}$
0.89	$362.7 \pm 0.1$	314.6
0.85	$353.6 \pm 0.9$	315.6
0.83	$345.0 \pm 1.1$	315.5
0.81	$331.8 \pm 0.1$	315.3
0.79	$328.4 \pm 0.1$	315.7
0.75	–	315.1
0.71	$322.5 \pm 0.1$	314.7
0.69	$323.5 \pm 0.1$	314.3
0.68	$324.3 \pm 0.3$	314.7
0.65	$323.8 \pm 0.3$	317.9
0.60	–	319.5
0.55	$325.5 \pm 0.3$	319.1
0.47	$352.2 \pm 0.3$	–
0.44	–	322.3
0.40	$336.5 \pm 0.3$	323.8
0.38	$342.3 \pm 0.9$	323.0
0.34	$350.5 \pm 0.1^*$	320.5
0.30	$351.3 \pm 0.1^*$	324.9

\*solid-solid transition

Table S2 Solid–liquid equilibria data of choline chloride/hydroquinone eutectic system.

Hydroquinone mole fraction	$T^{\text{liq}} / \text{K}$	$T_e / \text{K}$
0.89	$434.2 \pm 0.9$	317.8
0.81	$418.9 \pm 0.2$	318.5
0.75	$386.8 \pm 1.6$	318.6
0.71	$358.3 \pm 0.1$	318.9
0.70	–	315.3
0.67	$341.2 \pm 0.9$	318.7
0.63	–	317.4
0.60	–	315.3
0.57	$324.3 \pm 0.1$	313.3
0.46	–	324.5
0.45	–	325.7
0.41	–	326.2
0.40	–	327.1
0.37	$340.9 \pm 0.2$	326.5
0.32	$351.3 \pm 0.1^*$	326.7
0.30	$352.1 \pm 0.2^*$	326.4

\*solid-solid transition

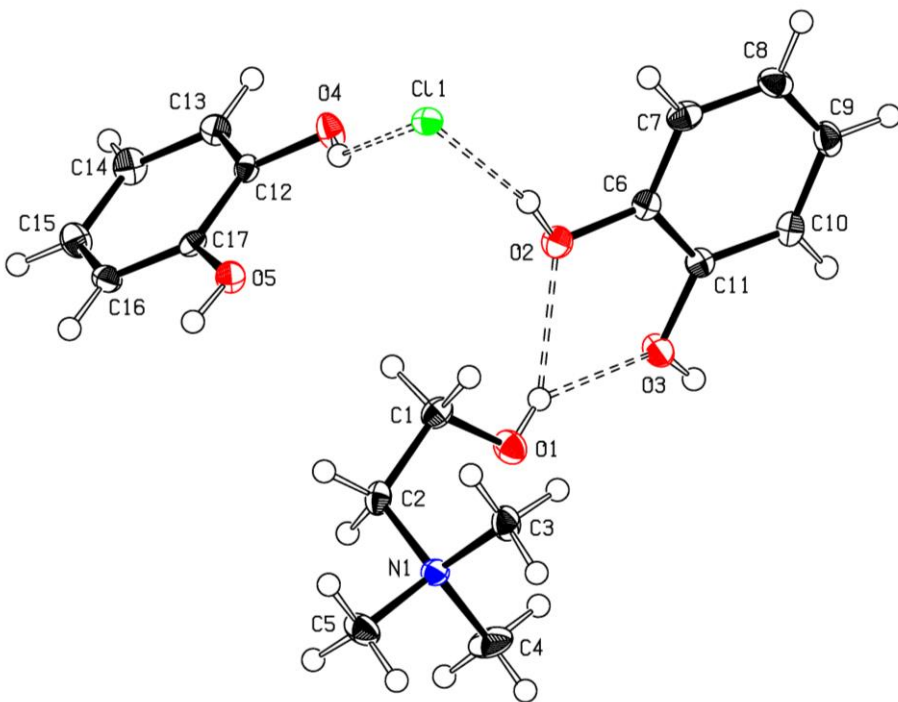


Figure S1: Asymmetric unit of the crystal structure of the choline chloride/catechol cocrystal with a ratio of 1:2. Ellipsoids are displayed at the 50% probability level.

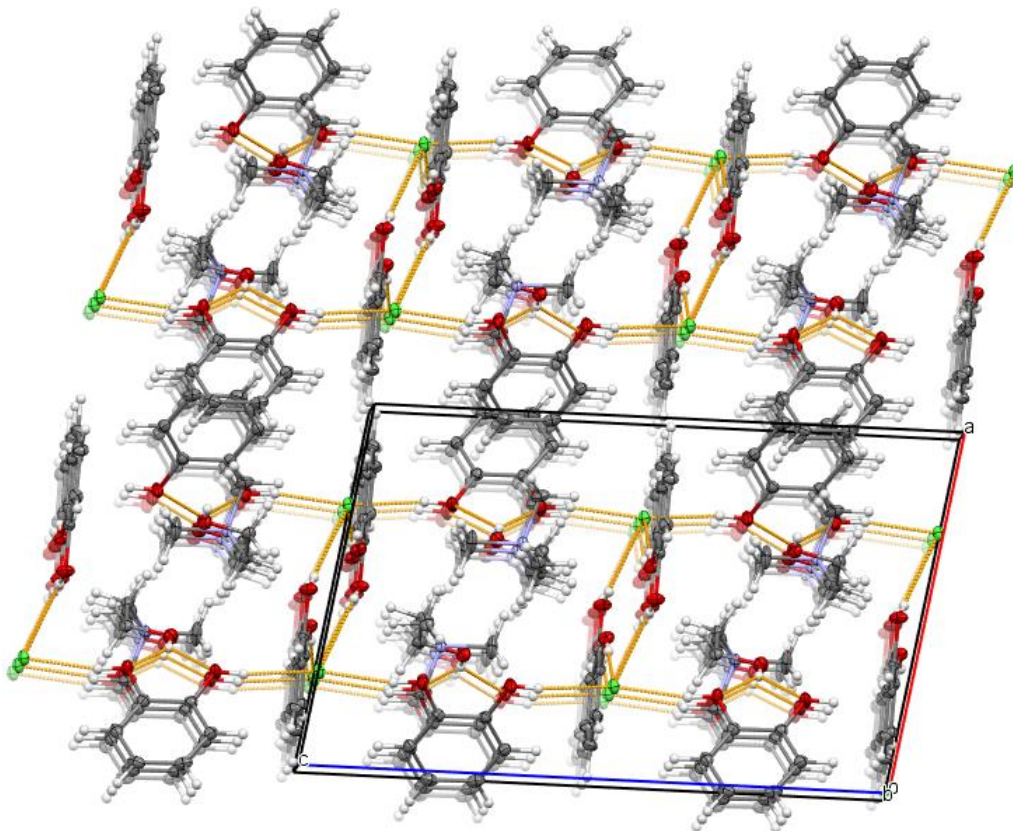


Figure S2: Packing diagram of the choline chloride/catechol cocrystal with a ratio of 1:2 viewed along the b-axis.

Table S3: Structure and refinement details for the choline chloride/catechol cocrystal with a ratio of 1:2.

Deposition number	CCDC 2125062	
Chemical formula	$C_{17}H_{26}ClNO_5$	
Crystal description	colourless fragment	
Formula weight	<u>359.84</u>	
Temperature	<u>100 K</u>	
Wavelength	0.71073 Å	
Crystal size	<u>0.39</u> × <u>0.34</u> × <u>0.17</u> mm	
Crystal system	monoclinic	
Space group	<u><math>P2_1/c</math></u>	
Unit cell dimensions	a = 10.7901(14) Å	a = 90°
	b = 9.9623(13) Å	b = 99.194(4)°
	c = 17.303(3) Å	c = 90°
Volume	1836.1(5) Å <sup>3</sup>	
Z	4	
Density (calculated)	<u>1.302</u> g cm <sup>-3</sup>	
Absorption coefficient	<u>0.23</u> mm <sup>-1</sup>	
F(000)	<u>768</u>	
θ range	2.4-27.5°	
Absorption correction	multi-scan (SADABS)	
T <sub>min</sub> , T <sub>max</sub>	<u>0.681</u> , <u>0.746</u>	
Reflections measured	<u>58129</u>	
Independent reflections	<u>4196</u>	
Reflections I > 2σ(I)	<u>3949</u>	
R <sub>int</sub>	<u>0.030</u>	
Refinement method	full matrix least squares on F <sup>2</sup>	
Data, restraints, parameters	<u>4196</u> , 0, <u>240</u>	
R1 [I > 2σ(I)]	<u>0.029</u>	
wR2 (all data)	<u>0.073</u>	
Goodness of fit	1.05	
Weighting scheme	W = 1/[Σ <sup>2</sup> (F <sub>o</sub> <sup>2</sup> ) + (0.0312P) <sup>2</sup> + 0.8905P] where P = (F <sub>o</sub> <sup>2</sup> + 2F <sub>c</sub> <sup>2</sup> )/3	
Largest difference peak and hole	0.31 and -0.25 eÅ <sup>-3</sup>	



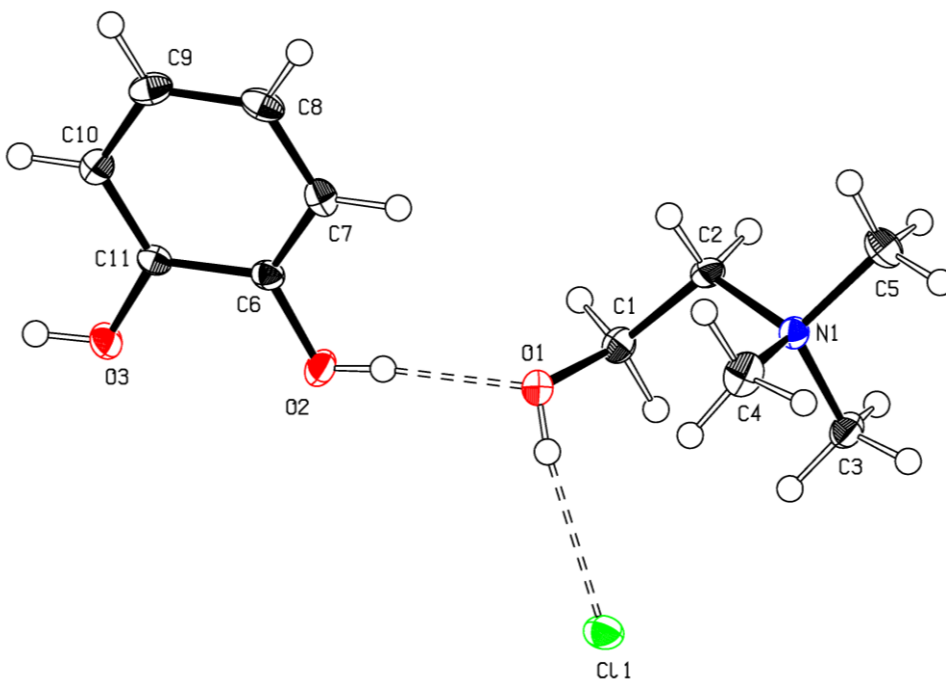


Figure S3: Asymmetric unit of the crystal structure of the choline chloride/catechol cocrystal with a ratio of 1:1. Ellipsoids are displayed at the 50% probability level.

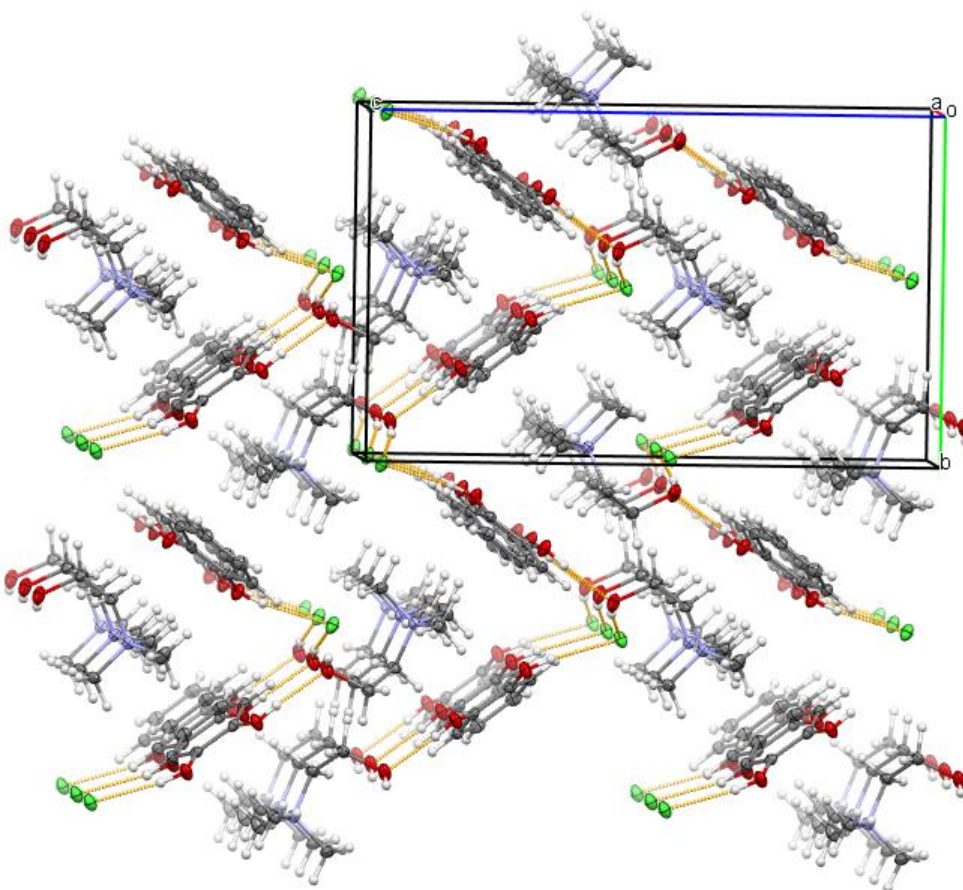


Figure S4: Packing diagram of the choline chloride/catechol cocrystal with a ratio of 1:1 viewed along the a-axis.

Table S4: Structure and refinement details for the choline chloride/catechol cocrystal with a ratio of 1:1.

Deposition number	CCDC 2125061	
Chemical formula	$C_{11}H_{20}ClNO_3$	
Crystal description	colourless fragment	
Formula weight	249.73	
Temperature	123 K	
Wavelength	0.71073 Å	
Crystal size	$0.40 \times 0.19 \times 0.04$ mm	
Crystal system	orthorhombic	
Space group	$P2_12_12_1$	
Unit cell dimensions	a = 6.9117(4) Å	a = 90°
	b = 10.7352(7) Å	b = 90°
	c = 17.5585(10) Å	c = 90°
Volume	1302.81(14) Å <sup>3</sup>	
Z	4	
Density (calculated)	1.273 g cm <sup>-3</sup>	
Absorption coefficient	0.29 mm <sup>-1</sup>	
F(000)	536	
θ range	3.2-26.0°	
Absorption correction	multi-scan (SADABS)	
T <sub>min</sub> , T <sub>max</sub>	0.678, 0.745	
Reflections measured	22895	
Independent reflections	2569	
Reflections I > 2σ(I)	2387	
R <sub>int</sub>	0.044	
Refinement method	full matrix least squares on F <sup>2</sup>	
Data, restraints, parameters	2569, 0, 160	
Absolute structure parameter (Flack, Parsons) <sup>9</sup>	0.01(2)	
R1 [I > 2σ(I)]	0.025	
wR2 (all data)	0.061	
Goodness of fit	1.07	
Weighting scheme	$W = 1/[\Sigma^2(F_o^2) + (0.0301P)^2 + 0.3073P]$ where $P = (F_o^2 + 2F_c^2)/3$	
Largest difference peak and hole	0.16 and -0.21 eÅ <sup>-3</sup>	

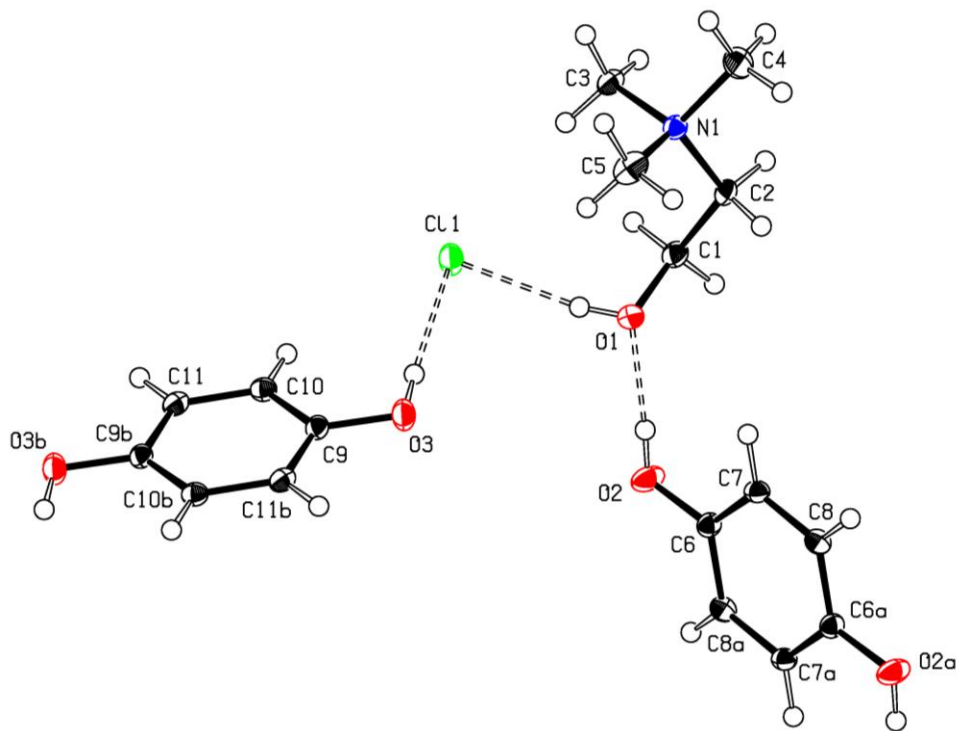


Figure S5: Asymmetric unit (with completed fragments) of the crystal structure of the choline chloride/hydroquinone cocrystal with a ratio of 1:1. Ellipsoids are displayed at the 50% probability level. Symmetry code to create equivalent position: a)  $1 - x, -y, 1 - z$ ; b)  $2 - x, 2 - y, 1 - z$ .

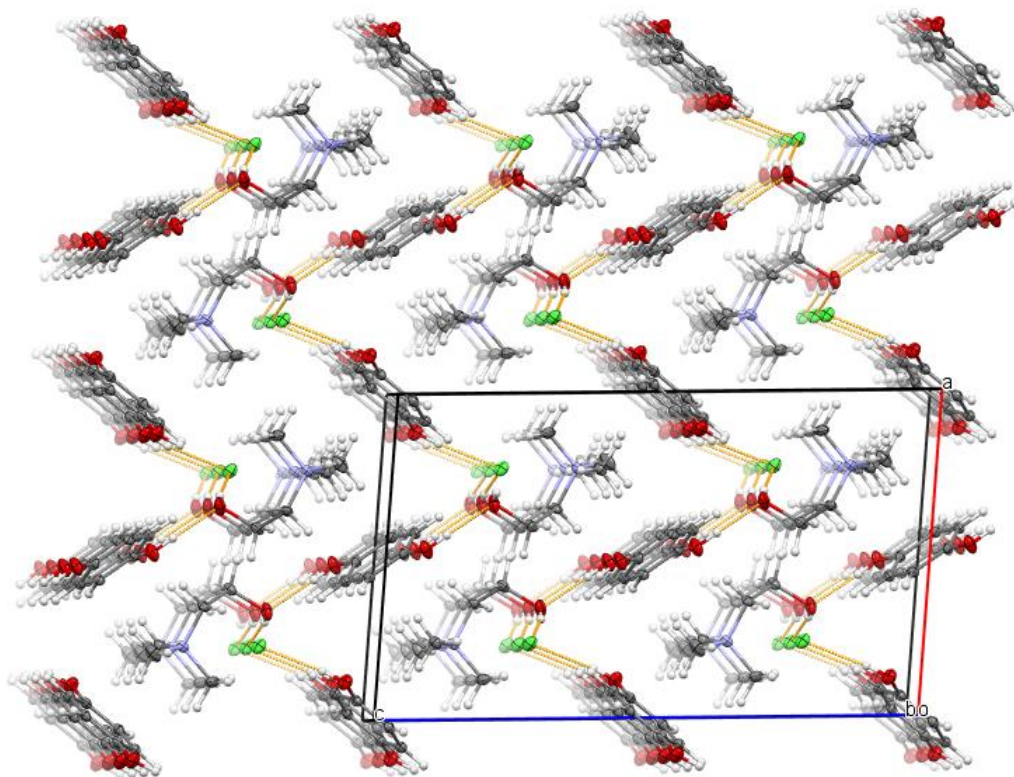


Figure S6: Packing diagram of the choline chloride/hydroquinone cocrystal with a ratio of 1:1 viewed along the b-axis.

Table S5: Structure and refinement details for the choline chloride/hydroquinone cocrystal with a ratio of 1:1.

Deposition number	CCDC 2125060	
Chemical formula	C <sub>11</sub> H <sub>20</sub> ClNO <sub>3</sub>	
Crystal description	colourless fragment	
Formula weight	<u>249.73</u>	
Temperature	123 K	
Wavelength	0.71073 Å	
Crystal size	<u>0.56</u> × <u>0.42</u> × <u>0.24</u> mm	
Crystal system	monoclinic	
Space group	<u>P2<sub>1</sub>/c</u>	
Unit cell dimensions	a = 10.7084(10) Å	a = 90°
	b = 6.9493(6) Å	b = 94.833(3)°
	c = 17.8691(16) Å	c = 90°
Volume	1325.0(2) Å <sup>3</sup>	
Z	4	
Density (calculated)	<u>1.252</u> g cm <sup>-3</sup>	
Absorption coefficient	<u>0.28</u> mm <sup>-1</sup>	
F(000)	<u>536</u>	
θ range	2.3-26.4°	
Absorption correction	multi-scan (SADABS)	
T <sub>min</sub> , T <sub>max</sub>	0.701, 0.745	
Reflections measured	21818	
Independent reflections	2678	
Reflections I > 2σ(I)	2534	
R <sub>int</sub>	0.025	
Refinement method	full matrix least squares on F <sup>2</sup>	
Data, restraints, parameters	2534, 0, 160	
R1 [I > 2σ(I)]	0.027	
wR2 (all data)	0.072	
Goodness of fit	1.07	
Weighting scheme	W = 1/[Σ <sup>2</sup> (F <sub>o</sub> <sup>2</sup> ) + (0.0335P) <sup>2</sup> + 0.5679P] where P = (F <sub>o</sub> <sup>2</sup> + 2F <sub>c</sub> <sup>2</sup> )/3	
Largest difference peak and hole	0.26 and -0.19 eÅ <sup>-3</sup>	

## Rietveld refinements

Rietveld refinements were performed using TOPAS.<sup>10</sup> Refinements of the single phases with fixed atomic sites were used to determine the cell parameters at the measurement temperature of 253 K. Then, quantitative phase analysis was performed with fixed unit cell parameters of these phases.

Table S6: Resulting unit cell parameters at 253 K of the relevant single phases from Rietveld refinement.

	a [Å]	b [Å]	c [Å]	$\alpha$ [°]	$\beta$ [°]	$\gamma$ [°]	Rwp
choline chloride (ChCl)	5.8835(4)	11.1249(8)	11.5895(8)	90	90	90	10.919
catechol (cat)	10.0107(9)	5.5331(5)	10.9268(8)	90	118.840(6)	90	11.358
hydroquinone (hyd)	38.462(2)	38.462(2)	5.6424(5)	90	90	120	12.117
ChCl/cat 1:1 cocrystal	6.9641(5)	10.8219(8)	17.669(1)	90	90	90	9.299
ChCl/cat 1:2 cocrystal	10.8770(8)	10.0382(7)	17.394(1)	90	99.202(7)	90	8.123
ChCl/hyd 1:1 cocrystal	10.7953(8)	6.9764(6)	17.989(2)	90	94.991(5)	90	11.260

Table S7: Results of quantitative phase analysis via Rietveld refinement in the cholin chloride/catechol system.

	% weight				Rwp
	ChCl	ChCl/cat 1:1 cocr.	ChCl/cat 1:2 cocr.	cat	
choline chloride (ChCl)	99.5(6)	0.0(2)	0.5(4)	0.0(3)	11.472
catechol (cat)	0.0(2)	0.4(4)	0.3(4)	99.3(6)	11.698
ChCl/cat 1:1 mixture	0.5(2)	94.6(4)	4.3(3)	0.6(2)	8.103
ChCl/cat 1:2 mixture	0.4(2)	0.1(2)	99.0(4)	0.5(2)	9.126
ChCl/cat 2:3 mixture	0.2(1)	42.2(3)	57.3(3)	0.2(1)	6.849
ChCl/cat 1:3 mixture	0.5(2)	0.2(2)	69.8(4)	29.6(4)	8.747
ChCl/cat 2:1 mixture	45.7(3)	51.3(4)	2.6(2)	0.4(1)	7.018

Table S8: Results of quantitative phase analysis via Rietveld refinement in the cholin chloride/hydroquinone system.

	% weight			Rwp
	ChCl	ChCl/hyd 1:1 cocr.	hyd	
choline chloride (ChCl)	97.5(7)	0.8(4)	1.7(6)	11.408
hydroquinone (hyd)	0.5(2)	0.0(3)	99.5(4)	12.057
ChCl/hyd 1:1	0.8(3)	97.1(5)	2.1(5)	11.400
ChCl/hyd 1:2	0.0(1)	77.8(4)	22.1(3)	8.369
ChCl/hyd 1:3	0.0(1)	53.0(3)	47.0(3)	6.675
ChCl/hyd 2:1	30.0(3)	69.9(4)	0.1(3)	8.027
$x_{\text{hyd}} = 0.85$	0.2(1)	67.4(3)	32.5(3)	6.372

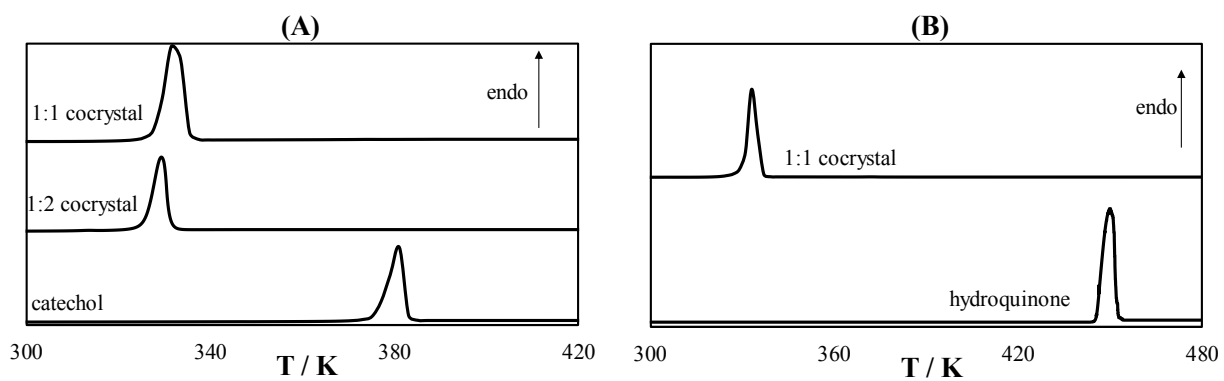


Figure S7. Differential scanning calorimetry curve of cocrystals and pure components of (A) choline chloride (ChCl)/catechol and (B) ChCl/hydroquinone eutectic systems.

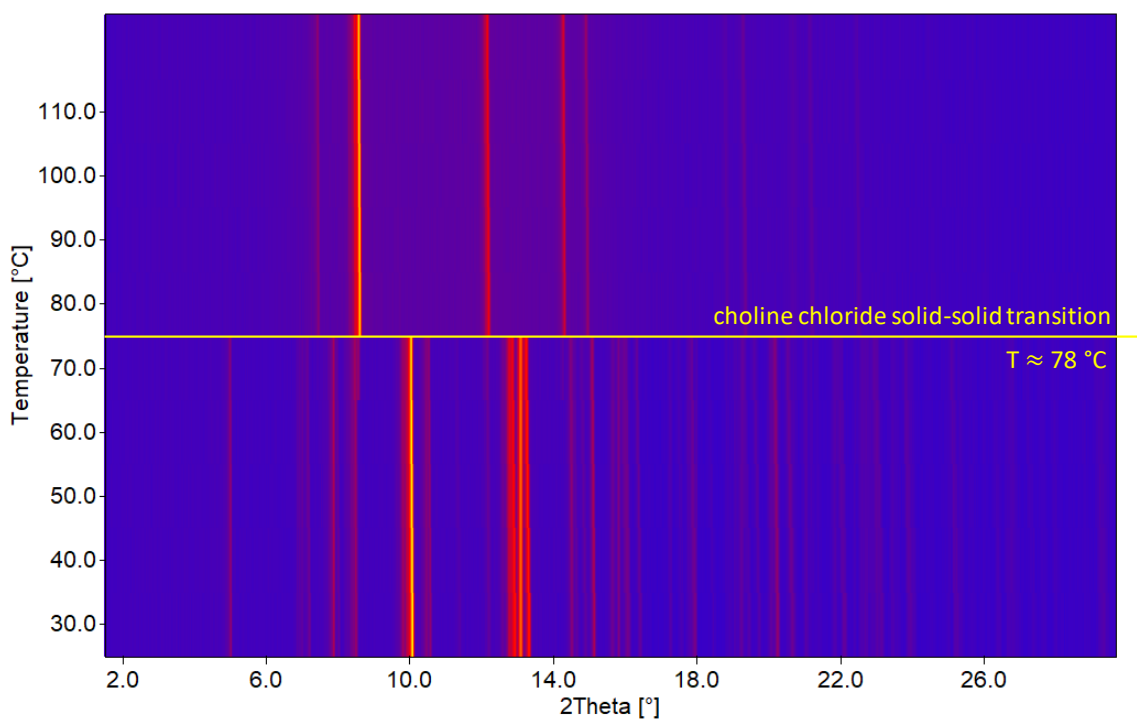


Figure S8: Variable-temperature X-ray powder diffraction study of choline chloride.

## References

1. *APEX suite of crystallographic software*, APEX 3, Version 2019-1.0, Bruker AXS Inc., Madison, Wisconsin, USA, 2019.
2. *SAINT*, Version 8.40A and *SADABS*, Version 2016/2, Bruker AXS Inc., Madison, Wisconsin, USA, 2016/2019.
3. Sheldrick, G. M. *Acta Crystallogr. Sect. A* **2015**, *71*, 3–8.
4. Sheldrick, G. M. *Acta Crystallogr. Sect. C* **2015**, *71*, 3–8.
5. Hübschle, C. B.; Sheldrick, G. M.; Dittrich, B. *J. Appl. Cryst.* **2011**, *44*, 1281–1284.
6. *International Tables for Crystallography, Vol. C* (Ed.: A. J. Wilson), Kluwer Academic Publishers, Dordrecht, The Netherlands, **1992**.
7. Spek, A. L. *Acta Crystallogr. Sect. D* **2009**, *65*, 148–155.
8. C. F. Macrae, I. J. Bruno, J. A. Chisholm, P. R. Edgington, P. McCabe, E. Pidcock, L. Rodriguez-Monge, R. Taylor, J. van de Streek, P. A. Wood, *J. Appl. Cryst.* **2008**, *41*, 466–470.
9. Flack, H. D. *Acta Crystallogr. Sect A* **1983**, *39*, 876–881; Parsons, S.; Flack, H. D.; Wagner, T. *Acta Crystallogr. Sect B* **2013**, *69*, 249–259.
10. *TOPAS*, Version 6, Bruker AXS Inc., Madison, Wisconsin, USA, 2016.

### 3.6 Paper VI

#### **Cocrystal Formation in L-Menthol/Phenol Eutectic System: Experimental Study and Thermodynamic Modeling**

**A. Alhadid, C. Jandi, L. Mokrushina, and M. Minceva**, *Cryst. Growth Des.* **2022**, *22*, 6, 3973–3980.

Author contribution: The thesis author conceptualized the paper's idea, performed the investigations and formal analysis (excluding powder and SC-XRD), interpreted the results, and wrote the manuscript.

Summary: Paper VI demonstrates the potential of predictive and correlative thermodynamic models to describe SLE in eutectic systems with cocrystal formation. The SLE data of the L-menthol/phenol eutectic system were obtained by a combination of DSC and XRD measurements. Two cocrystals were identified in the L-menthol/phenol eutectic system. The crystal structure of the two cocrystals was solved by the SC-XRD technique and from powder XRD data. The obtained crystal structures showed that hydrogen bonds are the main feature in the cocrystal forming helical chains between the OH groups of the molecules.

This study is the first to use COSMO-RS to model SLE in eutectic systems with cocrystal formation. COSMO-RS calculations were performed using TZVP and TZVPD\_FINE parameterization. It was found that COSMO-RS calculations at the TZVPD\_FINE level provides better predictions for the liquidus lines of pure constituents and cocrystals compared to the TZVP level. The two eutectic points predicted by the NRTL and COSMO-RS models were in good agreement with the experimentally determined eutectic temperatures.

Paper VI emphasizes the importance of experimental investigation of cocrystal formation for SLE modeling, whether using correlative or predictive thermodynamics models. The proper evaluation of the performance of thermodynamic models in predicting the eutectic temperature of eutectic mixtures with cocrystal formation should rely on SLE data obtained by a combination of DSC and XRD analyses.

Despite the significant negative deviation from ideal behavior, the measured eutectic temperature of the system was not far from the eutectic temperature calculated using the ideal solution model. This was attributed to the formation of the two cocrystals. If no cocrystals are formed, the eutectic temperature determined by NRTL and COSMO-RS was significantly lower



### 3.6 Paper VI

than the experimentally observed one. Therefore, cocrystal formation could revoke the influence of nonideality on the depression of the melting temperature at the eutectic point.

### 3.6 Paper VI

Reprinted with permission from Alhadid et al., *Cryst. Growth Des.*, **2022**, 22 (6), 3973-3980. DOI: 10.1021/acs.cgd.2c00362. Copyright 2022 American Chemical Society.

Article full text: <http://pubs.acs.org/articlesonrequest/AOR-3FTJ2S7WIHUD5KXIKNZ2>

# Cocrystal Formation in L-Menthol/Phenol Eutectic System: Experimental Study and Thermodynamic Modeling

Ahmad Alhadid, Christian Jandl, Liudmila Mokrushina, and Mirjana Minceva\*

Cite This: <https://doi.org/10.1021/acs.cgd.2c00362>

Read Online

ACCESS |



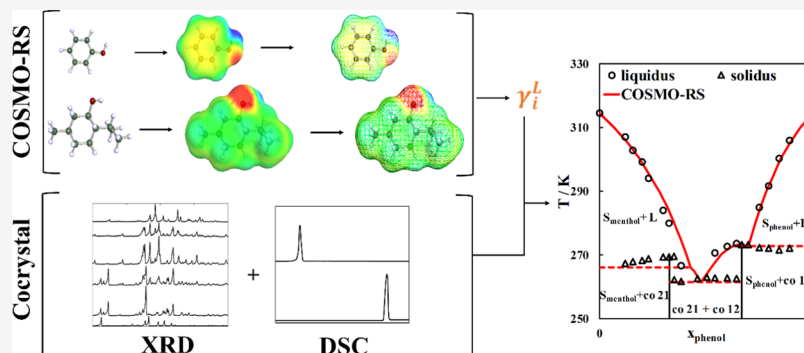
Metrics &amp; More



Article Recommendations



Supporting Information



**ABSTRACT:** Deep eutectic solvents (DESs) are eutectic mixtures containing a hydrogen-bond acceptor and donor, forming a mixture with a significantly lower melting temperature than those of its pure constituents. DESs containing cyclohexyl and phenolic alcohols draw particular attention due to the observed large depression in the melting temperature of the mixture. The present study investigates in detail the solid–liquid equilibria (SLE) in the L-menthol/phenol eutectic system. Differential scanning calorimetry and powder X-ray diffraction (XRD) analysis were employed to obtain the phase diagram. Two cocrystals were identified with 1:2 and 2:1 ratios. The crystal structures were determined by single-crystal and powder XRD techniques. The SLE data were correlated using the nonrandom two-liquid (NRTL) model and the conductor-like screening model for realistic solvation (COSMO-RS). The two eutectic points determined by the NRTL and COSMO-RS models are  $x_{e,1}^{\text{NRTL}} = 0.69$ ,  $T_{e,1}^{\text{NRTL}} = 273.1$  K,  $x_{e,2}^{\text{NRTL}} = 0.47$ ,  $T_{e,2}^{\text{NRTL}} = 261.3$  K,  $x_{e,1}^{\text{COSMO}} = 0.70$ ,  $T_{e,1}^{\text{COSMO}} = 272.8$  K, and  $x_{e,2}^{\text{COSMO}} = 0.48$ ,  $T_{e,2}^{\text{COSMO}} = 261.5$  K, which are in good agreement with the experimental eutectic temperatures.

## 1. INTRODUCTION

Deep eutectic solvents (DESs) are eutectic mixtures formed by mixing two or more inexpensive and widely available substances to produce a novel solvent with unique properties. Soon after the term DES was introduced, the interest and research on using them as a new class of green and tunable solvents in various applications increased significantly.<sup>1</sup> Majority of studied DESs contain ionic constituents, which possess some advantages of ionic liquids (ILs), such as negligible volatility and nonflammability.<sup>1–6</sup> However, ionic DESs possess a significant drawback of being hygroscopic.<sup>7</sup> The hygroscopic nature of ionic DESs affects their physicochemical properties and limits their applicability. On the other hand, nonionic DESs—usually referred to as type V DES—could be formed by mixing simple organic substances.<sup>8–13</sup> Nonionic DESs have several advantages over ionic DESs, such as lower cost, melting temperature, and viscosity.<sup>14–16</sup>

The knowledge of solid–liquid equilibria (SLE) in DESs provides information about the melting temperature of the mixture at any molar ratio between constituents, which is

essential to select the constituents, determine the DES eutectic point, or select the mixture composition for a certain application.<sup>17</sup> So far, the SLE data available for nonionic DESs show that they follow ideal solution behavior,<sup>18–21</sup> with an exception for DESs formed by mixing cyclohexyl and phenolic alcohols, such as L-menthol/thymol and L-menthol/carvacrol.<sup>22,23</sup> Due to substantial negative deviation from ideality, DESs formed by mixing cyclohexyl and phenolic alcohols are suspected of glass formation.<sup>14</sup> Moreover, some phenolic alcohols are known cofomers that have been shown to form cocrystals with several substances.<sup>22,24–27</sup> Glass and cocrystal formations complicate measuring the SLE phase diagram of eutectic mixtures containing cyclohexyl and phenolic alcohols, which limited the number of SLE studies

**Received:** March 26, 2022

**Revised:** April 27, 2022

**Table 1. Melting Properties of Pure Components Used to Model the Solid–Liquid Equilibria of the L-Menthol/Phenol Eutectic System**

substance	$\Delta h_m/\text{kJ mol}^{-1}$	$T_m/\text{K}$	$\Delta c_p = a + bT/\text{J mol}^{-1} \text{K}^{-1}$			
			$a$		$b$	
			liquid	solid	liquid	solid
L-menthol	13.74 <sup>23</sup>	314.6 <sup>23</sup>	−195.20 <sup>50</sup>	−68.0 <sup>50</sup>	1.795 <sup>50</sup>	1.092 <sup>50</sup>
phenol	12.36 ± 0.07 <sup>a,b</sup>	313.9 ± 0.10 <sup>a</sup>	100.86 <sup>c</sup>	10.038 <sup>c</sup>	0.3203 <sup>c</sup>	0.392 <sup>c</sup>

<sup>a</sup>Measured in this work using DSC. <sup>b</sup>Uncertainties are the standard deviation of three samples. <sup>c</sup>Calculated using the experimental data from Andon et al.<sup>49</sup> (see Figure S1 in the SI).

available in the literature for this distinctive type of eutectic mixtures.<sup>22,23,28</sup>

Modeling SLE allows for the determination of the eutectic point of the system, which is difficult to determine experimentally. Prerequisites for modeling SLE are activity coefficients, which are a measure of intermolecular interactions between molecules in the liquid phase. The activity coefficients can be calculated using thermodynamic models. Correlative models, such as regular solution theory or the nonrandom two-liquid (NRTL) model, have been successfully used in the literature to model SLE in nonideal eutectic systems.<sup>29–33</sup> However, predictive models are preferable to prevent the need for experimental data to model SLE. The conductor-like screening model for realistic solvation (COSMO-RS) was proposed to calculate the activity coefficients and thus predict the eutectic point and the phase diagram of ionic and nonionic DESs.<sup>20,34,35</sup> SLE calculations using COSMO-RS have been exclusively performed assuming that the constituents crystallize in pure form, i.e., the simple eutectic behavior.<sup>20,34,35</sup> However, cocrystal formation has been identified in some DESs.<sup>22,25</sup> Cocrystal, hydrate, and solvate formations in binary eutectic mixtures have been successfully modeled using the perturbed-chain statistical associating fluid theory (PC-SAFT).<sup>36–39</sup> To the best of our knowledge, no study has evaluated the performance of COSMO-RS in predicting the phase diagram of binary eutectic systems with cocrystal formation, as COSMO-RS has been only used in several studies to screen and select suitable cofomers a priori.<sup>40–46</sup> Loschen and Klant<sup>47</sup> used COSMO-RS to predict the SLE phase diagram of several ternary systems containing an active ingredient, cofomer, and solvent. However, due to the strong association in the liquid phase, an additional binary interaction parameter was introduced and fitted to experimental data, which withdrew COSMO-RS predictive ability.

The present study investigates the SLE in the binary eutectic system L-menthol/phenol. The SLE data were measured using differential scanning calorimetry (DSC). Powder X-ray diffraction (XRD) analysis was performed on samples covering the whole composition range of the mixture to evaluate the formation of cocrystals. The melting properties of the cocrystals were measured by DSC. The SLE data were modeled considering the cocrystal formation using the correlative (NRTL) and predictive (COSMO-RS) thermodynamic models to obtain the solid–liquid phase diagram of the eutectic system.

## 2. MATERIALS AND METHODS

**2.1. Experimental SLE.** L-Menthol (water content 107.5 ± 0.9 ppm, purity ≥99%, Sigma-Aldrich) was mixed with phenol (water content 82.4 ± 5.0 ppm, purity ≥99%, Alfa Aesar) in different ratios. The pure constituents' water content was analyzed using Karl–Fischer Coulometer (Hanna Instrument) in triplicate. The eutectic

mixtures were heated gently to 315 K under continuous stirring inside closed glass vials to obtain clear homogeneous liquids.

Because the eutectic system is suspected of glass formation,<sup>14,23</sup> the samples were prepared by quenching and annealing as previously described.<sup>22</sup> In short, liquid mixtures were quenched at 193 K for several hours and then annealed at 253 K for several days to aid the crystallization. Generally, the annealing time to observe the complete solidification of the sample is between 1 and 5 days. The obtained solid was ground to a fine powder using a mortar and pestle within a cold room at 253 K and then directly introduced into DSC crucibles in triplicate. The DSC crucibles were immediately hermetically sealed.

The DSC (NETZSCH DSC 200 F3, Germany) was calibrated prior to measurements using adamantane, bismuth, cesium chloride, indium, tin, and zinc with a mass fraction purity of 99.999%. The DSC chamber was precooled to 253 K before introducing the samples. A cooling step to 193 K with a cooling rate of 10 K min<sup>−1</sup> was performed first. Then, a heating run to 320 K was performed with a heating rate of 5 K min<sup>−1</sup>. Measurements were performed under a nitrogen atmosphere. The melting temperatures of pure components and the solidus temperatures were determined as the onset temperatures and the liquidus temperatures as the peak maximum temperatures. The average standard uncertainty of the measured liquidus temperatures was 0.4 K.

**2.2. XRD.** Powder XRD analysis was performed to identify the crystallized solid phases. The crystallized samples with different compositions were finely ground within a cold room at 253 K and directly filled into 0.70 or 1.5 mm diameter glass capillaries (Hilgenberg, Germany). Powder XRD patterns were recorded in Debye–Scherrer geometry on a Stadi P diffractometer (Stoe & Cie, Germany) equipped with a Mo fine-focus sealed tube, a curved Ge monochromator selecting  $K\alpha_1$  radiation ( $\lambda = 0.7093 \text{ \AA}$ ), and a Mythen2 R 1K detector (Dectris, Switzerland). All data were collected with a step size of  $2\theta = 0.015^\circ$  per data point. The measurements were performed at 253 K using an 800 series cryostream (Oxford, UK) unless stated otherwise.

The crystal structures of the observed cocrystals were solved by single-crystal (SC)-XRD analysis and from powder XRD data. An SC with sufficient size and quality for SC-XRD analysis was obtained by mixing 1 g of the liquid 2:1 mixture with 1 mL of acetonitrile. The liquid mixture was stored at 253 K until suitable crystals appeared. Details on sample preparation and structure solution are provided in the Supporting Information (SI).

**2.3. Thermodynamic Modeling.** The phase diagram and the eutectic points of the eutectic mixture can be obtained by modeling experimental SLE data. For the regions where pure L-menthol and phenol crystallize, the liquidus lines were calculated as follows<sup>48</sup>

$$\ln x_i^L \gamma_i^L = -\frac{\Delta h_{m,i}}{RT} \left(1 - \frac{T}{T_{m,i}}\right) - \frac{1}{RT} \int_{T_m}^T \Delta c_p(T) dT + \frac{1}{R} \int_{T_m}^T \frac{\Delta c_p(T)}{T} dT \quad (1)$$

where  $x_i^L$  and  $\gamma_i^L$  are the mole fraction and activity coefficient of component  $i$  in the liquid solution, respectively;  $\Delta h_{m,i}$  and  $T_{m,i}$  are the melting enthalpy and melting temperature of pure component  $i$ , respectively;  $R$  and  $T$  are the universal gas constant and the temperature, respectively; and  $\Delta c_{p,i}$  is the difference between the

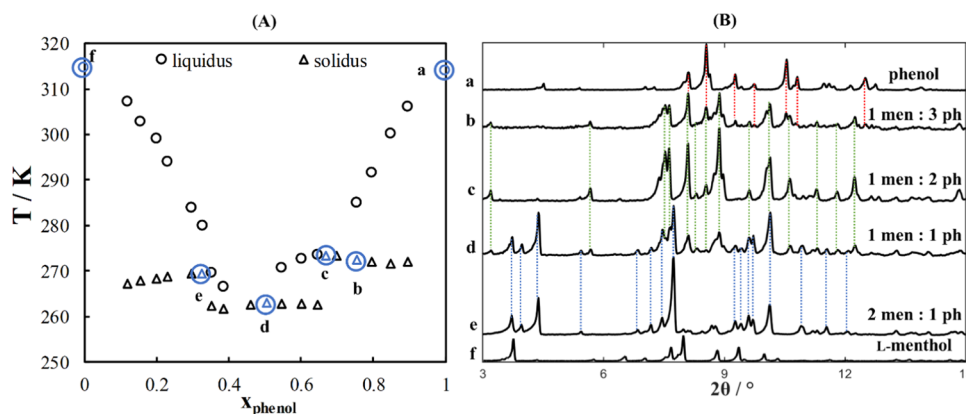


**Figure 1.** (A) Solid–liquid equilibria data for L-menthol/phenol eutectic system. (B) Powder X-ray diffraction (XRD) patterns of pure L-menthol (men), phenol (ph), and mixtures of different ratios marked with circles in (A). XRD measurements were performed at 253 K. The characteristic peaks are marked as follows: phenol (red dotted line), 1:2 cocystal (green dotted lines), 2:1 cocystal (blue dotted lines).

constant pressure heat capacities of component  $i$  in the liquid and solid states. Three approaches were used for considering the last two terms on the right-hand side of eq 1, namely, neglecting  $\Delta c_p$ , assuming constant  $\Delta c_p$  value calculated at the melting temperature, or temperature-dependent  $\Delta c_p$ . Experimental data on the heat capacity of pure L-menthol and phenol in the solid and liquid states were taken from the literature.<sup>49,50</sup> The pure components' melting properties used to model the SLE data using eq 1 are shown in Table 1.

To model the cocystal liquidus lines, the formation of a cocystal was considered via the following chemical reaction<sup>22,38</sup>



where  $\vartheta_A$  and  $\vartheta_B$  are the stoichiometric coefficients of components A and B in the cocystal, respectively. The equilibrium constant ( $K_a$ ) of the chemical reaction was defined as follows

$$K_a = \prod_i a_i^{\vartheta_i} = (x_A^L \gamma_A^L)^{\vartheta_A} (x_B^L \gamma_B^L)^{\vartheta_B} \quad (3)$$

The equilibrium constant of the chemical reaction at different temperatures was calculated using the Gibbs–Helmholtz equation

$$\ln K_a = \ln K_a^{\text{ref}} + \frac{\Delta h^{\text{ref}}}{R} \left( \frac{1}{T^{\text{ref}}} - \frac{1}{T} \right) \quad (4)$$

where  $T^{\text{ref}}$  is a reference temperature,  $K_a^{\text{ref}}$  is the equilibrium constant at  $T^{\text{ref}}$ , and  $\Delta h^{\text{ref}}$  is the melting enthalpy of the cocystal at  $T^{\text{ref}}$ . The equilibrium constant at  $T^{\text{ref}}$  was calculated as follows

$$K_a^{\text{ref}} = (x_A^{\text{ref}} \gamma_A^{\text{ref}})^{\vartheta_A} (x_B^{\text{ref}} \gamma_B^{\text{ref}})^{\vartheta_B} \quad (5)$$

where  $x^{\text{ref}}$  and  $\gamma^{\text{ref}}$  are the mole fraction and the activity coefficient of the component at the cocystal stoichiometry, respectively.

The activity coefficients of components  $\gamma_i^L$  for modeling the liquidus lines of pure constituents (eq 1) and cocystals (eqs 3–5) were calculated using the NRTL and COSMO-RS models. The NRTL equation was used to calculate the activity coefficients as follows<sup>48</sup>

$$\ln \gamma_i^L = x_j^2 \left[ \tau_{ji} \left( \frac{G_{ji}}{x_i + x_j G_{ji}} \right)^2 + \frac{\tau_{ij} G_{ij}}{(x_j + x_i G_{ij})^2} \right] \quad (6)$$

$$G_{ij} = \exp(-\alpha \tau_{ij}) \quad G_{ji} = \exp(-\alpha \tau_{ji}) \quad (7)$$

$$\tau_{ij} = \frac{g_{ij} - g_{jj}}{RT} \quad \tau_{ji} = \frac{g_{ji} - g_{ii}}{RT} \quad (8)$$

The NRTL binary interaction parameters ( $g_{ij} - g_{jj}$ ) and ( $g_{ji} - g_{ii}$ ) were fitted to the experimental data on pure components' liquidus lines ( $T_i^{\text{exp}}$ ) by minimizing the following objective function

$$F(T) = \sum_{i=1}^n \left( \frac{(T_i^{\text{exp}} - T_i^{\text{cal}})^2}{n} \right)^{1/2} \quad (9)$$

where  $T_i^{\text{cal}}$  is the liquidus temperature of pure constituents calculated using the NRTL model and  $n$  is the number of experimental data points. The value of the nonrandomness parameter ( $\alpha$ ) in eq 7 was set to 0.3.

To predict the phase diagram of the eutectic system using COSMO-RS, the activity coefficients of components were calculated from the molecular structure.<sup>51–53</sup> The molecular geometry and the screening surface charge density were obtained by DFT calculations using the BP86 functional and the def-TZVP and def-TZVPD basis sets for TZVP and TZVPD\_FINE levels, respectively, employing Turbomole<sup>54</sup> (TURBOMOLE GmbH, version 6.6). The activity coefficients of components were calculated by COSMOtherm<sup>55</sup> (Dassault Systèmes, version 19) with the BP\_TZVP\_19.ctd and BP\_TZVPD\_FINE\_19.ctd parameter sets for TZVP and TZVPD\_FINE levels. The obtained activity coefficients were used to calculate the liquidus lines of pure constituents (eq 1) and cocystals (eqs 3–5).

### 3. RESULTS

**3.1. Experimental SLE.** DSC analysis was used to measure the solidus and liquidus temperatures of the L-menthol/phenol binary eutectic system. The obtained experimental data and the DSC curves are found in Table S1 and Figure S2 in the SI, respectively. Figure 1A shows the experimental liquidus and solidus temperatures (points). As seen in Figure 1A, the system shows three different solidus temperatures. The solidus temperatures in the ranges  $x_{\text{phenol}} = 0.67–1.0$ ,  $0.33–0.67$ , and  $0–0.33$  are  $\sim 273$ ,  $262$ , and  $268$  K, respectively.

The three different solidus temperatures observed for the system hint at cocystal formation. Figure 1B shows the powder XRD patterns of pure components (points a and f) and samples with 1:3 (point b), 1:2 (point c), 1:1 (point d), and 2:1 (point e) for L-menthol:phenol ratios (marked with circles in Figure 1A). Dotted lines connect the matching peaks observed in the XRD patterns of samples. Starting from samples in the phenol-rich composition range, it is clear from Figure 1B that the 1:3 ratio sample XRD pattern is the sum of the XRD patterns of pure phenol (red dotted lines) and the 1:2 ratio sample (green dotted lines), indicating that the solid phase of the 1:3 ratio sample consists of both pure phenol and the solid phase of the 1:2 ratio sample. The 1:2 ratio sample XRD pattern does not contain the XRD pattern peaks of pure

phenol or L-menthol. Thus, it is postulated that a cocrystal with a ratio of 1:2 is formed.

For the 1:2 cocrystal, it was not possible to obtain SCs suitable for SC-XRD analysis. As an alternative, powder XRD data were used for the structure determination. During a long-term measurement of the sample divided into eight identical runs of approximately 90 min duration, distinct changes over the first three runs in the powder XRD pattern were observed, indicating a phase transition (see Figures S3 and S4 in the SI). Thus, it can be concluded that the primary cocrystal formed at 1:2 and 1:3 ratios (Figure 1B) is metastable and transforms into the more stable structure that is observed in further runs. This could also justify the difficulty in obtaining an SC suitable for SC-XRD analysis. However, powder XRD data of the stable polymorph were sufficient for structure determination and confirmed the 1:2 ratio of L-menthol and phenol (see Table 2).

**Table 2. Unit Cell Data of the Crystal Structures of the 2:1 and 1:2 L-Menthol:Phenol Cocrystals Solved from Powder Diffraction Data<sup>a</sup>**

	L-menthol/phenol 2:1	L-menthol/phenol 1:2
formula	2(C <sub>10</sub> H <sub>20</sub> O), C <sub>6</sub> H <sub>6</sub> O	C <sub>10</sub> H <sub>20</sub> O, 2(C <sub>6</sub> H <sub>6</sub> O)
molecular weight (g mol <sup>-1</sup> )	406.63	344.48
Bravais lattice	monoclinic P	orthorhombic P
space group	P2 <sub>1</sub>	P2 <sub>1</sub> 2 <sub>1</sub> 2 <sub>1</sub>
a (Å)	6.099	20.3936
b (Å)	21.7903	16.8032
c (Å)	10.4267	6.2151
α (°)	90	90
β (°)	100.9126	90
γ (°)	90	90
volume (Å <sup>3</sup> )	1360.649	2129.77
Z	2	4

<sup>a</sup>See Table S3 in the SI for more details.

Based on powder XRD analysis, the solidus temperatures observed at 1:3 (point b, ~272 K) and 1:2 (point c, ~273 K) ratio samples represent the eutectic temperature in the phenol-rich region ( $x_{\text{phenol}} > 0.67$ ) and the 1:2 cocrystal melting temperature, respectively.

Examining the 1:1 ratio sample XRD pattern, it can be seen that the solid phase of the 1:1 ratio sample consists of the 1:2 cocrystal and the solid phase of the 2:1 ratio sample. The 2:1 ratio sample XRD pattern does not contain the peaks of pure phenol, L-menthol, or the 1:2 cocrystal. This hints at the formation of a second cocrystal at a 2:1 ratio. The structure of the 2:1 L-menthol:phenol cocrystal was obtained from powder XRD data and was confirmed by single-crystal XRD (see Table 2 and Table S2 in the SI). Figure 2 shows the overlay of the asymmetric units of the structures of the 2:1 cocrystal obtained by SC-XRD and powder XRD data. As seen, a good agreement between the two obtained crystal structures is observed, which proves the reliability of our structure solutions from powder XRD data. The slight difference in unit cell dimensions is due to the temperature at which the measurements were performed, i.e., SC-XRD at 100 K and powder XRD at 253 K. Moreover, the small variation in the molecular geometries of constituents observed in Figure 2 is attributed to the input geometries of the molecular fragments used for the powder structure solution and rigid-body refinement. Figures 3 and 4 show the packing diagrams of the structures of the 1:2 and 2:1

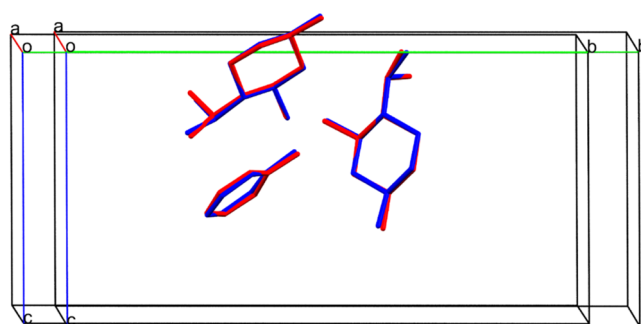


**Figure 2.** Overlay of the asymmetric units of the structures of the 2:1 L-menthol:phenol cocrystal from single-crystal (red) and powder (blue) X-ray diffraction data. Unit cells are shifted for better comparison.

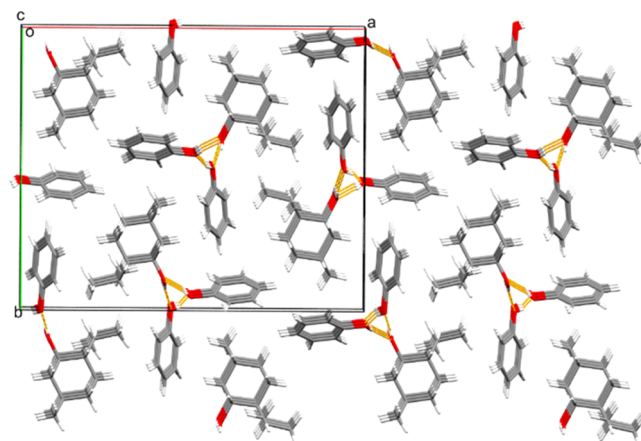


**Figure 3.** Packing diagram of the structure of the 1:2 L-menthol:phenol cocrystal viewed along the c axis. The structure was obtained from powder X-ray diffraction data.

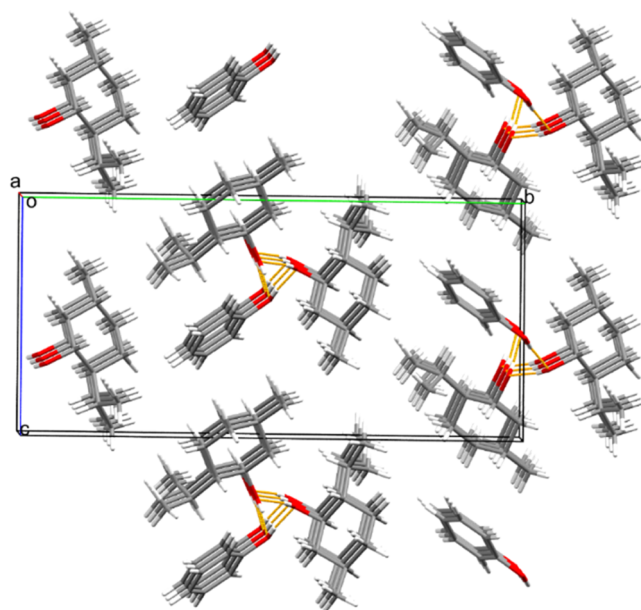


**Figure 4.** Packing diagram of the structure of the 2:1 L-menthol:phenol cocrystal viewed along the a-axis. The structure was obtained from single-crystal X-ray diffraction data.

cocrystals. As seen, hydrogen bonds are the dominant feature forming helical chains between the OH groups of the

molecules along the *c*- and *a*-axes in the 1:2 and 2:1 cocrystals, respectively. The hydrophobic parts of the molecules are then facing outwards, and these strains of molecules are arranged in parallel along the respective axis.

As seen in Figure 1A, at the 2:1 ratio (point e), along with the observed solidus temperature, a liquidus temperature is observed, which indicates that the 2:1 cocrystal melts incongruently (peritectic transition). To confirm the peritectic transition, powder XRD analysis was performed on the 2:1 ratio sample at two temperatures, lower and higher than the solidus temperature observed in the L-menthol-rich region (268 K). Figure 5 shows the powder XRD pattern of pure L-

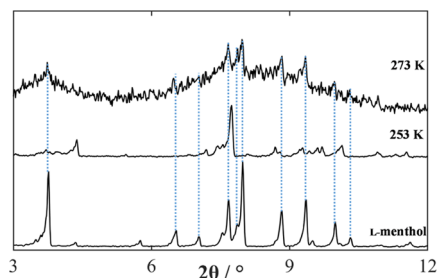


**Figure 5.** Powder X-ray diffraction pattern for pure L-menthol at 253 K and 2:1 cocrystal at 253 and 273 K.

menthol at 253 K, 2:1 cocrystal at 253 K, and 2:1 cocrystal at 273 K; blue dotted lines extended the characteristic peaks of the L-menthol XRD pattern. As seen in Figure 5, it is clear that no peaks corresponding to pure L-menthol are observed in the 2:1 cocrystal XRD pattern at 253 K. In contrast, the characteristic peaks of pure L-menthol can be observed in the 2:1 ratio sample XRD pattern at 273 K. Thus, the 2:1 cocrystal decomposes at the solidus temperature observed in the L-menthol-rich region (~268 K) to a liquid phase and solid L-menthol. Accordingly, the solidus temperatures observed in Figure 1A at 1:1 (point d, ~262 K) and 2:1 (point e, ~268 K) ratio samples correspond to the eutectic temperature in the middle composition range and the decomposition temperature of the 2:1 cocrystal.

In conclusion, the DSC and powder XRD analyses performed on samples of the L-menthol/phenol eutectic system covering the complete composition range showed that the system is not of the simple eutectic type. Two cocrystals with melting temperatures of 273.3 and 269.4 K were observed at 1:2 and 2:1 ratios. The system has two eutectic temperatures: the first is around 272 K in the phenol-rich composition range, and the second is around 263 K in the middle composition range.

**3.2. Thermodynamic Modeling.** The experimental liquidus data and the information about the formed cocrystals acquired by DSC and XRD analyses were used to model the phase diagram of the L-menthol/phenol system. The correlative thermodynamic model NRTL was shown to be successful in describing the SLE in eutectic mixtures with cocrystal formation.<sup>22,25</sup> In this work, the predictive thermodynamic model COSMO-RS performance was evaluated in describing cocrystal formation in eutectic mixtures.

The NRTL parameters were obtained by fitting the experimental liquidus data of pure components and assuming three approaches regarding the heat capacity terms in eq 1, namely, neglecting the heat capacity terms, assuming constant  $\Delta c_p$  calculated at the melting temperature of the pure

component, and temperature-dependent  $\Delta c_p$ . Table 3 shows the obtained NRTL binary interaction parameters and RMSD

**Table 3.** Obtained Binary Interaction Parameters and RMSD from Modeling the Pure Components Liquidus Lines Using Different Approaches Considering the Heat Capacity Term

	$(g_{12}-g_{22})/\text{kJ mol}^{-1}$	$(g_{21}-g_{11})/\text{kJ mol}^{-1}$	RMSD/K
$\Delta c_p = 0$	-3.1628	-2.3630	2.3
constant $\Delta c_p$	-2.9026	-1.4834	1.9
temperature-dependent $\Delta c_p$	-2.8372	-1.5449	2.0

between calculated and experimental liquidus temperatures of pure components. As seen in Table 3, the smallest RMSD is observed when considering constant or temperature-dependent  $\Delta c_p$ . Moreover, the obtained binary interaction parameters are quite similar in both cases. On the other hand, the largest RMSD is observed when neglecting the  $\Delta c_p$  term. Therefore, the binary interaction parameters obtained assuming constant  $\Delta c_p$  values—best fit—were used further to obtain the phase diagram in the middle composition range.

The phase diagram in the middle composition range—representing the crystallization of the two cocrystals—was modeled using eqs 3–5. The melting properties of the cocrystals were measured using DSC, and the results are shown in Table 4. The activity coefficients were calculated

**Table 4.** Melting Properties of the 1:2 and 2:1 for L-Menthol:Phenol Cocrystals Used in Modeling their Liquidus Lines

cocrystal	$\Delta h_m/\text{kJ mol}^{-1}$	$T_m/\text{K}$
1:2 cocrystal	$27.48 \pm 0.24$	$273.3 \pm 0.1$
2:1 cocrystal	$20.35 \pm 0.25$	$269.4 \pm 0.1$

using the NRTL model with binary interaction parameters obtained when assuming constant  $\Delta c_p$  (Table 3). Figure 6 shows the phase diagram of the L-menthol/phenol eutectic system modeled considering cocrystal formation. As seen in Figure 6A, the NRTL model provides an adequate description of the liquidus temperatures (circles) of pure components and cocrystals. Moreover, the eutectic points determined by the NRTL model ( $x_{e,1}^{\text{NRTL}} = 0.69$ ,  $T_{e,1}^{\text{NRTL}} = 273.1$  K and  $x_{e,2}^{\text{NRTL}} = 0.47$ ,  $T_{e,2}^{\text{NRTL}} = 261.3$  K) are in good agreement with the measured solidus temperatures (triangles) in the phenol-rich and middle composition regions ( $T_{e,1}^{\text{exp}} = 272.3$  K and  $T_{e,2}^{\text{exp}} = 262.5$  K).

Figure 6B shows the COSMO-RS predictions at the TZVP (blue lines) and TZVPD\_FINE (red lines) levels for the SLE phase diagram of the L-menthol/phenol eutectic system considering the formation of the two cocrystals. COSMO-RS satisfactorily predicts the course of the phenol liquidus line at the TZVPD\_FINE (red lines) level, while at the TZVP level (blue lines), COSMO-RS underestimates the nonideality of phenol in the liquid phase. In contrast, the COSMO-RS model at the TZVP level well describes the nonideality of the L-menthol in the liquid phase, while at the TZVPD\_FINE level, COSMO-RS underestimates the nonideality of L-menthol. Accordingly, COSMO-RS better describes the peritectic point of the 2:1 cocrystal at the TZVP level compared to the TZVPD\_FINE level. However, the COSMO-RS predictions for SLE in the middle composition range corresponding to the

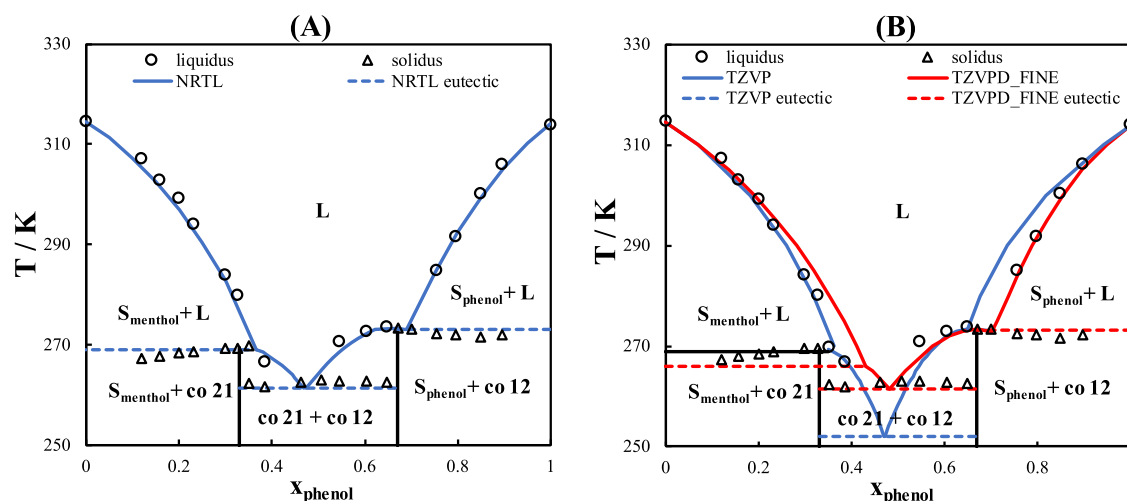


**Figure 6.** Solid–liquid phase diagram of L-menthol/phenol eutectic system modeled using the (A) NRTL and (B) COSMO-RS models.

crystallization of the cocrystals are significantly improved at the TZVPD\_FINE level compared to the TZVP level. The two eutectic points predicted by COSMO-RS at the TZVPD\_FINE level are  $x_{e,1}^{\text{COSMO}} = 0.70$ ,  $T_{e,1}^{\text{COSMO}} = 272.8$  K, and  $x_{e,2}^{\text{COSMO}} = 0.48$ ,  $T_{e,2}^{\text{COSMO}} = 261.5$  K. Bearing in mind that the model is purely predictive, COSMO-RS predictions at the TZVPD\_FINE level for the two eutectic points are quite reasonable, comparable with the correlative thermodynamic model predictions, and agree well with those observed experimentally.

Nevertheless, a good estimation for the eutectic points of the system using the NRTL and COSMO-RS models was obtained when considering the formation of the two cocrystals. Figure 7 shows COSMO-RS predictions neglecting cocrystal formation. As seen in Figure 7, the estimated eutectic temperature by the COSMO-RS model at the TZVPD\_FINE level is  $x_e^{\text{COSMO}} = 0.55$  and  $T_e^{\text{COSMO}} = 228.0$  K, while COSMO-RS calculations at the TZVP level fail to estimate the eutectic temperature within

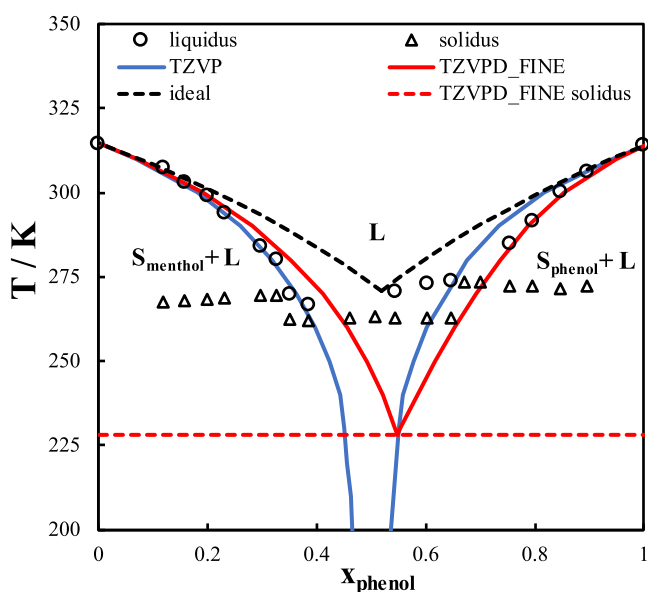


**Figure 7.** Solid–liquid phase diagram of L-menthol/phenol eutectic system modeled using the COSMO-RS models assuming the simple eutectic type.

a reasonable temperature range. Therefore, it is evident that for a proper determination of the eutectic point of eutectic systems, cocrystal formation should be investigated beforehand. Moreover, the unreliable COSMO-RS predictions for the eutectic point of some DESs observed in previous studies found in the literature might result from ruling out cocrystal formation.<sup>34,35</sup> Furthermore, as seen in Figure 7, the observed eutectic temperature of the system in the middle composition region ( $T_{e,2}^{\text{exp}} = 262.5$  K) is not far from the eutectic temperature calculated by the ideal solution model ( $T_e^{\text{ideal}} = 270.8$  K). The small difference between the ideal and observed eutectic temperatures of the system despite the observed significant negative deviation from ideal behavior is attributed to the formation of the two cocrystals.

#### 4. CONCLUSIONS

This study reports the phase diagram of the L-menthol/phenol eutectic system. The SLE data were measured using DSC, and the solid phases were characterized by powder XRD. The formation of two cocrystals with the ratios 1:2 and 2:1 for L-menthol:phenol was observed. The crystal structure of the two cocrystals was solved by SC-XRD analysis and the structure solution from powder XRD data. It was found that the 1:2 cocrystal melts congruently while the 2:1 cocrystal melts incongruently.

The phase diagram was obtained by modeling the measured SLE data using the NRTL and COSMO-RS models. It was found that assuming simple eutectic behavior, the estimated eutectic temperatures by both models are significantly lower than the experimentally observed eutectic temperatures. However, both models can satisfactorily describe the SLE in the L-menthol/phenol eutectic system when considering the formation of the two cocrystals.

This work shows that a reasonable estimation for the eutectic point of DES systems could be obtained by predictive thermodynamic models. However, possible cocrystal formation should always be experimentally investigated beforehand and accounted for while modeling the SLE.

#### ■ ASSOCIATED CONTENT

##### Supporting Information

The Supporting Information is available free of charge at <https://pubs.acs.org/doi/10.1021/acs.cgd.2c00362>.



Solid–liquid equilibria data for the L-menthol/phenol eutectic system; heat capacity of pure phenol in the solid and liquid states; DSC curves for the L-menthol/phenol eutectic system at different phenol mole fractions; variation in the powder XRD of the 1:2 L-menthol:phenol cocrystal with measuring time; powder XRD pattern of the 1:2 L-menthol:phenol cocrystal at different runs; SC-XRD details; SC-XRD data for the 2:1 L-menthol:phenol cocrystal; procedure for the structure solution from powder data; structure and refinement details of the crystal structures of the 2:1 and 1:2 L-menthol:phenol cocrystals solved from powder diffraction data (PDF)

### Accession Codes

CCDC 2153851–2153853 contain the supplementary crystallographic data for this paper. These data can be obtained free of charge via [www.ccdc.cam.ac.uk/data\\_request/cif](http://www.ccdc.cam.ac.uk/data_request/cif), or by emailing [data\\_request@ccdc.cam.ac.uk](mailto:data_request@ccdc.cam.ac.uk), or by contacting The Cambridge Crystallographic Data Centre, 12 Union Road, Cambridge CB2 1EZ, UK; fax: +44 1223 336033.

### AUTHOR INFORMATION

#### Corresponding Author

Mirjana Minceva – Biothermodynamics, TUM School of Life Sciences, Technical University of Munich (TUM), Freising 85354, Germany; Email: [mirjana.minceva@tum.de](mailto:mirjana.minceva@tum.de)

#### Authors

Ahmad Alhadid – Biothermodynamics, TUM School of Life Sciences, Technical University of Munich (TUM), Freising 85354, Germany; [orcid.org/0000-0003-1443-1517](https://orcid.org/0000-0003-1443-1517)

Christian Jandl – Catalysis Research Center, Department Chemie, Technical University of Munich (TUM), Garching 85748, Germany

Liudmila Mokrushina – Separation Science & Technology, Friedrich-Alexander-Universität Erlangen-Nürnberg (FAU), Erlangen 91058, Germany

Complete contact information is available at: <https://pubs.acs.org/10.1021/acs.cgd.2c00362>

#### Author Contributions

A.A. contributed to conceptualization. Investigation and formal analysis were conducted by A.A. and C.J. A.A. performed writing—original draft. Writing—review & editing was performed by C.J., L.M., and M.M. Supervision was conducted by M.M.

#### Notes

The authors declare no competing financial interest.

### REFERENCES

- (1) Smith, E. L.; Abbott, A. P.; Ryder, K. S. Deep Eutectic Solvents (DESs) and Their Applications. *Chem. Rev.* **2014**, *114*, 11060–11082.
- (2) Huang, J.; Guo, X.; Xu, T.; Fan, L.; Zhou, X.; Wu, S. Ionic deep eutectic solvents for the extraction and separation of natural products. *J. Chromatogr. A* **2019**, *1598*, 1–19.
- (3) González de Castilla, A.; Bittner, J. P.; Müller, S.; Jakobtorweihen, S.; Smirnova, I. Thermodynamic and Transport Properties Modeling of Deep Eutectic Solvents: A Review on gE-Models, Equations of State, and Molecular Dynamics. *J. Chem. Eng. Data* **2020**, *65*, 943–967.
- (4) Martins, M. A. R.; Pinho, S. P.; Coutinho, J. A. P. Insights into the Nature of Eutectic and Deep Eutectic Mixtures. *J. Solution Chem.* **2019**, *48*, 962–982.

(5) Abbott, A. P.; Capper, G.; Davies, D. L.; Munro, H. L.; Rasheed, R. K.; Tambyrajah, V. Preparation of novel, moisture-stable, Lewis-acidic ionic liquids containing quaternary ammonium salts with functional side chains. *Chem. Commun.* **2001**, 2010–2011.

(6) Abbott, A. P.; Barron, J. C.; Ryder, K. S.; Wilson, D. Eutectic-Based Ionic Liquids with Metal-Containing Anions and Cations. *Chem. - Eur. J.* **2007**, *13*, 6495–6501.

(7) Abranches, D. O.; Silva, L. P.; Martins, M. A. R.; Coutinho, J. A. P. Differences on the impact of water on the deep eutectic solvents betaine/urea and choline/urea. *J. Chem. Phys.* **2021**, *155*, No. 034501.

(8) van Osch, D. J. G. P.; Dietz, C. H. J. T.; Warrag, S. E. E.; Kroon, M. C. The Curious Case of Hydrophobic Deep Eutectic Solvents: A Story on the Discovery, Design, and Applications. *ACS Sustainable Chem. Eng.* **2020**, *8*, 10591–10612.

(9) van Osch, D. J. G. P.; Dietz, C. H. J. T.; van Spronsen, J.; Kroon, M. C.; Gallucci, F.; van Sint Annaland, M.; Tuinier, R. A Search for Natural Hydrophobic Deep Eutectic Solvents Based on Natural Components. *ACS Sustainable Chem. Eng.* **2019**, *7*, 2933–2942.

(10) Lee, J.; Jung, D.; Park, K. Hydrophobic deep eutectic solvents for the extraction of organic and inorganic analytes from aqueous environments. *TrAC, Trends Anal. Chem.* **2019**, *118*, 853–868.

(11) Dwamena, A. K. Recent advances in hydrophobic deep eutectic solvents for extraction. *Separations* **2019**, *6*, No. 9.

(12) Florindo, C.; Branco, L. C.; Marrucho, I. M. Quest for Green-Solvent Design: From Hydrophilic to Hydrophobic (Deep) Eutectic Solvents. *ChemSusChem* **2019**, *12*, 1549–1559.

(13) Abranches, D. O.; Coutinho, J. A. P. Type V deep eutectic solvents: Design and applications. *Curr. Opin. Green Sustainable Chem.* **2022**, *35*, No. 100612.

(14) Alhadid, A.; Mokrushina, L.; Minceva, M. Influence of the Molecular Structure of Constituents and Liquid Phase Non-Ideality on the Viscosity of Deep Eutectic Solvents. *Molecules* **2021**, *26*, No. 4208.

(15) Gajardo-Parra, N. F.; Cotroneo-Figueroa, V. P.; Aravena, P.; Vesovic, V.; Canales, R. I. Viscosity of Choline Chloride-Based Deep Eutectic Solvents: Experiments and Modeling. *J. Chem. Eng. Data* **2020**, *65*, 5581–5592.

(16) Lemaoui, T.; Darwish, A. S.; Attoui, A.; Abu Hatab, F.; Hammoudi, N. E. H.; Benguerba, Y.; Vega, L. F.; Alnashef, I. M. Predicting the density and viscosity of hydrophobic eutectic solvents: towards the development of sustainable solvents. *Green Chem.* **2020**, *22*, 8511–8530.

(17) Alhadid, A.; Mokrushina, L.; Minceva, M. Modeling of Solid–Liquid Equilibria in Deep Eutectic Solvents: A Parameter Study. *Molecules* **2019**, *24*, 2334.

(18) Alhadid, A.; Mokrushina, L.; Minceva, M. Design of Deep Eutectic Systems: A Simple Approach for Preselecting Eutectic Mixture Constituents. *Molecules* **2020**, *25*, 1077.

(19) Martins, M. A. R.; Crespo, E. A.; Pontes, P. V. A.; Silva, L. P.; Bülow, M.; Maximo, G. J.; Batista, E. A. C.; Held, C.; Pinho, S. P.; Coutinho, J. A. P. Tunable Hydrophobic Eutectic Solvents Based on Terpenes and Monocarboxylic Acids. *ACS Sustainable Chem. Eng.* **2018**, *6*, 8836–8846.

(20) Abdallah, M. M.; Müller, S.; González de Castilla, A.; Gurikov, P.; Matias, A. A.; Bronze, M. D.; Fernández, N. Physicochemical Characterization and Simulation of the Solid–Liquid Equilibrium Phase Diagram of Terpene-Based Eutectic Solvent Systems. *Molecules* **2021**, *26*, No. 1801.

(21) Corvis, Y.; Négrier, P.; Lazerges, M.; Massip, S.; Léger, J.-M.; Espeau, P. Lidocaine/l-Menthol Binary System: Cocrystallization versus Solid-State Immiscibility. *J. Phys. Chem. B* **2010**, *114*, 5420–5426.

(22) Alhadid, A.; Jandl, C.; Mokrushina, L.; Minceva, M. Experimental Investigation and Modeling of Cocrystal Formation in L-Menthol/Thymol Eutectic System. *Cryst. Growth Des.* **2021**, *21*, 6083–6091.

(23) Alhadid, A.; Mokrushina, L.; Minceva, M. Formation of glassy phases and polymorphism in deep eutectic solvents. *J. Mol. Liq.* **2020**, *314*, No. 113667.

- (24) Jamróz, M. E.; Palczewska-Tulińska, M.; Wyrzykowska-Stankiewicz, D.; Szafranski, A. M.; Polaczek, J.; Dobrowolski, J. C.; Jamróz, M. H.; Mazurek, A. P. The urea–phenol(s) systems<sup>†</sup>. *Fluid Phase Equilib.* **1998**, *152*, 307–326.
- (25) Alhadid, A.; Jandl, C.; Mokrushina, L.; Minceva, M. Cocrystal Formation in Choline Chloride Deep Eutectic Solvents. *Cryst. Growth Des.* **2022**, *22*, 1933–1942.
- (26) A. I., Kitaigorodskii, *Mixed Crystals*, Springer-Verlag: Berlin, 1984.
- (27) Hall, C. L.; Potticary, J.; Hamilton, V.; Gaisford, S.; Buanz, A.; Hall, S. R. Metastable crystalline phase formation in deep eutectic systems revealed by simultaneous synchrotron XRD and DSC. *Chem. Commun.* **2020**, *56*, 10726–10729.
- (28) Abranches, D. O.; Martins, M. A. R.; Silva, L. P.; Schaeffer, N.; Pinho, S. P.; Coutinho, J. A. P. Phenolic hydrogen bond donors in the formation of non-ionic deep eutectic solvents: the quest for type V DES. *Chem. Commun.* **2019**, *55*, 10253–10256.
- (29) van den Bruinhorst, A.; Kollau, L. J. B. M.; Vis, M.; Hendrix, M. M. R. M.; Meuldijk, J.; Tuinier, R.; Esteves, A. C. C. From a eutectic mixture to a deep eutectic system via anion selection: Glutaric acid + tetraethylammonium halides. *J. Chem. Phys.* **2021**, *155*, No. 014502.
- (30) Kollau, L. J. B. M.; Tuinier, R.; Verhaak, J.; den Doelder, J.; Filot, I. A. W.; Vis, M. Design of Nonideal Eutectic Mixtures Based on Correlations with Molecular Properties. *J. Phys. Chem. B* **2020**, *124*, 5209–5219.
- (31) Kollau, L. J. B. M.; Vis, M.; van den Bruinhorst, A.; de With, G.; Tuinier, R. Activity modelling of the solid–liquid equilibrium of deep eutectic solvents. *Pure Appl. Chem.* **2019**, *91*, 1341–1349.
- (32) Kollau, L. J. B. M.; Vis, M.; van den Bruinhorst, A.; Esteves, A. C. C.; Tuinier, R. Quantification of the liquid window of deep eutectic solvents. *Chem. Commun.* **2018**, *54*, 13351–13354.
- (33) Alkhatib, I. I. I.; Bahamon, D.; Llovel, F.; Abu-Zahra, M. R. M.; Vega, L. F. Perspectives and guidelines on thermodynamic modelling of deep eutectic solvents. *J. Mol. Liq.* **2020**, *298*, No. 112183.
- (34) Abranches, D. O.; Larriba, M.; Silva, L. P.; Melle-Franco, M.; Palomar, J. F.; Pinho, S. P.; Coutinho, J. A. P. Using COSMO-RS to design choline chloride pharmaceutical eutectic solvents. *Fluid Phase Equilib.* **2019**, *497*, 71–78.
- (35) Song, Z.; Wang, J.; Sundmacher, K. Evaluation of COSMO-RS for solid–liquid equilibria prediction of binary eutectic solvent systems. *Green Energy Environ.* **2021**, *6*, 371–379.
- (36) Lange, L.; Sadowski, G. Polymorphs, Hydrates, Cocrystals, and Cocrystal Hydrates: Thermodynamic Modeling of Theophylline Systems. *Cryst. Growth Des.* **2016**, *16*, 4439–4449.
- (37) Lange, L.; Sadowski, G. Thermodynamic Modeling for Efficient Cocrystal Formation. *Cryst. Growth Des.* **2015**, *15*, 4406–4416.
- (38) Tumakaka, F.; Prikhodko, I. V.; Sadowski, G. Modeling of solid–liquid equilibria for systems with solid-complex phase formation. *Fluid Phase Equilib.* **2007**, *260*, 98–104.
- (39) Lange, L.; Heisel, S.; Sadowski, G. Predicting the Solubility of Pharmaceutical Cocrystals in Solvent/Anti-Solvent Mixtures. *Molecules* **2016**, *21*, No. 593.
- (40) Wu, D.; Zhang, B.; Yao, Q.; Hou, B.; Zhou, L.; Xie, C.; Gong, J.; Hao, H.; Chen, W. Evaluation on Cocrystal Screening Methods and Synthesis of Multicomponent Crystals: A Case Study. *Cryst. Growth Des.* **2021**, *21*, 4531–4546.
- (41) Dash, S. G.; Thakur, T. S. Computational Screening of Multicomponent Solid Forms of 2-Aryl-Propionate Class of NSAID, Zaltoprofen, and Their Experimental Validation. *Cryst. Growth Des.* **2021**, *21*, 449–461.
- (42) Wu, D.; Li, J.; Xiao, Y.; Ji, X.; Li, C.; Zhang, B.; Hou, B.; Zhou, L.; Xie, C.; Gong, J.; Chen, W. New Salts and Cocrystals of Pymetrozine with Improvements on Solubility and Humidity Stability: Experimental and Theoretical Study. *Cryst. Growth Des.* **2021**, *21*, 2371–2388.
- (43) Loschen, C.; Klamt, A. Solubility prediction, solvate and cocrystal screening as tools for rational crystal engineering. *J. Pharm. Pharmacol.* **2015**, *67*, 803–811.
- (44) Cysewski, P. Efficacy of bi-component cocrystals and simple binary eutectics screening using heat of mixing estimated under super cooled conditions. *J. Mol. Graphics Modell.* **2016**, *68*, 23–28.
- (45) Przybyłek, M.; Ziółkowska, D.; Mroczynska, K.; Cysewski, P. Applicability of Phenolic Acids as Effective Enhancers of Cocrystal Solubility of Methylxanthines. *Cryst. Growth Des.* **2017**, *17*, 2186–2193.
- (46) Cysewski, P. In silico screening of dicarboxylic acids for cocrystallization with phenylpiperazine derivatives based on both cocrystallization propensity and solubility advantage. *J. Mol. Model.* **2017**, *23*, No. 136.
- (47) Loschen, C.; Klamt, A. Cocrystal Ternary Phase Diagrams from Density Functional Theory and Solvation Thermodynamics. *Cryst. Growth Des.* **2018**, *18*, 5600–5608.
- (48) Prausnitz, J. M.; Lichtenthaler, R. N.; Azevedo, E. G. d. *Molecular Thermodynamics of Fluid-Phase Equilibria*; Prentice Hall PTR: Upper Saddle River, NJ, 1999.
- (49) Andon, R. J. L.; Counsell, J. F.; Herington, E. F. G.; Martin, J. F. Thermodynamic properties of organic oxygen compounds. Part 7.—Calorimetric study of phenol from 12 to 330 °K. *Trans. Faraday Soc.* **1963**, *59*, 830–835.
- (50) Corvis, Y.; Espeau, P. Interpretation of the global heat of melting in eutectic binary systems. *Thermochim. Acta* **2018**, *664*, 91–99.
- (51) Eckert, F.; Klamt, A. Fast solvent screening via quantum chemistry: COSMO-RS approach. *AIChE J.* **2002**, *48*, 369–385.
- (52) Klamt, A.; Jonas, V.; Bürger, T.; Lohrenz, J. C. W. Refinement and Parametrization of COSMO-RS. *J. Phys. Chem. A* **1998**, *102*, 5074–5085.
- (53) Klamt, A. Conductor-like Screening Model for Real Solvents: A New Approach to the Quantitative Calculation of Solvation Phenomena. *J. Phys. Chem. A* **1995**, *99*, 2224–2235.
- (54) TURBOMOLE V6.6 2014, a development of University of Karlsruhe and Forschungszentrum Karlsruhe GmbH, 1989-2007; TURBOMOLE GmbH, <https://www.turbomole.org>.
- (55) BIOVIA COSMOtherm, Release 2019; Dassault Systèmes, <http://www.3ds.com>.

## Supplementary Information

### Cocrystal Formation in L-Menthol/Phenol Eutectic System: Experimental Study and Thermodynamic Modeling

Ahmad Alhadid <sup>1</sup>, Christian Jandl <sup>2</sup>, Liudmila Mokrushina <sup>3</sup>, and Mirjana Minceva <sup>\* 1</sup>

<sup>1</sup> Biothermodynamics, TUM School of Life Sciences, Technical University of Munich (TUM), Germany

<sup>2</sup> Catalysis Research Center, Department Chemie, Technical University of Munich (TUM), Germany

<sup>3</sup> Separation Science & Technology, Friedrich-Alexander-Universität Erlangen-Nürnberg (FAU),  
Germany

\*Corresponding author e-mail: [mirjana.minceva@tum.de](mailto:mirjana.minceva@tum.de)

Table S1. Solid–liquid equilibria data for L-menthol/phenol eutectic system.

Phenol mole fraction	T <sup>liq</sup> / K	T <sub>e</sub> / K	Solid phase *
0.90	306.1 ± 0.4	272.1	Phenol
0.85	300.3 ± 0.5	271.5	Phenol
0.80	291.7 ± 1.1	272.2	Phenol
0.75	284.9 ± 1.0	272.3	Phenol
0.70	–	272.3	Phenol + 1:2 cocrystal
0.67	–	273.3	1:2 cocrystal
0.65	273.7 ± 0.2	262.6	1:2 cocrystal
0.60	272.8 ± 0.9	262.8	1:2 cocrystal
0.55	270.7 ± 0.3	262.9	1:2 cocrystal
0.51	–	263.0	1:2 cocrystal + 2:1 cocrystal
0.46	–	262.6	1:2 cocrystal + 2:1 cocrystal
0.39	266.7 ± 0.9	261.7	2:1 cocrystal
0.35	269.7 ± 0.1	262.3	2:1 cocrystal
0.33	280.0 ± 0.2	269.4	L-menthol
0.30	284.0 ± 0.3	269.4	L-menthol

0.23	$294.1 \pm 0.1$	268.8	L-menthol
0.20	$299.2 \pm 0.4$	268.4	L-menthol
0.16	$302.9 \pm 0.3$	267.9	L-menthol
0.12	$307.2 \pm 0.4$	267.3	L-menthol

\* the crystallized solid phase at the liquidus temperature. Standard uncertainties are  $u(T) = 0.4 \text{ K}$  and  $u_c(x) = 0.005$

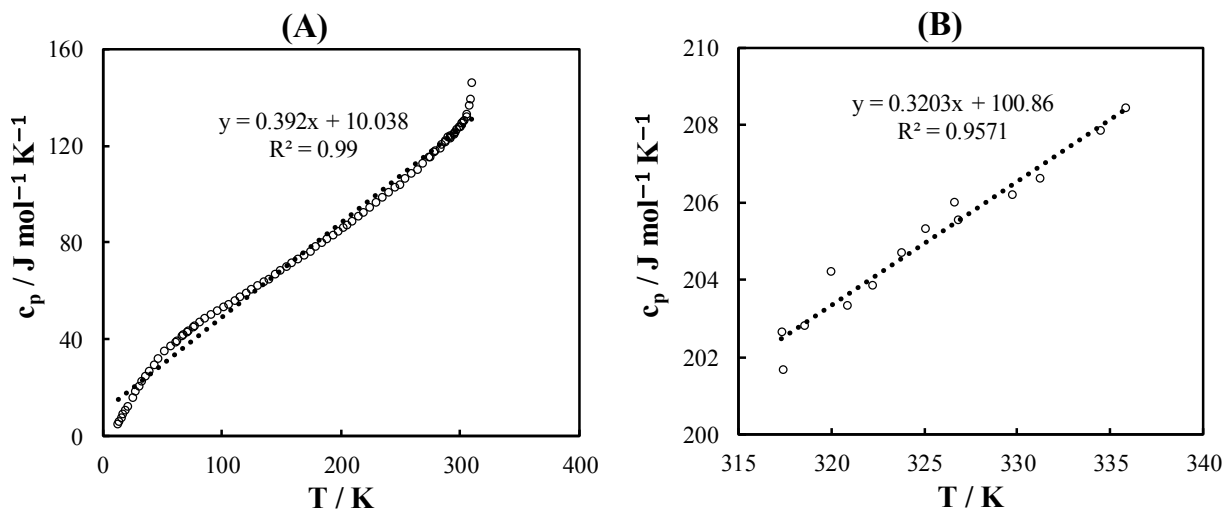


Figure S1. Heat capacity of pure phenol in the (A) solid and (B) liquid states. Data were taken from Andon et al. <sup>1</sup>

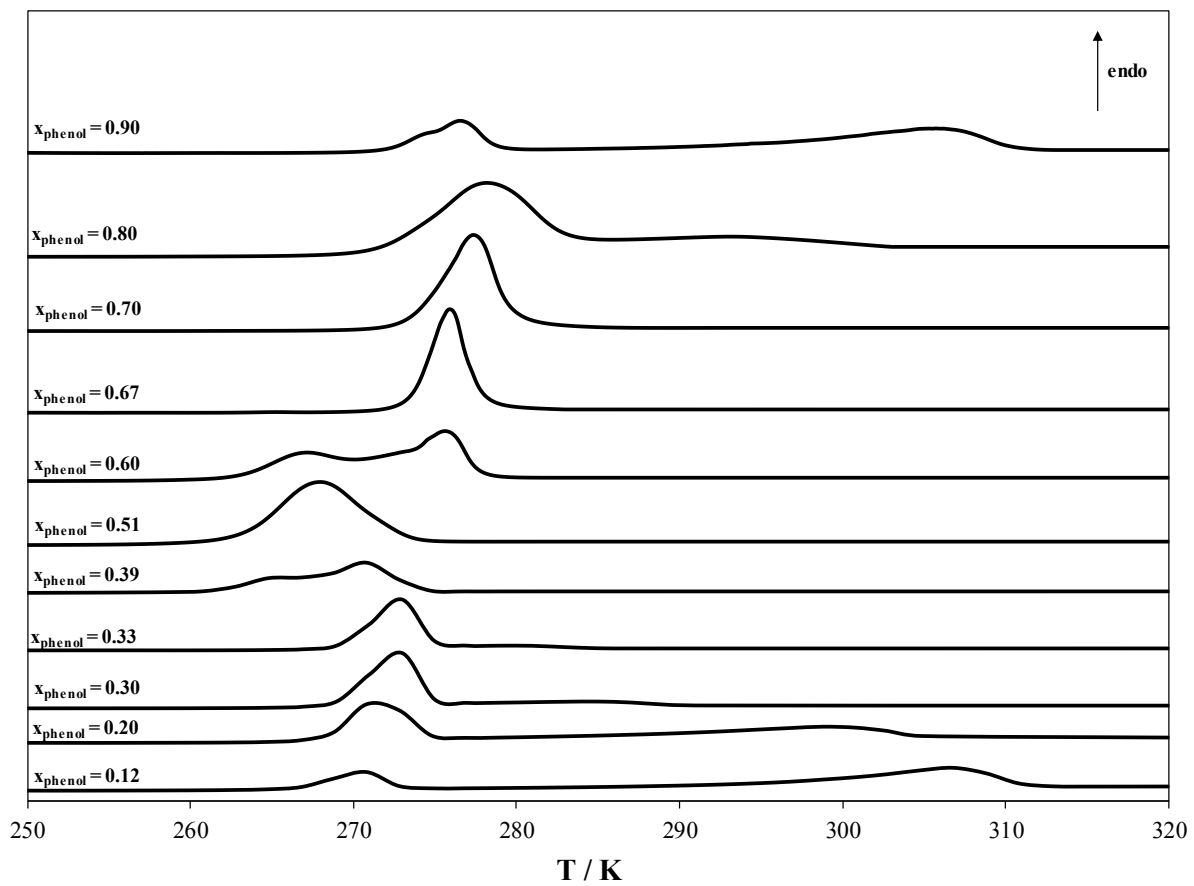


Figure S2. Differential scanning calorimetry curves for L-menthol/phenol eutectic system at different phenol mole fractions.

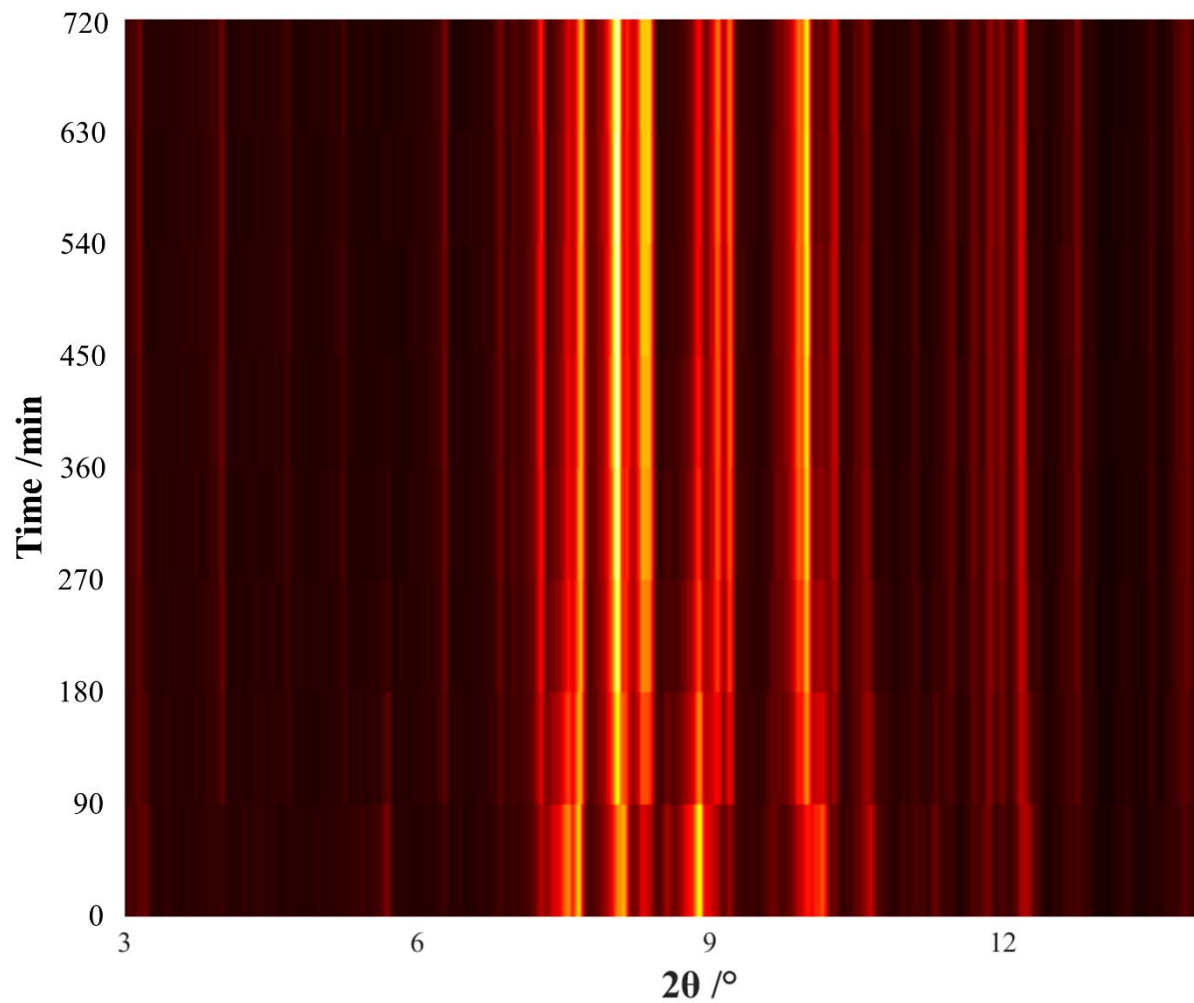


Figure S3. The variation in the powder X-ray diffraction pattern of the 1:2 L-menthol:phenol cocrystal with measuring time.

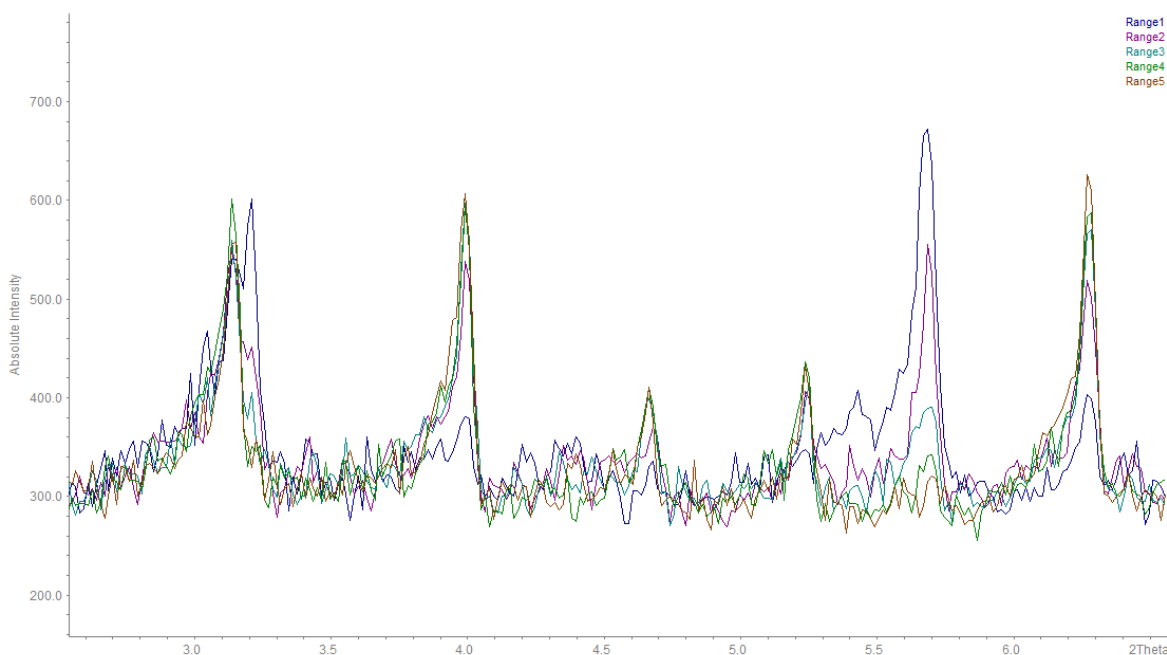


Figure S4. Powder X-ray diffractions pattern of the 1:2 L-menthol:phenol cocrystal at different runs (range). The changing peaks were magnified for clarity.

## SC-XRD

Data were collected on a single crystal X-ray diffractometer equipped with a CMOS detector (Bruker Photon-100), a TXS rotating anode with MoK $\alpha$  radiation ( $\lambda = 0.71073 \text{ \AA}$ ) and a Helios optic using the APEX3 software package.<sup>2</sup> The measurements were performed on single crystals coated with perfluorinated ether. The crystals were fixed on top of a kapton micro sampler and frozen under a stream of cold nitrogen. A matrix scan was used to determine the initial lattice parameters. Reflections were corrected for Lorentz and polarisation effects, scan speed, and background using SAINT.<sup>3</sup> Absorption correction, including odd and even ordered spherical harmonics was performed using SADABS.<sup>3</sup> Space group assignment was based upon systematic absences, E statistics, and successful refinement of the structure. The structures were solved using SHELXT with the aid of successive difference Fourier maps, and were refined against all data using SHELXL in conjunction with SHELXLE.<sup>4-6</sup> Hydrogen atoms (except on heteroatoms) were calculated in ideal positions as follows: Methyl hydrogen atoms were refined as part of rigid rotating groups, with a C–H distance of  $0.98 \text{ \AA}$  and  $U_{\text{iso(H)}} = 1.5 \cdot U_{\text{eq(C)}}$ . Non-methyl H atoms were placed in calculated positions and refined using a riding model with methylene, aromatic, and other C–H distances of  $0.99 \text{ \AA}$ ,  $0.95 \text{ \AA}$ , and  $1.00 \text{ \AA}$ , respectively, and  $U_{\text{iso(H)}} = 1.2 \cdot U_{\text{eq(C)}}$ . Non-

hydrogen atoms were refined with anisotropic displacement parameters. Full-matrix least-squares refinements were carried out by minimizing  $\Sigma w(F_o^2 - F_c^2)^2$  with the SHELXL weighting scheme.<sup>4</sup> Neutral atom scattering factors for all atoms and anomalous dispersion corrections for the non-hydrogen atoms were taken from *International Tables for Crystallography*.<sup>7</sup> Images of the crystal structure were generated with Mercury and PLATON.<sup>8-10</sup> Deposition Number 2153853 contains the supplementary crystallographic data for this paper. These data are provided free of charge by the joint Cambridge Crystallographic Data Centre and Fachinformationszentrum Karlsruhe Access Structures service [www.ccdc.cam.ac.uk/structures](http://www.ccdc.cam.ac.uk/structures).

## 2:1 Cocrystal L-Menthol/Phenol (CCDC 2153853)

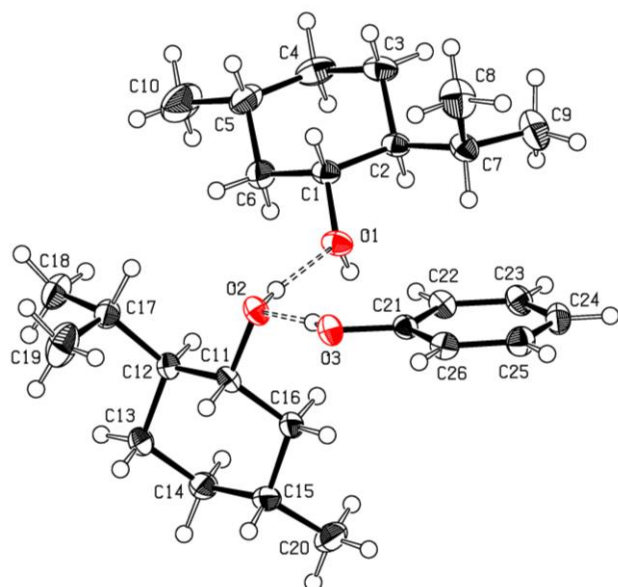


Figure S5: Asymmetric unit of the structure of the 2:1 L-menthol:phenol cocrystal from single-crystal XRD data with ellipsoids at the 50% probability level.

Table S2. Structure and refinement details for the 2:1 L-menthol:phenol cocrystal.

Deposition number	CCDC 2153853	
Chemical formula	$C_{26}H_{46}O_3$	
Crystal description	colourless block	
Formula weight	406.63	
Temperature	100 K	
Wavelength	0.71073 Å	
Crystal size	0.24 × 0.27 × 0.45 mm	
Crystal system	monoclinic	
Space group	$P 2_1$	
Unit cell dimensions	a = 6.0315(4) Å	$\alpha = 90^\circ$
	b = 21.5189(14) Å	$\beta = 100.277(2)^\circ$



	$c = 10.3083(7) \text{ \AA}$	$\gamma = 90^\circ$
Volume	$1316.46(15) \text{ \AA}^3$	
Z	2	
Density (calculated)	$1.026 \text{ g cm}^{-3}$	
Absorption coefficient	$0.065 \text{ mm}^{-1}$	
F(000)	452	
$\theta$ range	$2.76\text{-}26.73^\circ$	
Absorption correction	multi-scan (SADABS)	
$T_{\min}, T_{\max}$	0.985, 0.972	
Reflections measured	38249	
Independent reflections	5579	
Reflections $I > 2\sigma(I)$	5440	
$R_{\text{int}}$	0.02	
Refinement method	full matrix least squares on $F^2$	
Data, restraints, parameters	5579, 1, 280	
$R1 [I > 2\sigma(I)]$	<u>0.029</u>	
wR2 (all data)	0.076	
Goodness of fit	1.02	
Weighting scheme	$W = 1/[\sigma^2(F_o^2) + (0.0475P)^2 + 0.1413P]$ where $P = (F_o^2 + 2F_c^2)/3$	
Largest difference peak and hole	0.17 and $-0.14 \text{ e\AA}^{-3}$	

## P-XRD

Samples were finely ground within a cold room at 253 K and directly filled into 0.70 or 1.5 mm diameter glass capillaries (Hilgenberg, Germany). Powder XRD patterns were recorded in Debye-Scherrer geometry on a Stadi P diffractometer (Stoe & Cie, Germany) equipped with a Mo fine-focus sealed tube, a curved Ge monochromator selecting  $K\alpha_1$  radiation ( $\lambda = 0.7093 \text{ \AA}$ ), and a Mythen2 R 1K detector (Dectris, Switzerland) using the WinXPOW software package.<sup>12</sup> All data were collected as overlapping step scans so that every data point is measured 4 times during one run with a data point resolution of  $0.015^\circ 2\theta$ . Multiple consecutive runs were performed and the step duration as well as the number of runs (3-8) were adjusted to the diffraction intensity of the sample. The measurements were performed at 253 K using an 800 series cryostream (Oxford, UK), unless stated otherwise. Pattern fitting and indexing for cell determination was performed using WinXPOW. Pawley fitting, space group determination and cell refinement were performed using DASH.<sup>13</sup> Structure solution via simulated annealing was performed with DASH using molecular geometries from the Cambridge Structural Database (L-menthol from ZEGDIA [CCDC 832350], phenol from PHENOL03 [CCDC 1232404]) and a fixed torsion angle for the isopropyl-group on menthol.<sup>12-16</sup> Initial rigid body Rietveld refinement was performed with DASH and the hydroxy-groups were oriented in the direction of likely hydrogen bonds.<sup>13</sup> Final rigid body Rietveld

refinement was performed using Jana2006 with global isotropic displacement parameters for C and O atoms and riding isotropic displacement parameters for H atoms  $U_{\text{iso}}(\text{H}) = 1.2 \cdot U_{\text{iso}}(\text{C/O})$ .<sup>17</sup> Deposition Numbers 2153851-2153852 contain the supplementary crystallographic data for this paper. These data are provided free of charge by the joint Cambridge Crystallographic Data Centre and Fachinformationszentrum Karlsruhe Access Structures service [www.ccdc.cam.ac.uk/structures](http://www.ccdc.cam.ac.uk/structures).

Table S3. Structure and refinement details of the crystal structures of the 2:1 and 1:2 L-menthol:phenol cocrystals solved from powder diffraction data.

	<b>L-Menthol/Phenol 2:1</b>	<b>L-Menthol/Phenol 1:2</b>
Deposition number	2153851	2153852
Formula	2(C <sub>10</sub> H <sub>20</sub> O), C <sub>6</sub> H <sub>6</sub> O	C <sub>10</sub> H <sub>20</sub> O, 2(C <sub>6</sub> H <sub>6</sub> O)
Molecular weight /g mol <sup>-1</sup>	406.63	344.48
Bravais lattice	monoclinic P	orthorhombic P
Spacegroup	P2 <sub>1</sub>	P2 <sub>1</sub> 2 <sub>1</sub> 2 <sub>1</sub>
a /Å	6.099	20.3936
b /Å	21.7903	16.8032
c /Å	10.4267	6.2151
α /°	90	90
β /°	100.9126	90
γ /°	90	90
Volume /Å <sup>3</sup>	1360.649	2129.77
Z	2	4
Density (calc.) /g cm <sup>-3</sup>	0.992	1.074
F(000)	452	752
2θ range /°	1.5–26.0	1.5–27.0
Background	30 Legendre polynomials	30 Legendre polynomials
Profile function	Pseudo-Voigt	Pseudo-Voigt
R <sub>p</sub>	0.0436	0.0252
R <sub>wp</sub>	0.0580	0.0336
R <sub>exp</sub>	0.0148	0.0125
R(all)	0.0796	0.0342
wR(all)	0.0734	0.0373
R	0.0700	0.0322
wR	0.0727	0.0372
GOF	3.93	2.69

## References

1. R. J. L. Andon, J. F. Counsell, E. F. G. Herington and J. F. Martin, *Transactions of the Faraday Society*, 1963, **59**, 830-835.
2. *APEX suite of crystallographic software*, APEX 3, Version 2019-1.0, Bruker AXS Inc., Madison, Wisconsin, USA, 2019.
3. *SAINTE*, Version 8.40A and *SADABS*, Version 2016/2, Bruker AXS Inc., Madison, Wisconsin, USA, 2016/2019.
4. G. M. Sheldrick, *Acta Crystallogr. Sect. A* **2015**, *71*, 3–8.
5. G. M. Sheldrick, *Acta Crystallogr. Sect. C* **2015**, *71*, 3–8.
6. C. B. Hübschle, G. M. Sheldrick, B. Dittrich, *J. Appl. Cryst.* **2011**, *44*, 1281–1284
7. *International Tables for Crystallography, Vol. C* (Ed.: A. J. Wilson), Kluwer Academic Publishers, Dordrecht, The Netherlands, **1992**, Tables 6.1.1.4 (pp. 500–502), 4.2.6.8 (pp. 219–222), and 4.2.4.2 (pp. 193–199).
8. C. F. Macrae, I. J. Bruno, J. A. Chisholm, P. R. Edgington, P. McCabe, E. Pidcock, L. Rodriguez-Monge, R. Taylor, J. van de Streek, P. A. Wood, *J. Appl. Cryst.* **2008**, *41*, 466–470.
9. A. L. Spek, *Acta Crystallogr. Sect. D* **2009**, *65*, 148–155.
10. H. D. Flack, *Acta Crystallogr. Sect A* **1983**, *39*, 876–881.
11. S. Parsons, H. D. Flack, T. Wagner, *Acta Crystallogr. Sect B* **2013**, *69*, 249–259.
12. *WinXPow*, Version 3.6.0.1, Stoe & Cie GmbH, Darmstadt, Germany, 2018.
13. W. I. F. David, K. Shankland, J. van de Streek, E. Pidcock, W. D. S. Motherwell, J. C. Cole, *J. Appl. Cryst.* **2006**, *39*, 910-915.
14. C. R. Groom, I. J. Bruno, M. P. Lightfoot, S. C. Ward, *Acta Crystallogr. Sect B* **2016**, *72*, 171–179.
15. Y. Corvis, P. Negrier S. Massip, J.-M. Leger, P. Espeau, *Cryst. Eng. Commun.* **2012**, *14*, 7055–7064.
16. V. E. Zavodnik, V. K. Bel'skii, P. M. Zorkii, *Zh. Strukt. Khim.* **1987**, *28*, 793–795.
17. V. Petricek, M. Dusek, L. Palatinus, *Z. Kristallogr.* **2014**, *229*, 345–352.

## 4. Discussion

The results of Papers I–VI are discussed in two sections, one with the focus on measuring and modeling methods to obtain SLE data for eutectic mixtures of various complexity (Section 4.1), and the other on the characteristics of the pure constituents and the mixture leading to the formation of eutectic mixtures with deep depression at the eutectic point (Section 4.2).

### *4.1 Measuring and modeling SLE*

Since the term DES was introduced, considerable efforts have been made to understand DES formation. Despite the numerous approaches employed to unravel the unique DES characters, SLE studies have provided the most valuable insights. The SLE phase diagram is used to determine the melting temperature of the DES at any ratio between constituents. Moreover, modeling SLE data provides information about intermolecular interactions between unlike molecules. Nevertheless, as depicted in Papers III–VI, measuring and modeling SLE is not a straightforward task and often accompanies many difficulties. These difficulties are usually attributed to the solid rather than the liquid phase. For eutectic systems with a large depression in the melting temperature, the high viscosity of the liquid solution in the vicinity of its melting temperature might hinder the crystallization, preventing the determination of the solidus or the liquidus temperatures of the eutectic system. Furthermore, crystallization of constituents at low temperatures might lead to the formation of metastable polymorphs. For modeling SLE data, the melting properties of pure constituents are required, which can be unavailable due to their thermal instability or polymorphism—the pure constituent can exist in different crystal structures. Moreover, information on the solid phases crystallized from the liquid solution is a prerequisite for adequate modeling of SLE. Nevertheless, obtaining such information becomes very complicated in the case of glass or cocrystal formations or if the melting temperature of the mixture is significantly lower than room temperature, which consequently requires special handling and preparation for the samples. Therefore, it is evident that measuring and modeling SLE in many DES are rather complicated and nontrivial tasks.

This thesis provides several advancements in measuring and modeling SLE in binary eutectic mixtures. In the literature, SLE data of DES were commonly measured by visual methods or DSC. Nevertheless, these measurements were obtained assuming that the system is of the simple eutectic type without carefully analyzing the formed solid phases. The conventional DSC protocol—in situ crystallization of the liquid solution at the DSC (see Section 2.3.2.2)—was found

unsuitable for determining the SLE phase diagram of eutectic systems prone to glass formation. As shown in Paper III, annealing the DSC samples prior to measurements allows for determining the solidus temperature of the mixture. Nevertheless, the samples only partially crystallized even after annealing for one month. To overcome long annealing times, an efficient sample preparation method was proposed in Paper IV and applied in Papers V and VI, which allowed for fully crystallizing the samples within days instead of months. Compared to the conventional DSC protocol, the method used in Papers IV–VI allows for overcoming glass and metastable phases formation, enabling the proper determination of SLE data for the systems. By obtaining the solidus temperature and SLE data over the entire composition range of the system, cocrystal formation can be adequately investigated. Moreover, the method allows for combined DSC and powder XRD analyses, which aid in accurately interpreting DSC curves by assigning the observed peaks to the corresponding solid observed in the XRD pattern.

The eutectic composition can be obtained experimentally from the DSC analysis by constructing Tammann's plot. Tammann's plot can be constructed by plotting the area of the solidus peak as a function of the mole fraction of one constituent. The determined solidus peak area at each composition is fitted linearly in the hypereutectic and hypoeutectic regions, and the eutectic composition corresponds to the intercept of the two lines, i.e., supposedly, the composition at which the sample contains only pure eutectic phase. Nevertheless, determining the eutectic point composition experimentally using Tammann's plot is quite tedious, especially in the case of glass formation or polymorphism. The components might crystallize partially or in two different polymorphs, and the determined eutectic transition area might not correspond to the actual mole fraction of the eutectic phase in the sample. Moreover, for eutectic systems with cocrystal formation in which the cocrystal melting temperature is not far from the eutectic temperature, the solidus and liquidus peaks might overlap. Hence, the area of the solidus peak cannot be determined correctly. As an alternative to Tammann's plot, Papers III–VI show that correlative thermodynamic models (NRTL) can reasonably predict the eutectic composition.

Thermodynamic models are used for describing the nonideality of the liquid phase to obtain the SLE phase diagram and the eutectic point of the eutectic system. However, as shown in Papers IV–VI, not all eutectic systems are of the simple eutectic type. Therefore, experimental investigation for cocrystal formation is needed to model the SLE phase diagram. For modeling SLE in eutectic systems with cocrystal formation, the melting properties and stoichiometry of the cocrystal are required. The melting properties can be obtained by DSC, and a combination of

powder XRD and DSC analyses can hint at the cocrystal stoichiometry. Nevertheless, confirming the postulated stoichiometry of the cocrystal from powder XRD and DSC is not straightforward. SC-XRD technique provides definite proof for the cocrystal stoichiometry. However, obtaining a single-crystal suitable for SC-XRD analysis can be impossible in many cases, mainly due to kinetic limitations in crystallization. In the L-menthol/thymol eutectic system, no single crystals could be obtained for the observed cocrystals, and the crystal structure could not be solved from the powder XRD data. In contrast, the crystal structure of four never reported before cocrystals was solved by SC-XRD, namely, ChCl:catechol 1:2 and 1:1 ratios, ChCl:hydroquinone 1:1 ratio, and L-menthol:phenol 2:1 ratio. The crystal structure of the L-menthol:phenol 1:2 and 2:1 cocrystals was obtained from powder XRD data.

COSMO-RS has been used in the literature to predict the SLE phase diagram of eutectic systems. However, as COSMOtherm software was used to perform the SLE calculations, the calculations were limited to eutectic systems of the simple eutectic type. Moreover, the solid–solid transition of pure constituents was neglected in many cases due to the limitations of the implemented SLE calculations algorithm in COSMOtherm software for considering the solid–solid transition. Paper VI was the first to employ COSMO-RS to calculate SLE in eutectic systems with cocrystal formation, and satisfactory predictions were obtained using the TZVPD\_FINE parameterization. Besides showing that COSMO-RS can be a valuable tool to predict the SLE phase diagram of nonideal eutectic systems with cocrystal formation, the study highlights two important outcomes. First, COSMOtherm SLE calculations limitations and assumptions should not restrict using the model for predicting the SLE phase diagram of eutectic systems with a complex character or to justify the simplification of SLE calculations by assuming simple eutectic behavior and neglecting the solid–solid transition. Second, both TZVP and TZVPD\_FINE parameterizations should be used, as COSMO-RS predictions might differ significantly at the two levels.

Eventually, SLE studies are challenging, particularly for eutectic systems with a significant depression in the melting temperature besides solid complex formation. To obtain the SLE phase diagram of eutectic systems with a complex character, rigorous thermal and solid characterization analyses and advanced thermodynamic modeling should be combined. However, the sample preparation method is the crucial factor that would allow or hinder the experimental determination of SLE data. Without experimental SLE data over the entire composition range and information about the formed solid phases, the efforts for modeling the

liquid phase nonideality could be unavailing. Therefore, in SLE studies, experimental investigations and thermodynamic modeling are complementary and should be carried out jointly.

#### 4.2 DES formation

Two different definitions for DES have been proposed in the literature. The first definition states that DESs are a unique type of solvents formed by mixing HBA and HBD at a specific ratio. In contrast, the second definition states that DES are common nonideal eutectic mixtures with a significant difference between the eutectic temperature and the ideal eutectic temperature.

In Paper I, the influence of the melting enthalpy and entropy as well as the nonideality of the liquid phase on the eutectic temperature of the eutectic mixture was studied. It was demonstrated that both the activity coefficients and the melting entropy and enthalpy of components influence the depression at the eutectic point similarly. As an example, the depression at the eutectic point in the ideal eutectic system L-menthol/cyclohexanecarboxylic acid ( $T_{m,men} - T_e = 49.6$  K, Paper II) is similar to that observed in L-menthol/thymol ( $T_{m,men} - T_e = 41.5$  K, Paper IV) and L-menthol/phenol ( $T_{m,men} - T_e = 41.8$  K, Paper VI), though the latter two systems show significant negative deviation from ideality. This is attributed to the lower melting enthalpy of cyclohexanecarboxylic acid ( $\Delta h_m = 10.69$  kJ mol<sup>-1</sup>) than thymol ( $\Delta h_m = 20.64$  kJ mol<sup>-1</sup>) and phenol ( $\Delta h_m = 12.36$  kJ mol<sup>-1</sup>) and cocrystal formation in L-menthol/thymol and L-menthol/phenol. However, in none of these systems, the depression at the eutectic point was significant, i.e., < 100K, as that observed in ChCl-based DES. Based on Paper I, significant depression at the eutectic point, as depicted in ChCl-based DES, can only be realized in nonideal eutectic mixtures formed by constituents with low melting enthalpy and entropy. Therefore, it is evident that neither the nonideality of the mixture nor the melting properties of pure constituents alone aid in the formation of DES but rather a combination of both.

A simple approach was proposed in Paper II based on Paper I conclusions to select the eutectic system constituents with low melting entropy from a pool of chemical substances sharing the same chemical nature and melting temperature. It was shown in Paper II that constituents with a more rigid and symmetrical molecular structure could form eutectic mixtures with larger depression at the eutectic point compared to constituents with flexible and asymmetrical molecular structures. However, as shown in Section 2.4.1, substances with low melting entropy would have higher melting temperatures. Moreover, molecules that are rotationally symmetrical



are packed more efficiently in the crystal lattice, leading to a more ordered crystal structure and higher melting enthalpy. The interrelation between rotational symmetry and melting temperature and enthalpy can justify the odd-even effect in alkanes and dicarboxylic acids<sup>149</sup> and the difference in the melting properties of sugar alcohol stereoisomers.<sup>108</sup> For example, sorbitol and mannitol are stereoisomers, but their melting properties are quite different. The melting temperatures, enthalpies, and entropies are  $T_m = 372.0$  and  $441.0$  K,  $\Delta h_m = 35.9$  and  $59.5$  kJ mol<sup>-1</sup>, and  $\Delta s_m = 96.5$  and  $134.9$  J mol<sup>-1</sup> K<sup>-1</sup> for sorbitol and mannitol, respectively. Despite the mannitol being rotationally symmetrical and sorbitol being asymmetrical, mannitol has a higher melting entropy than sorbitol, which could be attributed to the more ordered crystal structure of mannitol, depicted by its higher melting enthalpy. The entropy gain due to the transition from the more ordered crystal of mannitol to a liquid is expected to be higher than the transition from the less ordered crystal structure of sorbitol to a liquid. The approach proposed in Paper II does not take into account the influence of the crystal structure of constituents on their melting enthalpy, which can largely affect the eutectic temperature of their mixtures. Hence, the low melting entropy might not result from the rotational symmetry and rigidity of the molecular structure but from the disorder of the crystal structure.

As mentioned previously, the majority of DES reported in the literature are ChCl-based. To understand the unique character of ChCl as a HBA forming DES, it is necessary to assess its melting properties and activity coefficients in the liquid solution. However, ChCl decomposes before melting; hence its melting properties are unavailable. Without the melting properties of ChCl, the activity coefficients cannot be calculated from experimental SLE data. In Paper V, an alternative method to calculate the activity coefficients of ChCl was proposed by mixing ChCl with known coformers to form eutectic mixtures with cocrystal formation. The liquidus data of the formed cocrystals were used to fit the binary interaction parameters of the correlative thermodynamic model (NRTL) to describe the nonideality of ChCl in the liquid phase. Accordingly, ChCl nonideality was evaluated in two eutectic systems, namely, ChCl/catechol and ChCl/hydroquinone. The calculated activity coefficients of ChCl showed that ChCl shows a negative deviation from ideal behavior in the liquid solution, contrary to the ideal or near-ideal solution behavior observed in the literature studies. This contradictory observation is attributed to the approach used in the literature to estimate the melting properties of ChCl. In the literature approach, ChCl melting properties were estimated assuming the ideal solution model, which, as shown in Paper I, can reasonably predict the SLE data of the ChCl liquidus line. However, the

estimated melting enthalpy assuming the ideal solution model may conceal the nonideality of ChCl in the liquid solution.

As widely known and explicitly shown in Paper V, ChCl undergoes solid–solid transition at around 352 K, which was disregarded in most SLE studies of ChCl-based DES in the literature, mainly due to the lack of proper solid phase characterization and measuring SLE visually. To estimate ChCl melting properties, SLE data above the solid–solid transition are needed. However, no experimental liquidus temperatures for ChCl above its solid–solid transition temperature could be measured. Accordingly, no distinct melting properties of ChCl could be estimated in Paper V. Instead, the melting entropy range of substances with a highly disordered crystal structure like ChCl high-temperature form was screened to obtain a pair of melting enthalpy and temperature values at each melting entropy. The SLE of the ChCl liquidus line below the solid–solid transition temperature can be well described using any combination of melting enthalpy, entropy, and temperature. It was shown that the lowest possible melting temperature of ChCl, estimated at the highest possible melting entropy of a substance with a disordered crystal structure, is still higher than the estimated melting temperature of ChCl found in the literature. In addition, the lowest possible melting enthalpy of ChCl, estimated at the lowest possible melting entropy of a substance with a disordered crystal structure, is higher than the estimated melting enthalpy of ChCl found in the literature. Thus, it was concluded that the melting properties of ChCl found in the literature could be unreasonable.

Although the same argument about the interrelation between melting properties and activity coefficients can be used to question the range of melting properties of ChCl estimated in Paper V, various evidence can support the outcomes of Paper V regarding the nonideality and melting properties of ChCl over the ones in the literature. First, ChCl solid–solid transition was not considered in the literature for modeling SLE data of the ChCl liquidus line. Second, liquidus temperatures above ChCl solid–solid transition were used to estimate the melting properties of ChCl in the literature, which, as shown in Paper V, could not be measured. Therefore, the estimated melting properties of ChCl could be more reasonable than those of the literature studies. Accordingly, the evaluation of the liquid phase nonideality of ChCl-based DES in Paper V could be more realistic than that found in the literature. Given the melting properties and activity coefficients of ChCl found in Paper V, it is clear that the reason why ChCl can form DES is its estimated low melting entropy and enthalpy and the negative deviation from ideality in the liquid phase. These findings well confirm those of Paper I.

## Discussion

Substances with symmetrical and disordered crystal structures are called plastic crystalline materials. Plastic crystalline materials have very low melting entropy and enthalpy but high melting temperature compared to their chemical isomers with ordered crystal structures.<sup>150, 151</sup> The melting entropy of plastic crystalline materials is between 0.5–2 R.<sup>152</sup> Various plastic crystalline materials have been used in the literature as DES constituents besides ChCl. However, the influence of the solid phase plasticity on the observed depression at the eutectic point has not been addressed. Martins et al.<sup>143</sup> studied the eutectic mixtures containing L-menthol or thymol with camphor, borneol, and sobrerol. Camphor and borneol are known plastic crystalline materials. Although all the eutectic systems show ideal solution behavior and the melting temperature of camphor and borneol is higher than sobrerol, the eutectic temperatures observed for eutectic systems containing either camphor or borneol are significantly lower than those containing sobrerol. The eutectic temperatures are: L-menthol/camphor ( $T_e \sim 283$  K), L-menthol/borneol ( $T_e \sim 283$  K), and L-menthol/sorbrerol ( $T_e \sim 331$  K). Therefore, it is evident that plastic crystalline materials can form eutectic mixtures with a large depression at the eutectic point.

Eventually, for the purpose of forming eutectic mixtures with a large depression in the melting temperature of the mixture, constituents with low melting entropy should be selected. The low melting entropy can result from the rigidity and rotational symmetry of molecular structures (Paper II) or the disorder and symmetry of the crystal structure (Paper V). The large depression in the melting temperature of the mixture might aid in extending the number of constituents that can be used or the ratio at which the mixture is liquid below the desired application temperature.

## 5. Conclusion

The work done in this thesis aims to understand the formation of eutectic mixtures with significant depression in the melting temperature of the mixture at the eutectic point. To achieve this goal, SLE in eutectic systems of different complexity was studied based on various theoretical and experimental methods. The SLE phase diagram of 11 binary eutectic systems was reported in the six published papers. The SLE phase diagrams were acquired by rigorous thermal analysis by DSC, solid characterization by powder XRD and SC-XRD, and thermodynamic modeling using correlative and predictive thermodynamic models. In addition to the reported SLE phase diagrams, seven cocrystals in four eutectic systems were identified, five of which were deposited at the Cambridge Crystallographic Data Centre (CCDC).

This thesis shows that the typical DSC protocol used to estimate the SLE data in binary eutectic systems, i.e., in situ crystallization within the DSC run, is unsuitable for measuring the SLE data of eutectic systems prone to glass or cocrystal formation or in the case of polymorphism. In contrast, the proposed sample preparation method in this thesis allowed for measuring the SLE in eutectic systems with large depression at the eutectic point and with significantly low liquidus and solidus temperatures. Moreover, the proposed method allows for combined DSC and XRD analyses, unraveling polymorphism, solid–solid transition, solid solution region, and cocrystal formation.

Correlative and thermodynamic models were found to be capable of well predicting the eutectic point and the SLE phase diagram of eutectic systems of various complexity. However, for modeling SLE in eutectic systems with cocrystal formation, the melting properties and the stoichiometry of the cocrystals are needed, which can be acquired by powder and SC-XRD. Therefore, solid characterization techniques complement SLE modeling to obtain good predictions for the SLE phase diagram and eutectic point of eutectic systems.

By combining the obtained experimental results with the performed theoretical studies, the thesis shows that the reason for DES formation is a combination of strong negative deviation from ideality as well as small melting entropy of pure constituents. The eutectic mixture constituents selection can be based on their molecular structure (rigid and rotationally symmetrical) or crystal structure (plastic crystalline materials).

## 6. Outlook

The majority of DES studied in the literature are ChCl-based eutectic systems. In this thesis, the SLE phase diagram of two ChCl-based DES was reported. Two cocrystals were identified in ChCl/catechol, and one cocrystal was identified in ChCl/hydroquinone. The SLE data of the coformer and cocrystals liquidus lines were used to evaluate the liquid phase nonideality in the two eutectic systems. It was shown that ChCl-based eutectic mixtures show a deep depression at the eutectic point due to strong negative deviation from ideality and low melting enthalpy and entropy of ChCl. However, ChCl is hygroscopic and thermally unstable. Moreover, ChCl-based eutectic mixtures are highly viscous. Therefore, other plastic crystalline materials that can be used as DES constituents while overcoming the drawbacks of ChCl should be sought.

Based on the findings of this thesis, exploring eutectic mixtures containing plastic crystalline materials is encouraged. The complex phase behavior of plastic crystalline materials and their eutectic mixtures, i.e., multiple solid–solid transitions, require expertise in thermal and solid characterization techniques. The measuring and modeling methods presented in this thesis facilitate further research on the phase behavior of eutectic mixture containing plastic crystalline materials. Plastic crystalline materials have already been used in several applications, for example, as phase-change and conducting materials.<sup>153, 154</sup> Therefore, as the melting temperature and physicochemical properties of eutectic mixtures or cocrystals containing plastic crystalline materials could be tuned, further potential applications for eutectic mixtures containing plastic crystalline materials could be found.

So far, there is no robust method to predict the melting properties of thermally unstable substances. In the literature, the melting properties of a thermally unstable substance can be estimated from binary SLE or solubility data. However, estimating the melting properties of thermally unstable substances from solubility or SLE data requires a robust thermodynamic model to predict the nonideality of the liquid solution. The proposed method in Paper V applied to ChCl can be used to indirectly assess the melting properties and activity coefficients of thermally unstable substances. A cocrystal of the thermally unstable substance with a coformer can be prepared, and the liquidus or solubility data of the cocrystal can be used to obtain the correlative thermodynamic model parameters. Then, the SLE or solubility data and the calculated activity coefficients of the thermally unstable substance can be used to estimate the melting

## Outlook

properties of the thermally unstable substance indirectly. The method can be further applied to bioactive thermally unstable substances, such as vitamins and amino acids.

Cocrystal stoichiometry and melting properties are needed to use correlative or predictive thermodynamic models to model SLE in eutectic systems with cocrystal formation. In the case of unavailable melting enthalpy of cocrystals, two approaches have been proposed in the literature for their estimation.<sup>155</sup> In the first approach, the melting enthalpy of the cocrystal is calculated using the melting enthalpy and temperature of pure components and the stoichiometry of the cocrystal. However, it was shown that this approach provides unreliable estimates in many cases. In the second approach, the cocrystal melting properties are estimated by regressing the experimental liquidus data. Obviously, the second approach restricts the advantage of using predictive models for SLE calculations. Therefore, methods for predicting the melting enthalpy of cocrystals are needed to allow for fully predictive modeling of SLE in eutectic systems with cocrystal formation.

In the literature, PC-SAFT was used to successfully model cocrystal solubility in various solvents by calculating the ternary phase diagram of a compound, a coformer, and a solvent<sup>155-158</sup> COSMO-RS was also used in the literature to predict the ternary SLE phase diagram with cocrystal formation.<sup>159</sup> Loschen and Klamt<sup>159</sup> employed COSMO-DARE<sup>160</sup> method, which includes two additional model parameters. The COSMO-DARE parameters were obtained by fitting experimental cocrystal solubility data, which ultimately eliminated the predictive ability of COSMO-RS. Nevertheless, as the work of Loschen and Klamt<sup>159</sup> is the only study employing COSMO-RS for predicting ternary SLE phase diagrams with cocrystal formation, further studies are encouraged to assess COSMO-RS ability to predict binary and ternary SLE phase diagrams with cocrystal formation.

## Abbreviations

CCDC	Cambridge Crystallographic Data Centre
ChCl	choline chloride
COSMO-RS	conductor-like screening model for realistic solvation
DES	deep eutectic solvent
DSC	differential scanning calorimetry
GC	group contribution
HBA	hydrogen bond acceptor
HBD	hydrogen bond donor
IL	ionic liquid
NRTL	non-random two-liquid
RK	Redlich-Kister
SLE	solid-liquid equilibria
SC-XRD	single-crystal X-ray diffraction
XRD	X-ray diffraction

## Symbols

$A^{COSMO}$	COSMO molecular surface area
$a_{eff}$	Effective contact area
$\alpha$	Solid $\alpha$
$\beta$	Solid $\beta$
$Co$	Cocrystal
$c_p$	Constant pressure heat capacity
$\gamma$	Activity coefficient
$\Delta c_{p,m}$	Heat capacity difference at the melting temperature
$\Delta g$	Gibbs energy
$\Delta h$	enthalpy
$\Delta h_m$	Melting enthalpy
$\Delta h^{ref}$	Cocrystal melting enthalpy
$\Delta s$	Entropy
$\Delta s_m$	Melting entropy
$\Delta s_m^{rot}$	Rotational entropy
$\Delta s_m^{conf}$	Conformational entropy
$\Delta s_m^{expan}$	Transitional entropy
$e(\sigma, \sigma')$	Total interaction energy in COSMO-RS
$e_{hb}(\sigma, \sigma')$	Hydrogen bonding interaction energy
$e_{misfit}(\sigma, \sigma')$	Misfit interaction energy
$\varepsilon$	Eccentricity



## Symbols

$f$	Fugacity
$f_0$	Standard state fugacity
$g^E$	Excess Gibbs energy
$K_a$	Equilibrium constant
$L$	Liquid
$\mu_s$	Pseudo-chemical potential
$\mu$	Chemical potential
$\vartheta$	Stoichiometric coefficient
$p(\sigma)$	Probability distribution
$\sigma$	Rotational symmetry number
$R$	Universal gas constant
$S$	solid
$T$	Temperature
$T_m$	Melting temperature
$T^{ref}$	Cocrytal melting temperature
$V^{COSMO}$	COSMO molecular volume
$\Phi$	Flexibility number
$x$	Mole fraction

## List of figures

Figure 1. Schematic representation of solid–liquid phase diagram of (A) binary mixture with miscibility in the solid state and (B) binary eutectic mixture. ....	11
Figure 2. Schematic representations of solid–liquid phase diagrams of different types, defining the crystallized solid phases in each binary eutectic system. ....	12
Figure 3. Schematic structure of differential scanning calorimetry chamber. ....	15
Figure 4. Schematic representation of a phase diagram of a hypothetical binary eutectic mixture and the observed differential scanning calorimetry curve at each labeled point. ....	16
Figure 5. Determining the melting, solidus, and liquidus temperatures and phase transition enthalpy from a differential scanning calorimetry curve. ....	17
Figure 6. Schematic representation of solid–liquid phase diagrams of different types and the obtained Tammann’s plot for each type. ....	18
Figure 7. Schematic representation of a differential scanning calorimetry (DSC) curve of a sample analyzed using the typical DSC protocol: first heating, cooling, and second heating runs. In (A), the sample in situ crystallizes in the DSC during the cooling run, while in (B), the sample undergoes cold crystallization, i.e., crystallization during the heating run. ....	20
Figure 8. Thermodynamic cycle used to derive the solid–liquid equilibrium equation. ....	22
Figure 9. (A) $\sigma$ -profile and (B) $\sigma$ -potential of oxalic acid calculated using density functional theory and COSMO-RS, respectively. ....	29

## References

1. P. Anastas and N. Eghbali. Green Chemistry: Principles and Practice. *Chem. Soc. Rev.* **2010**, 39 (1), 301-312. DOI: 10.1039/B918763B.
2. N. Winterton. The green solvent: a critical perspective. *Clean Technol. Environ. Policy* **2021**, 23 (9), 2499-2522. DOI: 10.1007/s10098-021-02188-8.
3. J. F. Brennecke and E. J. Maginn. Ionic liquids: Innovative fluids for chemical processing. *AIChE J.* **2001**, 47 (11), 2384-2389. DOI: 10.1002/aic.690471102.
4. K. N. Marsh, A. Deev, A. C. T. Wu, E. Tran and A. Klamt. Room temperature ionic liquids as replacements for conventional solvents – A review. *Korean J. Chem. Eng.* **2002**, 19 (3), 357-362. DOI: 10.1007/BF02697140.
5. R. D. Rogers and K. R. Seddon, *Ionic Liquids as Green Solvents*, American Chemical Society, **2003**.
6. K. N. Marsh, J. A. Boxall and R. Lichtenthaler. Room temperature ionic liquids and their mixtures—a review. *Fluid Phase Equilib.* **2004**, 219 (1), 93-98. DOI:10.1016/j.fluid.2004.02.003.
7. S. Werner, M. Haumann and P. Wasserscheid. Ionic Liquids in Chemical Engineering. *Annu. Rev. Chem. Biomol. Eng.* **2010**, 1 (1), 203-230. DOI: 10.1146/annurev-chembioeng-073009-100915.
8. P. Wasserscheid. Volatile times for ionic liquids. *Nature* **2006**, 439 (7078), 797-797. DOI: 10.1038/439797a.
9. C. Jork, C. Kristen, D. Pieraccini, A. Stark, C. Chiappe, Y. A. Beste and W. Arlt. Tailor-made ionic liquids. *J. Chem. Thermodyn.* **2005**, 37 (6), 537-558. DOI:10.1016/j.jct.2005.04.013.
10. B. Tang and K. Row. Recent developments in deep eutectic solvents in chemical sciences. *Monatsh. Chem.* **2013**, 144 (10), 1427-1454. DOI: 10.1007/s00706-013-1050-3.
11. P. E. Rakita, in *Ionic Liquids as Green Solvents*, American Chemical Society, **2003**, 856 (3), 32-40.
12. A. P. Abbott, G. Capper, D. L. Davies, H. L. Munro, R. K. Rasheed and V. Tambyrajah. Preparation of novel, moisture-stable, Lewis-acidic ionic liquids containing quaternary

## References

- ammonium salts with functional side chains. *Chem. Commun.* **2001**, (19), 2010-2011. DOI: 10.1039/B106357J.
13. A. P. Abbott, G. Capper, D. L. Davies, R. K. Rasheed and V. Tambyrajah. Novel solvent properties of choline chloride/urea mixtures. *Chem. Commun.* **2003**, (1), 70-71. DOI: 10.1039/b210714g.
  14. A. P. Abbott, D. Boothby, G. Capper, D. L. Davies and R. K. Rasheed. Deep Eutectic Solvents Formed between Choline Chloride and Carboxylic Acids: Versatile Alternatives to Ionic Liquids. *J. Am. Chem. Soc.* **2004**, 126 (29), 9142-9147. DOI: 10.1021/ja048266j.
  15. E. L. Smith, A. P. Abbott and K. S. Ryder. Deep Eutectic Solvents (DESs) and Their Applications. *Chem. Rev.* **2014**, 114 (21), 11060-11082. DOI: 10.1021/cr300162p.
  16. S. L. Perkins, P. Painter and C. M. Colina. Experimental and computational studies of choline chloride-based deep eutectic solvents. *J. Chem. Eng. Data* **2014**, 59 (11), 3652-3662. DOI: 10.1021/je500520h.
  17. G. García, M. Atilhan and S. Aparicio. The impact of charges in force field parameterization for molecular dynamics simulations of deep eutectic solvents. *J. Mol. Liq.* **2015**, 211, 506-514. DOI:10.1016/j.molliq.2015.07.070.
  18. G. García, M. Atilhan and S. Aparicio. An approach for the rationalization of melting temperature for deep eutectic solvents from DFT. *Chem. Phys. Lett.* **2015**, 634, 151-155. DOI:10.1016/j.cplett.2015.06.017.
  19. D. V. Wagle, C. A. Deakyne and G. A. Baker. Quantum Chemical Insight into the Interactions and Thermodynamics Present in Choline Chloride Based Deep Eutectic Solvents. *J. Phys. Chem. B* **2016**, 120 (27), 6739-6746. DOI: 10.1021/acs.jpccb.6b04750.
  20. S. Zahn, B. Kirchner and D. Mollenhauer. Charge Spreading in Deep Eutectic Solvents. *Chem. Phys. Chem.* **2016**, 17 (21), 3354-3358. DOI: 10.1002/cphc.201600348.
  21. S. Zhu, H. Li, W. Zhu, W. Jiang, C. Wang, P. Wu, Q. Zhang and H. Li. Vibrational analysis and formation mechanism of typical deep eutectic solvents: An experimental and theoretical study. *J. Mol. Graphics Modell.* **2016**, 68, 158-175. DOI: 10.1016/j.jmgm.2016.05.003.
  22. T. Aissaoui, Y. Benguerba and I. M. AlNashef. Theoretical investigation on the microstructure of triethylene glycol based deep eutectic solvents: COSMO-RS and TURBOMOLE prediction. *J. Mol. Struct.* **2017**, 1141, 451-456. DOI: 10.1016/j.molstruc.2017.04.009

## References

23. M. Atilhan and S. Aparicio. Behavior of Deep Eutectic Solvents under External Electric Fields: A Molecular Dynamics Approach. *J. Phys. Chem. B* **2017**, *121* (1), 221-232. DOI: 10.1021/acs.jpcc.6b09714.
24. R. Stefanovic, M. Ludwig, G. B. Webber, R. Atkin and A. J. Page. Nanostructure, hydrogen bonding and rheology in choline chloride deep eutectic solvents as a function of the hydrogen bond donor. *PCCP* **2017**, *19* (4), 3297-3306. DOI: 10.1039/C6CP07932F.
25. S. Zahn. Deep eutectic solvents: similia similibus solvuntur? *PCCP* **2017**, *19* (5), 4041-4047. DOI: 10.1039/C6CP08017K.
26. V. Alizadeh, F. Malberg, A. A. H. Pádua and B. Kirchner. Are There Magic Compositions in Deep Eutectic Solvents? Effects of Composition and Water Content in Choline Chloride/Ethylene Glycol from Ab Initio Molecular Dynamics. *J. Phys. Chem. B* **2020**, *124* (34), 7433-7443. DOI: 10.1021/acs.jpcc.0c04844.
27. S. Kaur, M. Kumari and H. K. Kashyap. Microstructure of Deep Eutectic Solvents: Current Understanding and Challenges. *J. Phys. Chem. B* **2020**, *124* (47), 10601-10616. DOI: 10.1021/acs.jpcc.0c07934.
28. L. Percevault, A. Jani, T. Sohler, L. Noirez, L. Paquin, F. Gauffre and D. Morineau. Do Deep Eutectic Solvents Form Uniform Mixtures Beyond Molecular Microheterogeneities? *J. Phys. Chem. B* **2020**, *124* (41), 9126-9135. DOI: 10.1021/acs.jpcc.0c06317.
29. A. P. Abbott, K. J. Edler and A. J. Page. Deep eutectic solvents—The vital link between ionic liquids and ionic solutions. *J. Chem. Phys.* **2021**, *155* (15), 150401. DOI: 10.1063/5.0072268.
30. S. Kaur, A. Gupta and H. K. Kashyap. Nanoscale Spatial Heterogeneity in Deep Eutectic Solvents. *J. Phys. Chem. B* **2016**, *120* (27), 6712-6720. DOI: 10.1021/acs.jpcc.6b04187.
31. O. S. Hammond, D. T. Bowron and K. J. Edler. Liquid structure of the choline chloride-urea deep eutectic solvent (reline) from neutron diffraction and atomistic modelling. *Green Chem.* **2016**, *18* (9), 2736-2744. DOI: 10.1039/C5GC02914G.
32. I. I. I. Alkhatib, D. Bahamon, F. Llovel, M. R. M. Abu-Zahra and L. F. Vega. Perspectives and guidelines on thermodynamic modelling of deep eutectic solvents. *J. Mol. Liq.* **2020**, *298*, 112183. DOI:10.1016/j.molliq.2019.112183.
33. S. Mainberger, M. Kindlein, F. Bezold, E. Elts, M. Minceva and H. Briesen. Deep eutectic solvent formation: a structural view using molecular dynamics simulations with classical force fields. *Mol. Phys.* **2017**, *115* (9-12), 1309-1321. DOI: 10.1080/00268976.2017.1288936.

## References

34. T. Zhekenov, N. Toksanbayev, Z. Kazakbayeva, D. Shah and F. S. Mjalli. Formation of type III Deep Eutectic Solvents and effect of water on their intermolecular interactions. *Fluid Phase Equilib.* **2017**, *441*, 43-48. DOI:10.1016/j.fluid.2017.01.022.
35. L. Yang, C.-W. Chang and S.-T. Lin. A novel multiscale approach for rapid prediction of phase behaviors with consideration of molecular conformations. *AIChE J.* **2016**, *62* (11), 4047-4054. DOI: 10.1002/aic.15290.
36. Y. Cui, K. D. Fulfer, J. Ma, T. K. Weldeghiorghis and D. G. Kuroda. Solvation dynamics of an ionic probe in choline chloride-based deep eutectic solvents. *PCCP* **2016**, *18* (46), 31471-31479. DOI: 10.1039/C6CP06318G.
37. A. D. Pauric, I. C. Halalay and G. R. Goward. Combined NMR and molecular dynamics modeling study of transport properties in sulfonamide based deep eutectic lithium electrolytes: LiTFSI based binary systems. *PCCP* **2016**, *18* (9), 6657-6667. DOI: 10.1039/C5CP05811B.
38. M. Jasik and B. Szefczyk. Parameterization and optimization of the menthol force field for molecular dynamics simulations. *J. Mol. Model.* **2016**, *22* (10), 234. DOI: 10.1007/s00894-016-3082-1.
39. A. R. Harifi-Mood, R. Ghobadi, S. Matic, B. Minofar and D. Řeha. Solvation analysis of some Solvatochromic probes in binary mixtures of reline, ethaline, and glyceline with DMSO. *J. Mol. Liq.* **2016**, *222*, 845-853. DOI:10.1016/j.molliq.2016.07.036.
40. V. Lesch, A. Heuer, B. R. Rad, M. Winter and J. Smiatek. Atomistic insights into deep eutectic electrolytes: the influence of urea on the electrolyte salt LiTFSI in view of electrochemical applications. *PCCP* **2016**, *18* (41), 28403-28408. DOI: 10.1039/C6CP04217A.
41. R. Ullah, M. Atilhan, B. Anaya, M. Khraisheh, G. Garcia, A. ElKhattat, M. Tariq and S. Aparicio. A detailed study of cholinium chloride and levulinic acid deep eutectic solvent system for CO<sub>2</sub> capture via experimental and molecular simulation approaches. *PCCP* **2015**, *17* (32), 20941-20960. DOI: 10.1039/C5CP03364K.
42. A. Das, S. Das and R. Biswas. Density relaxation and particle motion characteristics in a non-ionic deep eutectic solvent (acetamide + urea): Time-resolved fluorescence measurements and all-atom molecular dynamics simulations. *J. Chem. Phys.* **2015**, *142* (3), 034505. DOI:10.1063/1.4906119.

## References

43. D. Shah and F. S. Mjalli. Effect of water on the thermo-physical properties of Reline: An experimental and molecular simulation based approach. *PCCP* **2014**, *16* (43), 23900-23907. DOI: 10.1039/C4CP02600D.
44. H. Sun, Y. Li, X. Wu and G. Li. Theoretical study on the structures and properties of mixtures of urea and choline chloride. *J. Mol. Model.* **2013**, *19* (6), 2433-2441. DOI: 10.1007/s00894-013-1791-2.
45. F. Dommert, K. Wendler, R. Berger, L. Delle Site and C. Holm. Force Fields for Studying the Structure and Dynamics of Ionic Liquids: A Critical Review of Recent Developments. *Chem. Phys. Chem.* **2012**, *13* (7), 1625-1637. DOI: 10.1002/cphc.201100997.
46. T. Pal and R. Biswas. Heterogeneity and viscosity decoupling in (acetamide + electrolyte) molten mixtures: A model simulation study. *Chem. Phys. Lett.* **2011**, *517* (4–6), 180-185. DOI:10.1016/j.cplett.2011.11.002.
47. M. A. R. Martins, S. P. Pinho and J. A. P. Coutinho. Insights into the Nature of Eutectic and Deep Eutectic Mixtures. *J. Solution Chem.* **2019**, *48* (7), 962-982. DOI: 10.1007/s10953-018-0793-1.
48. A. González de Castilla, J. P. Bittner, S. Müller, S. Jakobtorweihen and I. Smirnova. Thermodynamic and Transport Properties Modeling of Deep Eutectic Solvents: A Review on gE-Models, Equations of State, and Molecular Dynamics. *J. Chem. Eng. Data.* **2019**, *65* (3), 943-967. DOI: 10.1021/acs.jced.9b00548.
49. L. J. B. M. Kollau, M. Vis, A. van den Bruinhorst, A. C. C. Esteves and R. Tuinier. Quantification of the liquid window of deep eutectic solvents. *Chem. Commun.* **2018**, *54* (95), 13351-13354. DOI: 10.1039/C8CC05815F.
50. J. K. U. Ling and K. Hadinoto. Deep Eutectic Solvent as Green Solvent in Extraction of Biological Macromolecules: A Review. *Int. J. Mol. Sci.* **2022**, *23* (6). DOI: 10.3390/ijms23063381.
51. A. Kalyniukova, J. Holuša, D. Musiolek, J. Sedlakova-Kadukova, J. Płotka-Wasyłka and V. Andruch. Application of deep eutectic solvents for separation and determination of bioactive compounds in medicinal plants. *Ind. Crops Products* **2021**, *172*. DOI: 10.1016/j.indcrop.2021.114047.
52. L. Lomba, C. B. García, M. P. Ribate, B. Giner and E. Zuriaga. Applications of deep eutectic solvents related to health, synthesis, and extraction of natural based chemicals. *Appl. Sci.* **2021**, *11* (21). DOI: 10.3390/app112110156.

## References

53. A. S. Dheyab, M. F. A. Bakar, M. Alomar, S. F. Sabran, A. F. M. Hanafi and A. Mohamad. Deep eutectic solvents (DESs) as green extraction media of beneficial bioactive phytochemicals. *Separations* **2021**, 8 (10). DOI: 10.3390/SEPARATIONS8100176.
54. Y. H. Choi and R. Verpoorte. Green solvents for the extraction of bioactive compounds from natural products using ionic liquids and deep eutectic solvents. *Curr. Opin. Food Sci.* **2019**, 26, 87-93. DOI: 10.1016/j.cofs.2019.04.003.
55. D. C. Murador, L. M. de Souza Mesquita, N. Vannuchi, A. R. C. Braga and V. V. de Rosso. Bioavailability and biological effects of bioactive compounds extracted with natural deep eutectic solvents and ionic liquids: advantages over conventional organic solvents. *Curr. Opin. Food Sci.* **2019**, 26, 25-34. DOI: 10.1016/j.cofs.2019.03.002 Scopus.
56. K. M. Jeong, J. Ko, J. Zhao, Y. Jin, D. E. Yoo, S. Y. Han and J. Lee. Multi-functioning deep eutectic solvents as extraction and storage media for bioactive natural products that are readily applicable to cosmetic products. *J. Clean. Prod.* **2017**, 151, 87-95. DOI:10.1016/j.jclepro.2017.03.038.
57. I. Wazeer, M. K. Hadj-Kali and I. M. Al-Nashef. Utilization of Deep Eutectic Solvents to Reduce the Release of Hazardous Gases to the Atmosphere: A Critical Review. *Molecules* **2021**, 26 (1). DOI: 10.3390/molecules26010075.
58. F. Soltanmohammadi, A. Jouyban and A. Shayanfar. New aspects of deep eutectic solvents: extraction, pharmaceutical applications, as catalyst and gas capture. *Chem. Pap.* **2020**, (75), 439-453. DOI: 10.1007/s11696-020-01316-w.
59. S. E. E. Warrag, C. J. Peters and M. C. Kroon. Deep eutectic solvents for highly efficient separations in oil and gas industries. *Curr. Opin. Green Sustain. Chem.* **2017**, 5, 55-60. DOI:10.1016/j.cogsc.2017.03.013.
60. Y. Liu, Z. Dai, Z. Zhang, S. Zeng, F. Li, X. Zhang, Y. Nie, L. Zhang, S. Zhang and X. Ji. Ionic liquids/deep eutectic solvents for CO<sub>2</sub> capture: Reviewing and evaluating. *Green Energy Environ.* **2021**, 6 (3), 314-328. DOI:10.1016/j.gee.2020.11.024.
61. A. Krishnan, K. P. Gopinath, D.-V. N. Vo, R. Malolan, V. M. Nagarajan and J. Arun. Ionic liquids, deep eutectic solvents and liquid polymers as green solvents in carbon capture technologies: a review. *Environ. Chem. Lett.* **2020**, 18 (6), 2031-2054. DOI: 10.1007/s10311-020-01057-y.
62. F. Bezold and M. Minceva. A water-free solvent system containing an L-menthol-based deep eutectic solvent for centrifugal partition chromatography applications. *J. Chromatogr. A* **2019**, 1587, 166-171. DOI:10.1016/j.chroma.2018.11.083.



## References

63. T. Cai and H. Qiu. Application of deep eutectic solvents in chromatography: A review. *TrAC, Trends Anal. Chem.* **2019**, *120*, 115623. DOI:10.1016/j.trac.2019.115623.
64. J. Huang, X. Guo, T. Xu, L. Fan, X. Zhou and S. Wu. Ionic deep eutectic solvents for the extraction and separation of natural products. *J. Chromatogr. A* **2019**, *1598*, 1-19. DOI:10.1016/j.chroma.2019.03.046.
65. I. Pacheco-Fernández and V. Pino. Green solvents in analytical chemistry. *Curr. Opin. Green Sustain. Chem.* **2019**, *18*, 42-50. DOI:10.1016/j.cogsc.2018.12.010.
66. F. Bezold, M. E. Weinberger and M. Minceva. Computational solvent system screening for the separation of tocopherols with centrifugal partition chromatography using deep eutectic solvent-based biphasic systems. *J. Chromatogr. A* **2017**, *1491*, 153-158. DOI:10.1016/j.chroma.2017.02.059.
67. S. Roehrer, F. Bezold, E. M. Garcia and M. Minceva. Deep eutectic solvents in countercurrent and centrifugal partition chromatography. *J. Chromatogr. A* **2016**, *1434*, 102-110. DOI: 10.1016/j.chroma.2016.01.024.
68. N. R. Rodríguez, A. S. B. González, P. M. A. Tijssen and M. C. Kroon. Low transition temperature mixtures (LTTMs) as novel entrainers in extractive distillation. *Fluid Phase Equilib.* **2015**, *385*, 72-78. DOI:10.1016/j.fluid.2014.10.044.
69. F. S. Oliveira, A. B. Pereiro, L. P. N. Rebelo and I. M. Marrucho. Deep eutectic solvents as extraction media for azeotropic mixtures. *Green Chem.* **2013**, *15* (5), 1326-1330. DOI: 10.1039/C3GC37030E.
70. L. Manyoni, B. Kabane and G. G. Redhi. Deep eutectic solvent as a possible entrainer for industrial separation problems: Pre-screening tool for solvent selection. *Fluid Phase Equilib.* **2022**, *553*, 113266. DOI:10.1016/j.fluid.2021.113266.
71. F. Bai, C. Hua, Y. Bai and M. Ma. Design Optimization of Deep Eutectic Solvent Composition and Separation Performance of Cyclohexane and Benzene Mixtures with Extractive Distillation. *Processes* **2021**, *9* (10). DOI: 10.3390/pr9101706.
72. V. Hamilton, I. Andrusenko, J. Potticary, C. Hall, R. Stenner, E. Mugnaioli, A. E. Lanza, M. Gemmi and S. R. Hall. Racemic Conglomerate Formation via Crystallization of Metaxalone from Volatile Deep Eutectic Solvents. *Cryst. Growth Des.* **2020**, *20* (7), 4731-4739. DOI: 10.1021/acs.cgd.0c00497.
73. C. L. Hall, J. Potticary, V. Hamilton, S. Gaisford, A. Buanz and S. R. Hall. Metastable crystalline phase formation in deep eutectic systems revealed by simultaneous

## References

- synchrotron XRD and DSC. *Chem. Commun.* **2020**, 56 (73), 10726-10729. DOI: 10.1039/d0cc04696e.
74. F. Wolbert, C. Brandenbusch and G. Sadowski. Selecting Excipients Forming Therapeutic Deep Eutectic Systems-A Mechanistic Approach. *Mol. Pharm.* **2019**, 16 (7), 3091-3099. DOI: 10.1021/acs.molpharmaceut.9b00336.
75. A. Gutiérrez, S. Aparicio and M. Atilhan. Design of arginine-based therapeutic deep eutectic solvents as drug solubilization vehicles for active pharmaceutical ingredients. *PCCP* **2019**, 21 (20), 10621-10634. DOI: 10.1039/C9CP01408J.
76. M. S. Álvarez and Y. Zhang. Sketching neoteric solvents for boosting drugs bioavailability. *J. Controlled Release* **2019**, 311-312, 225-232. DOI:10.1016/j.jconrel.2019.09.008.
77. A. R. C. Duarte, A. S. D. Ferreira, S. Barreiros, E. Cabrita, R. L. Reis and A. Paiva. A comparison between pure active pharmaceutical ingredients and therapeutic deep eutectic solvents: Solubility and permeability studies. *Eur. J. Pharm. Sci.* **2017**, 114, 296-304. DOI:10.1016/j.ejpb.2017.02.003.
78. I. M. Aroso, J. C. Silva, F. Mano, A. S. D. Ferreira, M. Dionísio, I. Sá-Nogueira, S. Barreiros, R. L. Reis, A. Paiva and A. R. C. Duarte. Dissolution enhancement of active pharmaceutical ingredients by therapeutic deep eutectic systems. *Eur. J. Pharm. Sci.* **2016**, 98, 57-66. DOI:10.1016/j.ejpb.2015.11.002.
79. I. M. Aroso, R. Craveiro, Â. Rocha, M. Dionísio, S. Barreiros, R. L. Reis, A. Paiva and A. R. C. Duarte. Design of controlled release systems for THEDES—Therapeutic deep eutectic solvents, using supercritical fluid technology. *Int. J. Pharm.* **2015**, 492 (1–2), 73-79. DOI:10.1016/j.ijpharm.2015.06.038.
80. H. Gamsjäger, W. Lorimer John, P. Scharlin and G. Shaw David, Glossary of terms related to solubility (IUPAC Recommendations 2008), *Pure Appl. Chem.* **2008**, 80 (2), 233-276. DOI:10.1351/pac200880020233
81. J. Gmehling, M. Kleiber, B. Kolbe and J. Rarey, *Chemical Thermodynamics for Process Simulation*, Wiley, **2019**.
82. A. I. Kitaigorodskii, *Mixed crystals*, Springer-Verlag, Berlin, **1984**.
83. L. Rycerz. Practical remarks concerning phase diagrams determination on the basis of differential scanning calorimetry measurements. *J. Therm. Anal. Calorim.* **2013**, 113 (1), 231-238. DOI: 10.1007/s10973-013-3097-0.

## References

84. A. van den Bruinhorst, L. J. B. M. Kollau, M. C. Kroon, J. Meuldijk, R. Tuinier and A. C. C. Esteves. A centrifuge method to determine the solid–liquid phase behavior of eutectic mixtures. *J. Chem. Phys.* **2018**, *149* (22), 224505. DOI: 10.1063/1.5051515.
85. L. P. Silva, M. A. R. Martins, J. H. F. Conceição, S. P. Pinho and J. A. P. Coutinho. Eutectic Mixtures Based on Polyalcohols as Sustainable Solvents: Screening and Characterization. *ACS Sustain. Chem. Eng.* **2020**, *8* (40), 15317-15326. DOI: 10.1021/acssuschemeng.0c05518.
86. L. P. Silva, C. F. Araújo, D. O. Abranches, M. Melle-Franco, M. A. R. Martins, M. M. Nolasco, P. J. A. Ribeiro-Claro, S. P. Pinho and J. A. P. Coutinho. What a difference a methyl group makes – probing choline–urea molecular interactions through urea structure modification. *PCCP* **2019**, *21* (33), 18278-18289. DOI: 10.1039/C9CP03552D.
87. L. P. Silva, L. Fernandez, J. H. F. Conceição, M. A. R. Martins, A. Sosa, J. Ortega, S. P. Pinho and J. A. P. Coutinho. Design and Characterization of Sugar-Based Deep Eutectic Solvents Using Conductor-like Screening Model for Real Solvents. *ACS Sustain. Chem. Eng.* **2018**, *6* (8), 10724-10734. DOI: 10.1021/acssuschemeng.8b02042.
88. E. A. Crespo, L. P. Silva, M. A. R. Martins, M. Bülow, O. Ferreira, G. Sadowski, C. Held, S. P. Pinho and J. A. P. Coutinho. The Role of Polyfunctionality in the Formation of [Ch]Cl-Carboxylic Acid-Based Deep Eutectic Solvents. *Ind. Eng. Chem. Res.* **2018**, *57* (32), 11195-11209. DOI: 10.1021/acs.iecr.8b01249.
89. E. A. Crespo, L. P. Silva, M. A. R. Martins, L. Fernandez, J. Ortega, O. Ferreira, G. Sadowski, C. Held, S. P. Pinho and J. A. P. Coutinho. Characterization and Modeling of the Liquid Phase of Deep Eutectic Solvents Based on Fatty Acids/Alcohols and Choline Chloride. *Ind. Eng. Chem. Res.* **2017**, *56* (42), 12192-12202. DOI: 10.1021/acs.iecr.7b02382.
90. L. Fernandez, L. P. Silva, M. A. R. Martins, O. Ferreira, J. Ortega, S. P. Pinho and J. A. P. Coutinho. Indirect assessment of the fusion properties of choline chloride from solid-liquid equilibria data. *Fluid Phase Equilib.* **2017**, *448*, 9-14. DOI: 10.1016/j.fluid.2017.03.015.
91. X. Meng, K. Ballerat-Busserolles, P. Husson and J.-M. Andanson. Impact of water on the melting temperature of urea + choline chloride deep eutectic solvent. *New J. Chem.* **2016**, *40* (5), 4492-4499. DOI: 10.1039/C5NJ02677F.

## References

92. I. Chojnacka, L. Rycerz, M. Berkani and M. Gaune-Escard. Phase diagram and electrical conductivity of the DyBr<sub>3</sub>–RbBr binary system. *J. Therm. Anal. Calorim.* **2012**, *108* (2), 481-488. DOI: 10.1007/s10973-011-2017-4.
93. R. M. Saeed, J. Schlegel, C. Castano and R. Sawafta. Uncertainty of thermal characterization of phase change material by differential scanning calorimetry analysis. *Int. J. Eng. Res. Technol* **2016**, *5* (1), 405-412.
94. Y. Corvis, P. Négrier, M. Lazerges, S. Massip, J.-M. Léger and P. Espeau. Lidocaine/l-Menthol Binary System: Cocrystallization versus Solid-State Immiscibility. *J. Phys. Chem. B* **2010**, *114* (16), 5420-5426. DOI: 10.1021/jp101303j.
95. Y. Corvis, P. Négrier, S. Massip, J.-M. Leger and P. Espeau. Insights into the crystal structure, polymorphism and thermal behavior of menthol optical isomers and racemates. *Cryst. Eng. Comm.* **2012**, *14* (20), 7055-7064. DOI: 10.1039/C2CE26025E.
96. A. van den Bruinhorst, L. J. B. M. Kollau, M. Vis, M. M. R. M. Hendrix, J. Meuldijk, R. Tuinier and A. C. C. Esteves. From a eutectic mixture to a deep eutectic system via anion selection: Glutaric acid + tetraethylammonium halides. *J. Chem. Phys.* **2021**, *155* (1), 014502. DOI: 10.1063/5.0050533.
97. L. J. B. M. Kollau, R. Tuinier, J. Verhaak, J. den Doelder, I. A. W. Filot and M. Vis. Design of Nonideal Eutectic Mixtures Based on Correlations with Molecular Properties. *J. Phys. Chem. B* **2020**, *124* (25), 5209-5219. DOI: 10.1021/acs.jpccb.0c01680.
98. L. J. B. M. Kollau, M. Vis, A. van den Bruinhorst, R. Tuinier and G. de With. Entropy models for the description of the solid–liquid regime of deep eutectic solutions. *J. Mol. Liq.* **2020**, *302*, 112155. DOI:10.1016/j.molliq.2019.112155.
99. M. Kick, P. Keil and A. König. Solid–liquid phase diagram of the two Ionic Liquids EMIMCl and BMIMCl. *Fluid Phase Equilib.* **2013**, *338*, 172-178. DOI:10.1016/j.fluid.2012.11.007.
100. D. O. Abranches, M. A. R. Martins, L. P. Silva, N. Schaeffer, S. P. Pinho and J. A. P. Coutinho. Phenolic hydrogen bond donors in the formation of non-ionic deep eutectic solvents: the quest for type V DES. *Chem. Commun.* **2019**, *55* (69), 10253-10256. DOI: 10.1039/c9cc04846d.
101. E. Gómez, N. Calvar, Á. Domínguez and E. A. Macedo. Thermal Analysis and Heat Capacities of 1-Alkyl-3-methylimidazolium Ionic Liquids with NTf<sub>2</sub><sup>-</sup>, TFO<sup>-</sup>, and DCA<sup>-</sup> Anions. *Ind. Eng. Chem. Res.* **2013**, *52* (5), 2103-2110. DOI: 10.1021/ie3012193.
102. J. M. Prausnitz, R. N. Lichtenthaler and E. G. d. Azevedo, *Molecular Thermodynamics of Fluid-Phase Equilibria*, Prentice Hall PTR, Upper Saddle River, NJ, **1999**.

## References

103. A. Jain, G. Yang and S. H. Yalkowsky. Estimation of Melting Points of Organic Compounds. *Ind. Eng. Chem. Res.* **2004**, 43 (23), 7618-7621. DOI: 10.1021/ie049378m.
104. S. H. Yalkowsky. Carnelley's Rule and the Prediction of Melting Point. *J. Pharm. Sci.* **2014**, 103 (9), 2629-2634. DOI: 10.1002/jps.24034.
105. B. Lian and S. H. Yalkowsky. Molecular Geometry and Melting Point Related Properties. *Ind. Eng. Chem. Res.* **2012**, 51 (51), 16750-16754. DOI: 10.1021/ie302574y.
106. J. S. Chickos, G. Nichols and P. Ruelle. The Estimation of Melting Points and Fusion Enthalpies Using Experimental Solubilities, Estimated Total Phase Change Entropies, and Mobile Order and Disorder Theory. *J. Chem. Inf. Comput. Sci.* **2002**, 42 (2), 368-374. DOI: 10.1021/ci010341b.
107. J. S. Chickos, W. E. Acree Jr and J. F. Liebman. Estimating solid-liquid phase change enthalpies and entropies. *J. Phys. Chem. Ref. Data* **1999**, 28 (6), 1535-1673.
108. W. Acree and J. S. Chickos. Phase Transition Enthalpy Measurements of Organic and Organometallic Compounds. Sublimation, Vaporization and Fusion Enthalpies From 1880 to 2015. Part 1. C1 – C10. *J. Phys. Chem. Ref. Data* **2016**, 45 (3), 033101. DOI: 10.1063/1.4948363.
109. A. Bondi. *Physical properties of molecular crystals, liquids, and glasses*. Wiley, **1968**.
110. S. H. Yalkowsky. Estimation of Entropies of Fusion of Organic Compounds. *Ind. Eng. Chem. Fund.* **1979**, 18 (2), 108-111. DOI: 10.1021/i160070a003.
111. R.-M. Dannenfelser and S. H. Yalkowsky. Estimation of Entropy of Melting from Molecular Structure: A Non-Group Contribution Method. *Ind. Eng. Chem. Res.* **1996**, 35 (4), 1483-1486. DOI: 10.1021/ie940581z.
112. A. Jain, G. Yang and S. H. Yalkowsky. Estimation of Total Entropy of Melting of Organic Compounds. *Ind. Eng. Chem. Res.* **2004**, 43 (15), 4376-4379. DOI: 10.1021/ie0497745.
113. P. Walden. Über die Schmelzwärme, spezifische Kohäsion und Molekulargröße bei der Schmelztemperatur. *Zeitschrift für Elektrochemie und angewandte physikalische Chemie* **1908**, 14 (43), 713-724. DOI: 10.1002/bbpc.19080144302.
114. B. Lian and S. H. Yalkowsky. Molecular geometry and boiling related thermodynamic properties. *J. Chem. Thermodyn.* **2012**, 54, 250-253. DOI:10.1016/j.jct.2012.04.009.
115. D. S. Mishra and S. H. Yalkowsky. Ideal Solubility of a Solid Solute: Effect of Heat Capacity Assumptions. *Pharm. Res.* **1992**, 9 (7), 958-959. DOI: 10.1023/A:1015873521067.

## References

116. D. J. W. Grant, M. Mehdizadeh, A. H. L. Chow and J. E. Fairbrother. Non-linear van't Hoff solubility-temperature plots and their pharmaceutical interpretation. *Int. J. Pharm.* **1984**, 18 (1), 25-38. DOI:10.1016/0378-5173(84)90104-2.
117. H. T. Do, Y. Z. Chua, J. Habicht, M. Klinksiek, M. Hallermann, D. Zaitsau, C. Schick and C. Held. Melting properties of peptides and their solubility in water. Part 1: dipeptides based on glycine or alanine. *RSC Advances* **2019**, 9 (56), 32722-32734. DOI: 10.1039/C9RA05730G.
118. S. H. Yalkowsky and M. Wu. Estimation of the ideal solubility (crystal-liquid fugacity ratio) of organic compounds. *J. Pharm. Sci.* **2010**, 99 (3), 1100-1106. DOI:10.1002/jps.21897.
119. G. D. Pappa, E. C. Voutsas, K. Magoulas and D. P. Tassios. Estimation of the differential molar heat capacities of organic compounds at their melting point. *Ind. Eng. Chem. Res.* **2005**, 44 (10), 3799-3806. DOI: 10.1021/ie048916s.
120. J. Hildebrand, J. Prausnitz and R. Scott. *Regular and related solutions: the solubility of gases. Liquids, and Solids*, Van Nostrand Reinhold Co., New York, **1970**.
121. M. Wu and S. Yalkowsky. Estimation of the molar heat capacity change on melting of organic compounds. *Ind. Eng. Chem. Res.* **2009**, 48 (2), 1063-1066. DOI: 10.1021/ie801587c.
122. S. H. Neau, S. V. Bhandarkar and E. W. Hellmuth. Differential molar heat capacities to test ideal solubility estimations. *Pharm. Res.* **1997**, 14 (5), 601-605. DOI: 10.1023/A:1012148910975.
123. R. Shaw. Heat capacities of liquids. Estimation of heat capacity at constant pressure and 25.deg., using additivity rules. *J. Chem. Eng. Data.* **1969**, 14 (4), 461-465. DOI: 10.1021/je60043a036.
124. V. Růžička Jr and E. S. Domalski. Estimation of the heat capacities of organic liquids as a function of temperature using group additivity. I. Hydrocarbon compounds. *J. Phys. Chem. Ref. Data* **1993**, 22 (3), 597-618. DOI: 10.1063/1.555923.
125. Z. Kolská, J. Kukul, M. Záborský and V. Růžička. Estimation of the heat capacity of organic liquids as a function of temperature by a three-level group contribution method. *Ind. Eng. Chem. Res.* **2008**, 47 (6), 2075-2085. DOI: 10.1021/ie071228z.
126. L. J. B. M. Kollau, M. Vis, A. van den Bruinhorst, G. de With and R. Tuinier. Activity modelling of the solid-liquid equilibrium of deep eutectic solvents. *Pure Appl. Chem.* **2019**, 91 (8), 1341-1349. DOI:10.1515/pac-2018-1014.

## References

127. G. M. Wilson. Vapor-liquid equilibrium. XI. A new expression for the excess free energy of mixing. *J. Am. Chem. Soc.* **1964**, *86* (2), 127-130.
128. H. Renon and J. M. Prausnitz. Local compositions in thermodynamic excess functions for liquid mixtures. *AIChE J.* **1968**, *14* (1), 135-144. DOI:10.1002/aic.690140124.
129. A. Klamt. The COSMO and COSMO-RS solvation models. *WIREs Comput. Mol. Sci.* **2011**, *1* (5), 699-709. DOI: 10.1002/wcms.56.
130. F. Eckert and A. Klamt. Fast solvent screening via quantum chemistry: COSMO-RS approach. *AIChE J.* **2004**, *48* (2), 369-385. DOI: 10.1002/aic.690480220.
131. F. Eckert and A. Klamt. Fast solvent screening via quantum chemistry: COSMO-RS approach. *AIChE J.* **2002**, *48* (2), 369-385. DOI: 10.1002/aic.690480220.
132. A. Klamt, F. Eckert and M. Hornig. COSMO-RS: A novel view to physiological solvation and partition questions. *J. Comput. Aided Mol. Des.* **2001**, *15* (4), 355-365. DOI: 10.1023/A:1011111506388.
133. M. M. Abdallah, S. Müller, A. González de Castilla, P. Gurikov, A. A. Matias, M. D. Bronze and N. Fernández. Physicochemical Characterization and Simulation of the Solid-Liquid Equilibrium Phase Diagram of Terpene-Based Eutectic Solvent Systems. *Molecules* **2021**, *26* (6). DOI: 10.3390/molecules26061801.
134. Z. Song, J. Wang and K. Sundmacher. Evaluation of COSMO-RS for solid-liquid equilibria prediction of binary eutectic solvent systems. *Green Energy Environ.* **2021**, *6* (3), 371-379. DOI:10.1016/j.gee.2020.11.020.
135. D. O. Abranches, M. Larriba, L. P. Silva, M. Melle-Franco, J. F. Palomar, S. P. Pinho and J. A. P. Coutinho. Using COSMO-RS to design choline chloride pharmaceutical eutectic solvents. *Fluid Phase Equilib.* **2019**, *497*, 71-78. DOI: 10.1016/j.fluid.2019.06.005.
136. S. M. Vilas-Boas, D. O. Abranches, E. A. Crespo, O. Ferreira, J. A. P. Coutinho and S. P. Pinho. Experimental solubility and density studies on aqueous solutions of quaternary ammonium halides, and thermodynamic modelling for melting enthalpy estimations. *J. Mol. Liq.* **2020**, *300*, 112281. DOI:10.1016/j.molliq.2019.112281.
137. N. R. Rodriguez, T. Gerlach, D. Scheepers, M. C. Kroon and I. Smirnova. Experimental determination of the LLE data of systems consisting of {hexane + benzene + deep eutectic solvent} and prediction using the Conductor-like Screening Model for Real Solvents. *J. Chem. Thermodyn.* **2017**, *104*, 128-137. DOI:10.1016/j.jct.2016.09.021.

## References

138. A. S. L. Gouveia, F. S. Oliveira, K. A. Kurnia and I. M. Marrucho. Deep Eutectic Solvents as Azeotrope Breakers: Liquid–Liquid Extraction and COSMO-RS Prediction. *ACS Sustain. Chem. Eng.* **2016**, 4 (10), 5640-5650. DOI: 10.1021/acssuschemeng.6b01542.
139. F. Bezold, M. E. Weinberger and M. Minceva. Assessing solute partitioning in deep eutectic solvent-based biphasic systems using the predictive thermodynamic model COSMO-RS. *Fluid Phase Equilib.* **2017**, 437, 23-33. DOI:10.1016/j.fluid.2017.01.001.
140. X. Liu, Y. Nie, Y. Liu, S. Zhang and A. L. Skov. Screening of Ionic Liquids for Keratin Dissolution by Means of COSMO-RS and Experimental Verification. *ACS Sustain. Chem. Eng.* **2018**, 6 (12), 17314-17322. DOI: 10.1021/acssuschemeng.8b04830.
141. H. Qin, Z. Wang, T. Zhou and Z. Song. Comprehensive Evaluation of COSMO-RS for Predicting Ternary and Binary Ionic Liquid-Containing Vapor–Liquid Equilibria. *Ind. Eng. Chem. Res.* **2021**, 60 (48), 17761-17777. DOI: 10.1021/acs.iecr.1c03940.
142. T. Aissaoui, I. M. AlNashef and Y. Benguerba. Dehydration of natural gas using choline chloride based deep eutectic solvents: COSMO-RS prediction. *J. Nat. Gas Sci. Eng.* **2016**, 30, 571-577. DOI: 10.1016/j.jngse.2016.02.007.
143. M. A. R. Martins, L. P. Silva, N. Schaeffer, D. O. Abranches, G. J. Maximo, S. P. Pinho and J. A. P. Coutinho. Greener Terpene–Terpene Eutectic Mixtures as Hydrophobic Solvents. *ACS Sustain. Chem. Eng.* **2019**, 7 (20), 17414-17423. DOI: 10.1021/acssuschemeng.9b04614.
144. C.-C. Huang and Y.-P. Chen. Measurements and model prediction of the solid–liquid equilibria of organic binary mixtures. *Chem. Eng. Sci.* **2000**, 55 (16), 3175-3185. DOI: 10.1016/S0009-2509(99)00593-X.
145. J. A. P. Coutinho. Predictive local composition models: NRTL and UNIQUAC and their application to model solid–liquid equilibrium of n-alkanes. *Fluid Phase Equilib.* **1999**, 158-160, 447-457. DOI:10.1016/S0378-3812(99)00085-0.
146. J. A. P. Coutinho. Predictive UNIQUAC: A New Model for the Description of Multiphase Solid–Liquid Equilibria in Complex Hydrocarbon Mixtures. *Ind. Eng. Chem. Res.* **1998**, 37 (12), 4870-4875. DOI: 10.1021/ie980340h.
147. J. A. P. Coutinho and E. H. Stenby. Predictive Local Composition Models for Solid/Liquid Equilibrium in n-Alkane Systems: Wilson Equation for Multicomponent Systems. *Ind. Eng. Chem. Res.* **1996**, 35 (3), 918-925. DOI: 10.1021/ie950447u.



## References

148. A. Alhadid, L. Mokrushina and M. Minceva. Influence of the Molecular Structure of Constituents and Liquid Phase Non-Ideality on the Viscosity of Deep Eutectic Solvents. *Molecules* **2021**, 26 (14). DOI: 10.3390/molecules26144208.
149. R. Srinivasa Gopalan, P. Kumaradhas, G. U. Kulkarni and C. N. R. Rao. An experimental charge density study of aliphatic dicarboxylic acids. *J. Mol. Struct.* **2000**, 521 (1), 97-106. DOI:10.1016/S0022-2860(99)00293-8.
150. R. N. Rogers and L. W. Ortiz. Thermal characterization of the plastic crystalline phase. *Thermochim. Acta* **1972**, 3 (5), 379-381. DOI:10.1016/0040-6031(72)87051-5.
151. J. Timmermans. Plastic crystals: A historical review. *J. Phys. Chem. Solids* **1961**, 18 (1), 1-8. DOI:10.1016/0022-3697(61)90076-2.
152. R. J. C. Brown and R. F. C. Brown. Melting Point and Molecular Symmetry. *J. Chem. Educ.* **2000**, 77 (6), 724. DOI: 10.1021/ed077p724.
153. S. Das, A. Mondal and C. M. Reddy. Harnessing molecular rotations in plastic crystals: a holistic view for crystal engineering of adaptive soft materials. *Chem. Soc. Rev.* **2020**, 49 (24), 8878-8896. DOI: 10.1039/D0CS00475H.
154. P.-J. Alarco, Y. Abu-Lebdeh, A. Abouimrane and M. Armand. The plastic-crystalline phase of succinonitrile as a universal matrix for solid-state ionic conductors. *Nature Materials* **2004**, 3 (7), 476-481. DOI: 10.1038/nmat1158.
155. F. Tumakaka, I. V. Prikhodko and G. Sadowski. Modeling of solid-liquid equilibria for systems with solid-complex phase formation. *Fluid Phase Equilib.* **2007**, 260 (1), 98-104. DOI:10.1016/j.fluid.2007.05.028.
156. L. Lange and G. Sadowski. Polymorphs, Hydrates, Cocrystals, and Cocrystal Hydrates: Thermodynamic Modeling of Theophylline Systems. *Cryst. Growth Des.* **2016**, 16 (8), 4439-4449. DOI: 10.1021/acs.cgd.6b00554.
157. L. Lange, S. Heisel and G. Sadowski. Predicting the Solubility of Pharmaceutical Cocrystals in Solvent/Anti-Solvent Mixtures. *Molecules* **2016**, 21 (5). DOI: 10.3390/molecules21050593.
158. L. Lange and G. Sadowski. Thermodynamic Modeling for Efficient Cocrystal Formation. *Cryst. Growth Des.* **2015**, 15 (9), 4406-4416. DOI: 10.1021/acs.cgd.5b00735.
159. C. Loschen and A. Klamt. Cocrystal Ternary Phase Diagrams from Density Functional Theory and Solvation Thermodynamics. *Cryst. Growth Des.* **2018**, 18 (9), 5600-5608. DOI: 10.1021/acs.cgd.8b00923.

## References

160. T. Sachsenhauser, S. Rehfeldt, A. Klamt, F. Eckert and H. Klein. Consideration of dimerization for property prediction with COSMO-RS-DARE. *Fluid Phase Equilib.* **2014**, 382, 89-99. DOI: 10.1016/j.fluid.2014.08.030.